# Geothermal Systems in District Heating and Cooling: Multi-objective and Artificial Neural Network Methods for Exergo- and Enviro-economic Optimization

## Dissertation

Doctoral thesis submitted in fulfillment of the requirements
for the degree of Doktor-Ingenieur (Dr.-Ing.)
at the
Department of Material and Earth Sciences,
Technical University of Darmstadt

TECHNISCHE
UNIVERSITÄT
DARMSTADT

Graduate School of
Energy Science
and Engineering


Submitted by

M.Sc. Hoofar Hemmatabady
born on 16.09.1985 in Tehran, Iran

Supervisor Prof. Dr. Ingo Sass
Co-supervisor Prof. Dr. Johannes Janicka


Darmstadt 2022

Hemmatabady, Hoofar: Geothermal Systems in District Heating and Cooling: Multi-objective and Artificial Neural Network Methods for Exergo- and Enviro-economic Optimization
Darmstadt, Technische Universität Darmstadt
Year thesis published in TUprints: 2022
URN: urn:nbn:de:tuda-tuprints-221805
Date of viva voce: 14th June 2022

Board of examiners

| | |
|---|---|
| Supervisor: | Prof. Dr. Ingo Sass |
| Co-supervisor: | Prof. Dr. Johannes Janicka |
| Examiner: | Prof. Dr. Eva Schill |
| Examiner: | Prof. Dr. Christoph Schüth |

## Declaration

I hereby declare that the presented dissertation is based on original research and is the result of my own work. I certify that this dissertation contains no material which has been accepted for the award of any other degree in my name, in any university or other tertiary institution and, to the best of my knowledge and belief, contains no material previously published or written by another person, except where due reference has been made in the text.

Darmstadt, 27th March 2021

## Abstract

The significant share of heating, the increasing demand of cooling and the increasing trend towards smart energy systems has made sustainable district heating and cooling (DHC) a viable option for future energy supply in European households. The temporal mismatch between supply and demand is a major obstacle towards the increased utilization of solar energy and waste heat, which can be overcome by seasonal energy storage technologies. Borehole thermal energy storage (BTES) is such a technology. Due to complexity of smart DHC networks, BTES systems need to be implemented considering their interaction with other system components. This has been a main issue that has led to reduced efficiency of some existing projects. Consequently, to exploit BTES systems in sustainable thermal load supply, design guidelines are required for their efficient integration in DHC networks.

In this study, Considering the experience from demonstration and pilot projects, different configurations of BTES systems are proposed. The scenarios are categorized into solar-coupled or standalone for heating or combined heating and cooling applications, which are modelled and parametrized in TRNSYS. The proposed scenarios need to be evaluated from technical, economic and environmental points of view in order to ensure efficient operation and to promote market growth. To do so, a dynamic exergo-economic assessment approach is adapted to geothermal systems and is utilized to optimize the scenarios from technical and economic aspects. Moreover, an enviro-economic method is utilized to simultaneously minimize cost and emissions. Finally, the results from exergo- and enviro-economic methods are compared and discussed.

For conducting multi-objective optimizations using the proposed evaluation methods, different computational models are proposed and improved at each stage of this study. Initially, a direct optimization approach is developed by coupling TRNSYS and MATLAB. Thereafter, to cope with the high computational cost of the required long-term assessments of geothermal systems, an indirect optimization method is proposed. The indirect method utilizes an artificial neural network (ANN) as a proxy model in an intermediate step of the multi-objective optimization procedure. Furthermore, parallel computation of the objective functions is implemented in the computational model to enhance the speed of the direct and indirect optimizations. Finally, a step-wise optimization method is developed for the operational optimization and control of geothermal systems.

Utilizing the developed computational models, multi-objective optimization results of solar-coupled and standalone geothermal layouts reveal that the lowest emissions are realized by central solar-coupled systems, which are discharged actively by heat pumps. Lowering grid temperature level of solar-coupled systems using decentral heat pumps leads to efficient system designs with lower costs, though the most efficient system layouts consist of central heat pumps. Moreover, standalone geothermal systems with passive cooling are suggested as systems with the lowest costs as well as reasonably low emissions and thermodynamic inefficiencies for combined heating and cooling applications. Finally, a hybrid design of solar-coupled and standalone geothermal layouts for combined heating and cooling applications improves the system's performance compared to each layout separately.

The comparison between the results of exergo- and enviro-economic optimization methods confirms that an increase in exergetic efficiency leads to a decrease in environmental impacts and both methods show the same ranking for the evaluated scenarios. Enviro-economic approach is

suggested for defining dimensions of geothermal systems, which needs to be supplemented by the developed dynamic exergy analysis to analyze and optimize the operation of different components of a geothermal layout. Finally, the combination of an ANN and multi-objective optimization methods has proven to be an accurate and robust approach for long-term evaluation and comparison of geothermal heating and cooling systems.

**Acknowledgement**

Foremost, I would like to thank my advisor Prof. Dr. Ingo Sass for his supervision and support. He enabled me to pursue my interest in renewable energies and gave me space to develop my own ideas. He endorsed me to be a member of the Darmstadt Graduate School of Excellence Energy Science and Engineering, which provided me the opportunity to exchange ideas with other scientist in an interdisciplinary environment. I would also like to thank Prof. Dr.-Ing. Johannes Janicka for the co-supervision of my study and his support at the graduate school.

Furthermore, I would like to express my special thanks to my colleagues Dr.-Ing Bastian Welsch and Dr.-Ing Daniel Schulte, who were always there to provide me with valuable advices and supports to enhance my work. Many warm thanks go to my colleague Julian Formhals for his personal and technical supports. We had many constructive talks about our research and his ideas improved this thesis a lot.

I would also like to thank the German Research Foundation (DFG) for 39 months of the scholarship in the framework of the Excellence Initiative, Darmstadt Graduate School of Excellence Energy Science and Engineering (GSC 1070). In this context, I thank Dr. Tanja Drobek, who managed the graduate school, for her supports. Moreover, I thank Simone Roß-Krichbaum and Eva Ruffing, for their friendly administrative supports.

Last but not least, many special thanks go to my family, especially my father and mother, for their indefinite support and love.

## Preface

The PhD dissertation is based on a research proposal at the Geothermal Science and Technology group of TU Darmstadt to assess efficient integration of geothermal systems in DHC grids. My research was funded through a scholarship by the Darmstadt Graduate School of Excellence Energy Science and Engineering (GSC 1070), which is financed by the German Research Foundation (DFG) in the framework of the Excellence Initiative.

Technical, environmental and economic assessment of geothermal systems were already a main focus of the works of my colleague Dr.-Ing. Bastian Welsch. He conducted comprehensive parametric studies to optimize BTES systems separately (Welsch et al. 2016a) or as a component of DH grids (Welsch et al. 2018). My colleague Dr.-Ing. Daniel Schulte assessed numerical modelling and simulation of BTES systems (Schulte 2016). He carried out optimization studies to optimize the size of the BTES systems, utilizing Proxy models (Schulte et al. 2016a). In parallel to me, my colleague Julian Formhals focused on model development of BTES systems (Formhals et al. 2021b) in Modelica, MoBTES. Later on, he complemented his work by developing components of SDH, called MoSDH. Utilizing the developed models, he assessed different transition strategies towards a SDH grid with integrated BTES (Formhals et al. 2021a).

As a complement of the previous works in our working group, I focused on development of evaluation methodologies and multi-objective optimization methods for designing geothermal systems in DHC grids. The highlights of my work can be summarized as follow:

1) Simulation and validation of geothermal systems in district heating and cooling grids.
2) Technical, environmental and economic assessment of geothermal layouts.
3) Development of computational models to perform coupled simulation and multi-objective optimization.
4) Implementation of machine learning methods to evaluate and optimize the performance of geothermal systems.

The investigated geothermal layouts, which are mainly proposed based on real case studies, are discussed (chapter 3) and simulated in TRNSYS. Exergo- and enviro-economic methods are utilized for the assessment of the proposed layouts (chapter 4). In this context, a dynamic exergy analysis method is adapted for the technical assessment of the geothermal layouts as well as separate BHE arrays for different operational modes (chapter 4.1). After parametrizing the TRNSYS models based on the evaluation criteria, a computational model is developed that couples MATLAB with TRNSYS, for conducting multi-objective optimizations (chapter 5.2). Thereafter, to cope with high computational costs of the long-term assessments of geothermal layouts, the coupled model is supplemented by an ANN method as a mid-stage of the optimization procedure (chapter 5.3). Moreover, a parallel computation approach is proposed to further enhance the speed of optimizations (chapter 5.4). Furthermore, a step-wise optimization method is developed for the operational optimization and control of geothermal systems at each time step (chapter 5.5). Utilizing the developed computational models and the evaluation criteria, the multi-objective optimization of the proposed layouts are conducted (chapter 6). Finally, results are summarized (chapter 7) and outlooks for future studies are presented (chapter 8). The dissertation is written in a cumulative form including four peer-reviewed publications, which are introduced in different chapters. The full papers can be found in the Appendix.

## Table of Contents

## List of Figures

## List of Tables

## Index of Abbreviations and Symbols

*Abbreviations*

| | |
|---|---|
| ActCen | Active central |
| ActDec | Active decentral |
| ActSer | Active serial |
| ActPar | Active parallel |
| ANN | Artificial neural network |
| ASHP | Air-source heat pump |
| BHE | Borehole heat exchanger |
| BTES | Borehole thermal energy storage |
| Comp | Compromise |
| CHP | Combined heat and power |
| DC | District cooling |
| DL | District loop |
| Des. | Destruction |
| DH | District heating |
| DHC | District heating and cooling |
| Eco | Economical |
| Eff | Efficient |
| Env | Environmentally-friendly |
| Exe. | Exergy |
| GB | Gas boiler |
| GSHP | Ground-source heat pump |
| HEX | Heat exchanger |
| HP | Heat pump |
| IC | Initial cost |
| LCA | Life cycle assessment |
| LCC | Life cycle cost |
| LCOH | Levelized cost of heat |
| LHV | Lower heating value |
| MC | Maintenance cost |
| NG | Natural gas |
| NPV | Net present value |
| NSGA | Non-dominated sorting genetic algorithm |
| OC | Operational cost |
| PasCen | Passive central |
| PasSer | Passive serial |
| PasPar | Passive parallel |
| SDH | Solar district heating |
| STC | Solar thermal collector |
| TRCM | Thermal Resistance and Capacitance Model |

*Formula symbols*

| | | |
|---|---|---|
| A | [$m^2$] | Area of solar collector |
| $a_0$ | [-] | Intercept efficiency |
| $a_1$ | [kJ $hr^{-1}$ $m^{-2}$ $K^{-1}$] | Efficiency slope |
| $a_2$ | [kJ $hr^{-1}$ $m^{-2}$ $K^{-2}$] | Efficiency curvature |
| $c_p$ | [kJ $kg^{-1}$ $K^{-1}$] | Specific heat capacity |
| c | [€ $tCO_2^{-1}$], [€ $kWh^{-1}$] | Specific cost |
| C | [€ $yr^{-1}$] | Cost rate |
| Cap | [kW] | Capacity |
| EC | [€ $kWh^{-1}$] | Emission cost |
| $\dot{E}$ | [kW] | Thermal exergy rate |
| EF | [g CO2 eq $kWh^{-1}$] | Emission factor |
| f | [kWh] | Fuel consumption |
| GWP | [g $CO_2$ eq $kWh^{-1}$] | Global warming potential |
| i | [-] | Discount rate |

| | | |
|---|---|---|
| I | [kJ $hr^{-1}$ $m^{-2}$] | Incident radiation on solar collectors |
| L | [m] | Length |
| LCOE | [€ $kWh^{-1}$] | Levelized cost of energy |
| LHV | [kJ] | Lower heating value |
| $\dot{m}$ | [kg $s^{-1}$] | Flow rate |
| n | [-] | Year |
| N | [-] | Number |
| $\dot{Q}$ | [kW] | Heat flux |
| S | [m] | Spacing |
| T | [°C] | Temperature |
| Vol | [$m^3$] | Volume |
| η | [%] | Efficiency |

*Subscripts and superscripts*

| | | | |
|---|---|---|---|
| b | Boundary | MC | Maintenance cost |
| BHE | Borehole heat exchanger | NG | Natural gas |
| BST | Buffer storage tank | P | Product |
| BTES | Borehole thermal energy storage | Prod | Production |
| CL | Cooling load | ret | Return |
| elec | Electricity | Sa | Standalone |
| env | Environmental | Sc | Solar-coupled |
| Ext | Extraction | St | Storage |
| f | Fuel | sply | Supply |
| HL | Heating load | 0 | Reference |
| IC | Initial cost | | |

## Cumulative Dissertation

This cumulative dissertation comprises the following journal publications. The full papers can be found in the Appendix.

***Appendix A:*** Formhals J, **Hemmatabady H**, Welsch B, Schulte DO and Sass I (2020): A modelica toolbox for the simulation of borehole thermal energy storage systems, *Energies*, no. 9, p. 2327, doi: /10.3390/en13092327.

***Appendix B:*** **Hemmatabady H**, Formhals J, Welsch B, Schulte DO and Sass I (2020): Optimized layouts of borehole thermal energy storage systems in 4th generation grids, *Energies,* no. 17, p. 4405, doi: /10.3390/en13174405.

***Appendix C:*** Formhals J, Feike F, **Hemmatabady H**, Welsch B, Sass I (2021): Strategies for a transition towards a solar district heating grid with integrated seasonal geothermal energy storage, *Energy, 228, p.120662,* doi: /10.1016/j.energy.2021.1206.

***Appendix D:*** **Hemmatabady H**, Welsch B, Formhals J and Sass I (2022): AI-based enviro-economic optimization of solar-coupled and standalone geothermal systems for heating and cooling, Applied Energy, 311, 118652, doi:/10.1016/j.apenergy.2022.118652.

***Appendix A*** presents a toolbox for the simulation of borehole thermal energy storage (BTES) systems in Modelica. The presented MoBTES model facilitates the deployment of different modeling approaches for its sub-models, allowing for an adaption to the numerical requirements of varying applications. The currently implemented variants are based on well-known and proven approaches, which exploit the physical characteristics of BTES systems. Consequently, the comparison of MoBTES to 3D finite element method (FEM) benchmark models and monitoring data from an existing plant reveals only minor deviations in their performance figures. In contrast to existing borehole heat exchanger (BHE) models in Modelica, MoBTES is a dedicated BTES model and therefore should cover all relevant design features of such systems. Emphasis was put on the implementation of functionalities like serially connected BHEs, consideration of the stratigraphy at the storage site, flow reversal, hydraulic pressure loss, or partly insulated BHEs. The implemented model features allow for an accurate assessment of the impact of different designs on the storage performance, while maintaining a computational efficiency suitable for system simulation. Additionally, the flexibility of MoBTES enables the use of very fast models for extensive parameter studies or stochastic simulation. The versatile and multi-domain modeling approach of Modelica, allows for the integration of MoBTES into models of whole energy systems, including sector coupling and the combination with a wide range of other open source model libraries.

***Appendix B*** describes a dynamic exergo-economic assessment approach, which is adopted to evaluate various options for integrating BTES systems into 4th generation district heating and cooling grids in heating-dominated regions. For this purpose, different layouts are modeled and parameterized, which differ by their cooling approach (active or passive) and by the connection of the BTES system and the supplementary boiler in heating mode (serial or parallel). Multi-objective optimization is conducted, varying the most important design variables in order to maximize exergetic efficiency and to minimize levelized cost of energy (LCOE). A comparison of the optimal designs of the different layouts reveals that passive cooling together with maximizing the heating temperature shift, accomplished by a heat pump (HP), lead to optimal designs. Component-wise exergy and cost analysis of the most efficient designs highlights that HPs are responsible for the highest share in inefficiency while the installation of BTES has a

HPs are responsible for the highest share in inefficiency while the installation of BTES has a high impact in the LCOE. BTES and buffer storage tanks (BSTs) have the lowest exergy destruction for all layouts and increasing the BTES volume results in more efficient district heating and cooling (DHC) grids.

***Appendix C*** evaluates different strategies and technological pathways for the transition of an existing campus district heating (DH) grid towards a low-temperature solar DH system with an integrated medium-deep BTES for achieving emission reduction targets. It emphasizes the importance of considering the projected development of existing infrastructure. Therefore, a step-wise transition with a successive reduction of grid temperatures and specific heating demand is investigated. Dynamic system simulations serve to compare transition strategies until 2050 with regard to their environmental performance and economic efficiency. A combination of efficiency measures, integration of solar thermal collectors (STCs), waste heat utilization and seasonal storage is being considered to achieve these targets. The proposed strategies differ in dimensions of components as well as the timing of construction or decommissioning. Results indicate that the emission reduction target can be met most economically by a strategy with a gradual construction of STCs and a seasonal storage, accompanied by a concurrent scaling-down of the existing combined heat and power (CHP) capacity. The presented study demonstrates the feasibility of a step-wise transition of such a system

***Appendix D*** investigates solar-assisted and standalone geothermal layouts for heating as well as combined heating and cooling applications. The assessment routine is used in a multi-objective optimization approach to minimize the different system layouts' emission factor (EF) and LCOE. In order to cope with the high computational cost of the required multi-year simulations, an artificial neural network (ANN) has been used as a proxy model in an intermediate step of the multi-objective optimization procedure. The optimization results reveal that, for heating-only purposes, solar-assisted geothermal systems with active load supply via a HP are favorable over solar-assisted passive systems and standalone BHE systems in terms of both cost and greenhouse gas emissions. For the geothermal-only solutions, though, the rejection of heat into the subsurface from cooling applications actually leads to a significant reduction in the overall costs and emissions. Thus, this layout achieves the lowest overall LCOE while also obtaining a reasonably low EF. Nevertheless, the lowest emissions for combined heating and cooling systems are also realized by solar-assisted layouts. This study provides relations between optimized variables and the outputs of the multi-objective optimization, which can be used by designers for the evaluation of system dimensions and their effect on the enviro-economic objectives. In addition, the combination of an ANN and multi-objective optimization methods has proven to be an accurate and robust approach for long-term evaluation and comparison of geothermal heating and cooling systems. It can help provide design guidelines and contribute to a broader understanding of such systems, paving the way for their much wider application.

*Further publications*

In addition to the aforementioned publications, I published and presented my research on conferences and exhibitions both, in oral presentations and poster sessions, which are listed below in chronological order:

**Hemmatabady H**, Schulte DO, Welsch B, Formhals J and Sass I (2019): Design and analysis of borehole thermal energy storage in district heating and cooling grids, 10$^{th}$ European Geothermal PhD Day, Potsdam, Germany

**Hemmatabady H**, Schulte DO, Formhals J, Welsch B and Sass I (2019): Thermo-economic design of hybrid borehole thermal energy storage systems in district grids, 7th European Geothermal Workshop, October 10th, 2019, Karlsruhe, Germany

Formhals J, **Hemmatabady H**, Feike F, Welsch B, Sass I (2020): Dynamic transition to a renewable and efficient campus solar district heating grid with integrated medium deep borehole thermal energy storage, 6th International Conference on Smart Energy Systems, Alborg, Denmark

**Hemmatabady H**, Formhals J, Schulte DO, Welsch B and Sass I (2021): Exergo-economic optimization of borehole thermal energy storage in district heating and cooling grids, World Geothermal Congress 2020+1.

Formhals J, **Hemmatabady H**, Welsch B, Schulte DO and Sass I (2021b): MoBTES – A new borehole thermal energy storage model in Modelica, World Geothermal Congress 2020+1.

# 1 Introduction

Climate change is a serious issue that the world is confronted with. The Paris Agreement sets out a global framework to avoid dangerous climate change by limiting global warming to well below 2 °C and pursuing efforts to limit it to 1.5 °C (UN 2015a). Greenhouse gases (GHG) emitted by energy use from fossil fuels are the main reason for climate change (Ritchie 2020). In Europe, buildings consume 40% the overall energy and emit 36% of the GHG (EC 2021a). With 79%, heating and hot water have the largest share in the final energy demand of European households (EC 2021b). Cooling of buildings still has small share, but the demand is continuously rising due to climate change (Fleiter et al. 2016). It is estimated that by 2025 the installed cooling capacity in Europe is likely to be 55–60% higher than in 2010 (Werner 2016). According to Eurostat 2019 , approximately 75% of heating and cooling is still generated from fossil fuels while only 22% from renewable energy resources (Fleiter et al. 2016). Consequently, heating and cooling with reduced energy consumption and higher sustainability need to be considered as an important part of future energy systems.

By 2050, more than 80% of European residents are expected to live in urban areas (UN 2015b). This trend increases the benefits of district energy systems, which tend to be more economic for densely populated regions (Rezaie & Rosen 2012). The significant share of heating and cooling in European households as well as the increasing trend towards local energy supply has made district heating and cooling (DHC) an important option for future thermal energy systems. The DHC grids provide the opportunity of utilizing combined heat and power (CHP), waste heat from industrial processes as well as renewable energy resources. In the recent years the main focus has been on the efficiency improvement of these grids especially by lowering their temperature level in heating load supply. This makes the integration of sustainable energy sources, especially geothermal and solar energy, perfect options for the integration into DHC systems. More details about DHC grids and their design approaches can be found in chapter 2.1.

To increase sustainability of district energy systems by integrating various energy resources, seasonal mismatch between supply and demand needs to be dealt with. Solar thermal collectors (STC) can have a key contribution in sustainable heating load supply, which are hampered by the highest share of available solar energy in summer, when no heating is required. This mismatch is also a major drawback in CHP units or industrial applications as well as cooling cycles where the generated excess heat during summer time is not needed. To solve this problem, seasonal thermal energy storage (TES) technologies are essential. In these systems, the extra heat is stored seasonally in a storage medium in order to be extracted and used in heating seasons.

TES technologies can be categorized to sensible, latent and chemical heat storage. In sensible TES, energy is stored by changing the temperature of a storage medium such as water, rock beds or soil (Dincer & Rosen 2021). Compared with chemical and latent technologies, sensible TES systems are more suitable for large-scale (district) applications (Pinel et al. 2011). The sensible TES technologies that are appropriate for large-scale TES, can be categorized to large aboveground water tanks and underground heat storage (UTES) systems (Welsch 2019). In UTES, high underground thermal capacity can be utilized to store large quantities of fluctuating renewable or waste energy in district scale (Schulte et al. 2016a; Skarphagen et al. 2019). The most common types of UTES systems include tank TES (TTES), pit TES (PTES), aquifer TES (ATES) and borehole TES (BTES). Comprehensive details about each type can be found in (Schmidt et al. 2004; Mangold et al. 2012; Dincer & Rosen 2021). The main concentration of

this study is on shallow BTES systems. They utilize the high underground storage capacity using borehole heat exchanger (BHEs). The underground can be also used as an efficient heat source/sink for heating/cooling applications in conventional geothermal systems, where there is no extra heat for storage. More details about shallow geothermal systems as well as their design concepts can be found in Chapter 2.

Aforementioned benefits of exploiting the underground capacity for TES, makes the utilization of BTES an interesting concept which leads to increased sustainability of DHC grids. Main benefits of BTES systems have been already proven by several projects (e.g.,Dincer & Rosen 2007; Bauer et al. 2010; Sibbitt et al. 2012). A review of some of these projects can be found in (Lanahan & Tabares-Velasco 2017; Welsch 2019). However, inappropriate dimensioning considering the interaction of BTES with other system components is a main issue that has led to reduced efficiency of some existing projects. In an exemplary project in Germany (Bauer et al. 2010; Bauer et al. 2016), in which a BTES is charged by STCs and discharged by a HP, the low HP capacity resulted in its inefficient operation and caused the BTES to be discharged less than planned. Moreover, stagnation happened in STCs because of smaller dimensions of BTES and other system components (Bauer et al. 2016). A BTES should not be regarded in isolation, but merely as one component within a DHC network (Skarphagen et al. 2019). Design and optimization of BTES systems in DHC networks require guidelines that consider their interaction with other system components.

In this study, based on existing systems, different layouts of geothermal systems are proposed for heating as well as combined heating and cooling applications. The investigated layouts can be generally categorized to small- and large-scale systems, which are designed standalone or are coupled with STCs (cf. Chapter 3). To investigate the efficient implementation of BHE arrays in the proposed layouts considering other system components, comprehensive evaluation methods are utilized and adapted to geothermal systems in order to assess them from technical, economic and environmental aspects.

As mentioned, one of the main motives of integrating geothermal systems in DHC grids is lowering environmental emissions. Life cycle assessment (LCA) has been proven to be a useful tool for environmental evaluation of BTES and energy systems (Welsch et al. 2018; Karasu & Dincer 2020). LCA studies demonstrate that the integration of BTES systems yields a large reduction in global warming potential (GWP) (Welsch et al. 2018; Karasu & Dincer 2020; Formhals et al. 2021a; Elhashmi et al. 2020; Shah et al. 2020). As lowering environmental impacts is always associated with higher costs, enviro-economic assessments are needed to consider both objectives simultaneously. In this study, an enviro-economic method is utilized to simultaneously minimize cost and emissions of geothermal layouts (cf. Chapter 4.2).

Although environ-economic analysis is a suitable approach for the evaluation of energy systems, it lacks thermodynamic assessments (Nuss 2015). The thermodynamic inefficiencies of an energy system can be assessed using exergy analysis method. Exergo-economics is a branch of engineering that combines exergy analysis and economic principles. It can provide information to a system designer which are not available through conventional energy analysis and economic evaluations, but crucial to the design and operation of a cost-effective system (Bejan et al. 1995). Moreover, increasing exergetic efficiency leads to reduced environmental impacts and a higher sustainability (Nuss 2015). Therefore, technical, economic and environmental aspects can be taken into consideration using the exergo-economic analysis method (Hemmatabady et al. 2020). Results of exergy analysis of an installed BTES system show that a significant

energy saving can be done by conducting an exergy analysis (Kizilkan & Dincer 2015). Exergo-economic analysis method has been already used for the optimization of different geothermal layouts (Kavian et al. 2019; Kavian et al. 2020 Sayyadi & Nejatolahi 2011). However, for exergy calculations of the aforementioned literature, mainly a static approach has been used, which is mainly suggested for the systems at higher temperature levels. In this study, a dynamic exergo-economic assessment approach is adapted for the optimization of geothermal systems from technical and economic aspects (cf. Chapter 4.1). The proposed approach can be utilized for designing geothermal systems in district grids as well as dynamically optimizing the operation of exiting geothermal plants.

For the assessment of the proposed layouts utilizing the evaluation criteria, different computational models are proposed. The geothermal layouts are modeled and parameterized in TRNSYS 18 (Klein et al. 2017), which is coupled with MATLAB (The MathWorks Inc. 2016) for conducting optimization studies (direct optimization). Utilizing the underground as heat sink or heat source is associated with its temperature change after years of operation. This has a significant effect on the performance of geothermal systems and their sustainable operation. Consequently, long-term evaluation of geothermal systems during project lifetime should be considered as an important point in their optimal integration in DHC networks. This is associated with high computational costs, especially when multiple number of evaluations are required for the convergence of an optimization problem. In order to deal with that, an artificial neural network (ANN) has been used to create a proxy model as an intermediate step of the multi-objective optimization procedure (indirect optimization). The proposed approach of utilizing the sample points from initial optimization evaluations differ from other similar studies (Jiang et al. 2020; Razmi et al. 2020), in which sample points are mainly created randomly. Finally, a step-wise optimization method is proposed to optimize the operation of geothermal systems that are selected by direct or indirect optimization methods at each time step. The developed computational models are elaborated in Chapter 5.

Overall, different layouts of geothermal systems are proposed for heating as well as combined heating and cooling applications in district grids. The layouts are mainly based on reference cases, validated against real operational data. Based on the reference cases, alternative layouts and their control strategies are proposed. The evaluation of the proposed energy systems, which include different components of geothermal-based DHC grids are conducted utilizing exergo- and enviro-economic analysis methods. The assessments are done on two levels, for defining the optimum size of each component and for improving the operation of existing systems. By developing novel computational methods for the optimization of geothermal systems, the comparison of the proposed layouts as well as the evaluation methodologies are conducted. Results provide guidelines for designing geothermal systems in DHC grids.

# 2 Geothermal Systems in District Heating and Cooling Grids

To propose geothermal layouts for DHC, a comprehensive understanding of DHC characteristics and geothermal systems are required. In this chapter, the most important characteristics of DHC grids, 1st to 5th generation DHC grids, the most common shallow geothermal systems and design concepts, which are utilized for proposing different system layouts, are introduced and discussed.

## 2.1 District Heating and Cooling Grids

District heating comprises a network of pipes connecting the buildings in a neighborhood, town center or whole city (Lund et al. 2014). The required load is supplied to the buildings using different available sources using central plants or decentral units. In some countries, smaller grids are called local (block) heating grids. The concept “local heating” is mainly used when required load of multiple number of buildings in a neighborhood or a building complex is supplied (Mauthner & Herkel 2016; Nussbaumer 2017). On the other hand, with “district heating”, larger grids to supply required load of communities up to whole cities is meant (Mauthner & Herkel 2016). As the boundary between local and district grids is not clear and these concepts are restricted to some countries, the term “district heating” is generally used in this research. To determine a boundary, the district heating systems of this work are categorized into small- and large-scale systems. The small-scale systems are defined as those with yearly demand of lower than 1 GWh, while large-scale systems have higher demand.

The most common structures of a district heating include radial, ring and mesh networks (Figure 1). Radial networks have the shortest line length, the lowest investment costs and are mainly implemented in small- and medium-size grids. Mesh networks consist of multiple rings that make the integration of several heating plants possible, which leads to improved security of supply. This also increases the chances of integrating renewable energy resources, seasonal TES technologies and customer substations (e.g. 5th generation DHC), which leads to higher sustainability. However, their high investment costs make them more profitable for larger systems (Dötsch et al. 1998). Finally ring networks are a special case of mesh networks with a single circuit.

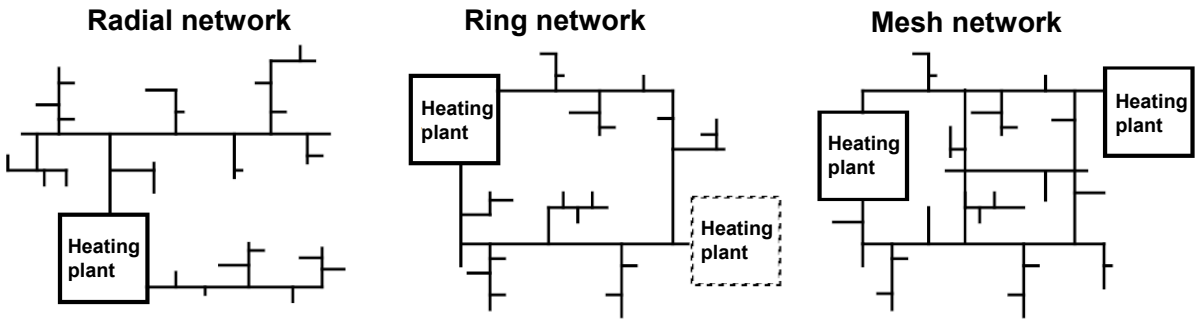


Figure 1: Structures of a district heating (after Dötsch et al. 1998).

The operation of a district network can be classified into three strategies considering the grid temperature change with ambient temperature (Figure 2). In a gliding operation strategy, which is only suitable for heating, network temperature changes continuously with the ambient temperature. This strategy is not appropriate for consumers that are independent of the weather, such as process heat and domestic hot water. The most common operational strategy

is gliding-constant operation, which allows simultaneous supply for space heating and hot water. This strategy is also suitable for district systems at lower temperature levels (4th and 5th generations), which are the most favorable options for integrating geothermal systems. Finally, a constant operation is suitable for process heat, domestic hot water supply and cooling.

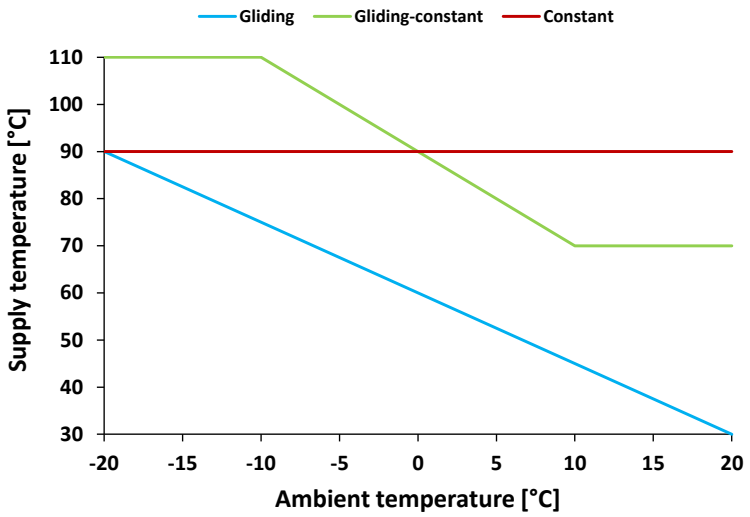


Figure 2: District heating temperature change with ambient temperature (after Nussbaumer 2017).

District heating systems can be also classified according to the number of pipes. The most common type is two-pipe system, with one supply and one return line between the heating center and the consumer. Another type is three-pipe system, which has two supply lines, one with gliding temperature profile for heating and the other with constant temperature for hot water supply. Moreover, a four-pipe system has two supply and two return lines, which is suitable for applications like central seasonal heat storage with decentralized solar heat generation. The four-pipe system design can be also used for DHC, in the case of simultaneous heating and cooling load supply.

DHC systems can be environmentally beneficial and pave the way toward the sustainable energy supply, if they are applied appropriately (Rezaie & Rosen 2012; Werner 2017). Technological development of DH systems led to the definition of 1st to 4th generation district heating (1GDH-4GDH) concepts. The 1GDH was introduced in 1880s and used steam as the heat carrier in steam lines with steam traps in concrete ducts and channels. In 1930s, the 2GDH was developed, by altering the heat carrier from steam to pressurized water distributing heat in concrete ducts and channels. In 1980s the 3GDH occurred, which was based on reduction of the supply temperature to below 100 °C and using prefabricated, pre-insulated pipes directly buried into the ground (Lund et al. 2021). Finally, to transform towards a sustainable heat supply, the 4GDH systems have been widely implemented since 2020. Figure 3 shows the development of 1GDH-4GDH systems. As it can be seen in the figure, the overall trend is temperature reduction, which leads to efficiency increase and more opportunities for integrating low-temperature energy sources.

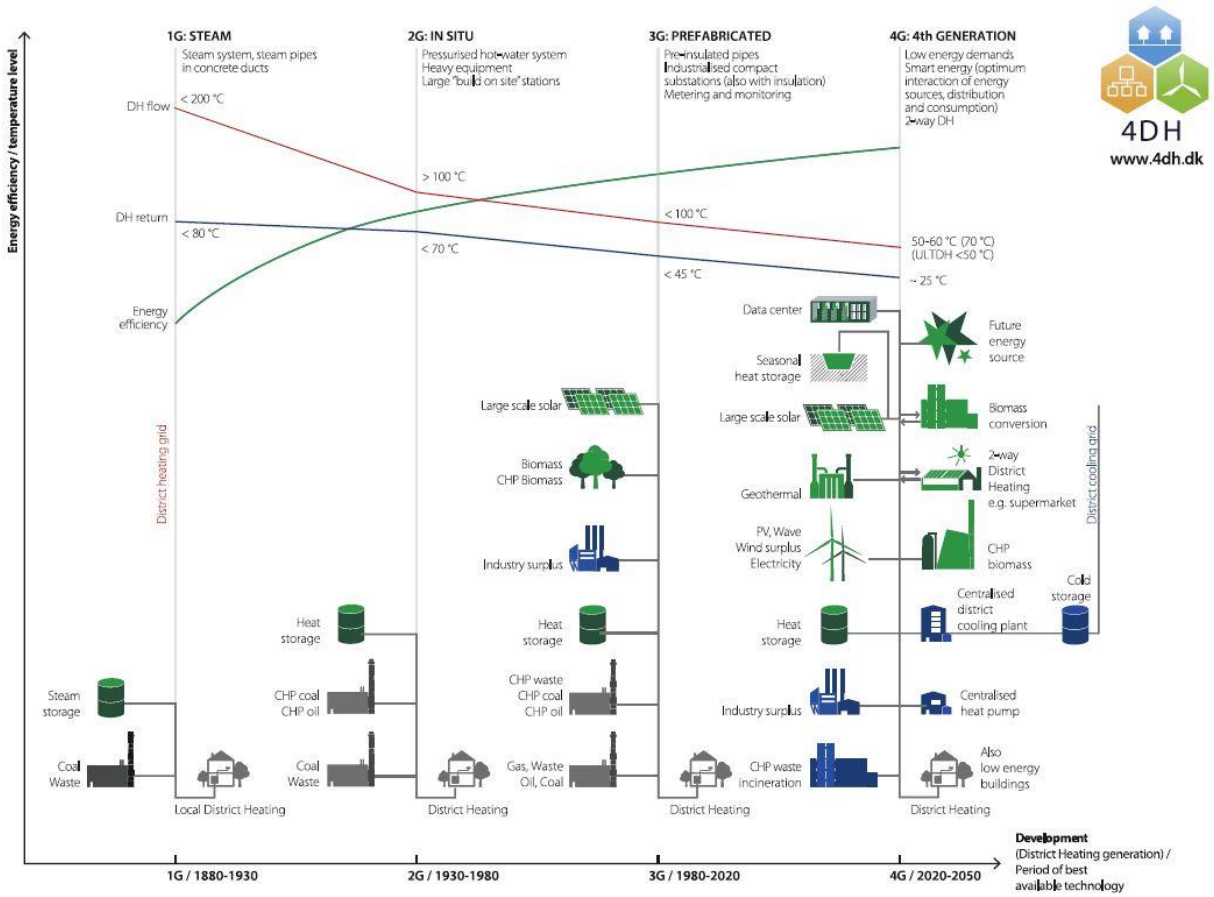


Figure 3: From the first to the fourth generation of district heating (Lund et al. 2021).

To extend the application of 4GDH systems in sustainable energy supply, some prerequisites need to be considered. The most important ones are the implementation of low-temperature DH networks, the ability to recycle heat from low-temperature sources such as solar and geothermal heat and the implementation as an integrated part of smart energy systems (Lund et al. 2014). A future 4th generation district cooling (DC) system can be defined as a system more interactive with the electricity, DH and gas grids (Lund et al. 2014). Overall, a 4th generation district heating and cooling grid can be considered as a low-temperature interactive energy grid for supplying heating and cooling demands (Hemmatabady et al. 2020).

The concept 5th generation district heating and cooling (5GDHC) network has been used in the recent years. The low-temperature 5GDHC networks operate at temperatures so close to the ground that it is not suitable for direct heating purpose (Buffa et al. 2019). 5GDHC can be regarded as a different technology compared to 1GDH-4GDH by introducing HPs at each consumer to adjust the supply temperature to the specific requirements, whether it is for heating or cooling purposes (Lund et al. 2021). The possibility to reverse the operation of the customer substations permits to simultaneously cover both heating and cooling demands of different buildings. Through hybrid substations, 5GDHC technology enhances sector coupling of thermal, electrical and gas grids in a decentralized smart energy system (Buffa et al. 2019).

## 2.2 Shallow Geothermal Systems

Geothermal systems can be generally classified into two groups considering the depth of the underground facilities, deep and shallow (Figure 4). Deep geothermal systems are generally with a depth of higher than 1 km and are used to generate electricity and/or to feed district heating networks. Shallow geothermal systems are up to a depth of 400 m and are used for heating and cooling (VDI 2010). An innovative concept is medium-deep geothermal systems for the depths of lower than 1 km for heating applications (Welsch et al. 2016a). Geothermal systems can be also categorized into open and closed loop systems. In the open systems the heat is transferred through groundwater extraction from geothermal wells. The closed systems utilize underground heat exchangers for heat transfer through conduction. The most common types of underground heat exchangers are BHEs. The main focus of this study is on shallow geothermal systems with vertical BHEs for heating as well as combined heating and cooling applications.

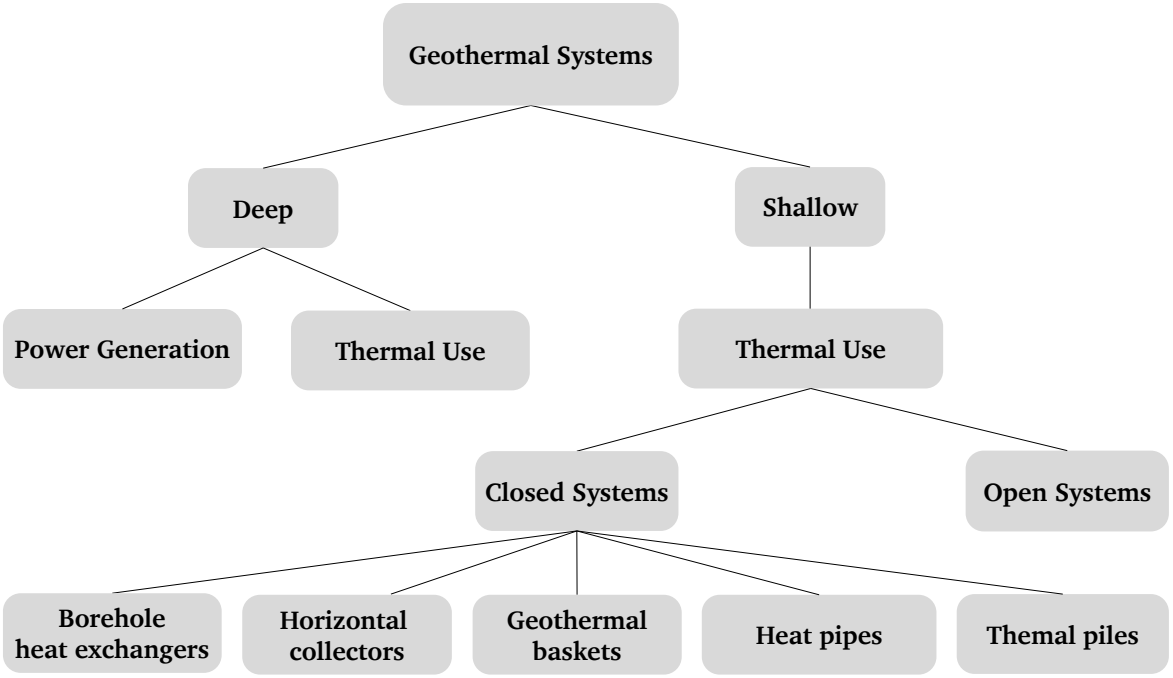


Figure 4: Categorization of geothermal systems (after Sass et al. 2016).

There are three main types of BHEs, single U-tube, double U-tube and coaxial heat exchangers (Figure 5) (Sass et al. 2016). Single U-tube and double U-tube BHEs are mainly installed in shallow geothermal systems, from which double U-tube BHEs are the most common ones (Sass et al. 2016, VDI 2019). Coaxial BHEs are mostly seen in geothermal installations with higher depths (Welsch 2019). Various materials are used for the pipes, mainly high-density polyethylene (HDPE), steel and copper. High-stress crack-resistant materials (PE100-RC) have had the highest market share in the last years (Sass et al. 2016). BHEs are installed inside drilled boreholes, which are backfilled with a cement-based grouting material. The grouting material stabilizes the borehole, provides hydraulic sealing and improves thermal contact with the underground. The heat transfer process starts by circulating a heat transfer fluid (usually a water-glycol mixture) in the pipes. In heating mode, the heat transfer medium extracts the required heat from the ground and decreases its temperature. In cooling mode, it rejects the excess heat to the ground and increases its temperature.

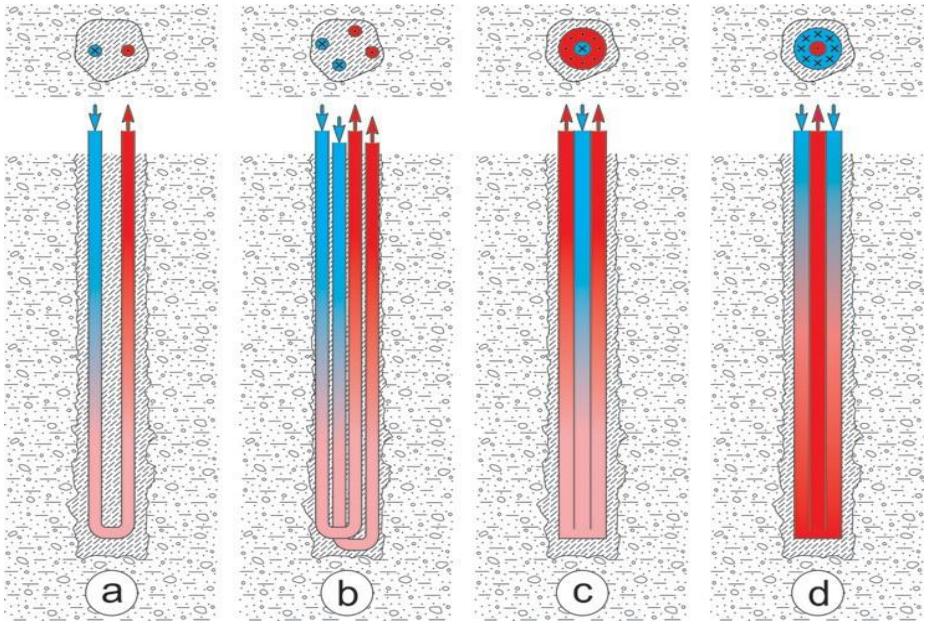


Figure 5: Types of BHEs: a) Single U-pipe BHE, b) Double U-pipe BHE, c) Coaxial BHE with internal return, d) Coaxial BHE with external return; red = flow, blue = return (Image source: Sass et al. 2016).

Depending on the underground and the required load-side temperatures, the heat extraction or rejection from or to the ground can be done with and/or without HPs (passively and/or actively) (cf. Chapter 2.3 for more details). The term heat pump refers to a group of technologies that transfer heat from a low temperature to a high temperature (Herold et al. 2016). Figure 6 shows the basic structure of a compression HP. In heating mode, the circulating fluid of the HP, which has a low boiling point, is vaporized by absorbing heat in the evaporator, from the ambient air in an air-source HPs (ASHP) and from the underground in a ground-source HP (GSHP). The vapor is then compressed in the compressor and its temperature increases. The compressor usually has one, two or three stages of compression or it can be variable-speed. Thereafter, the compressed vapor passes through the condenser, which is connected to the consumer. By transferring heat to the consumer, the vapor is condensed back to liquid at a moderate temperature. Finally, the throttle valve relieves the pressure and causes the liquid to enter the two-phase region with low temperature, ready to enter the evaporator to absorb heat again. In the cooling mode, the cycle is reversed and the evaporator absorbs the extra heat from the consumer with cooling demand. The absorbed excess heat is then rejected to a heat sink, which is the ambient air in an ASHP and the underground in a GSHP.

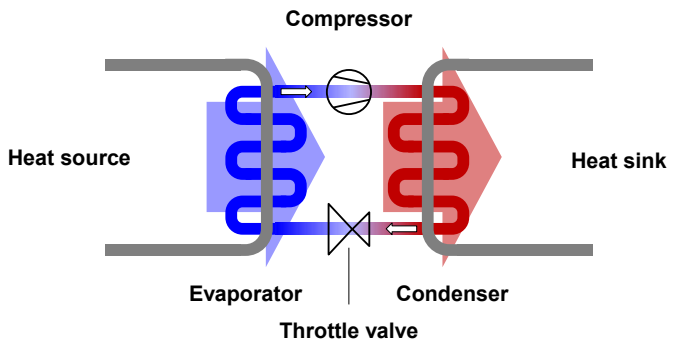


Figure 6: Basic structure of a heat pump.

Closed geothermal systems with BHEs can be classified into two groups. In the first group, no active recharging of the underground is done. In these systems, the extracted energy from the underground is not high enough for direct heating load supply and GSHPs are required to supply the heating demand. As the underground temperature is higher and more stable, compared to the ambient temperature, it results in more efficient system operation of GSHPs, compared with ASHPs. In the second group, the underground thermal capacity is exploited to store fluctuating renewable or waste energy, which can be on a seasonal basis, and is widely known as BTES. The most common applications of this group are BTES systems that are used to store excess solar energy or rejected waste heat from cooling cycles in non-heating seasons to be used in heating seasons. In this group, depending on the temperature level of the available energy, the extracted energy can be utilized with or without GSHPs.

## 2.3 Design Concepts

For the comparison of different geothermal layouts in this study, the most common system designs are considered. Geothermal systems are mostly designed individually (standalone) or they are coupled with STCs (solar-coupled). In the standalone geothermal systems, the underground is utilized as heat source and/or sink for heating and/or cooling. In the solar-coupled systems, STCs are used for supplementary heating and seasonal storage of solar energy. Finally, a hybrid system design is proposed, in which solar-coupled and standalone geothermal systems can be utilized simultaneously. Figure 7 shows a standalone and a solar-coupled geothermal system design in heating mode. More details can be found in Chapter 3 and Appendix B.

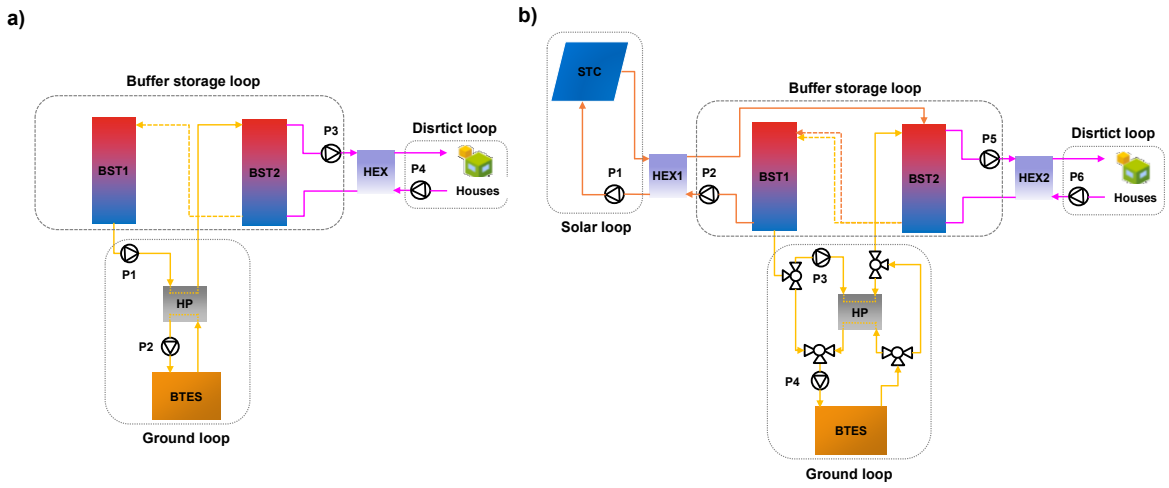


Figure 7: a) Standalone and b) solar-coupled geothermal system design in heating mode.

Utilizing the underground as an efficient heat source for heating as well as an efficient heat sink for cooling can be done actively or passively. In passive load supply, the temperature level of the underground is at a suitable level to be utilized directly without the use of HPs. In active load supply, it is not high/low enough to supply heating/cooling load passively. Consequently, HPs are needed to utilize the underground as their heat source/sink for supplying heating/cooling load. In combined active and passive mode, the underground is used for direct load supply when it is at a suitable temperature level and HPs start working otherwise.

The possibility of passive load supply is dependent on the design supply temperature. Passive cooling utilizing BHEs is suggested for a load-side supply temperature of more than 14 °C. The maximum temperature is assumed that does not exceed 20 °C (VDI 2019). Temperature difference between supply and return on the load-side is usually between 4 - 6 °C. Consequently, considering an average undisturbed underground temperature of 10 °C, it can be utilized as an appropriate heat sink for passive cooling load supply. Higher supply temperatures on the load-side results in higher share of the passive cooling and less supplementary cooling requirement. The supplementary cooling needs to be done actively by a HP, which is bypassed when the supply temperature is suitable for passive cooling. For the load-side supply temperatures of lower that 14 °C the active cooling is required, with the temperature difference usually in the range of 6 - 8 °C. Figure 8 shows an exemplary heat exchanger design and the corresponding temperature ranges on the load- and sink-side for passive and active cooling. Passive or active cooling utilizing BHEs is feasible in standalone geothermal layouts. The solar-coupled BTES systems cannot be used as heat sink for cooling purposes, as they are heated up by STCs during non-heating seasons.

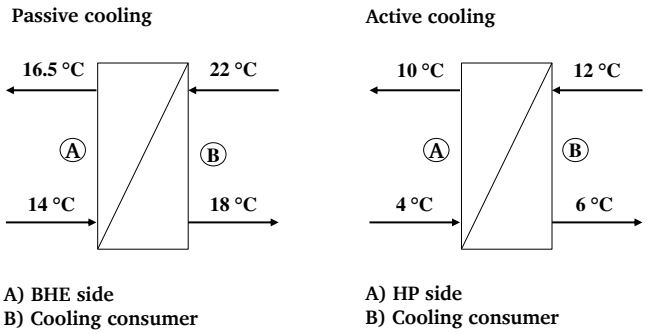


Figure 8: Exemplary heat exchanger design; left) passive cooling, right) active cooling.

The overall trend towards low-temperature DH systems, provides more opportunities for the integration of STCs as a main renewable energy source. The solar-coupled geothermal systems can be designed in passive and active heating modes. In both modes, the STCs store the collected solar energy in the BTES during non-heating periods. In the heating periods, STCs are generally utilized to supply part of the required heating demand and/or to improve the performance of GSHPs (Mehrpooya et al. 2015). In passive mode, the return temperature of the fluid from the BHEs is high enough for direct heating load supply. In active mode, a HP is required for supplementary heating, which is bypassed when the supply temperature is suitable for passive heating. A passive-only design is suggested for the systems with lower supply temperatures. A passive solar-coupled BTES system has been already proven to be a feasible option for DH with an average supply temperature of 37 °C and a peak temperature of 45 °C (Leidos 2014). At higher temperature levels the active design strategy is suggested. To define a margin between active or passive design strategy, details of the investigated project should be taken into account separately. Figure 9 shows an exemplary heat exchanger design and the corresponding temperature ranges on the load- and source-side for passive and active heating load supply.

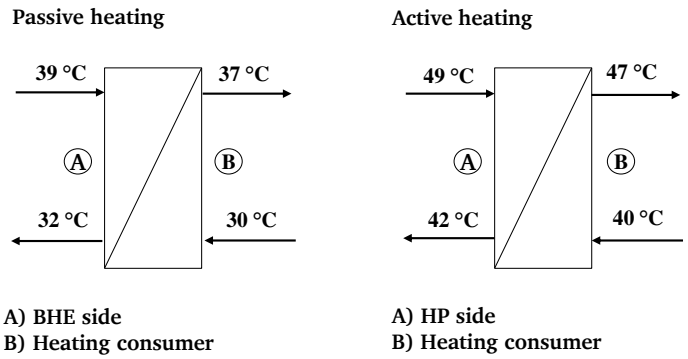


Figure 9: Exemplary heat exchanger design; left) passive heating, right) active heating.

Either standalone or solar-coupled geothermal systems need to be supplemented by auxiliary heating units to ensure the required load supply. The geothermal loop and the auxiliary loop (gas boiler, GB) can be connected in series or parallel, with different temperature shift and the maximum corresponding heating load that can be supplied efficiently by the ground loop in each mode. In serial mode, the geothermal loop partially shifts the return temperature and the rest is done by serial GBs. In parallel mode, the ground loop is designed on a temperature level, which is close to the supply temperature, and is in parallel operation with GBs. Each design strategy influences the choice of the system components (single- or double-stage HPs) and operational parameters (e.g. the bivalent point, flow rates etc.), which affect the techno-economic performance of the overall energy system, elaborated in Chapter 3 and Appendix B.

Regarding system's design in DHC grids, geothermal systems can supply the load directly (central systems, 4GDH) or can be designed on lower temperature levels with decentral heat pumps at each consumer (decentral systems, 5GDHC). The investigated layouts of this study are mainly based on 4GDH concept. There are various design options for a 5GDHC system design, which are mostly dependent on the specific project constrains. A simplified 5G concept with decentral HPs aims to compare the effects of lower DH design temperatures on the performance of a solar-coupled geothermal system. In Chapter 3, the investigated geothermal layouts of this study, which are proposed based on the introduced design concept are discussed.

# 3 Investigated Layouts of Geothermal Systems

Layouts of geothermal systems are proposed and investigated for smaller and larger load requirements (small-scale and large-scale systems). As mentioned earlier, the small-scale systems in this study are defined as those with yearly demand of lower than 1 GWh. The main focus of this research is on central standalone and solar-coupled systems. More details about the investigated layouts with regard to their design heating/cooling load and supply/return temperature as well as their characteristics can be found in this chapter.

## 3.1 Large-scale Systems

The Large-scale central layouts are evaluated in this chapter. Although high investment costs are a major obstacle for large-scale geothermal projects, they usually have lower specific energy costs. Four different standalone central layouts are designed to supply heating and cooling demand of a case study (Figure 10). The case study is a notional district in Frankfurt with the total annual heating and cooling demand of 8.47 GWh and 1.05 GWh respectively (Appendix B). The four scenarios differ by their cooling approach (active or passive) and by the connection

of the ground loop and the supplementary heating (serial or parallel). In cooling mode, supply and return temperatures ($T_{sup}/T_{ret}$) of the district are 6 °C/12 °C for active and 18 °C/22 °C for passive cooling. In heating mode, $T_{sup}$/ $T_{ret}$ are set to 45 °C/35 °C. The BTES system is actively discharged by HPs, which are connected to a BST for more steady operation. The supplementary heating is done by GBs that cover the heat demand which cannot be met by the ground loop. The connection of the GBs and the ground loop can be in serial or in parallel.

The layouts are compared with each other and a reference scenario that is designed based on conventional systems, in which the total heating demand is supplied by GBs and the cooling demand by ASHPs. As an example, the system layout of serial heating can be seen in Figure 11. The HP heats the water from the BST up to a set point temperature. The serial boiler GB2, provides the additional heat up to the grid supply temperature of 45 °C. GB1 supplies the heating load, which cannot be met by the ground loop and its serial boiler. In parallel scenario, the amount of heat which cannot be supplied by the ground loop will be supplied by a GB, which is in parallel operation with HPs. All four BTES-assisted systems are outlined in the following and more details can be found in Appendix B.

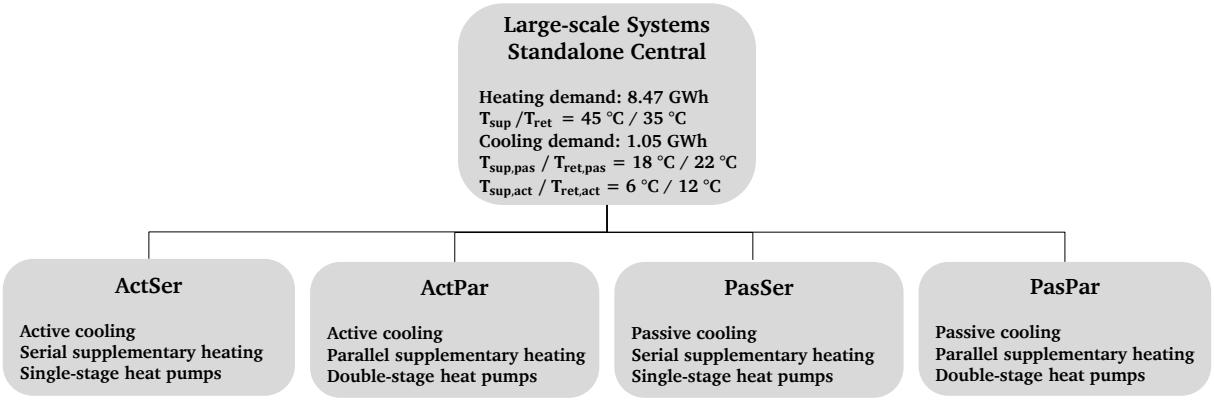


Figure 10: Investigated standalone central systems.

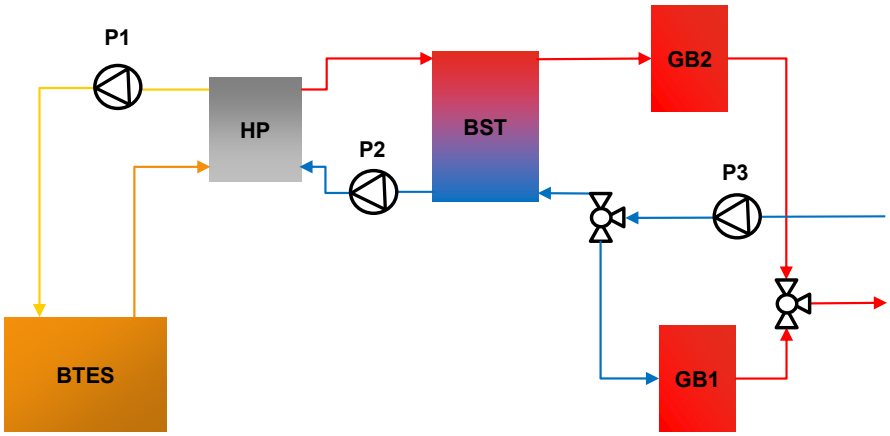


Figure 11: Exemplary System layout of the serial heating (L1) (Hemmatabady et al. 2020).

In parallel to this work, a large-scale solar-coupled central layout is proposed by Formhals et al. 2021a for TU Darmstadt's campus Lichtwiese district heating grid (Appendix C). The campus has an annual heating demand of approximately 25 GWh, which is mainly supplied by CHP units and GBs. To achieve the TU Darmstadt's emission reduction targets, integration of STCs,

waste heat utilization and seasonal storage is considered. As the existing campus building infrastructure does not allow for an immediate transition to a low-temperature grid, a stepwise transition accompanied by grid temperature reduction is assumed. The investigated strategies differ in dimensions of components as well as timing of construction or decommissioning. The strategies include immediate, progressive, step, gradual and conservative (Appendix C). The speed of transition towards more deployment of renewable energies decrease by moving from immediate towards conservative. The fastest transition strategy, immediate, is characterized by maximum deployment of renewable energies and decommissioning of all CHP units at transition stage 1. In contrast with that, conservative scenario keeps the system unchanged at stage 1 and results in the smallest SDH system. More details about the investigated strategies can be found in Appendix C.

## 3.2 Small-scale Systems

Small-scale geothermal projects can be implemented easier in neighborhoods and local consumers. Therefore, proper design of these systems can lead to increased utilization of geothermal energy in heating and cooling sector. In this part, a model of a well-known reference system from (Leidos 2014) is created, which is validated against real operational data. Subsequently, the boundary conditions are adapted to a case study in Germany, with total annual heating and cooling demands of 523 MWh and 62 MWh respectively (Appendix D). Based on the reference scenario, alternative central layouts and control strategies are proposed.

### 3.2.1 Reference Case

The selected reference case, Figure 12, is the BTES system of the Drake Landing Solar Community (Mesquita et al. 2017), which is implemented in TRNSYS. Figure 13 shows the simulation results against the measured numbers as given in the annual report (Leidos 2014). It can be seen that the simulation can represent the performance of the system in operation. More details about the model can be found in Appendix D.

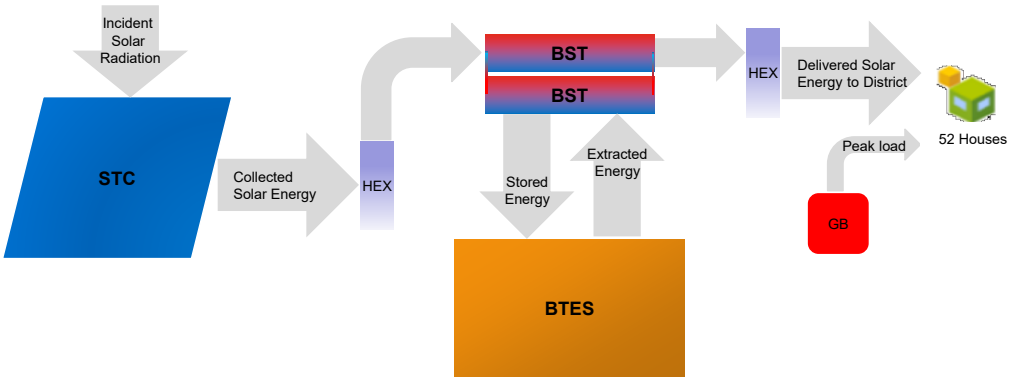


Figure 12: Energy flow diagram of the reference case, modified after (Leidos 2014).

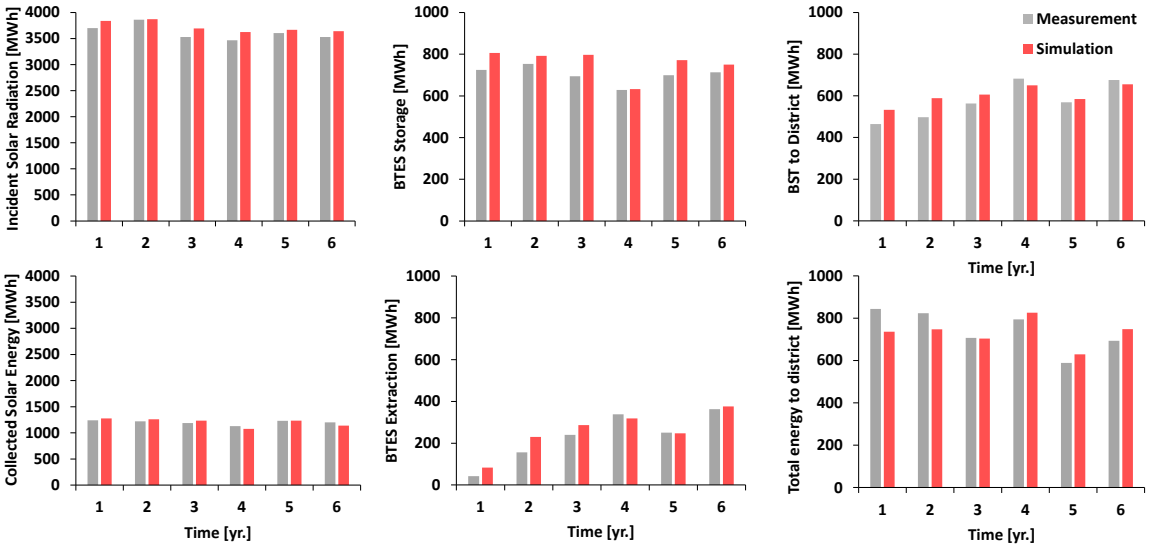


Figure 13: Simulation results (gray) vs. measurement data (red) of the reference case.

### 3.2.2 Standalone and Solar-coupled Layouts

Two different operational scenarios are considered: heating-only mode and combined heating and cooling mode. In heating mode, $T_{sup}$ varies between 37 °C and 42 °C with a gliding-constant operation mode (cf. Figure 2) and there is an average ΔT of 7 °C between supply and return temperatures. In cooling mode, $T_{sup}$ is set on 18 °C, which is suitable for passive load supply. The temperature of the grid is considered to have a constant operation mode (cf. Figure 2) and there is a ΔT of 4 °C between supply and return temperatures.

The investigated small-scale systems in heating-only mode can be seen in Figure 14. The evaluated systems can be either central or decentral. As mentioned earlier, the central systems (Appendix D) are based on a 4GDH concept, in which the heating systems supply the load directly. On the other hand, the decentral systems are based on a 5GDH concept, with lower grid temperature that is not appropriate for direct load supply. Consequently, decentral HPs are installed at each consumer to increase the temperature of the fluid from the low-temperature grid. The central systems are either solar-coupled or standalone. In the solar-coupled systems (H1 and H2), STCs charge a BTES system during non-heating seasons. During heating seasons, H1 supplies the load passively and H2 mostly actively using HPs. In the standalone system (H3), there is not storage or regeneration and a conventional GSHP supplies the load actively. In this study only one solar-coupled decentral layout (H4) is assessed, which is explained in Chapter 3.2.2.3.

The investigated small-scale systems in combined heating and cooling mode are shown in Figure 15. For the solar-assisted scenarios (HC1 and HC2, Appendix D), as the BTES is heated up by STCs during cooling seasons, the cooling load is assumed to be supplied by an ASHP. As for the heating-only scenarios, the heating load is supplies passively or actively. In the standalone scenario (HC3, Appendix D), the cooling cycle rejects its waste heat to the BTES, which is stored and can be discharged actively using HPs in heating mode. Additionally, a hybrid system design option for combined heating and cooling mode (HC4) is proposed, which is based on a combination of HC2 and HC3 scenarios, to utilize solar-coupled and standalone BTES systems for combined heating and cooling operation (cf. Chapter 3.2.2.2).

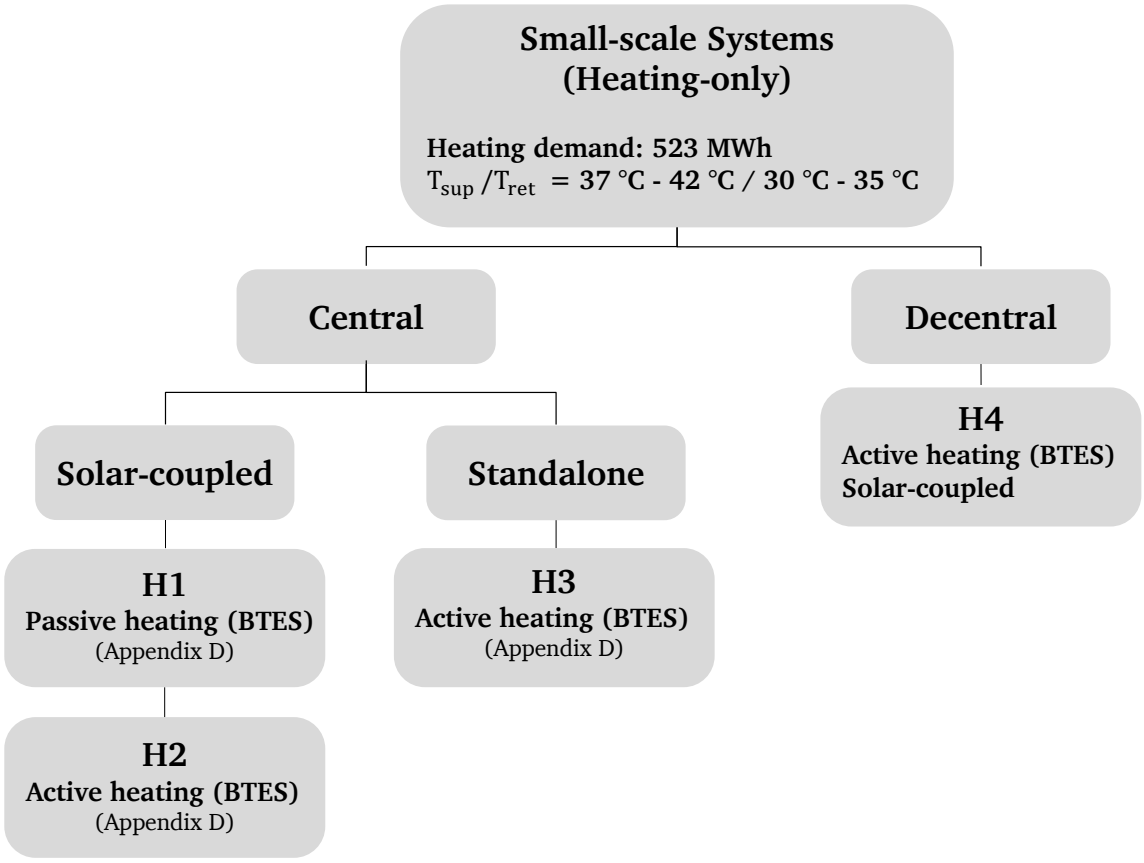


Figure 14: Investigated small-scale systems in heating-only mode.

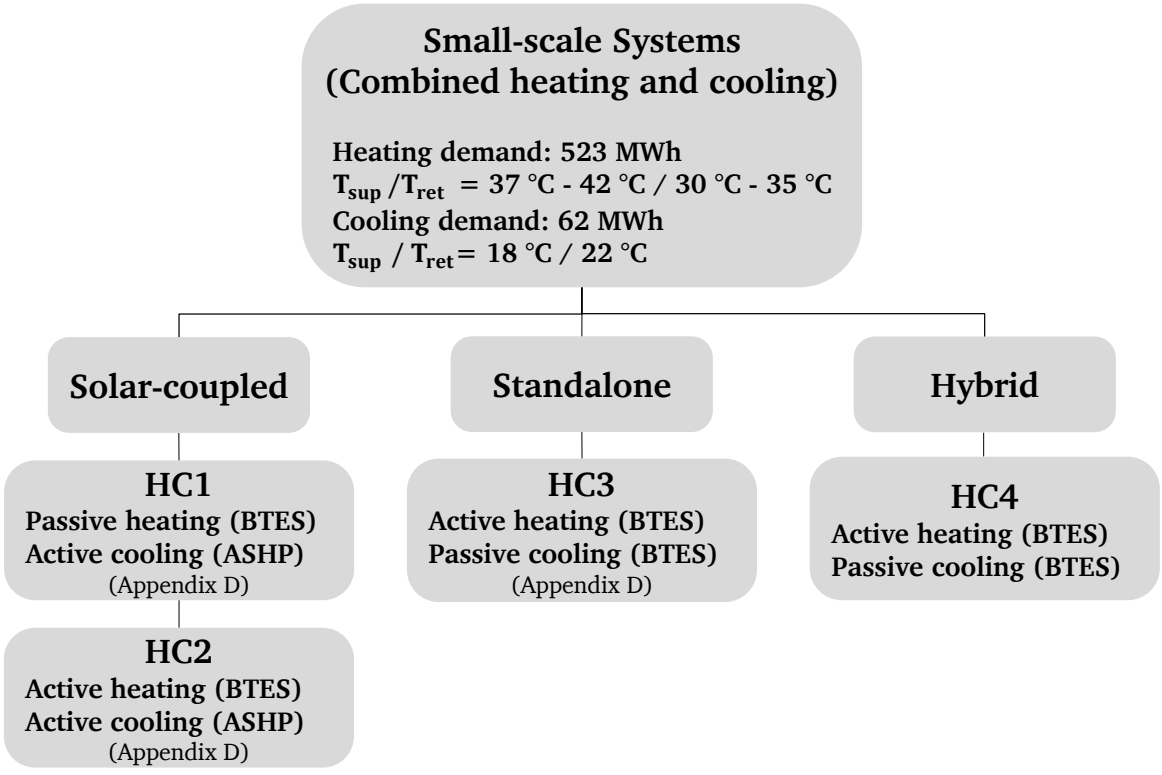


Figure 15: Investigated small-scale systems in combined heating and cooling mode.

### 3.2.2.1 Standalone and Solar-coupled Central Layouts

As an example, a simplified representation of system layout H1, which is based on the reference case, is illustrated in Figure 16. During summer operation, the collected solar energy is delivered to the BSTs via HEX1. A variable-speed pump (P1) assures a design temperature difference (ΔT) of 15 K for STCs (Saloux & Candanedo 2019). Charging/discharging of the BTES is controlled by a differential controller, based on the ΔT between the BTES center and the warmer/colder BST. In heating seasons, another variable-speed pump (P4) delivers the energy from the BSTs to the district via HEX2 and is controlled so that the supply temperature to the district is heated up to set point. Finally, the district loop pump (P5) is controlled to meet the district design ΔT. Operational strategy of H2 layout is very similar to H1 with the difference that the HP discharges the BTES actively and is bypassed when the BTES temperature is high enough to supply the load passively. In the H3 layout, which is a standalone design, a GSHP supplies the heating load actively. The system layouts H2 and H3 as well as more details about the operational strategies of the layouts H1-H3 can be found in Appendix D.

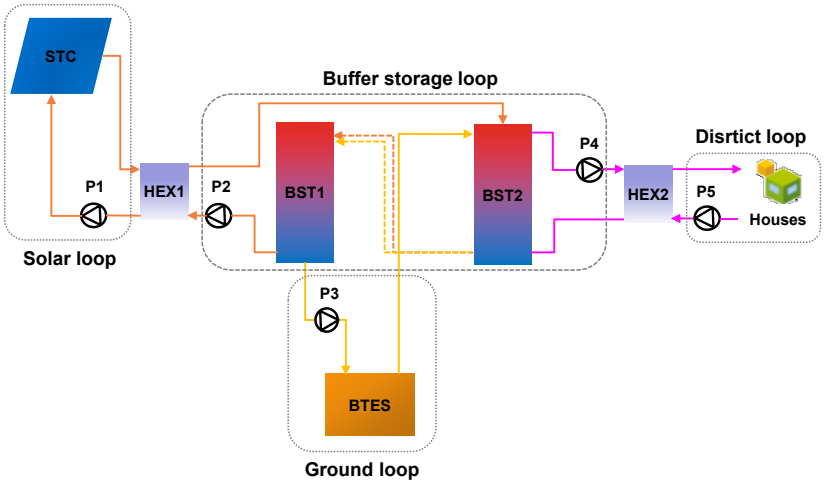


Figure 16: Exemplary system layout of the passive heating (H1).

Figure 17 shows a simplified representation of system layout HC3, in cooling mode. A differential controller monitors ΔT between the BTES center and the BST1. The cooling load is supplied passively when the BTES temperature is low enough to supply the load directly and the active cooling mode is activated with higher BTES temperatures. As mentioned earlier, in solar-coupled BTES systems (HC1 and HC2), ASHPs supply the cooling load actively, based on a manufacturer's catalog (Viessmann 2020b).

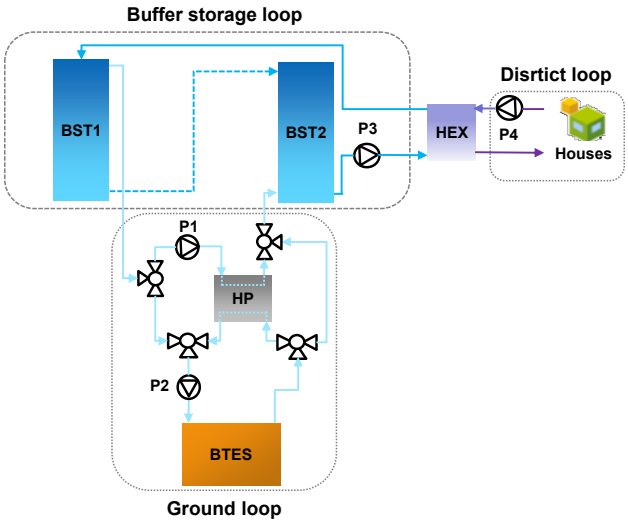


Figure 17: System layout of the BTES in cooling mode (HC3).

#### 3.2.2.2 Hybrid Central Layouts

The solar-coupled BTES systems cannot be used as heat sink for cooling purposes, as they are heated up to high temperature (HT) by STCs during non-heating seasons. A design option for combined heating and cooling mode is adding a second low-temperature (LT) BTES for cooling. The rejected waste heat from the cooling cycle is stored in the LT-BTES (cf. Figure 18a), which is discharged actively in the heating season. The heating load is then supplied by the hybrid BTES system consisting of the HT-BTES and the LT-BTES (cf. Figure 18b). The hybrid BTES systems can be designed to supply the heating load in serial or in parallel modes. In parallel mode, both BTES systems are used to shift the return fluid temperature up to the design supply temperature. In serial mode, the LT- BTES system partially shifts the fluid temperature and the rest is done by the HT-BTES up to the design supply temperature. In both modes, GBs supply the peak demand. Due to low design temperature shifts of the case study (Appendix D), serial configuration requires very low temperature shifts of each system, which leads to very high flow rates. Very high flow rates increase mixing in BSTs and electricity consumption of the pumps. Therefore, the serial configuration is suggested for system designs with higher temperature shifts. As a part of this study, the parallel configuration of the hybrid design scenario (Figure 18) will be compared with the other combined heating and cooling scenarios, explained in Chapter 3.2.2.1. It should be also mentioned that no thermal interaction between the BTES systems is assumed.

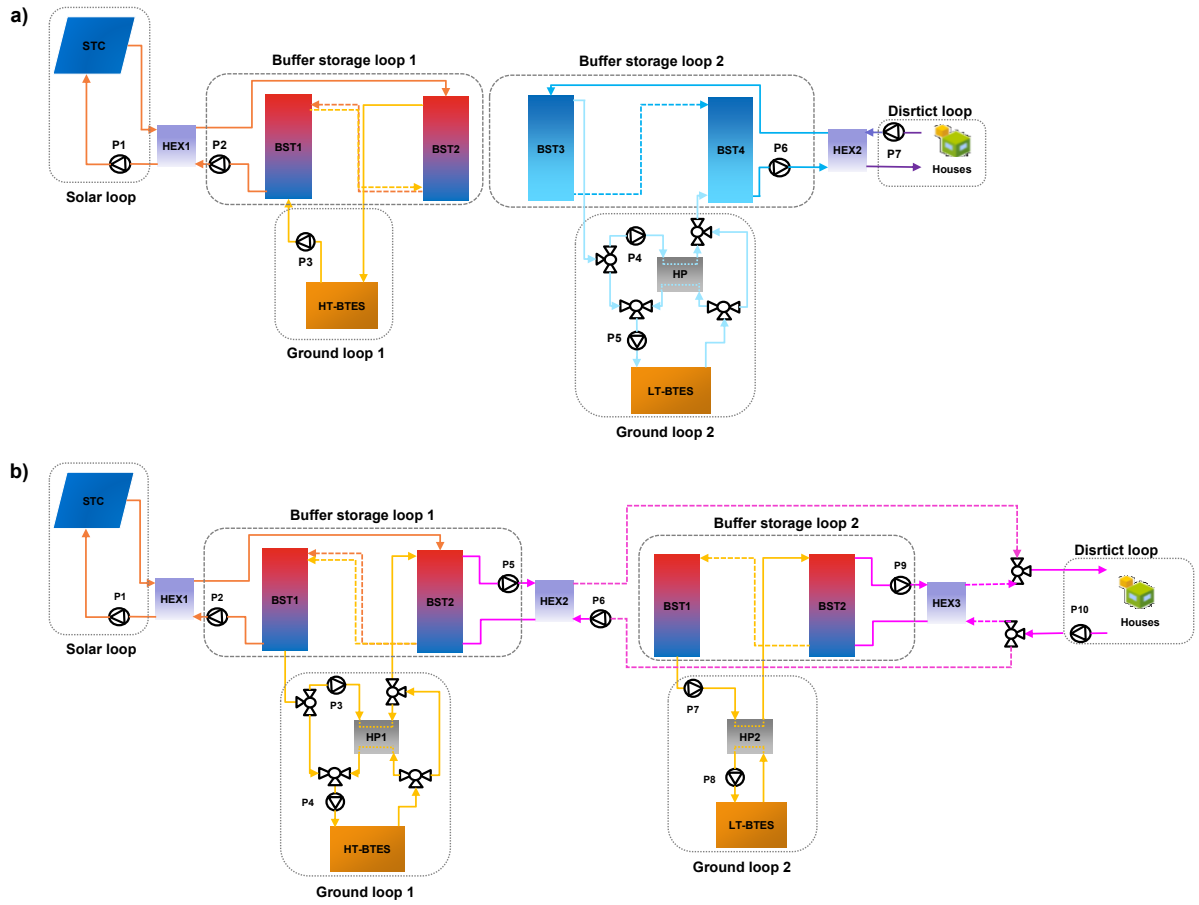


Figure 18: Hybrid central layout (HC4); a) cooling and storage mode, b) heating mode.

### 3.2.2.3 Solar-coupled Decentral Layouts

As mentioned in Chapter 2.1, 5GDHC can differ from 4GDH by introducing HPs at each consumer to shift the supply temperature to the specific requirements. The main purpose of this part of the study is comparing geothermal layouts based on a simplified definition of 4GDH and 5GDH concepts (i.e., central and decentral). To increase heat generation efficiency and to lower district heating losses, geothermal projects can be designed on lower temperature levels, which are not suitable for direct load supply. Consequently, supplementary heaters (HPs) are needed to increase their temperature at the location of each individual consumer. Based on the validated reference scenario in TRNSYS, explained in Chapter 3.2.1, an alternative solar-coupled geothermal layout based on 5GDH concept with decentral HPs in each individual building is proposed (H4, Figure 19). The proposed decentral layout, is then compared with solar-coupled central layouts (H1-H2, Appendix D). For the case study, the same quarter as Appendix D is considered, assuming that no cooling load is supplied.

In H4, the control strategies of the solar, BTES and BST loops are almost similar to H1 (cf. Chapter 3.2.2.1) with the difference that they are adapted to reduced district $T_{sup}$. The district $T_{sup}$ is set on 25 °C to reach the highest COP of the decentral HPs, which are parametrized with data from a manufacturer's catalog (Viessmann 2020a). The lower grid temperature in comparison with the previous layouts will also lead to lower losses from the district pipes, which is one of the motives behind using 5GDH networks. To reduce uncertainties regarding district heating design, it has been assumed that it has the same pipe length as the reference case.

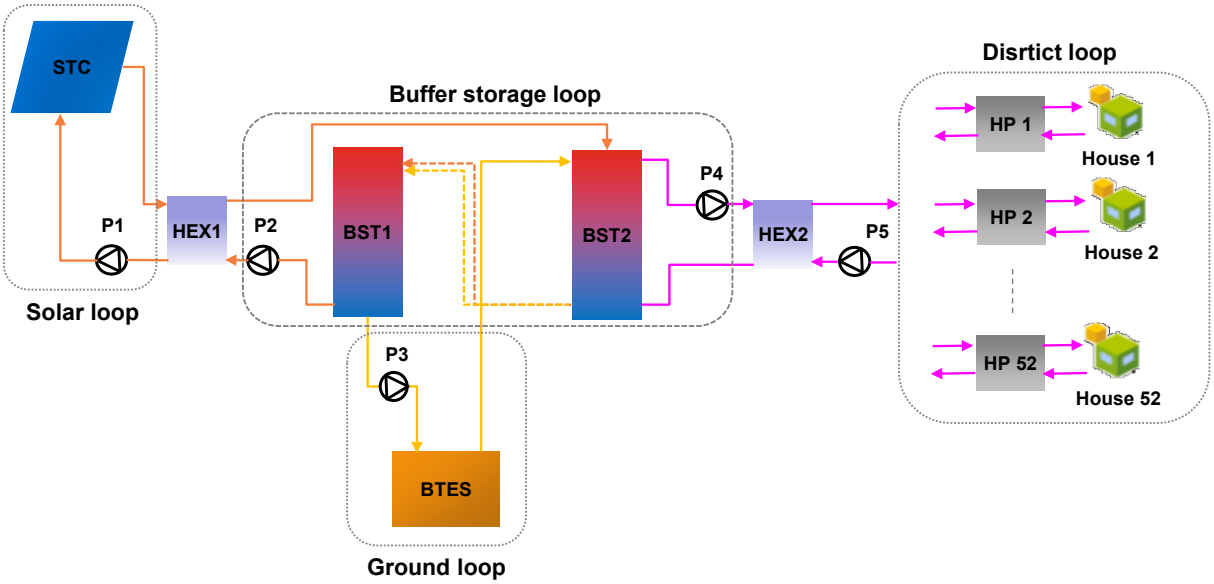


Figure 19: System layout of the active heating with decentral HPs (H4).

# 4 Evaluation Criteria

In this part different evaluation criteria, utilized for technical, economic and environmental assessment of geothermal layouts, are discussed. For technical and economic assessment, a dynamic exergo-economic assessment approach is adapted to geothermal systems (Chapter 4.1). To simultaneously minimize emissions and costs, an enviro-economic analysis method is used (Chapter 4.2).

## 4.1 Exergo-economic Analysis

In an exergo-economic evaluation, the aim is to minimize cost (min LCOE) and to maximize the exergetic efficiency (max $\eta_{exergy}$). A multi-objective optimization is required to find the best solutions for both objectives.

### 4.1.1 Exergy Analysis

Exergy is the maximum amount of work that can be done by a subsystem as it approaches a thermodynamic equilibrium with its surroundings by a sequence of reversible processes (Rant 1956). In other words, exergy is defined as a system's potential to interact with its environment. For thermal systems, this corresponds to the temperature difference between the heat carrier medium and a predefined reference temperature.

In heating and cooling systems, operation temperatures could be close to the reference temperature. Consequently, the exergy analysis strongly depends on the definition of the reference environment and a dynamic exergy analysis method is suggested. More details about dynamic and static exergy analysis methods can be found in Appendix B and Sayadi et al. 2019. For the dynamic analysis, several possible reference temperatures like the indoor air temperature, the undisturbed ground temperature and the outdoor temperature are discussed (Sayadi et al. 2019). In this study, the outdoor temperature is considered as the reference temperature $T_0$. Thermal exergy of a fluid, which can be used for exergy calculations in heating and cooling systems (Sayadi et al. 2019), can be calculated using Equation (1).

$$\dot{E} = \dot{m} c_p \times ((T - T_0) - T_0 \ln \frac{T}{T_0}) \quad (1)$$

The exergetic efficiency ($\eta_{exergy}$) of a system is the ratio of the product exergy rate ($\dot{E}_P$) to the exergy rate of the expended resources ($\dot{E}_F$) to generate this output. By integrating $\dot{E}_F$ and $\dot{E}_p$ into each time step over a system's lifetime ($n_{end}$), its overall average $\eta_{exergy}$ can be calculated (Equation (2)).

$$\eta_{exergy} = \frac{\sum_{n=0}^{n_{end}} \dot{E}_{P,n}}{\sum_{n=0}^{n_{end}} \dot{E}_{F,n}} \times 100\% \quad (2)$$

Dynamic exergy calculations of $\dot{E}_P$ and $\dot{E}_F$ for the whole system are adopted from Sayadi et al. 2019 to evaluate the integration of BTES systems into 4GDHC grids. For the standalone (Sa) layouts, $\dot{E}_P$ and $\dot{E}_F$ in heating load (HL) and cooling load (CL) supply can be calculated using Equations (3) and (4), respectively.

$$\dot{E}_{P,HL,Sa} = \begin{cases} \dot{E}_{sup} - \dot{E}_{ret} & T_0 < T_{ret} \\ \dot{E}_{sup} & T_{ret} < T_0 < T_{sup} \\ 0 & T_0 > T_{sup} \end{cases}$$

$$\dot{E}_{F,HL,Sa} = \begin{cases} \dot{E}_{elec} + \dot{E}_{gas} - \min(\dot{E}_{BTES}, 0) & T_0 < T_{ret} \\ \dot{E}_{elec} + \dot{E}_{gas} - \min(\dot{E}_{BTES}, 0) + \dot{E}_{ret} & T_{ret} < T_0 < T_{sup} \\ \dot{E}_{elec} + \dot{E}_{gas} - \min(\dot{E}_{BTES}, 0) + \dot{E}_{ret} - \dot{E}_{sup} & T_0 > T_{sup} \end{cases} \quad (3)$$

$$\dot{E}_{P,CL,Sa} = \begin{cases} \dot{E}_{sup} - \dot{E}_{ret} & T_0 > T_{ret} \\ \dot{E}_{sup} & T_{sup} < T_0 < T_{ret} \\ 0 & T_0 < T_{sup} \end{cases}$$

$$\dot{E}_{F,CL,Sa} = \begin{cases} \dot{E}_{elec} + \dot{E}_{gas} + \min(\dot{E}_{BTES}, 0) & T_0 > T_{ret} \\ \dot{E}_{elec} + \dot{E}_{gas} + \min(\dot{E}_{BTES}, 0) + \dot{E}_{ret} & T_{sup} < T_0 < T_{ret} \\ \dot{E}_{elec} + \dot{E}_{gas} + \min(\dot{E}_{BTES}, 0) + \dot{E}_{ret} - \dot{E}_{sup} & T_0 < T_{sup} \end{cases} \quad (4)$$

where $\dot{E}_{BTES}$ is the exergy which is stored in or extracted from the BTES system during heating and cooling seasons, it can be calculate using Equation (5). $T_b$ denotes the temperature on the boundary where heat transfer ($\dot{Q}_{BTES}$) occurs (Bejan et al. 1995), which is taken as the average storage temperature. In the calculation of $\dot{E}_{BTES}$, it is assumed that $\dot{Q}_{BTES}$ is positive when it is added to the BTES and negative when it is extracted from the BTES. Consequently, during the cooling seasons, if $T_0 > T_b$, the excess exergy is rejected from the system's control volume and it is deducted from the fuel exergy (cf. Equation 4), $\min(\dot{E}_{BTES}, 0)$ is negative. On the other hand, during the heating seasons if ambient temperature is lower than BTES temperature, $T_0 < T_b$, it means that the exergy from the ground is added to the overall fuel exergy (cf. Equation 3), $-\min(\dot{E}_{BTES}, 0)$ is positive.

$$\dot{E}_{BTES} = \dot{Q}_{BTES} \times (1 - \frac{T_0}{T_b}) \quad (5)$$

The chemical exergy of natural gas can be calculated using its lower heating value (LHV) (Bargel 2011), and the rate of exergy consumption ($\dot{E}_{gas}$) using the required LHV per time-step (Equation (6)).

$$\dot{E}_{gas} \approx 1.04 \times LHV \tag{6}$$

For solar-coupled heating-only scenarios, in which BHE arrays does not provide a direct source of exergy input to the system and merely acts as a medium to deliver the stored solar exergy, $\dot{E}_{F,HL}$ can be calculated using Equation (7). Consequently, the overall exergetic efficiency of the solar-coupled (Sc) systems can be calculated using Equation (7) and Equation (2).

$$\dot{E}_{P,HL,Sc} = \begin{cases} \dot{E}_{sup} - \dot{E}_{ret} & T_0 < T_{ret} \\ \dot{E}_{sup} & T_{ret} < T_0 < T_{sup} \\ 0 & T_0 > T_{sup} \end{cases}$$

$$\dot{E}_{F,HL,Sc} = \begin{cases} \dot{E}_{elec} + \dot{E}_{gas} + \dot{E}_{STC} & T_0 < T_{ret} \\ \dot{E}_{elec} + \dot{E}_{gas} + \dot{E}_{STC} + \dot{E}_{ret} & T_{ret} < T_0 < T_{sup} \\ \dot{E}_{elec} + \dot{E}_{gas} + \dot{E}_{STC} + \dot{E}_{ret} - \dot{E}_{sup} & T_0 > T_{sup} \end{cases} \tag{7}$$

$\dot{E}_{STC}$ is the input exergy from STCs and can be calculated using exergy-to-energy ratio for solar radiation having absorber temperature as heat transfer surface temperature and the ambient temperature as reference temperature, proposed by Petela 2003. This method is suggested when a comprehensive exergetic analysis of an existing system with specified dimensions is planned. However, due to limitations for the calculation of the absorber temperature in optimization studies, which is the purpose of this research, $\dot{E}_{STC}$ is assumed to be equal to the change in exergy content of the circulating fluid in STCs, which can be calculated using Equation (8).

$$\dot{E}_{STC} = (\dot{E}_{STC,out} - \dot{E}_{STC,in}) \tag{8}$$

To enhance the exergetic performance of a BTES-assisted system, it may be necessary to analyze the BTES during the storage (St) and extraction (Ext) periods separately, Equations (9) and (10). As it is mentioned before, it is assumed that $\dot{Q}_{BTES}$ is positive when it is added to the BTES and negative when it is extracted from the BTES. During the storage period, if the ambient temperature is lower than the BTES boundary temperature ($T_0 < T_b$), the exergy of the stored heat is the product exergy, $\max(\dot{E}_{BTES}, 0)$ is positive. On the other hand, $T_0$ can be considered as a reference point for the evaluation of storage preheating at lower temperature levels. It means that if $T_0 > T_b$ the exergy of the stored heat is considered as a part of the fuel exergy for storage preheating, $-\min(\dot{E}_{BTES}, 0)$ is positive. During the extraction period, if $T_0 < T_b$, the exergy of the extracted heat is a part of the fuel exergy, $-\min(\dot{E}_{BTES}, 0)$ is positive. On the other hand, if $T_0 > T_b$, the exergy of the extracted heat is deducted from the product exergy, $-\max(\dot{E}_{BTES}, 0)$ is negative, which means that the operation of the BTES system is not necessary to fulfill the exergy demand. Here, $\dot{E}_{elec}$ is the pumping power of the ground loop circulation pump. $\dot{E}_{in}$ and $\dot{E}_{out}$ are the exergy of the fluid, entering and leaving the BTES respectively.

$$\dot{E}_{P,BTES,St} = \max(\dot{E}_{BTES}, 0)$$
$$\dot{E}_{F,BTES,St} = \dot{E}_{in} - \dot{E}_{out} + \dot{E}_{elec} - \min(\dot{E}_{BTES}, 0) \tag{9}$$

$$\dot{E}_{P,BTES,Ext} = \dot{E}_{out} - \dot{E}_{in} - \max(\dot{E}_{BTES}, 0)$$
$$\dot{E}_{F,BTES,Ext} = \dot{E}_{elec} - \min(\dot{E}_{BTES}, 0) \quad (10)$$

Finally, by including dynamic exergetic performance of the BTES, fuel and product exergy of the whole system during storage and during extraction periods can be calculated separately using Equations 11 and 12.

$$\dot{E}_{P,Sc,St} = \max(\dot{E}_{BTES}, 0)$$
$$\dot{E}_{F,Sc,St} = \dot{E}_{F,HL,Sc} - \min(\dot{E}_{BTES}, 0) \quad (11)$$

$$\dot{E}_{P,Sc,Ext} = \dot{E}_{P,HL,Sc} - \max(\dot{E}_{BTES}, 0)$$
$$\dot{E}_{F,Sc,Ext} = \dot{E}_{F,HL,Sc} - \min(\dot{E}_{BTES}, 0) \quad (12)$$

### 4.1.2 Economic Analysis

Levelized cost of energy (LCOE) can be calculated using Equation (13), where the numerator is the net present value of the total life cycle cost and the denominator is the discounted total energy output (Short et al. 1995). The net present value of the total cost is calculated having capital investment costs ($C_{IC}$), maintenance costs ($C_{MC}$), fuel costs ($C_f$) and environmental costs ($C_{env}$). The system lifetime ($n_{end}$) and the discount rate (i) are assumed to be 30 years and 3%, respectively.

$$LCOE = \frac{\sum_{n=0}^{n_{end}} (C_{IC,n} + C_{MC,n} + C_{f,n} + C_{env,n}) \cdot (1+i)^{-n}}{\sum_{n=0}^{n_{end}} Q_{out,n} (1+i)^{-n}} \times 100\% \quad (13)$$

Investment cost and maintenance cost functions of the main components are listed in Appendix B. Fuel and environmental costs are calculated using Equations (14) and (15) by summing up electricity consumptions ($f_{elec}$) and gas consumptions ($f_{gas}$) in each time step over the system lifetime for each simulation. Electricity and natural gas costs ($c_{elec}$ and $c_{gas}$), Global Warming Potential as a result of the consumption of electricity and gas ($GWP_{elec}$ and $GWP_{NG}$) and the emission costs ($c_{CO2}$) as a function of the assessment year are calculated as given in Appendix B.

$$C_{f,n} = f_{elec,n}\, c_{elec,n} + f_{gas,n}\, c_{gas,n} \quad (14)$$

$$C_{env,n} = f_{elec,n}\, c_{CO2,n}\, GWP_{elec,n} + f_{gas,n}\, c_{CO2,n}\, GWP_{NG,n} \quad (15)$$

It should be mentioned that in exergo-economic optimization of the layouts, environmental costs are only included in the calculation of LCOE of the standalone layouts with larger BHE arrays (Table 1).

## 4.2 Enviro-economic Analysis

An enviro-economic optimization is utilized to simultaneously minimize cost (min LCOE) and emissions (min EF). As both target functions compete with each other, multi-objective optimization is required to find the best solutions for both.

### 4.2.1 Environmental Analysis

Environmental evaluations of the proposed system layouts are conducted by calculating their overall global warming potential (GWP) using Equation (16). It adds up the GWP associated with electricity ($GWP_{Elec,n}$) and natural gas consumption ($GWP_{NG,n}$) over the project lifetime ($n_{end}$) as well as emissions caused during the production of each system component ($GWP_{Prod,n}$). The overall EF is the ratio of GWP and the overall energy production using Equation (17).

$$GWP = \sum_{n=0}^{n_{end}} GWP_{Elec,n} + GWP_{NG,n} + GWP_{Prod,n} \tag{16}$$

$$EF = \frac{GWP}{\sum_{n=0}^{n_{end}} Q_{out,n}} \tag{17}$$

### 4.2.2 Economic Analysis

The economics of the various system layouts are compared on the basis of LCOE, Equation 13. It should be mentioned that for enviro-economic optimization of the layouts, environmental penalty costs are not added to LCOE and are considered in separate sensitivity analyses to assess their effects on optimized designs.

## 5 Computational Model Development

To utilize the discussed evaluation criteria for the assessment of the proposed geothermal layouts in DHC grids, suitable computational models are required. The proposed system layouts are mainly modeled and parameterized in TRNSYS (Appendixes B and D). MATLAB is coupled with TRNSYS for multi-objective optimization utilizing the non-dominated sorting genetic algorithm (NSGA II) (Deb et al. 2002) toolbox. Different computational models including direct and indirect optimization methods with or without parallel computation as well as step-wise optimization method are proposed and improved at each stage of this study.

### 5.1 Dynamic System Simulation

TRNSYS is used for the dynamic evaluation of the proposed layouts of this study. It is a simulation program for the transient simulation of different kinds of energy systems (Klein et al. 2017). TRNSYS simulations are constructed by connecting individual component models (known as Types) together into a complete mode, similarly to how they would be connected in real life (Klein et al. 2017). In this study, main components (TRNSYS types) include BTES, STC, BST and HP. Type 557, which is based on a duct storage model (Hellstrom 1992), is used for BTES modeling. Type 1a is used for the simulation of STCs, which is based on a quadratic efficiency performance model (Liu & Jordan 1963; Duffie & Beckman 2013). For the modelling of BSTs Type 534 is used, which divides the tank into a series of isothermal layers to account for stratification. Type 927 is used for simulating HPs, which works based on interpolation with four independent variables to read outputs based on inputs, from a provided catalog files. More details about utilized TRNSYS types as well as their parameters can be found in Appendixes A and D. Considering the system layout (Chapter 3), TRNSYS Types are connected and control strategies are implemented in equation blocks for dynamic system simulation and control.

In a parallel study, Formhals et al. 2021b developed a Modelica toolbox for the simulation of BTES systems (MoBTES, Appendixes A), based on Thermal Resistance and Capacitance Model

(TRCM), introduced by (Bauer et al. 2011). Modelica is a language for the modeling and simulation of multi-domain physical systems (Olsson 2017). It uses an object-oriented equation-based approach facilitating state of the art modeling, simulation, and optimization of district heating systems (Schweiger et al. 2017). The model outputs are compared with TRNSYS Type 557, a 3D finite element model and measured data of a real case study. MoBTES is proven to be a robust toolbox, which provides the designer with different alternatives, e.g. different BHE types, changing flow direction and separate thermophysical properties for different layers of the underground. More details about the model can be found in Appendix A. Utilizing MoBTES as well as other available or developed components in Modelica, Formhals et al. 2021a model a solar district heating grid with integrated seasonal geothermal energy storage. The model is then utilized to assess different transition strategies in achieving the TU Darmstadt's emission reduction targets until 2050 (Appendixes C).

## 5.2 Direct Optimization

For the direct optimization, estimates of the optimization algorithm for the systems design parameters under consideration are written to a text file, from which they are read by TRNSYS as input parameters for the system simulations. After a simulation in project lifetime is finished, the resulting objective functions in TRNSYS are sent back and evaluated by the optimization algorithm in MATLAB. This procedure is repeated for each scenario until the best Pareto front, which is the loci of the most optimal solutions, is selected. The stopping criterion depends on the settings of the optimization algorithm, which are suggested by MATLAB considering the number of variables and the required accuracy (MATLAB 2021). Figure 20 illustrates the computational model of the direct optimization method.

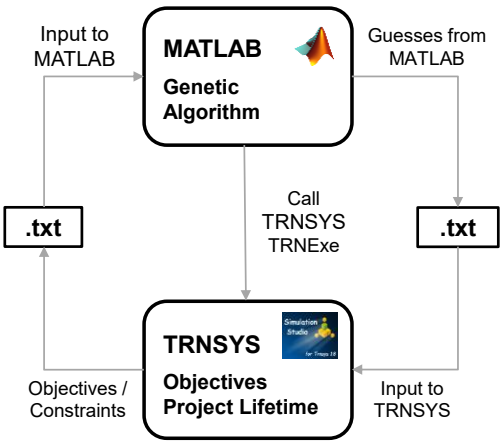


Figure 20: Computational model of the direct optimization method.

## 5.3 Indirect Optimization

The indirect optimization procedure is divided into three sequential stages, cf. Figure 21. In the first stage, an initial direct optimization is performed based on TRNSYS system simulations. The results are then used in the second stage to create a proxy model, which approximates the objective functions. This leads to a considerable reduction in computational costs for the required long-term assessments of geothermal systems. Finally, in the third stage, the proxy model is used to minimize LCOE and EF in a multi-objective optimization. The computational model is explained in more details in Appendix D.

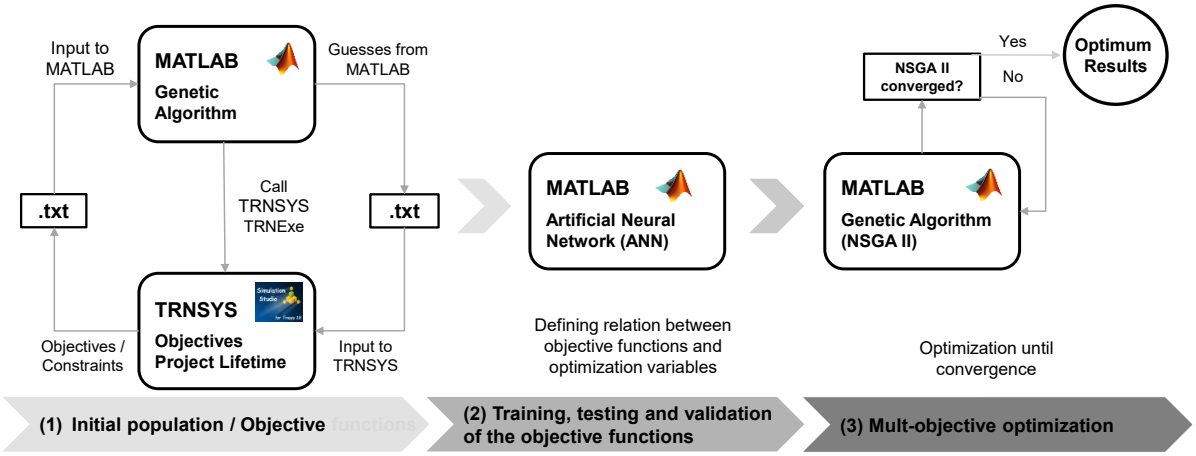


Figure 21: Computational model of the indirect optimization method.

## 5.4 Parallel Computation and Optimization

To decrease the computational effort, instead of calling TRNSYS once in each evaluation by the optimization algorithm, it can be called in parallel using multiple processor cores. Using parallel computing toolbox, multiple TRNSYS dck files are created by MATLAB, which replaces the values of the optimization variables in each file with the guessed values by the optimization algorithm (Figure 22). The resulting objective function values in TRNSYS, which are appended into a text file, are sent back and evaluated by the optimization algorithm in MATLAB. If sufficient number of processing cores are available, the parallel computation approach can be also used for a direct optimization. However, depending on the optimization problem, reaching final convergence of the algorithm may still not be feasible using direct parallel computation approach.

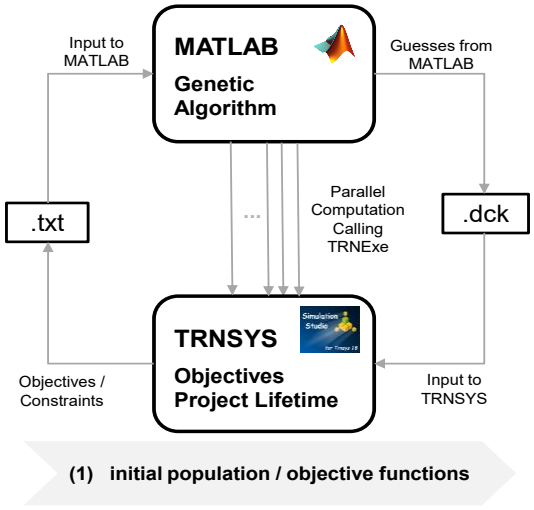


Figure 22: Computational model of the direct optimization method with parallel coupling of TRNSYS and MATLAB.

To achieve the final convergence, the first stage of the indirect optimization (cf. Figure 21) can be replaced by the parallel computation method (Figure 22). Therefore, a larger number of training input data can be given to the proxy model in the second stage within the same time frame (cf. Figure 23), which leads to more accuracy of the proxy model compared to the previous model.

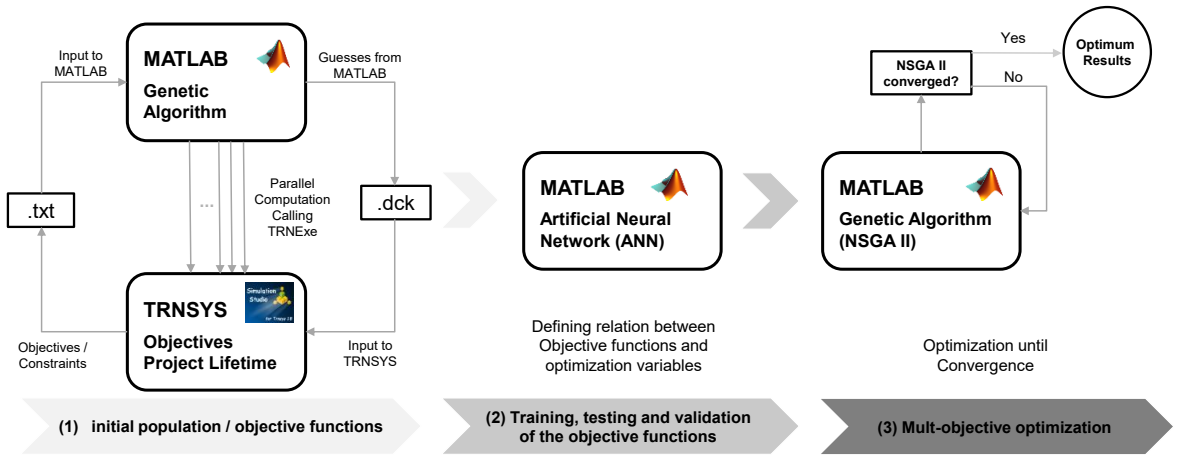


Figure 23: Computational model of the indirect optimization method with parallel coupling of TRNSYS and MATLAB.

## 5.5 Step-wise Optimization

In practical applications, a system may be needed to be optimized operationally. This means that the operation of the system (e.g. flow rate of a variable-speed pump, set point temperature of a thermostat etc.) is controlled so that an objective function (e.g. exergetic efficiency, LCOE) is optimized at each time-step. Figure 24 shows the proposed computational model for step wise optimization purposes. In the first stage, a model with optimized dimensions or an available system in operation is simulated in TRNSYS by generating random values for the controlled variable, using type 577 (uniform distribution (Dekking et al. 2005)). The random values of the controlled variable, the values of other influential variables and the corresponding values of the objective function are then used to train a model using ANN toolbox in MATLAB in the second stage. In the third stage, the influential variables in TRNSYS are passed to the proxy model in MATLAB at each time step, using type 155. The objective function, defined by the proxy model, is optimized in MATLAB and the corresponding value of the controlled variable is then given back to TRNSYS to operationally control the model at each time step. An exemplary application of the model is explained in Chapter 6.4.

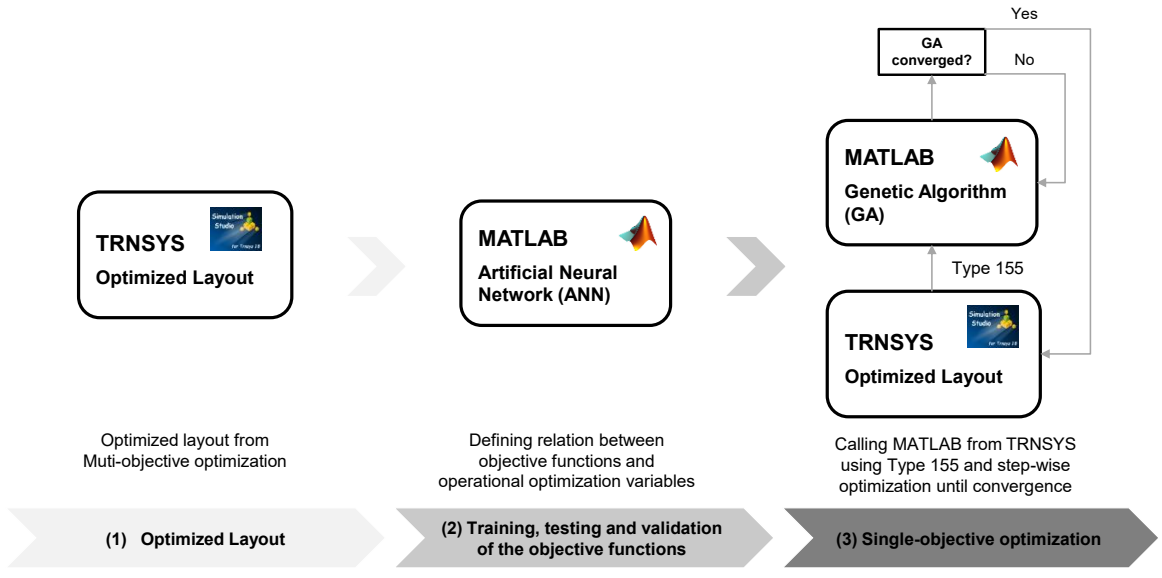


Figure 24. Step-wise optimization procedure.

# 6 Multi-objective Optimization of System Design Scenarios

In this part of the study, the developed computational models (Chapter 5) and the evaluation criteria (Chapter 4) are utilized to conduct multi-objective optimization of the proposed layouts (Chapter 3). As the title of this dissertation shows, the optimizations of this study are classified into two main groups, exergo- and enviro-economic optimization. For the large-scale systems, the direct optimization method is utilized for an exergo-economic optimization of the standalone layouts (Chapter 6.1). For the small-scale systems, an indirect enviro-economic optimization of the solar-coupled and standalone layouts are conducted (Chapter 6.2.1) and the results are compared with the optimization results of hybrid central layouts (Chapter 6.2.2). Furthermore, direct and indirect exergo-economic optimizations of the solar-coupled central and decentral layouts are carried out (Chapter 6.2.3) and the results of exergo- and enviro-economic optimization approaches are compared (Chapter 6.3). Finally, by conducting an step-wise optimization that optimizes an operational variable at each time step, the performance of a dimensionally-optimized model is improved (Chapter 6.4).

## 6.1 Large-scale Systems

The direct optimization (Chapter 5.2) is utilized for exergo-economic optimization of large-scale standalone central layouts explained in Chapter 3.1. Table 1 shows main components of each layout and their heating and cooling method. The objective functions, setup and boundaries of the optimization variables are summarized in Table 2.

Table 1. Characteristics of large-scale standalone central layouts.

| Scenario | Heating | Cooling | HPs | BST | GB |
|---|---|---|---|---|---|
| ActSer | Active (BTES) | Active (BTES) | Single stage | Vertical | Serial |
| ActPar | Active (BTES) | Active (BTES) | Double stage | Vertical | Parallel |
| PasSer | Active (BTES) | Passive (BTES) | Single stage | Vertical | Serial |
| PasPar | Active (BTES) | Passive (BTES) | Double stage | Vertical | Parallel |

Table 2. Objective functions, optimization variables and constraints (direct optimization) for large-scale standalone central layouts (Hemmatabady et al. 2020).

| Objective functions | Subject to |
|---|---|
| min $\eta_{exergy}$ | $30\text{m} \leq L_{BHE} \leq 400\text{m}$ |
| min LCOE | $30 \leq N_{BHE} \leq 1200$ |
| | $2\text{m} \leq S_{BHE} \leq 25\text{m}$ |
| | $50\text{kW} \leq Cap_{HP} \leq 8150\text{kW}$ |
| | $25\text{m}^3 \leq Vol_{BST} \leq 10000\text{m}^3$ |
| | $3\text{K} \leq \Delta T_{BST}{}^{b} \leq 10\text{K}$ |

Figure 25 shows the local evaluations by the algorithm for finding the points which do not violate the constraints. The non-dominated points for each scenario are located on a Pareto front, which is closest to the bottom right corner. Comparing the optimal designs of the different layouts shows that passive cooling and maximizing the heating temperature shift by the ground loop, lead to best designs (PasSer and ActPar). In Appendix B, results are elaborated, the ranges of the optimization variables on the Pareto fronts are specified, the component-wise exergy destruction and loss and composition of LCOE for characteristic designs are presented and discussed.

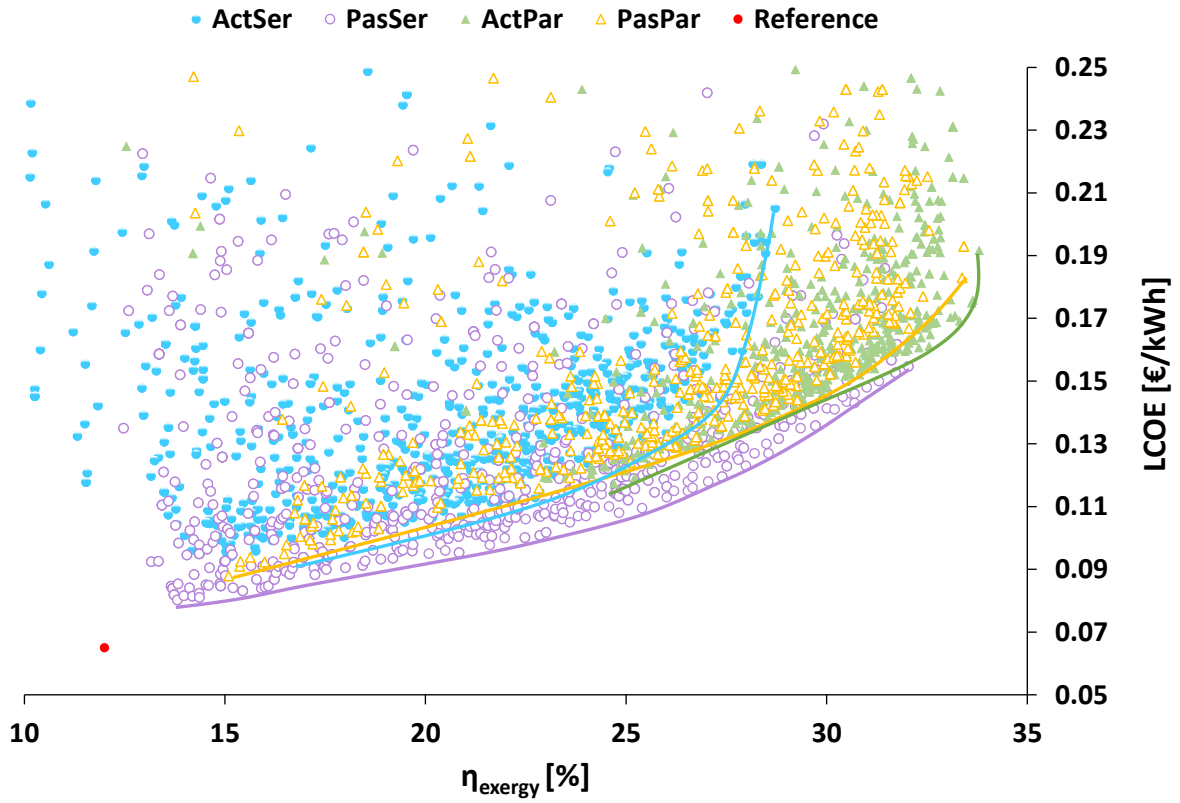


Figure 25. Exergo-economic optimization results of the large-scale standalone central layouts (Hemmatabady et al. 2020).

Formhals et al. 2021a investigate different transition strategies towards a solar-coupled central layout for TU Darmstadt's campus Lichtwiese utilizing an enviro-economic analysis method (Appendix C). Other than different dimensions of components as well as timing of construction or decommissioning in parallel with grid temperature reduction, briefly explained in Chapter 3.1, the transition strategies are assumed to be accompanied by lower emissions from electricity generation and higher gas prices during different stages of the project. Comprehensive results show that gradual construction of STCs and a BTES, accompanied by a simultaneous scaling-down of the CHP capacity leads to better results than their immediate construction. In Appendix C, comprehensive results are explained, the composition of the LCOE per transition phase for the selected systems is specified and sensitivity analyses are conducted.

## 6.2 Small-scale Systems

### 6.2.1 Enviro-economic Optimization of Small-scale Standalone and Solar-coupled Central Layouts

The indirect optimization approach (cf. Chapter 5.3) is utilized to minimize emissions and costs of the small-scale standalone and solar-coupled central layouts (Chapter 3.2.2.1). Table 3 summarizes main components of each layout and their heating and cooling method. The objective functions, setup and boundaries of the optimization variables are summarized in Table 4.

Table 3: Characteristics of small-scale standalone and solar-coupled central layouts.

| Scenario | Heating | Cooling | STC | GHE | BST | GB |
|---|---|---|---|---|---|---|
| H1 | Passive (BTES) | --- | Flat plate | 2U-tube | Vertical | Peak |
| H2 | Active (BTES) | --- | Flat plate | 2U-tube | Vertical | Peak |
| H3 | Active (GSHP) | --- | --- | 2U-tube | Vertical | Peak |
| HC1 | Passive (BTES) | Active (ASHP) | Flat plate | 2U-tube | Vertical | Peak |
| HC2 | Active (BTES) | Active (ASHP) | Flat plate | 2U-tube | Vertical | Peak |
| HC3 | Active (BTES) | Passive (BTES) | --- | 2U-tube | Vertical | Peak |

Table 4. Objective functions and optimization variables (indirect optimization) for small-scale standalone and solar-coupled central layouts.

| Objective functions | Subject to |
|---|---|
| min EF | $30\text{m} \leq L_{BHE} \leq 400\text{m}$ |
| min LCOE | $6 \leq N_{BHE} \leq 300$ |
| | $56.6\text{kW} \leq Cap_{HP}{}^{b} \leq 300\text{kW}$ |
| | $13.57m^2 \leq A_{STC} \leq 5000m^2$ |
| | $10m^3 \leq Vol_{BST} \leq 1000m^3$ |

[b] for active scenarios

Figure 26 presents the enviro-economic optimization results of the layouts H1-H3 and HC1-HC3. Among the heating-only layouts (H1-H3), the one with seasonal storage of solar energy and active discharging via a HP (H2) shows the best results. Among the combined heating and cooling layouts (HC1-HC3), seasonal storage of the waste heat from cooling and active discharging via a HP (HC3) achieves the lowest LCOE while also obtaining a reasonably low EF. Nevertheless, like the heating-only layouts, the lowest EFs can be only achieved by the solar-coupled layouts. Furthermore, the heating-only and the combined heating and cooling scenarios are compared, using specific and cumulative values (Figure 26 and Figure 27). For the solar-coupled layouts (H1/H2 and HC1/HC2) cooling reduces the specific cost and emissions per kWh of provided energy (LCOE and EF) (Figure 26). However, it obviously increases cumulative energy costs and emissions (i.e. the NPV and GWP, Figure 27). For the standalone scenarios (H3/HC3), in contrast, cooling improves both the specific and the cumulative evaluation criteria. More details about the comparison between the results, ranges of the optimized solutions

and relation between them as well as the composition of EF and LCOE for the characteristic designs can be found in Appendix D.

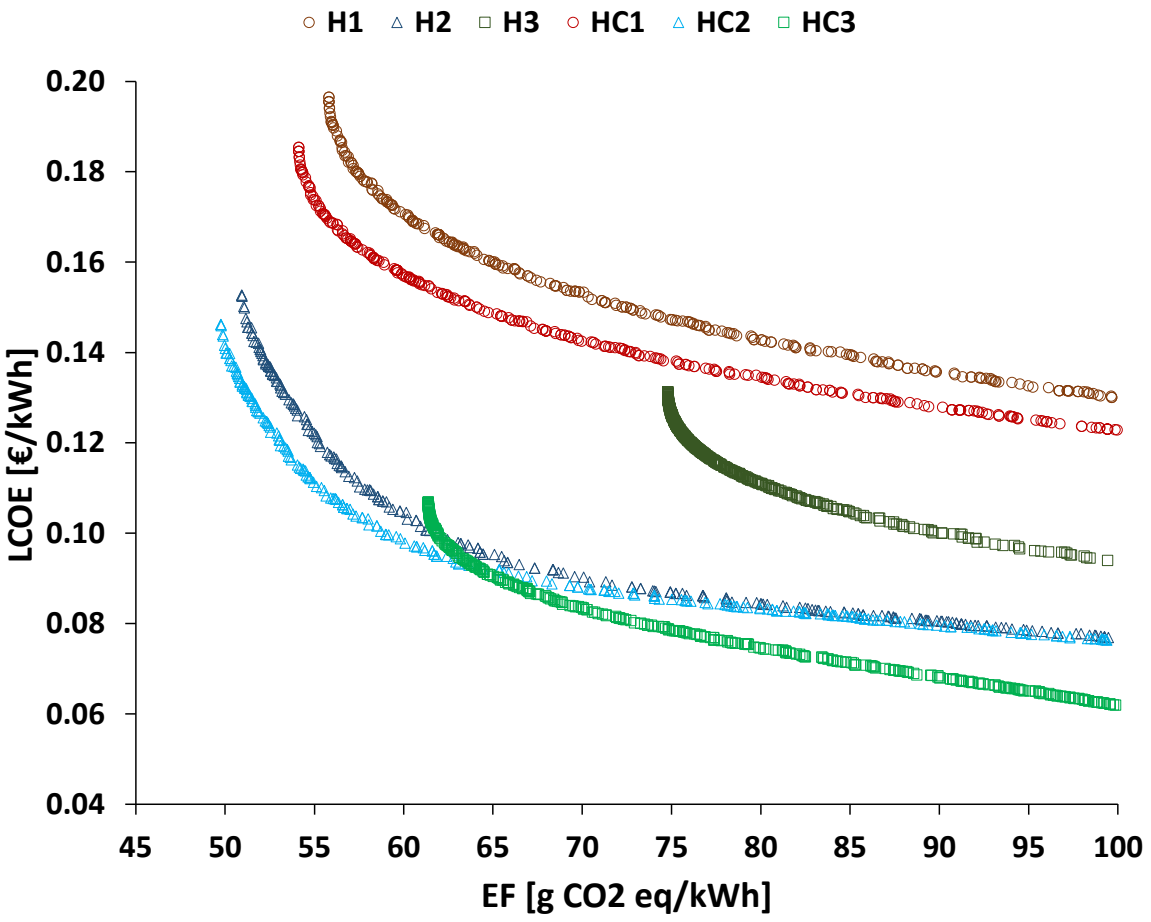


Figure 26. Enviro-economic optimization results of the layouts H1-H3 and HC1-HC3 (specific values).

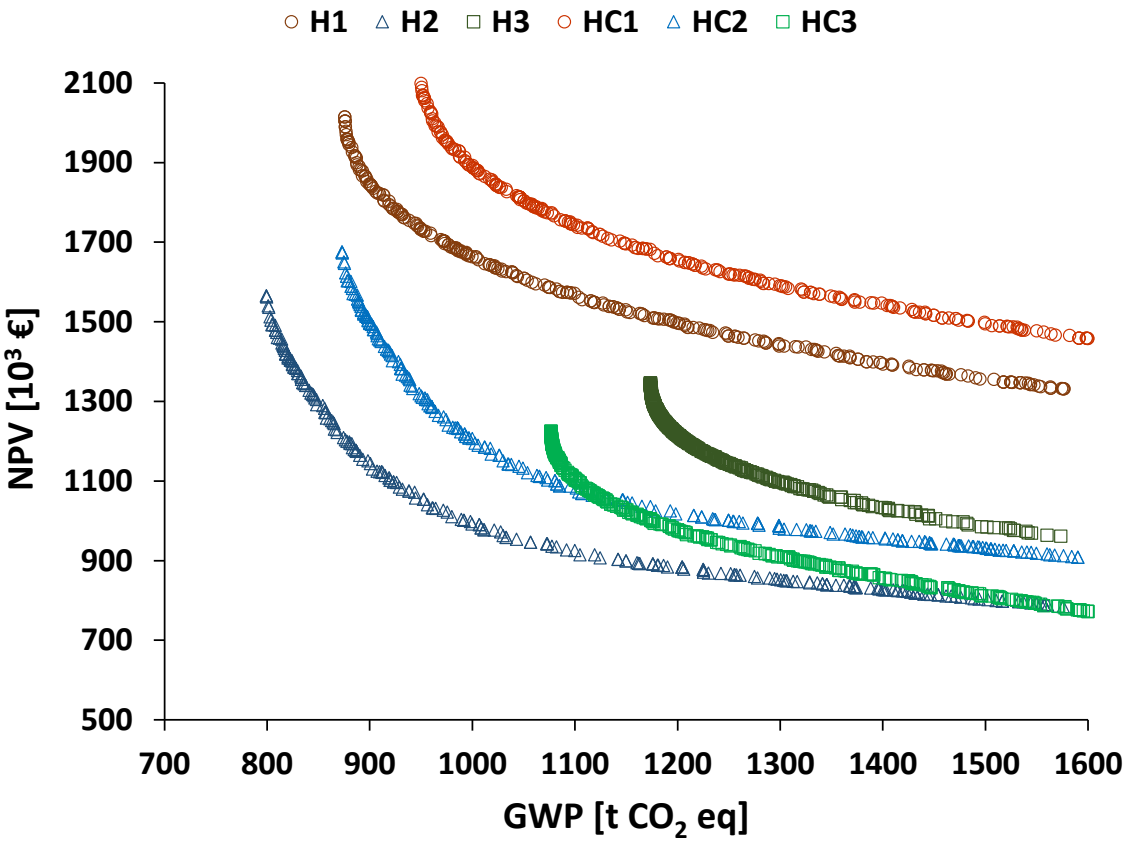


Figure 27. Enviro-economic optimization results of the layouts H1-H3 and HC1-HC3 (cumulative values).

For final validity check of the simulation against ANN method, the most economical (Eco), the most environmentally-friendly (Env) and the compromise (Comp) solutions on the Pareto fronts are chosen. After simulating the selected points with the TRNSYS models, the results are compared with the outputs from the ANN (Figure 28). As it can be seen in the figure, the ANN method can accurately predict the simulation results.

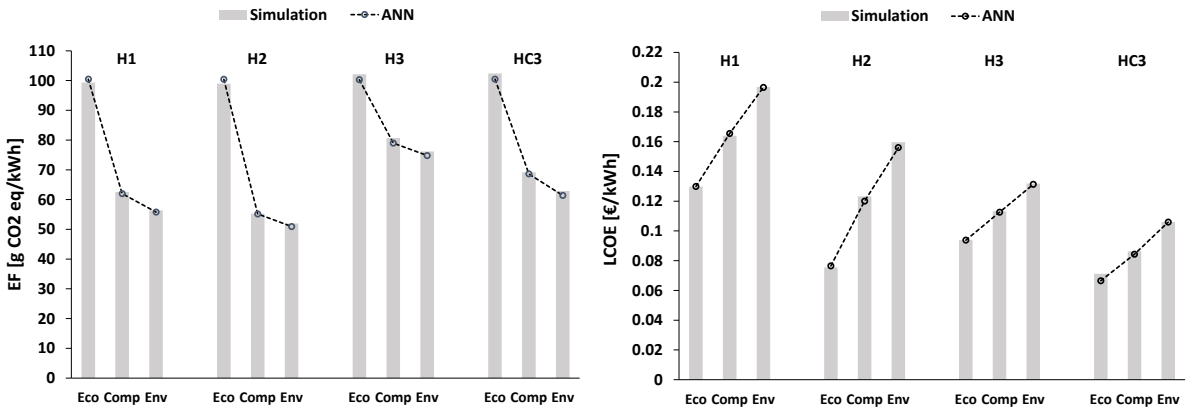


Figure 28. Simulation vs. ANN results of EF (a) and LCOE (b) for the characteristic designs of the layouts H1-H3 and HC3.

### 6.2.2 Enviro-economic Optimization of Small-scale Hybrid Central Layouts

In this part, enviro-economic optimization of the hybrid central layout (HC4), explained in Chapter 3.2.2.2, is conducted. Results are then compared with the other combined heating and cooling scenarios, HC1-HC3. Table 5 shows main components of the layouts and their heating and cooling method. The objective functions, setup and boundaries of the optimization variables are summarized in Table 6. To reduce the computational effort, upper boundaries of the optimization variables for each of the BTES systems in parallel are chosen from the optimization results of each layout separately (HC2 and HC3) (Appendix D). Moreover, optimum values for $Vol_{BST}$ are chosen to be approximately 0.25 $[m^3/m^2]\times A_{STC}$ and 0.8 $[m^3/kW]\times Cap_{HP}$, from optimization results of HC2 and HC3 scenarios respectively (Appendix D). Finally, α refers to the hybrid control signal, which is used for distributing the return fluid from the district loop between the HT and the LT loops. Higher α values show higher shares of the LT-BTES system in heating load supply.

Table 5: Characteristics of combined heating and cooling layouts.

| Scenario | Heating | Cooling | STC | GHE | BST | GB |
|---|---|---|---|---|---|---|
| HC1 | Passive (BTES) | Active (ASHP) | Flat plate | 2U-tube | Vertical | Peak |
| HC2 | Active (BTES) | Active (ASHP) | Flat plate | 2U-tube | Vertical | Peak |
| HC3 | Active (BTES) | Passive (BTES) | --- | 2U-tube | Vertical | Peak |
| HC4 | Active (BTES) | Passive (BTES) | Flat plate | 2U-tube | Vertical | Peak |

Table 6. Objective functions, optimization variables and constraints (indirect optimization) of the hybrid scenario.

| Objective functions | Subject to |
|---|---|
| min EF | $30m \leq L_{BHE1} \leq 85m$ |
| min LCOE | $6 \leq N_{BHE1} \leq 66$ |
| | $56.6kW \leq Cap_{HP1} \leq 113.2kW$ |
| | $30m \leq L_{BHE2} \leq 220m$ |
| | $6 \leq N_{BHE2} \leq 33$ |
| | $56.6kW \leq Cap_{HP2} \leq 113.2kW$ |
| | $13.57m^2 \leq A_{STC} \leq 1260m^2$ |
| | $0 \leq \alpha \leq 1$ |

The Pareto efficient solutions of the hybrid layout (HC4) are added to the optimization results of other combined heating and cooling scenarios (HC1-HC3), Figure 29. A comparison of the optimization results of all layouts reveals that the hybrid scenario achieves the lowest LCOE as

well as EF for a wide range of optimal solutions with EFs of approximately lower than 95 g CO2 eq/kWh.

The ranges of the optimized variables on the Pareto front of the Hybrid scenario is given in Table 7. α has optimum values between 0.32 and 0.52, which means lower shares of the LT-BTES system in heating load supply for most of the optimum designs. The optimum share of heating to cooling load supply by a standalone geothermal system is between 2-3 (Hemmatabady et al. ). As the cooling load is approximately 12% of the heating load, cf. Appendix D, a maximum α value of 0.36 could be already estimated. However, due to higher costs of solar-coupled BTES, higher values of α, up to 0.52, are also resulted by the optimization algorithm. The optimization variables in Table 7 lie in smaller ranges compared with HC2 and HC3 (Appendix D). Smaller $A_{STC}$ leads to the reduction in LCOE, compared with HC2 scenario. On the other hand, having STCs results in lower EFs in comparison with the standalone layout (HC3). Consequently, the parallel utilization of solar-coupled and standalone layouts for combined heating and cooling load supply results in enviro-economic improvement, compared with each of the layouts separately.

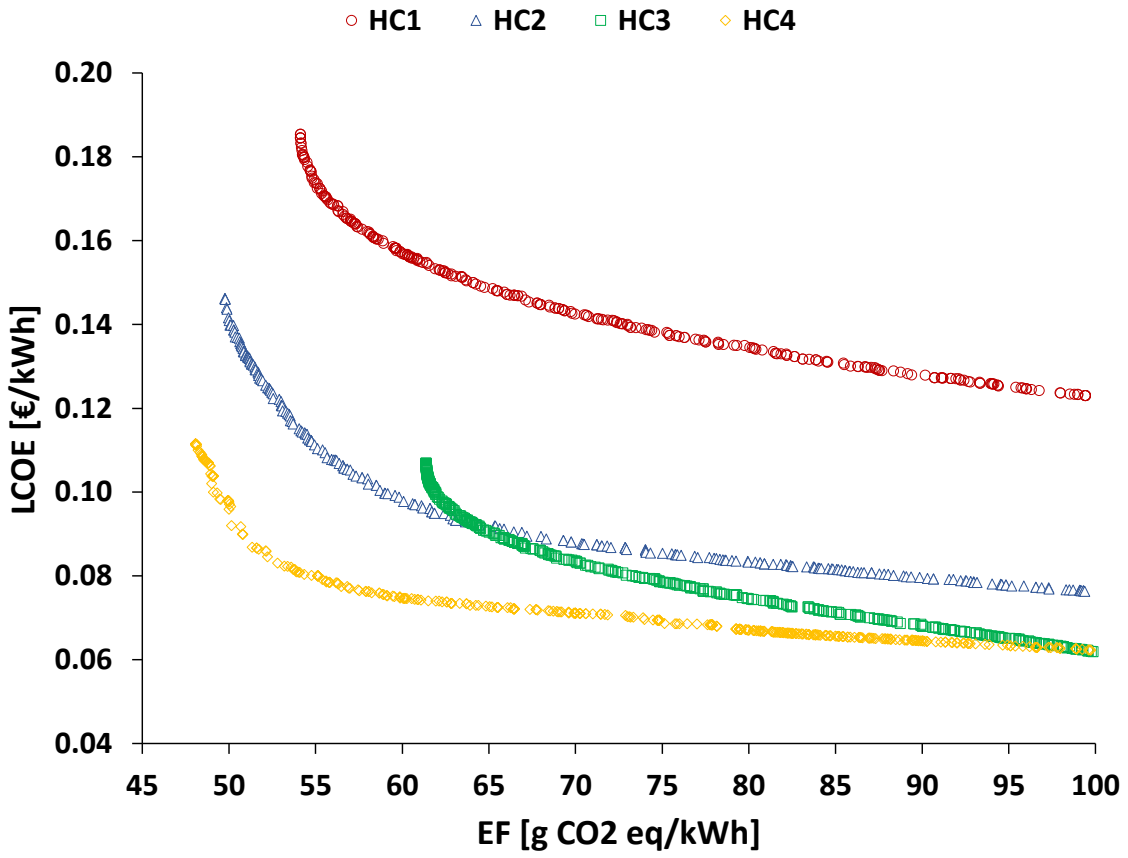


Figure 29. Enviro-economic optimization results of the layouts HC1-HC4.

The relation between the optimized variables of the designs on the Pareto fronts and their corresponding outputs is shown in Figures 30 and 31. Like previous layouts, EF decreases and LCOE increases by increase in total drilling length. Similarly, an increase in $A_{STC}$ decreases EF and increases LCOE. Figures 30 and 31 can be used to determine an optimal hybrid layout, depending on a project's constraints and the envisaged layout, by choosing a value for the objectives. For a chosen total drilling length of $L_{HT-BTES}$ and $L_{LT-BTES}$, $Cap_{HP1}$ and $Cap_{HP2}$ can be

selected from Figure 30. Optimal ratios of $L_{BHE}$ and $N_{BHE}$ for HT-BTES and LT-BTES can be derived from Table 7, considering that higher $L_{BHE}$ results in lower EF and higher LCOE (Figure 31a and 31b). Finally, having the values of the objectives, optimal value of α can be also derived from Figure 31c.

Table 7. Ranges of the optimized solutions on the Pareto fronts of the Hybrid scenario based on the BTES number; BTES1 (solar-coupled) and BTES2 (standalone).

| $0.32 \leq \alpha \leq 0.52$ | $A_{STC}$ [$m^2$] | $L_{BHE}$ [m] | $N_{BHE}$ | $Cap_{HP}$ [kW] | $Vol_{BST}$ [$m^3$] |
|---|---|---|---|---|---|
| HT-BTES | 81–977 | 30–65 | 18–36 | 56.6, 113.2 | 0.25 [$m^3/m^2$]×$A_{STC}$ |
| LT-BTES | – | 33–120 | 12–24 | 56.6 | 0.8 [$m^3$/Kw]×$Cap_{HP}$ |

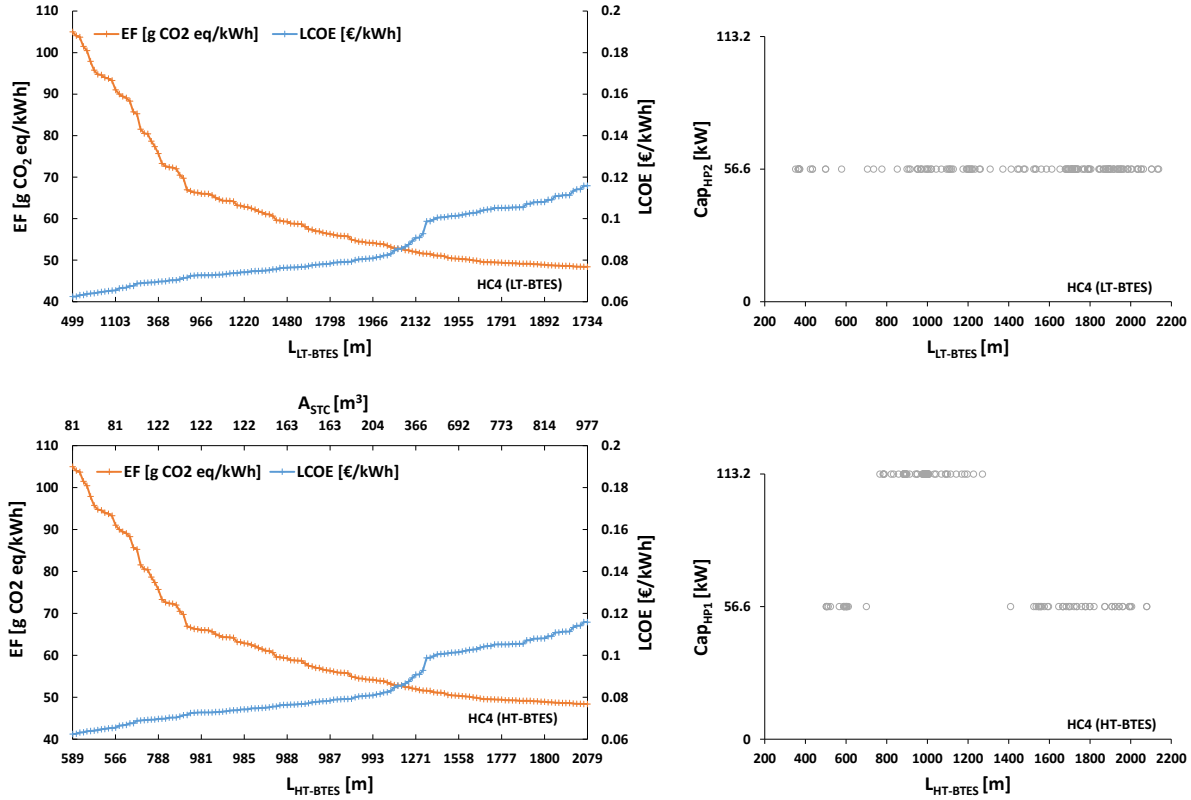


Figure 30. Ranges of the optimization variables on the Pareto fronts of the Hybrid scenario (HC4); HT-BTES (solar-coupled) and LT-BTES (standalone).

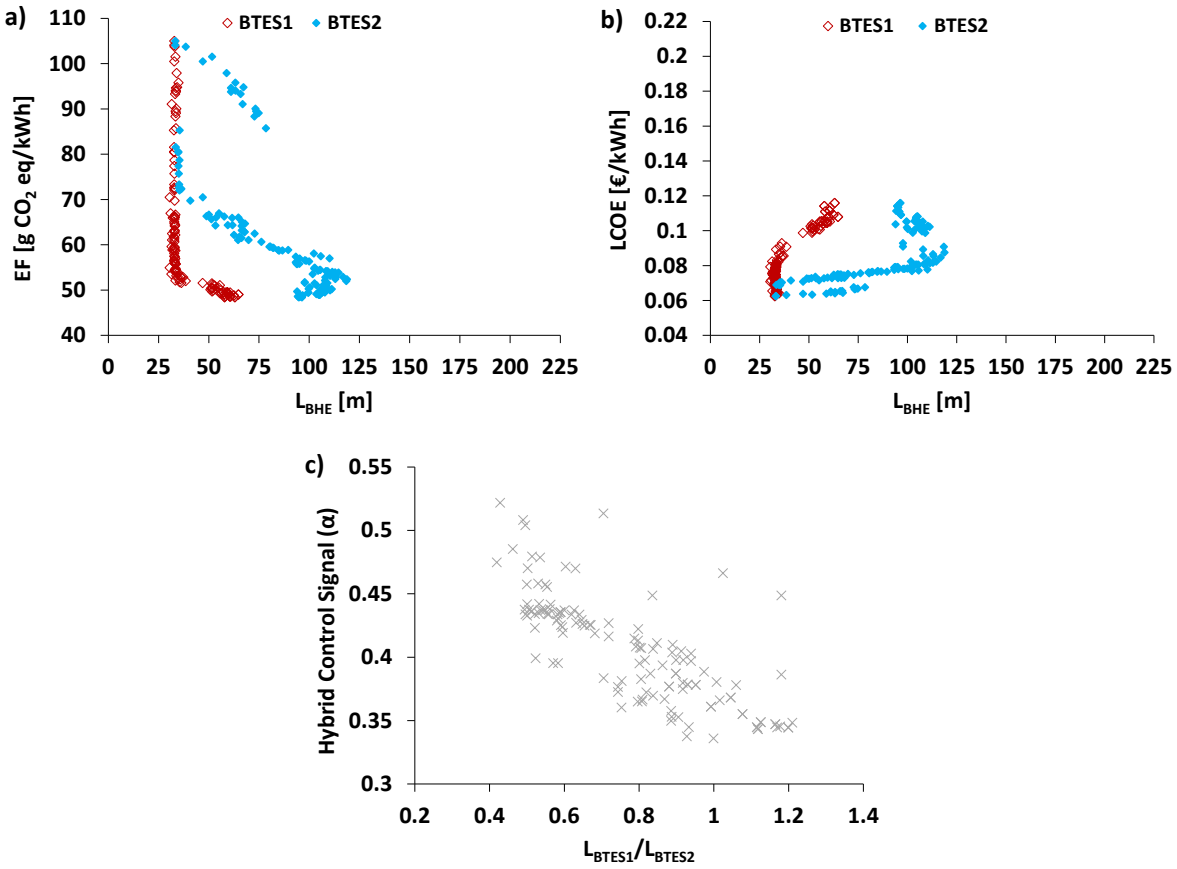


Figure 31. Change in EF and LCOE with $L_{BHE}$ (a and b) and α (c) on the Pareto front of the Hybrid scenario (HC4); BTES1 (solar-coupled) and BTES2 (standalone).

### 6.2.3 Exergo-economic Optimization of Small-scale Solar-coupled Decentral vs. Central layouts

In this part, multi-objective optimization is conducted to maximize exergetic efficiency and to minimize costs of the layouts H1, H2 and H4 (Chapter 3.2.2). Table 8 shows main components of each layout, their heating method and DH concept. As mentioned before, H1 and H2 are based on 4GDH with central heating systems to supply heating load passively or actively and H4 is based on a 5GDH concept, with decentral HPs in each individual building. The objective functions, setup and boundaries of the optimization variables are summarized in Table 9. Utilizing parallel computation method, the optimization is conducted twice for each layout, direct and indirect. The results from the direct optimization are used to train a proxy model for carrying out an indirect optimization (cf. Chapter 5.4), until final convergence of the optimization algorithm under more accurate optimization settings (i.e. higher number of generations and stall generations) is achieved.

Table 8: Characteristics of small-scale solar-coupled central and decentral layouts.

| Scenario | Concept | Heating | STC | GHE | HPs | BST | GB |
|---|---|---|---|---|---|---|---|
| H1 | 4GDH | Passive | Flat plate | 2U-tube | --- | Central | Peak |
| H2 | 4GDH | Active | Flat plate | 2U-tube | Central | Central | Peak |
| H4 | 5GDH | Active | Flat plate | 2U-tube | Decentral | Central/Decentral | Peak |

Table 9. Objective functions, optimization variables and constraints (parallel computation and optimization) for the layouts H1, H2 and H4.

| Objective functions | Subject to |
|---|---|
| max $\eta_{exergy}$ | $30\text{m} \leq L_{BHE} \leq 400\text{m}$ |
| min LCOE | $6 \leq N_{BHE} \leq 300$ |
| | $56.6\text{kW} \leq Cap_{HP}{}^{b} \leq 300\text{kW}$ |
| | $13.57m^2 \leq A_{STC} \leq 5000m^2$ |
| | $10m^3 \leq Vol_{BST} \leq 1000m^3$ |

[b] for active scenarios

The number of evaluations by direct and indirect optimization methods is shown in Table 10. The proxy model yields a better approximation of the objective functions when more points are used for training. However, due to computational limitations, i.e. maximum number of available processors and time restrictions, it may not be possible to use a large number of evaluations. As a part of this work, different numbers of training points were used to create the proxy models for the exergo-economic optimization. The minimum required number of evaluations to create a proxy model for each scenario with an acceptable accuracy, which is specified by the regression value R, are shown in Table 11. An R value of 1 means a close match between the guessed values and the actual values (cf. Appendix D). The acceptable R values are chosen to be higher than 0.999 for $\eta_{exergy}$ and 0.9999 for LCOE, considering that estimating $\eta_{exergy}$ is more difficult than LCOE. It can be seen in the table that the layouts H1 and H4, with 4 optimization variables, require at least 1500 and 2000 evaluations, while H2 with 5 optimization variables requires approximately 4500 runs. Moreover, more complex control strategies of H2 scenario results in a more difficult prediction of the proxy model. Furthermore, compared to the proxy model of the enviro-economic optimization (Appendix D), higher number of evaluations are required for the estimation of the exergo-economic objective functions. This is mainly due to more complexity for the calculation of dynamic exergetic efficiency (cf. Chapter 4.1.1) in comparison with the environmental objective, emission factor (cf. Chapter 4.2.1). Therefore, it can be concluded that an accurate estimation of the proxy model, utilizing the ANN approach, is strongly dependent on the number of variables, the control strategies and the objectives of the study.

Table 10. The number of evaluations by direct and indirect optimization methods to train exergo-economic proxy models for the layouts H1, H2 and H4.

| Optimization method | Number of evaluations | | |
|---|---|---|---|
| | **H1** | **H2** | **H4** |
| Direct | 4000 | 11000 | 5500 |
| Indirect | 40000 | 100000 | 40000 |

Table 11. The minimum required number of evaluations to train exergo-economic proxy models for the layouts H1, H2 and H4 and the corresponding regression values for estimating $\eta_{exergy}$ and LCOE.

| Optimization method | Number of evaluations | | |
|---|---|---|---|
| | **H1** | **H2** | **H4** |
| Minimum number of evaluations to train the ANN | 1500 | 4500 | 2000 |
| R value for $\eta_{exergy}$ | 0.99975 | 0.99918 | 0.99924 |
| R value for LCOE | 0.99997 | 0.99976 | 0.99997 |

Figure 32 shows the comparison between the direct and indirect exergo-economic optimization methods. As it is explained before, ANN-based optimization is conducted using the results from the direct optimization for the final convergence of the optimization. The non-dominated points of each layout are on a Pareto front, with higher efficiencies and lower costs, which is closest to the bottom right corner. As it can be seen in the figure, the final convergence results in better design points for both objectives, closer to the bottom right corners, which also leads to the specification of more accurate ranges for the optimization variables using indirect method. Moreover, it can be concluded that the direct optimization has acceptable results, with nearly the same shapes for the objective functions as those from the indirect method with approximately 10 times more evaluations. Consequently, the number of evaluations, shown in table 10, can be also considered as the required number for the convergence of a direct optimization method.

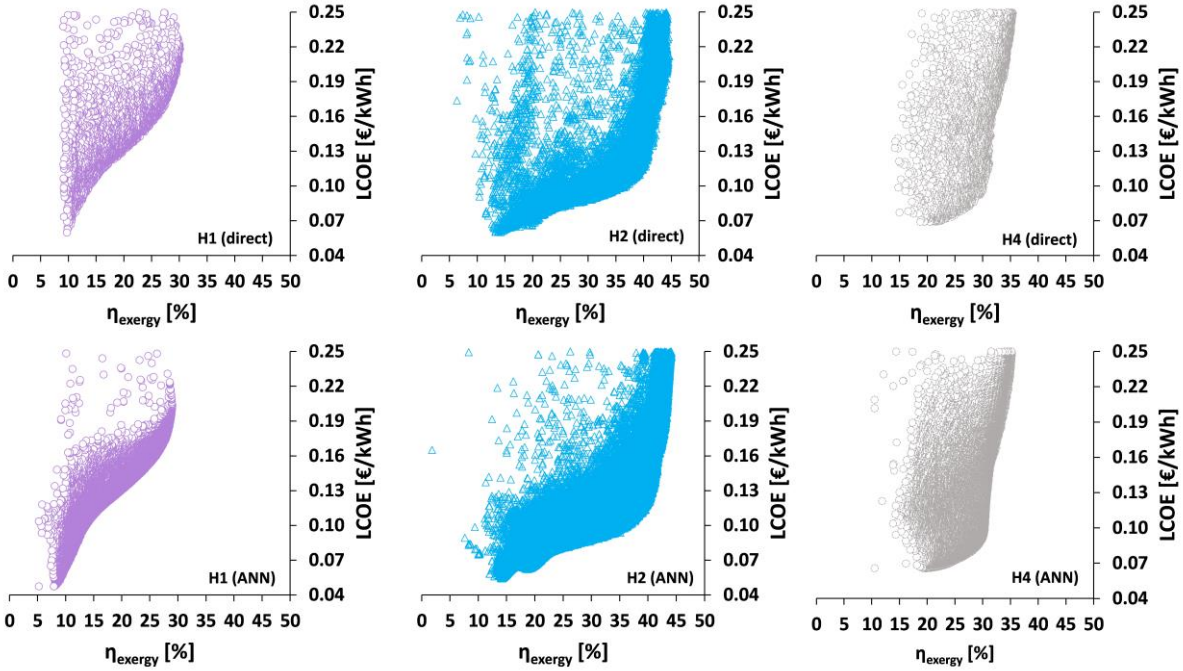


Figure 32. Direct (top) and indirect (bottom) exergo-economic optimization of the layouts H1, H2 and H4.

The Pareto fronts of direct and indirect optimization of different layouts can be seen together in Figure 33. The comparison between the Pareto fronts of the investigated layouts shows that H4 (i.e. the layout with seasonal storage and decentral HPs) and H2 (i.e. the layout with seasonal storage and active discharging via a central HP) yield better results than H1 (i.e. the layout with seasonal storage and passive discharging). For the exergetic efficiencies between 20% and 30%, H4 shows better results than H2. On the other hand, the highest values of $\eta_{exergy}$ (higher than 30%, that corresponds to the points with LCOE of higher than 8.6 [ct/kWh]) as well as the lowest values of LCOE (lower than 6.6 [ct/kWh], that corresponds to the points with $\eta_{exergy}$ of lower than 20%) can only be achieved by H2 scenario.

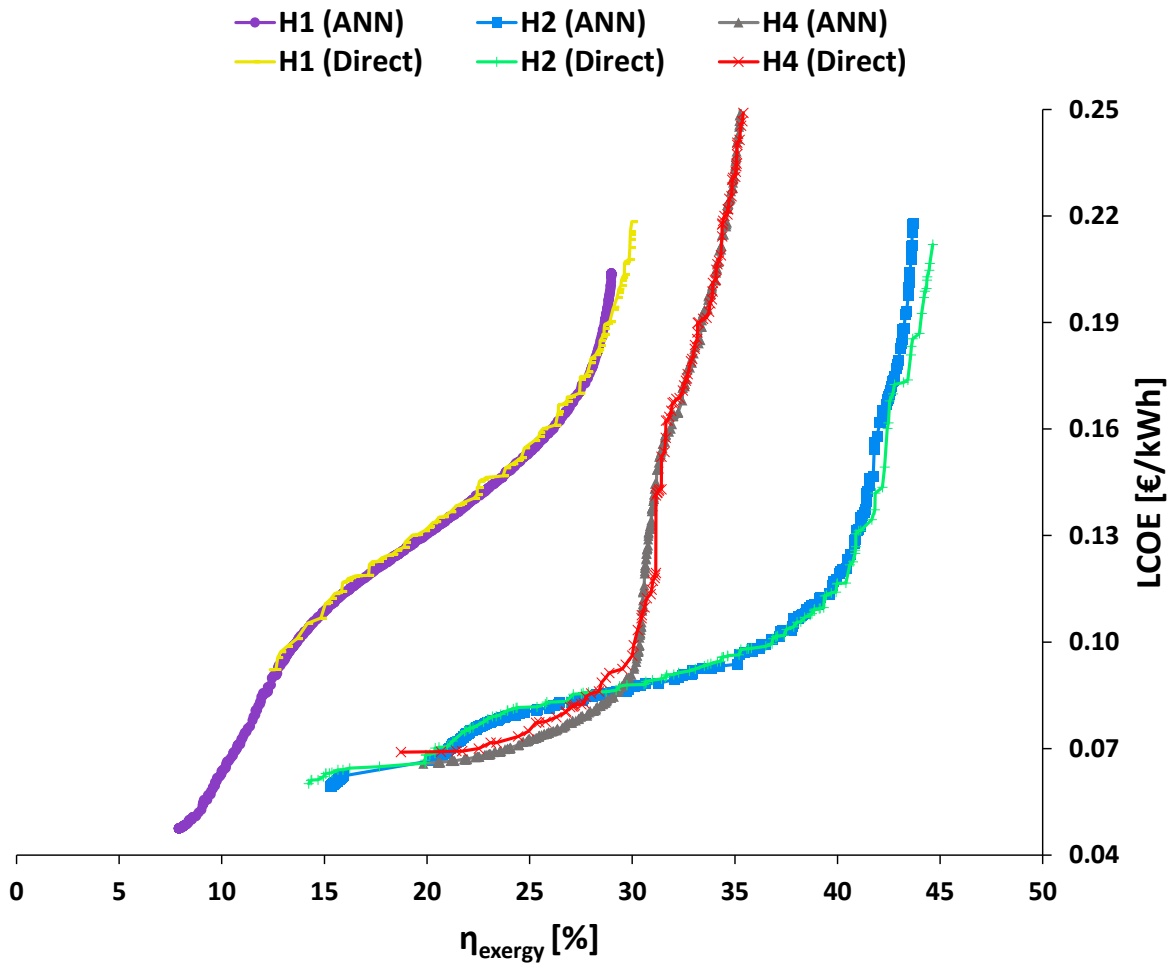


Figure 33. Exergo-economic optimization results of the layouts H1, H2 and H4

As the objective of many feasibility studies of renewable energy systems is reducing environmental emissions, the selected designs on the Pareto fronts need to be also investigated environmentally. This helps to specify the EF by having the $\eta_{exergy}$ of the investigated layout. Figure 34 shows the relation between $\eta_{exergy}$ and EF for the designs on the Pareto fronts of the layouts. As it can be seen in the figure, this relation can be defined as a separate function for every system.

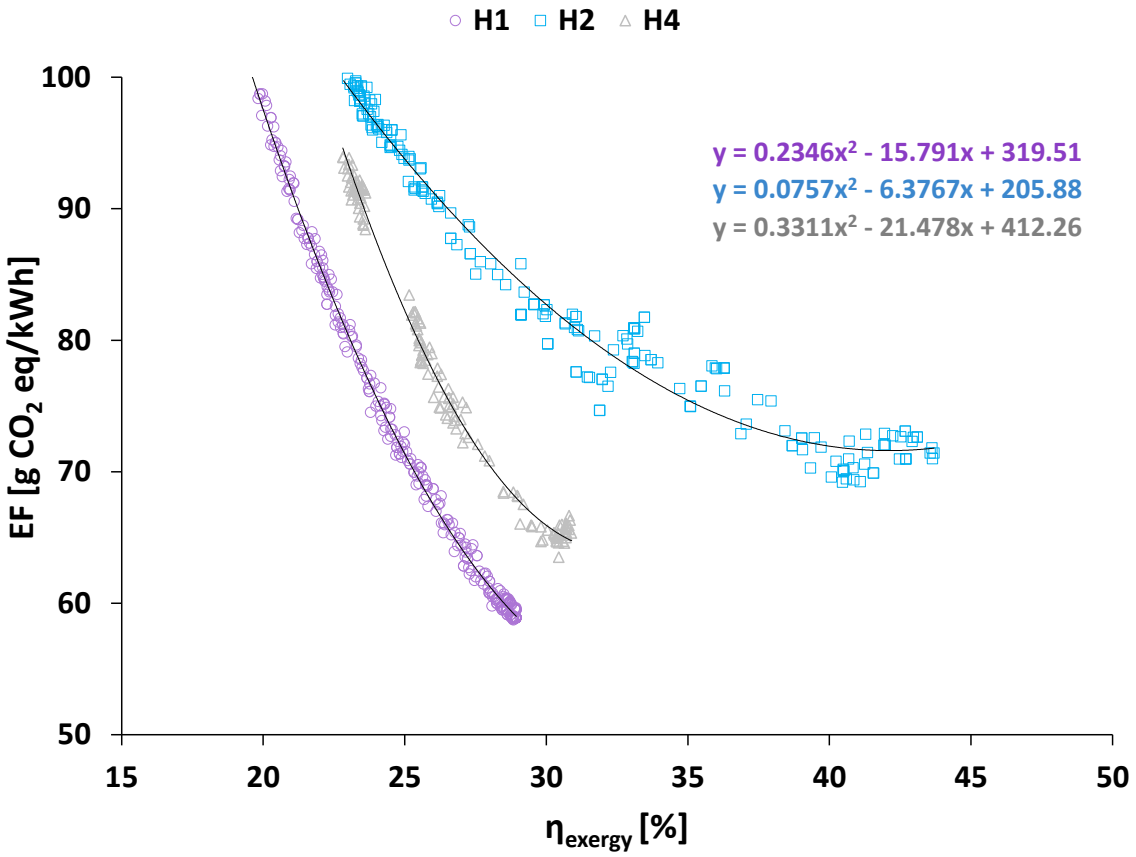


Figure 34. Relation between $\eta_{exergy}$ and EF for the designs on the Pareto fronts of the layouts H1, H2 and H4.

By limiting the highest acceptable LCOE on 20 [ct/kWh] and the maximum $\eta_{exergy}$ on the values corresponding to maximum EF of 100 [gr/kWh], the range of the optimized variables on the Pareto front of each scenario can be seen in Table 12. As it can be seen in the table, H1 requires the largest $A_{STC}$ and $Vol_{BST}$ for the diurnal storage of the collected solar energy. On the other hand, H2 has the smallest $A_{STC}$ which is compensated by the largest drilling lengths ($L_{BTES} = L_{BHE}\ N_{BHE}$). This means that STCs are utilized for preheating the BTES up to a temperature level which is suitable for active load supply rather than bypassing the HP to supply the load passively. Finally, H4 yields the lowest $L_{BTES}$ when more economical designs are planned. This means that preheating of the district loop which is fed to the decentral HPs is mostly done directly by STCs. For the most efficient designs this is supplemented by indirectly supplying the seasonally-stored solar energy, utilizing BTES, which means larger $A_{STC}$, $L_{BTES}$ and $Vol_{BST}$ are required.

Table 12. Range of the optimization variables on the Pareto fronts of the layouts H1, H2 and H4 with maximum EF of 100 [gr/kWh] and LCOE of 20 [ct/kWh]

| Scenario | **LCOE** [ct/kWh] | **$\eta_{exergy}$** [%] | **$L_{BHE}$** [m] | **$N_{BHE}$** | **$Cap_{HP}$** [kW] | **$A_{STC}$** [$m^2$] | **$Vol_{BST}$** [$m^3$] |
|---|---|---|---|---|---|---|---|
| H1 | 12.9 - 20 | 19.8 – 29 | 49 - 67 | 48 - 72 | - | 1872 - 2279 | 262 - 834 |
| H2 | 6.7 - 19.8 | 23.2 – 44.5 | 30 - 96 | 36 - 132 | 113.2 | 163 - 529 | 28 - 344 |
| H4 | 7.2 - 20 | 23.6 - 33.9 | 77 - 133 | 12 - 108 | 52×2.8 | 407 - 1221 | 10 - 310 |

The relation between the optimized variables of the sample points on the Pareto fronts and their corresponding outputs is shown in Figure 35. As it is expected, for all scenarios $\eta_{exergy}$ and LCOE increase by increasing $L_{BTES}$ for installing double U-tube BHEs. Similarly, an increase in $A_{STC}$ increases $\eta_{exergy}$ and LCOE. Figure 35 can be used to determine an optimal layout of the STC and the BTES, depending on a project's constraints and the envisaged layout, by choosing a value for the objectives. For a chosen total drilling length $L_{BTES}$, optimal ratios for $L_{BHE}$ and $N_{BHE}$ can be derived from Table 12, considering scattering of the decision variables $L_{BHE}$ and $Vol_{BST}$ and the corresponding values of the objectives $\eta_{exergy}$ and LCOE (cf. Figure 36).

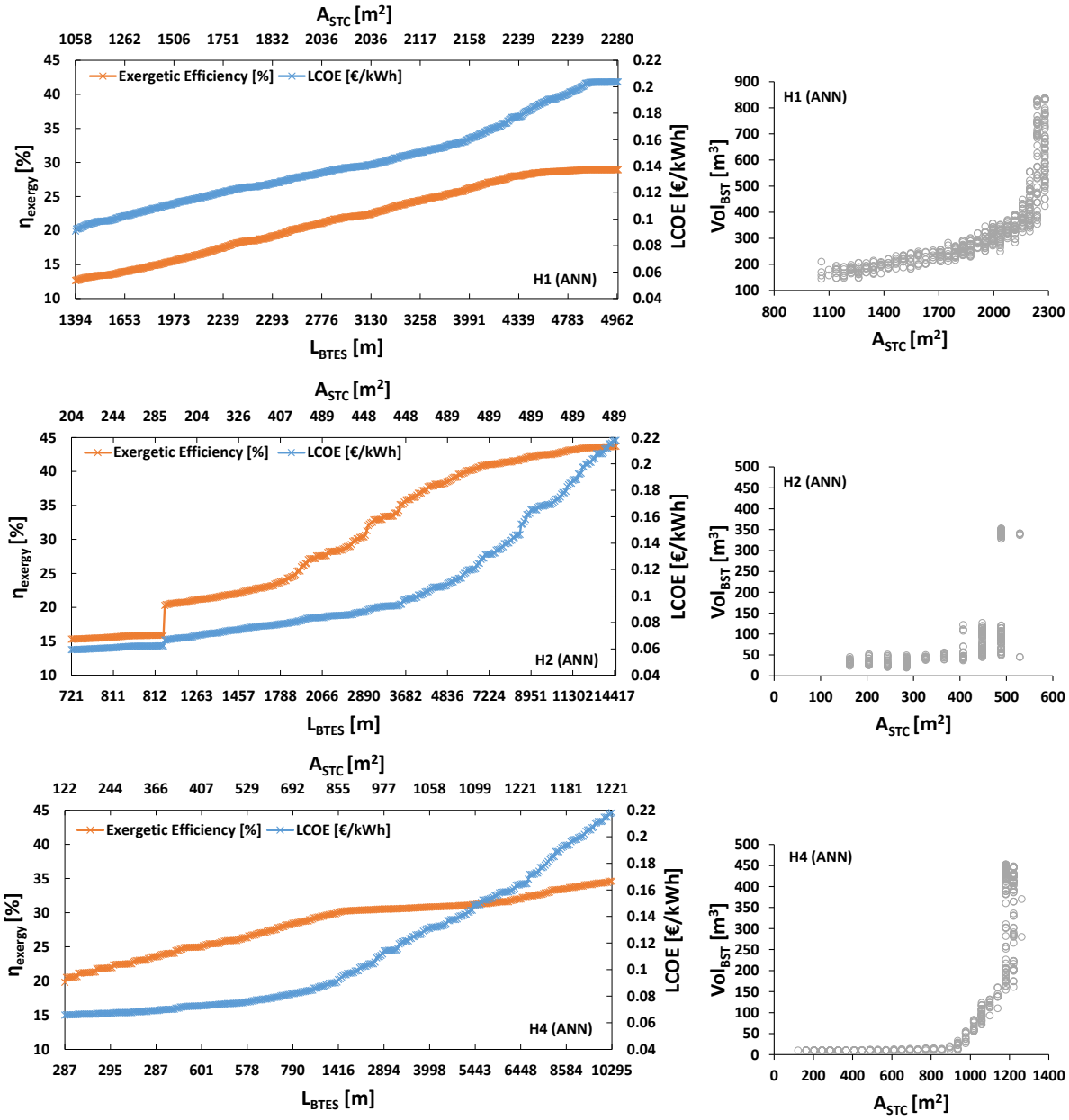


Figure 35. Ranges of the optimization variables on the Pareto fronts of the layouts H1, H2 and H4.

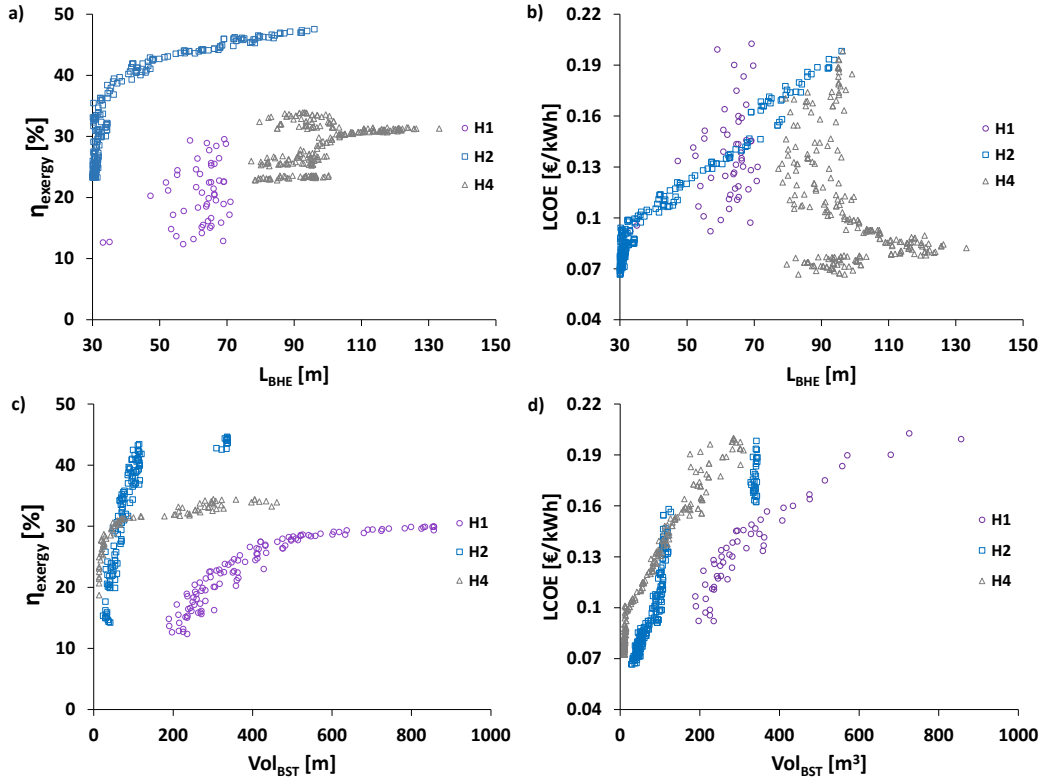


Figure 36. Change in $\eta_{exergy}$ and LCOE with $L_{BHE}$ (a and b) and $Vol_{BST}$ (c and d) for the designs on the Pareto fronts of the layouts H1, H2 and H4.

The characteristic designs and their corresponding optimized values for LCOE and EF of maximum 20 [ct/kWh] and 100 [gr/kWh] are given in Table 13. The characteristic points are simulated in TRNSYS and the results are then compared with the outputs from the ANN. As shown in Figure 37, the simulation results closely match the outputs from the ANN proxy model, which proves the validity of the ANN method for estimating $\eta_{exergy}$ and LCOE.

Table 13. The economical, the compromise and the efficient system designs of the Pareto fronts of the layouts H1, H2 and H4 with maximum EF of 100 [gr/kWh] and LCOE of 20 [ct/kWh]

| **Scenario** | | **LCOE** [ct/kWh] | **$\eta_{exergy}$** [%] | **EF** [gCO2eq /kWh] | **$L_{BHE}$** [m] | **$N_{BHE}$** | **$Cap_{HP}$** [kW] | **$A_{STC}$** [m²] | **$Vol_{BST}$** [m³] |
|---|---|---|---|---|---|---|---|---|---|
| | Economical | 12.9 | 19.8 | 98 | 52 | 48 | | 1913 | 265 |
| H1 | Compromise | 16.2 | 26.5 | 66 | 57 | 72 | | 2239 | 386 |
| | Most efficient | 20 | 29 | 58 | 66 | 72 | | 2239 | 834 |
| | Economical | 6.7 | 23.2 | 98 | 30 | 36 | 113.2 | 163 | 30 |
| H2 | Compromise | 12.1 | 42.9 | 76 | 47 | 132 | 113.2 | 489 | 104 |
| | Most efficient | 19.8 | 44.5 | 68 | 96 | 132 | 113.2 | 489 | 342 |
| | Economical | 7.2 | 23.6 | 95 | 94 | 12 | 52×2.8 | 407 | 10 |
| H4 | Compromise | 11 | 30.5 | 72 | 107 | 24 | 52×2.8 | 977 | 52 |
| | Most efficient | 20 | 33.9 | 63 | 94 | 96 | 52×2.8 | 1221 | 285 |

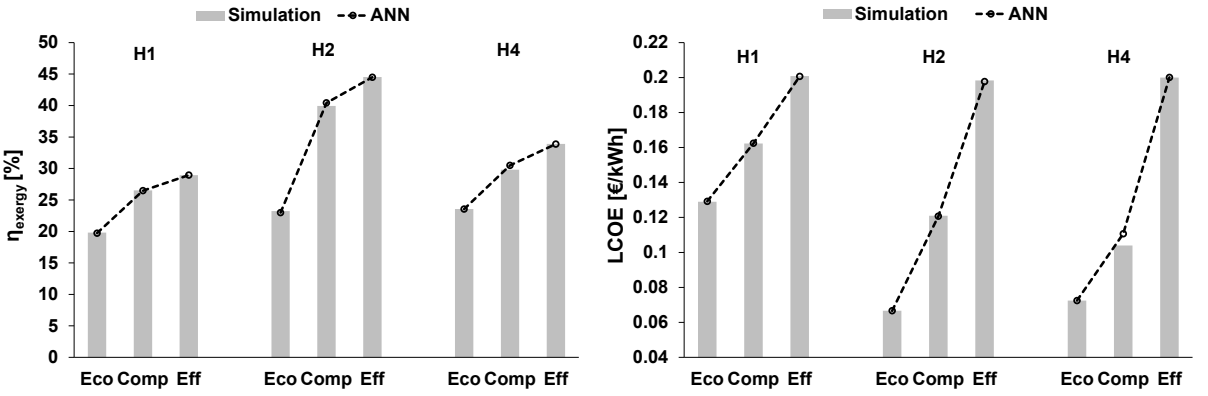


Figure 37. Simulation vs. ANN results of $\eta_{exergy}$ (a) and LCOE (b) for the characteristic designs of the layouts H1, H2 and H4

To gain deeper insight into the coherencies of the results, the component-wise exergy destruction and loss and composition of LCOE for all characteristic designs of Table 13 is shown in Figures 38 and 39. For all layouts, increase in initial costs (IC) of STCs (and correspondingly $Vol_{BST}$ and $L_{BTES}$) is the most important reason of increase in LCOE. ICs have the highest shares in all characteristic designs of the passive (H1) as well as in the efficient and the compromise designs of the active layouts (H2 and H4). Operational costs (OCs), mostly due to electricity consumption of HPs, have considerable shares in LCOE of all characteristic designs of the active layouts. Maintenance costs (MCs), which are mainly from STCs, are higher for the passive layout and increase with higher shares of STCs from the economical to the most efficient designs.

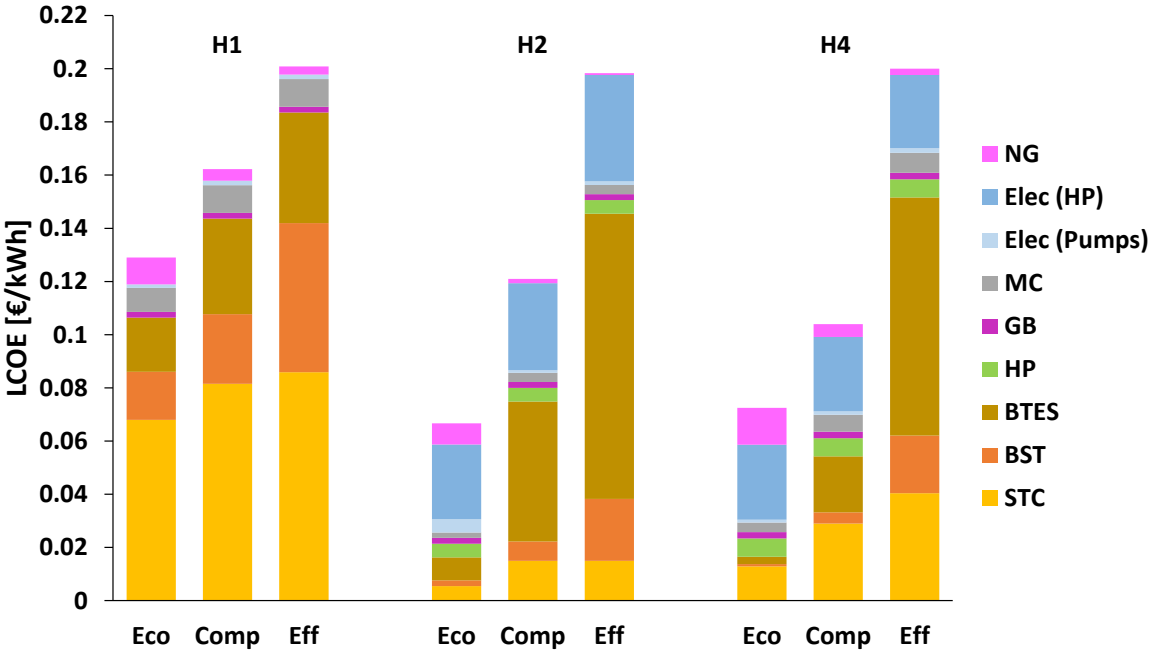


Figure 38. Component-wise LCOE of the characteristic designs of Table 13.

As it can be seen in Figure 39, the total exergy destruction and loss (called exergy destruction in other parts of this chapter) is reduced by moving from the economical to the efficient designs. For the economical designs, the highest exergy destruction is from the GB followed by the HPs in the active and the HEXs in the passive layouts. For the compromise solutions, these are almost balanced and for the most efficient designs, the HPs and the HEXs have considerable shares in

exergy destruction of the active and passive layouts respectively. For H1 scenario, the GB has high share in exergy destruction even in the most efficient layout. This is mainly the result of supplying a high percentage of the load by the GB during the first years of operation while the BTES has not reached the suitable temperature levels for passive load supply yet. Moreover, it can be implied that the exergy destruction of the BTES is strongly dependent on its temperature level. Consequently, H1 scenario, which has the highest temperature for supplying the load passively, has the largest exergy destruction in the BTES, compared to H2 and H4. Furthermore, exergy destruction in the BSTs, circulating pumps and DH pipes have the lowest shares in the overall exergy destruction, compared to the other components of the layouts. Finally, H4 scenario has the lowest exergy destruction in the DH pipes because of its lower temperature level. However, the effect of decentralization of the HPs in reducing the overall exergy destruction will be more influential in higher supply temperatures.

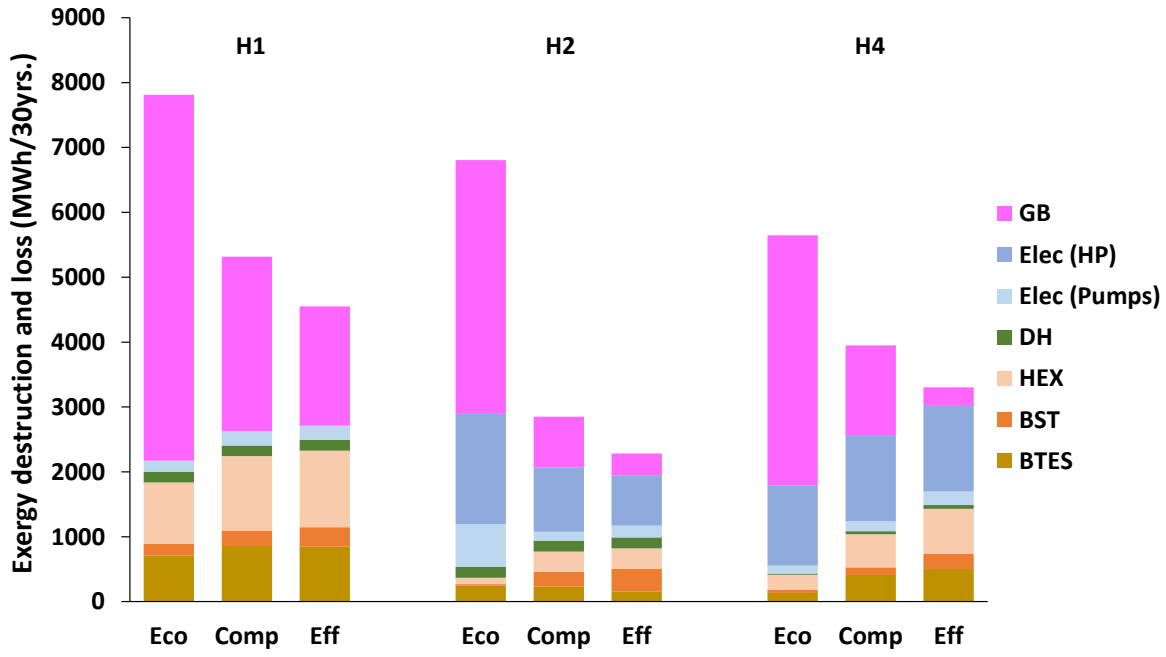


Figure 39. Component-wise exergy destruction and loss of the characteristic designs of Table 13.

To have a better understanding of the sources of inefficiencies, the Sankey diagrams of the compromise designs of the investigated layouts are presented. Each Sankey diagram shows exergy inputs to the system, being Natural Gas (NG Exe., Equation 6), exergy from the solar collector modules (Solar Exe., Equation 8) and electricity from grid. The input exergy constitutes either the product exergy (the exergy content of supplied heat demand) or the exergy destruction and loss (Exe. Des.) during the project lifetime of 30 years.

The exergy Sankey diagram of the compromise design of scenario H1 is illustrated in Figure 40. As it is mentioned before, for H1 scenario, with large required areas of STCs, the solar loop HEX and the BTES are the major sources of inefficiencies after the GB. This indicates the importance of choosing a solar loop HEX with higher effectiveness, which is taken as 0.8 according to the operational data from the reference case (Leidos 2014). Moreover, exergetically optimizing design temperature and flow rate of the solar loop will lead to reduced losses in the HEX and the BTES. The optimization of the design temperature does not necessarily mean its reduction. The reduction of the BTES storage temperature will increase the GB operation, especially during the

first years, when the BTES has not reached its suitable temperature level to supply the load directly. Therefore, supply temperature and flow rate of the solar loop are suggested to be added to the other dimensional optimization variables of scenario H1 for a more efficient system design. To reduce the degrees of freedom in the optimization study, this shall be done as a supplementary second stage, with specified values from the first stage dimensional optimization.

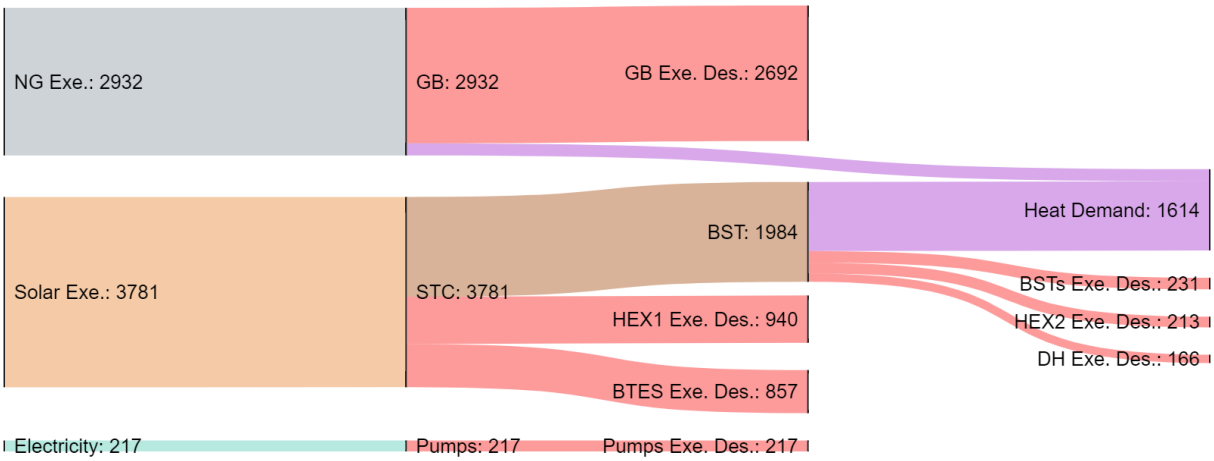


Figure 40. Sankey exergy diagram of the compromise point of layout H1 showing component-wise exergy destruction and loss [MWh/30yrs].

The exergy Sankey diagram of the compromise design of scenario H2 is illustrated in Figure 41. HP and GB are the main sources of exergy destruction for this design. In comparison with the compromise design of layout H1, smaller areas of STCs and larger BTES drilling lengths are yielded by the optimization. As mentioned earlier, the BTES is only heated up to lower temperature levels for active load supply. Consequently, there is lower exergy destruction in the solar loop HEX as well as the BTES. However, the overall exergy destruction of the ground loop (incl. HP and BTES) is slightly higher than for layout H1 (BTES), which is compensated by much lower destruction of the solar thermal exergy input and leads to more efficient operation of the overall system.

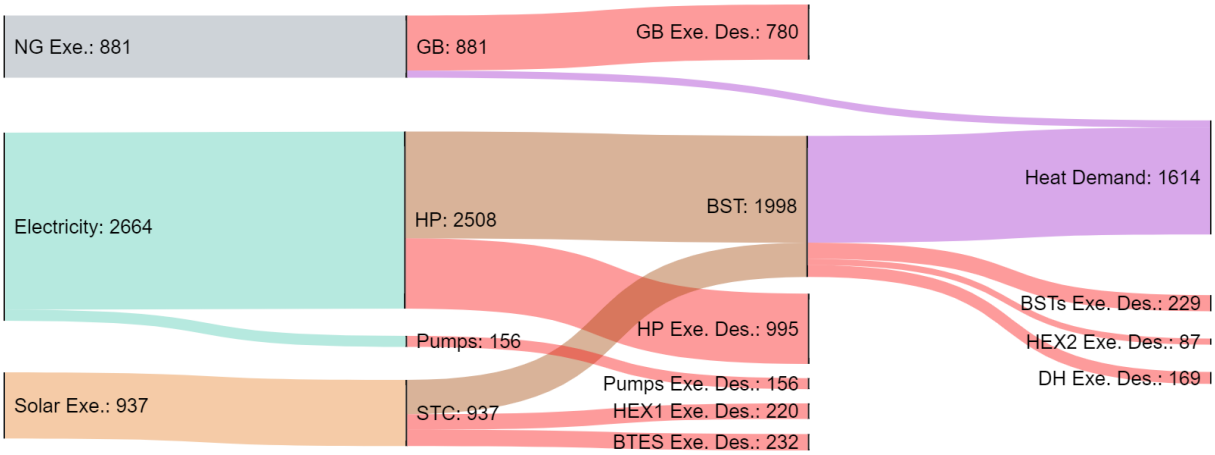


Figure 41. Sankey exergy diagram of the compromise point of layout H2 showing component-wise exergy destruction and loss [MWh/30yrs].

In the compromise point of H4 (Figure 42), the highest source of exergy destruction is from the decentral HPs, followed by the GBs. As mentioned in Chapter 3.2.2.3, to lower the exergy destruction of the HPs, the entering evaporator temperature (i.e. the district loop supply temperature, $T_{DL}$) is set on 25 °C, which is the maximum possible temperature based on the manufacturer's catalog (Viessmann 2020a). Figure 43 shows results of optimizing $T_{DL}$ for the compromise solution of Table 13. As it can be seen in the figure, $T_{DL}$ has an optimum value of 23.6 °C that is defined using TOPSIS method, which is the technique for order of preference by similarity to ideal solution (Hwang et al. 1993). This results in slightly higher exergetic efficiency with a slight increase in LCOE, compared with the initial set point temperature. However, the higher $T_{DL}$ is also associated with higher exergy destructions in the central units (incl. solar loop HEX, BTES and BST) and DH pipes. Consequently, $T_{DL}$ is suggested to be added to the other dimensional optimization variables of H4 layout for a more efficient system design.

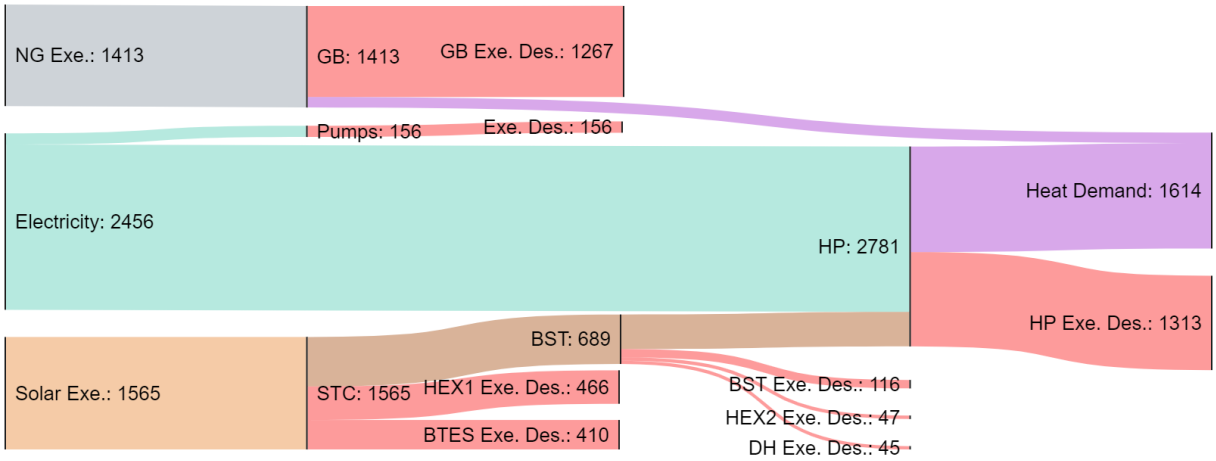


Figure 42. Sankey exergy diagram of the compromise point of layout H4 showing component-wise exergy destruction and loss [MWh/30yrs].

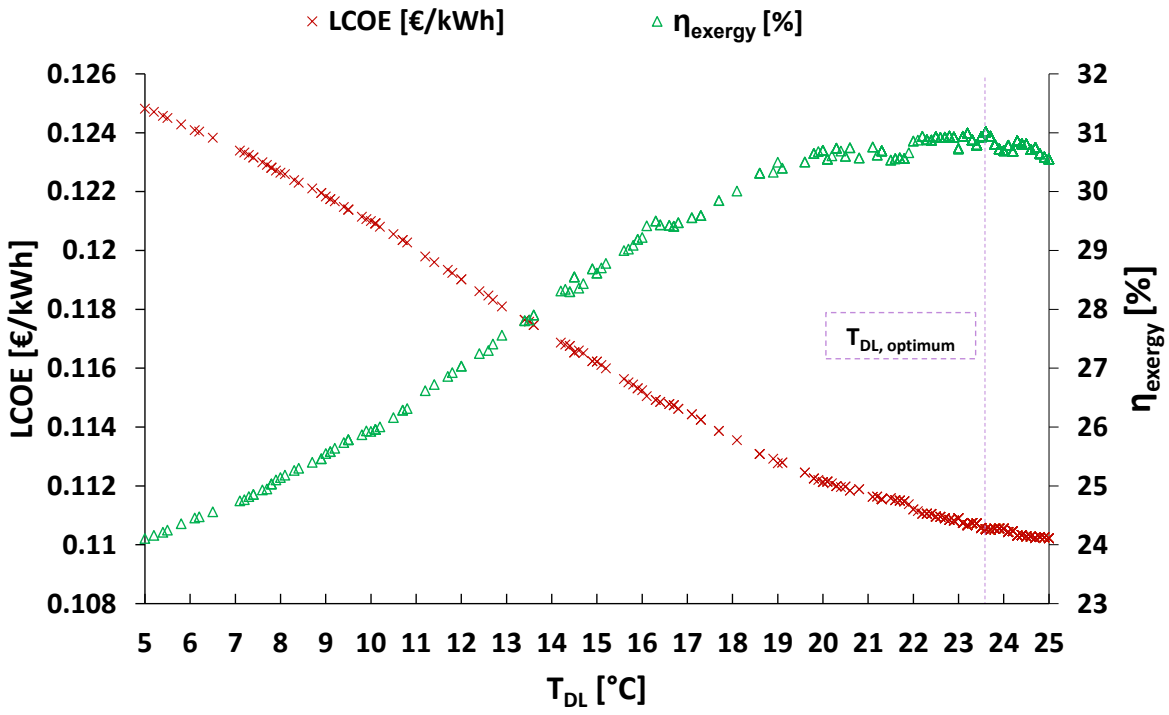


Figure 43. Optimization of grid supply temperature of the layout H4.

## 6.3 Comparison between Exergo- and Enviro-economic Optimization Methods

Choosing the right method is very important for the design of combined energy systems. In this part, enviro-economic and exergo-economic optimization methods for the evaluation of geothermal layouts are compared. The results of enviro-economic optimization of central solar-coupled layouts (H1 and H2) are explained in Chapter 6.2.1. In this chapter, exergo-economic optimization of central and decentral solar-coupled layouts (H1, H2 and H4) is conducted. To compare the two optimization methods for dimensioning central and decentral geothermal layouts, enviro-economic optimization of the decentral solar-coupled layout (H4) is also carried out in this part. Figure 44 shows Pareto fronts of enviro-economic optimization of the layouts H1, H2 and H4. As it can be seen in the figure, H2 shows the best results for the designs with EFs of approximately lower than 70 [g CO2 eq/kWh] and H4 yields better results with higher EFs. Moreover, Pareto fronts of the two methods are illustrated together in Figure 45. As it is shown in the figure, the ranking of the scenarios is the same for both methods, if designs with EFs of higher than 100 [g CO2 eq/kWh] (i.e. exergetic efficiency of lower than 20%, cf. Figure 34) are omitted from the exergo-economically optimized designs.

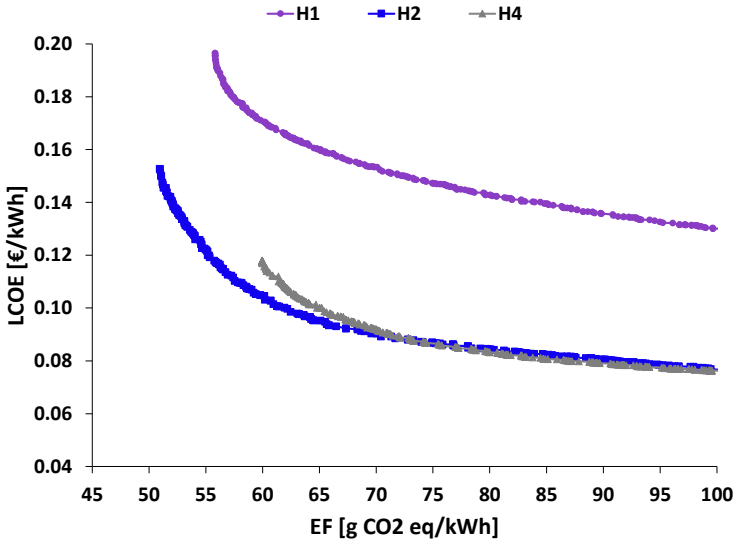


Figure 44. Enviro-economic optimization results of the layouts H1, H2 and H4.

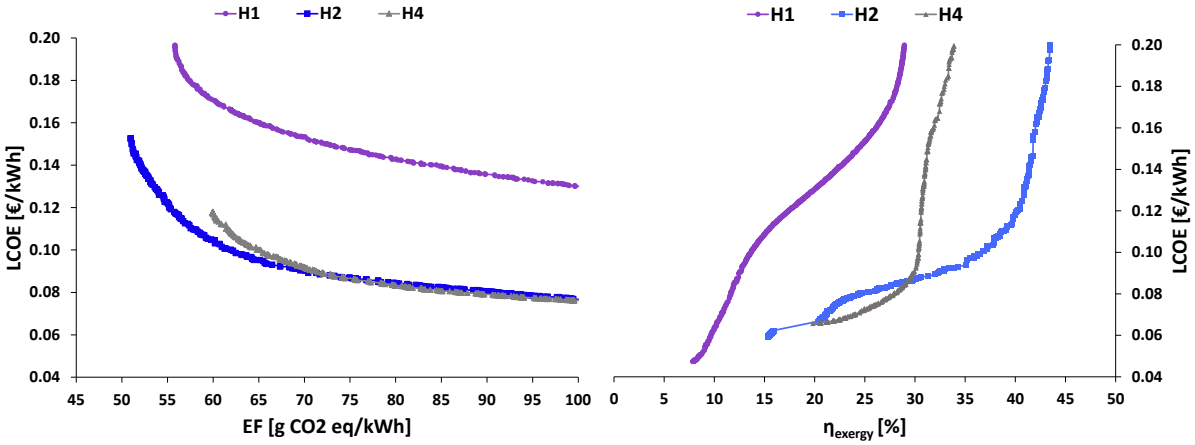


Figure 45. Comparison between enviro-economic (left) and exergo-economic (right) optimization results of the layouts H1, H2 and H4.

By limiting the maximum LCOE to the same values, ranges of the optimization variables resulted from the two methods can be compared (cf. Table 13). Moreover, the equivalent EFs of the designs on the Pareto front of the exergo-economic optimization method as well as the Pareto fronts of the enviro-economic method are shown together in Figure 46. As it is already mentioned, increasing exergetic efficiency leads to reduced environmental impacts and a higher sustainability. Enviro-economic and exergo-economic optimization of H1 layout almost yield the same range for the objectives (Figure 46) as well as the optimization variables (Table 14). However, the lowest EFs can only be reached by the enviro-economic optimization, which is mainly due to slightly higher $A_{STC}$ and $Vol_{BST}$. Similarly, for H4 layout, the two methods almost yield the same range for the objective functions and optimization variables, with higher $A_{STC}$ and $Vol_{BST}$ from the enviro-economic optimization. The enviro-economic method also yields higher $A_{STC}$ and $Vol_{BST}$ in H2 layout. However, in contrast with H1 and H4, the difference between the optimum values of the two methodologies is considerable. Lower $A_{STC}$ is compensated by longer $L_{BTES}$ chosen by the exergo-economic optimization method, which results in higher environmental emissions than the enviro-economic optimization method.

Table 14. Ranges of the optimized solutions on the Pareto fronts of the layouts H1, H2 and H4, comparing exergo- and enviro-economic optimization methods.

| Scenario | Optimization method | $A_{STC}$ [$m^2$] | $L_{BHE}$ [m] | $N_{BHE}$ | $Cap_{HP}$ [kW] | $Vol_{BST}$ [$m^3$] |
|---|---|---|---|---|---|---|
| H1 | Enviro-economic | 2080 - 2650 | 50 - 65 | 42 - 66 | - | 310 - 690 |
| H1 | Exergo-economic | 1872 - 2279 | 49 - 67 | 48 - 72 | - | 262 - 834 |
| H2 | Enviro-economic | 410 - 1260 | 30 - 85 | 30 - 66 | 113.2 | 30 - 490 |
| H2 | Exergo-economic | 163 - 529 | 30 - 79 | 36 - 132 | 113.2 | 28 - 128 |
| H4 | Enviro-economic | 325 - 1384 | 60 - 122 | 6 - 24 | 52×2.8 | 10 - 86 |
| H4 | Exergo-economic | 407 - 1017 | 77 - 107 | 6 - 30 | 52×2.8 | 10 - 56 |

The difference between the optimization results of the two methods for optimizing H2 is mainly because of neglecting the fuel exergy from the ground in exergetic evaluation of the solar-coupled systems. In other words, when STCs are just used to preheat the underground, that is discharged actively by HPs, geothermal heat also plays an important role. However, by adding the input exergy from the ground to the total fuel exergy, categorization of the exergy input from the STCs or the ground itself (geothermal exergy) is not possible. Moreover, adding the input exergy from the ground to the overall fuel exergy, which already includes input exergy from the STCs, leads to twice consideration of the input exergy from the STCs, when the source of exergy input from the ground is the stored heat from the STCs. Therefore, utilization of exergy analysis is suggested when there is a clear border between the source of input exergy, e.g. in H1 layout. This border also exists when storage and extraction exergetic efficiencies ($\eta_{exergy,St}$ and $\eta_{exergy,Ext}$, using Equations 11 and 12) are calculated separately. Consequently, a three-objective optimization study for maximizing $\eta_{exergy,St}$ and $\eta_{exergy,Ext}$ in addition to minimizing LCOE could be the proper approach for exergo-economic optimization of active solar-coupled central layouts (Table 15).

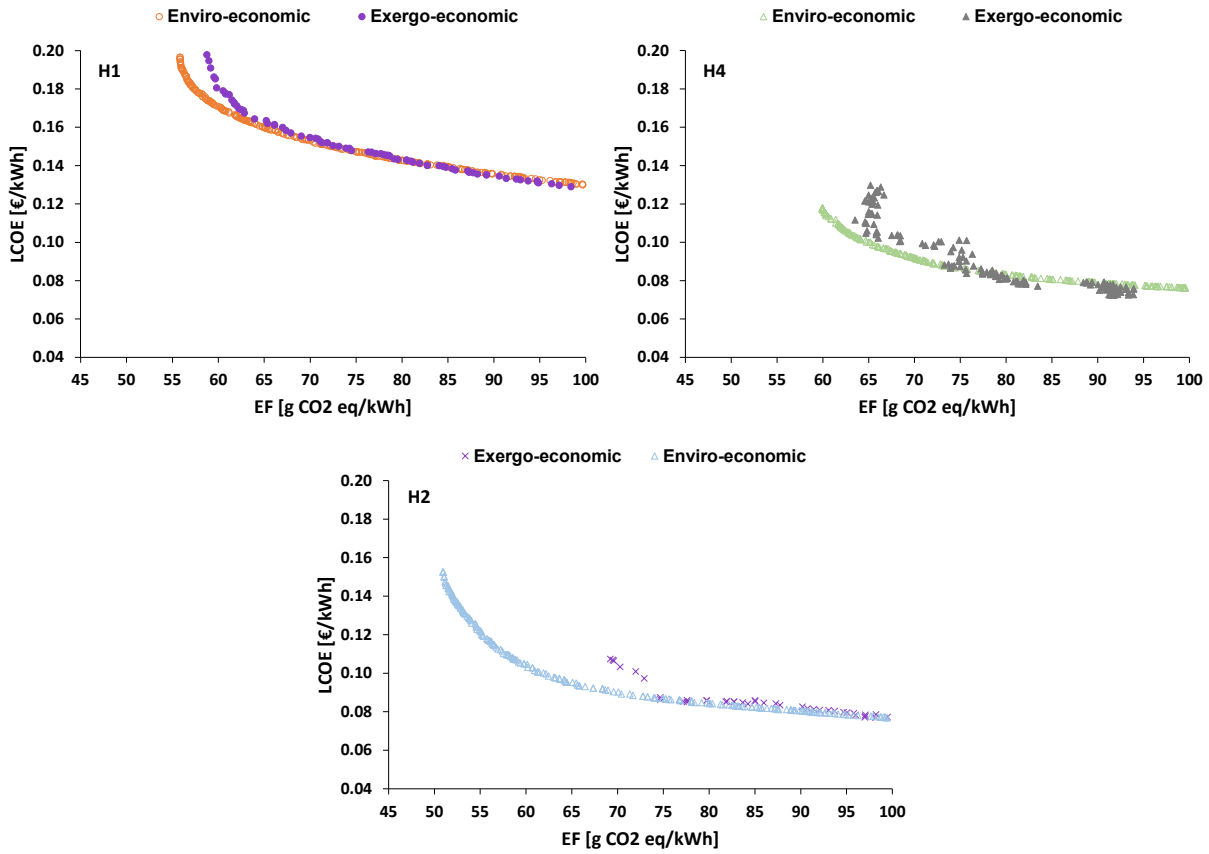


Figure 46. Comparison between enviro-economic and exergo-economic optimization results of the layouts H1, H2 and H4.

Table 15. Objective functions and optimization variables of the three-objective exergo-economic optimization for the layout H2.

| **Objective functions** | **Subject to** |
|---|---|
| max $\eta_{exergy,St}$ | $30m \leq L_{BHE} \leq 400m$ |
| max $\eta_{exergy,Ext}$ | $6 \leq N_{BHE} \leq 300$ |
| min LCOE | $56 \leq Cap_{HP} \leq 300kW$ |
| | $13.57m^2 \leq A_{STC} \leq 5000m^2$ |
| | $10m^3 \leq Vol_{BST} \leq 1000m^3$ |

Ranges of the optimization variables, resulted from three different optimization methods can be seen in Table 16. Compared with two-objective exergo-economic optimization method, the results of three-objective exergo-economic optimization are more similar to those of two-objective enviro-economic optimization, both having larger STCs, larger BSTs and smaller BTES. The three-objective method yields a wider range for the selection of $A_{STC}$, $L_{BHE}$ and $Cap_{HP}$.

Table 16. Ranges of the optimized solutions on the Pareto fronts of the layout H2, comparing exergo-economic (two-objective), enviro-economic (two-objective) and exergo-economic (three-objective) optimization methods.

| Scenario | Optimization method | $A_{STC}$ [$m^2$] | $L_{BHE}$ [m] | $N_{BHE}$ | $Cap_{HP}$ [kW] | $Vol_{BST}$ [$m^3$] |
|---|---|---|---|---|---|---|
| H2 | Enviro-economic (two objectives) | 410 - 1260 | 30 - 85 | 30 - 66 | 113.2 | 30 - 490 |
| H2 | Exergo-economic (two objectives) | 163 - 529 | 30 - 79 | 36 - 132 | 113.2 | 28 - 128 |
| H2 | Exergo-economic (three objectives) | 41 - 1576 | 30 - 107 | 36 - 54 | 56.6 , 113.2 | 10 - 410 |

To have a better understanding of the environmental impacts of a three-objective exergo-economic optimization, EFs of the designs on the Pareto front are calculated and can be seen together with those from the other optimization methods on Figure 47. As it can be seen in the figure, the three-objective method yields more ecological designs, compared with the two-objective exergo-economic optimization approach. For the designs with EFs of lower than 70 g CO2 eq/kWh, the enviro-economic optimization results in slightly lower EFs and LCOE, compared with the three-objective exergo-economic optimization method.

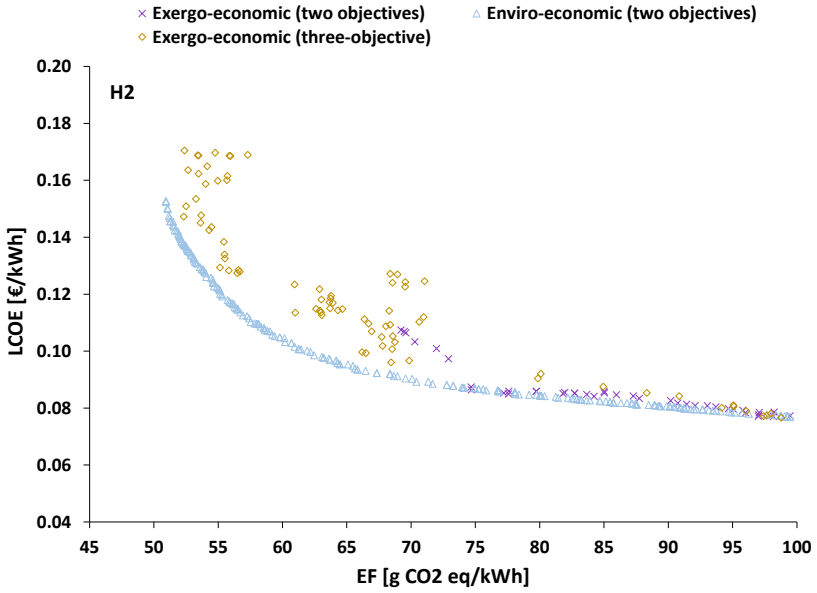


Figure 47. Comparison between the results of enviro-economic (two objectives), exergo-economic(two objectives) and exergo-economic(three objectives)optimization methods.

## 6.4 Step-wise Optimization of Geothermal Systems

In this part, utilizing the computational procedure explained in Chapter 5.5, a step-wise optimization of the compromise design on the Pareto front of the solar-coupled central layout with passive discharge of the BTES (H1) is carried out. The optimization is conducted to maximize the storage and extraction exergeric efficiency of the BTES (cf. Equation 9 and Equation 10) by defining the optimum ground loop pump flow rate at each time step. Having the inlet BTES temperature and the ambient (reference) temperature at each time step, a random control signal (between 0 and 1) is created, which specifies the flow rate of the variable-speed pump. The relation between the objective functions and the mentioned variables are then estimated by the ANN. Finally, the step-wise optimization is conducted by passing the BTES inlet temperature and ambient temperature as inputs to the proxy model, from TRNSYS to MATLAB. By maximizing the storage and extraction exergetic efficiency, the optimum value of the control signal is passed from MATLAB to TRNSYS at each time step. The step-wise optimization of the selected design during project lifetime, 30 years, takes approximately 360 hours. Table 17 shows the influence of utilizing the step-wise optimization approach on average storage and extraction exergetic efficiencies of the BTES within the project lifetime. As it can be seen in the table, the proposed approach enhances exergetic performance of the BTES during storage as well as extraction periods. Therefore, it is recommended for operational optimization of a systems in operation or a selected design from a dimensional optimization.

Table 17. Influence of utilizing the step-wise optimization approach on BTES average storage and extraction exergetic efficiencies within the project lifetime.

| Step-wise Optimization | $\eta_{exergy,BTES,St}$ [%] | $\eta_{exergy,BTES,Ext}$ [%] |
|---|---|---|
| No | 68.5 | 87.1 |
| Yes | 74.1 % | 90 |

# 7 Conclusions and Recommendations

This dissertation contains a comprehensive evaluation of geothermal layouts for DHC. There are various options for integrating geothermal systems in district energy systems, which depend on project objectives and constrains. One of the main aims of this dissertation is providing guidelines for designing geothermal systems in DHC grids. Consequently, the most common geothermal layouts are taken into consideration, which are categorized into solar-coupled and standalone. To lower uncertainties, the layouts are mainly proposed based on geothermal systems in operation.

As the title of the dissertation shows, performance assessments of the layouts were conducted using exergo- and enviro-economic optimization methods. Enviro-economic analysis method was utilized for simultaneously minimizing emissions and costs of the proposed layouts. As enviro-economic method lacks thermodynamic assessments (Nuss 2015), an exergo-economic optimization was adopted for the assessment of geothermal systems for DHC. Increasing exergetic efficiency leads to reduced environmental impacts (Nuss 2015). Consequently, the exergo-economic method takes not only technical and economic but also environmental aspects into consideration. The developed dynamic exergy analysis method can be utilized for dimensioning and technical assessment of standalone and solar-coupled geothermal layouts as well as separate BHE arrays. It can be coupled with an advanced control method for efficiency improvement of a system in operation or a dimensionally-optimized model.

The dynamic exergo-economic assessment was conducted, utilizing direct optimization method to evaluate the integration of standalone BHE arrays into large-scale 4GDHC grids. The investigated layouts differ by their cooling approach (active or passive) and by the connection of the BTES system and the supplementary boiler in heating mode (serial or parallel). The ranking of the optimized layouts shows that passive cooling together with maximizing heating temperature shift by a heat pump, leads to the most favorable designs. Comprehensive exergy and cost analyses of the Pareto efficient solutions indicates that the highest exergy destruction comes from HPs for the most efficient and from GBs for the least efficient designs. BTES and BSTs have the lowest exergy destruction for all layouts and increasing the BTES volume results in more efficient DHC grids.

To assess geothermal layouts considering required transient interaction between system components during project lifetime, the direct optimization method may not lead to final convergence of the optimization algorithm due to the required computational effort. Moreover, parametric studies may not lead to the best solutions for design purposes. As a highlight of this study, utilizing an indirect optimization approach, long-term assessment of geothermal systems has been considered in the convergence of the optimization procedure. ANN was utilized as a proxy model for estimating the objective functions. Results show that, using the initial evaluation points from direct optimization for training the model, leads to accurate approximation of the functions. Efforts were made to control the associated uncertainties by checking the functions from the training algorithm as well as by post-simulation of the selected final points. Moreover, by developing a parallel computation method, more training points can be fed to the ANN for more accurate prediction of the proxy model. It has been defined that the combination of an ANN and multi-objective optimization methods is an accurate and robust approach for long-term evaluation and comparison of geothermal heating and cooling systems. The proposed approach can be utilized for the optimization of different combined energy systems, where a large number of variables or long-term assessment of the models are required. Consequently, it

can help to avoid issues that has led to lower efficiencies of existing projects due to improper system designs. Finally, an AI-based step-wise optimization method was proposed to optimize an objective function by changing a control variable at each time step of the simulation. The step-wise method was proved to be an efficient method by improving storage and extraction exergetic efficiencies of a BTES system by changing its flow rate at each time step.

Utilizing the developed indirect optimization model, the enviro-economic optimization of small-scale solar-coupled and standalone geothermal layouts reveals that, for heating-only purposes, solar-coupled geothermal systems with active load supply are favorable over solar-coupled passive systems and standalone BHE systems. For combined heating and cooling purposes, passive cooling utilizing standalone BHE systems achieves the lowest overall costs while also obtaining reasonably low emissions. Nevertheless, the lowest emissions are also realized by solar-coupled layouts. Finally, results indicate that for combined heating and cooling load supply, a hybrid utilization of solar-coupled and standalone BHE arrays leads to more appropriate results, compared to each layout separately.

The parallel computation method was utilized for direct and indirect exergo-economic optimization of small-scale solar-coupled layouts in heating-only mode. The heating load was supposed to be supplied passively without HPs or actively, with central or decentral HPs. The comparison between the Pareto fronts of the investigated layouts shows that active load supply with decentral HPs (5GDH) yield better results for a wide range of compromise and economic solutions. The most efficient designs, though, can only be achieved by central HPs (4GDH). It can be concluded that the effect of decentralization of HPs in reducing the overall exergy destruction is more influential in higher supply temperatures.

To gain deeper insight into the differences between exergo- and enviro-economic optimization methods, optimization results of small-scale central and decentral solar-coupled layouts were compared using both methods. Comparison between the results confirms that an increase in exergetic efficiency leads to a decrease in environmental impacts. Results also indicate that both methods yield the same ranking of the scenarios and the relation between $\eta_{exergy}$ and EF can be written as a function for each layout separately. However, the utilization of exergo-economic approach for the optimization of geothermal systems is suggested when there is a clear border between the sources of input exergy from the underground. This can be considered by maximizing exergetic efficiencies during storage and extraction periods separately. Overall, the enviro-economic optimization is suggested for dimensioning different geothermal layouts, which needs to be supplemented by the developed dynamic exergetic analysis method to define operational variables that are influential on thermodynamic inefficiencies. Having defined the variables, an exergetic optimization method can improve the system's performance by defining their optimal range. Finally, a step-wise optimization is recommended to maximize exergetic efficiency of system components by controlling adaptable operational variables at defined time steps.

# 8 Outlook

Considering the results of this study, following future works are proposed for designing geothermal systems for DHC. More detailed outlooks are explained in Appendixes B and D.

- Hybrid utilization of two BTES systems is proven to be the most enviro-economically optimal design for combined heating and cooling applications. In this study, parallel use of BTES systems in heating mode is evaluated. Serial utilization of BTES systems, especially when higher grid supply temperatures are needed, as well as exergo-economic assessment of hybrid models are suggested as future work.
- ANN was used for estimating an objective function, as a function of a control signal, which can be then controlled in a step-wise optimization procedure. In this study, it is assumed that the values of the current time step can be used for the definition of the optimum control value of the next time step. By combining ANN and Model Predictive Control (MPC), the predicted value of each time step can be used for specifying its optimal control signal, which is suggested as a future study.
- The conventional dynamic exergy analysis method was adapted to assess thermodynamic performance of the geothermal layouts. Utilizing dynamic advanced exergy analysis method, which splits the exergy destruction into avoidable or unavoidable (Tsatsaronis & Park 2002) and endogenous or exogenous (Kelly et al. 2009) parts, is suggested to be developed in details for geothermal systems.
- Optimization of geothermal layouts using exergo-environmental analysis methods (Meyer et al. 2009), in which both exergy and environmental analyses are conducted and supplemented by assigning environmental impacts to exergy streams, is suggested as a future work.
- As mentioned in Chapter 1, there are different types of UTES. Comparing the optimum integration of these systems for different boundary conditions can provide a comprehensive guideline for increasing the share of seasonal TES in district energy grids.

## References


Bär K, Rühaak W, Welsch B, Schulte D, Homuth S and Sass I (2015): Seasonal high temperature heat storage with medium deep borehole heat exchangers, Energy Procedia, v. 76, p. 351-360.

Bargel S (2011): Entwicklung eines exergiebasierten Analysemodells zum umfassenden Technologievergleich von Wärmeversorgungssystemen unter Berücksichtigung des Einflusses einer veränderlichen Außentemperatur.

Bauer D, Drück H, Lang S, Marx R and Plaz T (2016): Weiterentwicklung innovativer Technologien zur solaren Nahwärme und saisonale Wärmespeicherung, Forschungsbericht zum BMWi-Vorhaben A, v. 325998.

Bauer D, Heidemann W, Müller-Steinhagen H and Diersch HJ (2011): Thermal resistance and capacity models for borehole heat exchangers, International Journal of Energy Research, v. 35, no. 4, p. 312-320.

Bauer D, Marx R, Nußbicker-Lux J, Ochs F, Heidemann W and Müller-Steinhagen H (2010): German central solar heating plants with seasonal heat storage, Solar Energy, v. 84, no. 4, p. 612-623.

Bejan A, Tsatsaronis G and Moran MJ (1995): Thermal design and optimization, John Wiley & Sons, New York.

Buffa S, Cozzini M, D'Antoni M, Baratieri M and Fedrizzi R (2019): 5th generation district heating and cooling systems: A review of existing cases in Europe, Renewable and Sustainable Energy Reviews, v. 104, p. 504-522.

Deb K, Pratap A, Agarwal S and Meyarivan T (2002): A fast and elitist multiobjective genetic algorithm: NSGA-II, IEEE transactions on evolutionary computation, v. 6, no. 2, p. 182-197.

Dekking FM, Kraaikamp C, Lopuhaä HP and Meester LE (2005): A Modern Introduction to Probability and Statistics: Understanding why and how, Springer Science & Business Media.

Dincer I and Rosen M (2007): A unique borehole thermal storage system at University of Ontario Institute of Technology, Thermal Energy Storage for Sustainable Energy Consumption, Springer, The Netherlands, p. 221-228.

Dincer I and Rosen MA (2021): Thermal energy storage systems and applications, John Wiley & Sons.

Dötsch C, Taschenberger J and Schönberg I (1998): Leitfaden nahwärme, Fraunhofer-IRB-Verlag.

Duffie JA and Beckman WA (2013): Solar engineering of thermal processes, John Wiley & Sons.

EC (2021a): European Commission. Energy performance of buildings directive. https://ec.europa.eu/energy/topics/energy-efficiency/energy-efficient-buildings/energy-performance-buildings-directive_en [accessed on 02 December 2021].

EC (2021b): European Commission. Heating and Cooling. https://ec.europa.eu/energy/topics/energy-efficiency/heating-and-cooling_en [accessed on 02 December 2021].

Elhashmi R, Hallinan KP and Chiasson AD (2020): Low-energy opportunity for multi-family residences: A review and simulation-based study of a solar borehole thermal energy storage system, Energy, v. 204, p. 117870.

Eurostat (2019 ), https://ec.europa.eu/eurostat [accessed on 02 December 2021].

Fleiter T, Steinbach J, Ragwitz M, Dengler J, Köhler B, Reitze F, Tuille F, Hartner M, Kranzl L and Forthuber S (2016): Mapping and analyses of the current and future (2020-2030) heating/cooling fuel deployment (fossil/renewables), European Commission, Directorate-General for Energy.

Formhals J, Feike F, Hemmatabady H, Welsch B and Sass I (2021a): Strategies for a transition towards a solar district heating grid with integrated seasonal geothermal energy storage, Energy, v. 228, p. 120662.
Formhals J, Hemmatabady H, Welsch B, Schulte DO and Sass I (2021b): MoBTES – A New Borehole Thermal Energy Storage Model in Modelica, World Geothermal Congress 2020+1.
Hellstrom G (1992): Ground heat storage: Thermal analyses of duct storage systems. I. Theory, PhD thesis, Lund University.
Hemmatabady H, Formhals J, Schulte DO, Welsch B and Sass I Exergoeconomic Optimization of Borehole Thermal Energy Storage in District Heating and Cooling Grids.
Hemmatabady H, Formhals J, Welsch B, Schulte DO and Sass I (2020): Optimized Layouts of Borehole Thermal Energy Storage Systems in 4th Generation Grids, Energies, v. 13, no. 17, p. 4405.
Herold KE, Radermacher R and Klein SA (2016): Absorption chillers and heat pumps, CRC press.
Hwang C-L, Lai Y-J and Liu T-Y (1993): A new approach for multiple objective decision making, Computers & operations research, v. 20, no. 8, p. 889-899.
Jiang H, Xi Z, Rahman AA and Zhang X (2020): Prediction of output power with artificial neural network using extended datasets for Stirling engines, Applied Energy, v. 271, p. 115123.
Karasu H and Dincer I (2020): Life cycle assessment of integrated thermal energy storage systems in buildings: A case study in Canada, Energy and Buildings, v. 217, p. 109940.
Kavian S, Aghanajafi C and Dizadji N (2019): Transient simulation and multi-objective optimization of a VSD ground source heat pump in various usage, Energy Conversion and Management, v. 197, p. 111847.
Kavian S, Aghanajafi C, Mosleh HJ, Nazari A and Nazari A (2020): Exergy, economic and environmental evaluation of an optimized hybrid photovoltaic-geothermal heat pump system, Applied Energy, v. 276, p. 115469.
Kelly S, Tsatsaronis G and Morosuk T (2009): Advanced exergetic analysis: Approaches for splitting the exergy destruction into endogenous and exogenous parts, Energy, v. 34, no. 3, p. 384-391.
Kizilkan O and Dincer I (2015): Borehole thermal energy storage system for heating applications: Thermodynamic performance assessment, Energy Conversion and Management, v. 90, p. 53-61.
Klein S, Beckman W, Mitchell J, Duffie J, Duffie N, Freeman T, Mitchell J, Braun J, Evans B and Kummer J (2017): TRNSYS 18 – A TRaNsient system simulation program, user manual, Solar Energy Laboratory. Madison: University of Wisconsin-Madison.
Lanahan M and Tabares-Velasco PC (2017): Seasonal thermal-energy storage: A critical review on BTES systems, modeling, and system design for higher system efficiency, Energies, v. 10, no. 6, p. 743.
Leidos (2014): Drake Landing Solar Community, Annual Performance Monitoring. https://www.dlsc.ca/reports/JUL2015/2012-2013%20Annual%20Report%20v07%20FINAL.pdf [accessed on 02 December 2021].
Liu BY and Jordan RC (1963): The long-term average performance of flat-plate solar-energy collectors: with design data for the US, its outlying possessions and Canada, Solar energy, v. 7, no. 2, p. 53-74.
Lund H, Østergaard PA, Nielsen TB, Werner S, Thorsen JE, Gudmundsson O, Arabkoohsar A and Mathiesen BV (2021): Perspectives on fourth and fifth generation district heating, Energy, v. 227, p. 120520.
Lund H, Werner S, Wiltshire R, Svendsen S, Thorsen JE, Hvelplund F and Mathiesen BV (2014): 4th Generation District Heating (4GDH): Integrating smart thermal grids into future sustainable energy systems, Energy, v. 68, p. 1-11.

Mangold D, Miedaner O, Tziggili EP, Schmidt T, Unterberger M and Zeh B (2012): Technisch-wirtschaftliche Analyse und Weiterentwicklung der solaren Langzeit-Wärmespeicherung, Schlussbericht zum BMU-Forschungsvorhaben N, v. 329607.

MATLAB (2021): The MathWorks Inc. https://www.mathworks.com/help/gads/gamultiobj.html [accessed on 02 December 2021].

Mauthner F and Herkel S (2016): Technology and demonstrators-Technical Report Subtask C–Part C1: Classification and benchmarking of solar thermal systems in urban environments, IEA Solar Heating & Cooling Technology Collaboration Programme, Gleisdorf.

Mesquita L, McClenahan D, Thornton J, Carriere J and Wong B (2017): Drake landing solar community: 10 years of operation, *in* Proceedings ISES Conference Proceedings, Abu Dhabi02.11.2017, p. 1-12.

Meyer L, Tsatsaronis G, Buchgeister J and Schebek L (2009): Exergoenvironmental analysis for evaluation of the environmental impact of energy conversion systems, Energy, v. 34, no. 1, p. 75-89.

Nuss P (2015): Life Cycle Assessment Handbook: A Guide for Environmentally Sustainable Products; Curran, A.M., Ed.; John Wiley & Sons, Inc.: Hoboken, NJ, USA; Scrivener Publishing LLC: Salem, MA, USA.

Nussbaumer T (2017): Planungshandbuch Fernwärme, EnergieSchweiz, Bundesamt für Energie, Bern.

Olsson H (2017): Modelica—A unified object-oriented language for physical systems modeling; Modelica Association., https://www.modelica.org/documents/ModelicaSpec34.pdf [accessed on 30.04.2021].

Petela R (2003): Exergy of undiluted thermal radiation, Solar Energy, v. 74, no. 6, p. 469-488.

Pinel P, Cruickshank CA, Beausoleil-Morrison I and Wills A (2011): A review of available methods for seasonal storage of solar thermal energy in residential applications, Renewable and Sustainable Energy Reviews, v. 15, no. 7, p. 3341-3359.

Rant Z (1956): Exergie, Ein neues Wort fur technische Arbeits-fahigkeit, Forsch. Ing.-Wes, v. 22, p. 36-37.

Razmi AR, Arabkoohsar A and Nami H (2020): Thermoeconomic analysis and multi-objective optimization of a novel hybrid absorption/recompression refrigeration system, Energy, v. 210, p. 118559.

Rezaie B and Rosen MA (2012): District heating and cooling: Review of technology and potential enhancements, Applied energy, v. 93, p. 2-10.

Ritchie H (2020): "Sector by sector: where do global greenhouse gas emissions come from?" https://ourworldindata.org/ghg-emissions-by-sector.

Rühaak W, Steiner S, Welsch B and Sass I (2015): Prognosefähigkeit numerischer Erdwärmesondenmodelle, Grundwasser, v. 20, no. 4, p. 243-251.

Saloux E and Candanedo JA (2019): Control-oriented model of a solar community with seasonal thermal energy storage: development, calibration and validation, Journal of Building Performance Simulation, v. 12, no. 5, p. 523-545.

Sass I, Brehm D, Coldewey W, Dietrich J, Klein R, Kellner T, Kirschbaum B, Lehr C, Marek A and Mielke P (2016): Shallow Geothermal Systems-Recommendations on Design, Construction, Operation and Monitoring, Ernst et Sohn.

Sayadi S, Tsatsaronis G and Morosuk T (2019): Dynamic exergetic assessment of heating and cooling systems in a complex building, Energy conversion and management, v. 183, p. 561-576.

Sayyadi H and Nejatolahi M (2011): Thermodynamic and thermoeconomic optimization of a cooling tower-assisted ground source heat pump, Geothermics, v. 40, no. 3, p. 221-232.

Schmidt T, Mangold D and Müller-Steinhagen H (2004): Central solar heating plants with seasonal storage in Germany, Solar energy, v. 76, no. 1-3, p. 165-174.

Schulte DO (2016): Simulation and optimization of medium deep borehole thermal energy storage systems.
Schulte DO, Rühaak W, Oladyshkin S, Welsch B and Sass I (2016a): Optimization of Medium-Deep Borehole Thermal Energy Storage Systems, Energy Technology, v. 4, no. 1, p. 104-113.
Schulte DO, Rühaak W, Welsch B and Sass I (2016b): BASIMO – Borehole Heat Exchanger Array Simulation and Optimization Tool, Energy Procedia, v. 97, p. 210-217.
Schweiger G, Larsson P-O, Magnusson F, Lauenburg P and Velut S (2017): District heating and cooling systems–Framework for Modelica-based simulation and dynamic optimization, Energy, v. 137, p. 566-578.
Shah SK, Aye L and Rismanchi B (2020): Multi-objective optimisation of a seasonal solar thermal energy storage system for space heating in cold climate, Applied Energy, v. 268, p. 115047.
Short W, Packey DJ and Holt T (1995): A manual for the economic evaluation of energy efficiency and renewable energy technologies, National Renewable Energy Lab., Golden, CO (United States)
Sibbitt B, McClenahan D, Djebbar R, Thornton J, Wong B, Carriere J and Kokko J (2012): The performance of a high solar fraction seasonal storage district heating system–five years of operation, Energy Procedia, v. 30, p. 856-865.
Skarphagen H, Banks D, Frengstad BS and Gether H (2019): Design Considerations for Borehole Thermal Energy Storage (BTES): A Review with Emphasis on Convective Heat Transfer, Geofluids, v. 2019.
The MathWorks Inc. (2016): MATLAB 2016a, Natick, MA.
Tsatsaronis G and Park M-H (2002): On avoidable and unavoidable exergy destructions and investment costs in thermal systems, Energy conversion and management, v. 43, no. 9-12, p. 1259-1270.
UN (2015a): Agreement United Nations Framework Convention on Climate Change, https://unfccc.int/sites/default/files/english_paris_agreement.pdf (accessed on 02.08.2021).
UN (2015b): World urbanization prospects: The 2014 revision, United Nations Department of Economics and Social Affairs, Population Division: New York, NY, USA, v. 41.
VDI (2010): VDI 4640 Thermal Use of the Underground, VDI-Gessellschaft Energie und Umwelt (GEU), Berlin.
VDI (2019): VDI 4640 Thermal Use of the Underground, VDI-Gessellschaft Energie und Umwelt (GEU), Berlin.
Viessmann (2020a), https://www.viessmann.de/de/wohngebaeude/waermepumpe/sole-wasser-waermepumpen/vitocal-300-g.html [accessed on 22.02.2021].
Viessmann (2020b): http://www.energas.co.za/wp-content/uploads/2019/02/A12.-Heat-Pumps.pdf [accessed on 22.02.2021].
Welsch B (2019): Technical, Environmental and Economic Assessment of Medium Deep Borehole Thermal Energy Storage Systems.
Welsch B, Göllner-Völker L, Schulte DO, Bär K, Sass I and Schebek L (2018): Environmental and economic assessment of borehole thermal energy storage in district heating systems, Applied energy, v. 216, p. 73-90.
Welsch B, Ruehaak W, Schulte DO, Baer K and Sass I (2016a): Characteristics of medium deep borehole thermal energy storage, International Journal of Energy Research, v. 40, no. 13, p. 1855-1868.
Welsch B, Rühaak W, Schulte DO, Bär K and Sass I (2016b): Characteristics of medium deep borehole thermal energy storage, International Journal of Energy Research, v. 40, no. 13, p. 1855-1868.
Werner S (2016): European space cooling demands, Energy, v. 110, p. 148-156.
Werner S (2017): International review of district heating and cooling, Energy, v. 137, p. 617-631.

## Appendix A – A Modelica toolbox for the simulation of borehole thermal energy storage systems

Published as:

Formhals J, **Hemmatabady H**, Welsch B, Schulte DO and Sass I (2020): A Modelica toolbox for the simulation of borehole thermal energy storage systems, *Energies*, no. 9, p. 2327, doi: /10.3390/en13092327.

energies

MDPI

*Article*

# A Modelica Toolbox for the Simulation of Borehole Thermal Energy Storage Systems

**Julian Formhals [1,2,*], Hoofar Hemmatabady [1,2], Bastian Welsch [1,2], Daniel Otto Schulte [1] and Ingo Sass [1,2]**

[1] Geothermal Science and Technology, Technical University of Darmstadt, Schnittspahnstraße 9, 64287 Darmstadt, Germany; hemmatabady@geo.tu-darmstadt.de (H.H.); welsch@geo.tu-darmstadt.de (B.W.); schulte@geo.tu-darmstadt.de (D.O.S.); sass@geo.tu-darmstadt.de (I.S.)

[2] Graduate School of Excellence Energy Science and Engineering, Technical University of Darmstadt, Otto-Berndt-Str. 3, 64287 Darmstadt, Germany

* Correspondence: formhals@geo.tu-darmstadt.de; Tel.: +49-6151-16-20443

Received: 31 March 2020; Accepted: 25 April 2020; Published: 7 May 2020


**Abstract:** Borehole thermal energy storage (BTES) systems facilitate the subsurface seasonal storage of thermal energy on district heating scales. These systems' performances are strongly dependent on operational conditions like temperature levels or hydraulic circuitry. Preliminary numerical system simulations improve comprehension of the storage performance and its interdependencies with other system components, but require both accurate and computationally efficient models. This study presents a toolbox for the simulation of borehole thermal energy storage systems in *Modelica*. The storage model is divided into a borehole heat exchanger (BHE), a local, and a global sub-model. For each sub-model, different modeling approaches can be deployed. To assess the overall performance of the model, two studies are carried out: One compares the model results to those of 3D finite element method (FEM) models to investigate the model's validity over a large range of parameters. In a second study, the accuracies of the implemented model variants are assessed by comparing their results to monitoring data from an existing BTES system. Both studies prove the validity of the modeling approaches under investigation. Although the differences in accuracy for the compared variants are small, the proper model choice can significantly reduce the computational effort.

**Keywords:** borehole thermal energy storage; Modelica; district heating; borehole heat exchanger; thermal resistance capacity model; model reduction

## 1. Introduction

Borehole thermal energy storage (BTES) systems are suitable for large-scale storage of thermal energy in the subsurface over periods of several months, thus facilitating seasonal storage of, e.g., solar thermal energy or waste heat [1–3]. The concept is principally based on storage of thermal energy in the subsurface, while the subsurface (i.e., soil or rock and pore water) serves as storage medium, the heat is injected and extracted with an array of borehole heat exchangers (BHE). For the construction of BHEs, a closed pipe loop is placed into a borehole and the remaining annular space between the piping and the borehole wall is backfilled to establish a good thermal contact between the pipes and the ground. Subsequently, heat can be injected or extracted by circulating a heat carrier fluid through the BHEs. The temperature difference between the heat carrier fluid and the rock determines the direction of heat transfer. For efficient operation of BTES systems, careful design based on a thorough understanding of its behavior is imperative. Operational conditions like the temperature and volume flow of the entering fluid have a strong impact on the storage performance. These conditions are defined by other components of the district heating system in which the BTES is embedded. Therefore,

a dynamic simulation of the whole system is necessary to account for all interactions and to achieve an accurate assessment of the heating system's performance. A language for the modeling and simulation of multi-domain physical systems is *Modelica* [4]. It uses an object-oriented equation-based approach facilitating state of the art modeling, simulation, and optimization of district heating systems [5–7]. While there are numerous analytical and numerical modeling approaches for the standalone assessment of BTES systems [8–10], only very few of those models are suited and implemented for dynamic system simulation software tools [11,12]. To overcome this and facilitate both accurate and efficient modeling and simulation of BTES systems in *Modelica*, a new model was developed. The model exploits typical characteristics of BTES systems for reducing the model complexity, while including the most important features of practical applications.

### 1.1. State-of-the-Art Modeling Approaches for BTES Systems

BTES systems are preferably built in areas with little to no groundwater flow to avoid larger dissipation of thermal energy by convective heat transport [13]. Thus, BTES models often disregard convective heat transport in the subsurface and focus on conductive processes [2,14]. However, the heat transport inside the BHE pipes is dominated by the circulation of the heat carrier fluid making convection the most important process. This difference in the prevailing heat transport processes inside and outside the BHE and their corresponding magnitudes have led to a variety of hybrid models [15–17]. These models usually consist of sub-models for the BHE and the surrounding ground. While the dimensions of the BHE models reach down to millimeters and seconds, the ground models focus primarily on scales from centimeters to dozens of meters and hours to years. This large range of magnitudes of the ground model has led to many approaches, which further divide the ground into a local and a global part. The local part covers the heat dissipation process around a single BHE and the global part considers only the heat transport between those local areas and the ground surrounding the storage [18]. Consequently, the division of the model decouples the different superposed heat diffusion processes of the storage system. When interactions with other model parts are disregarded, the underlying processes in all three models (the BHE model, the local, and the global model) exhibit distinct radial symmetric characteristics. This allows for a reduction of the model dimensions from 3D to 2D, which goes along with a significant reduction in the model's degrees of freedom (DoF). For each of the aforementioned sub-models, multiple analytical and numerical modeling approaches exist.

### 1.2. Existing BTES Models for Dynamic System Simulation

In general, there are many models for BHEs implemented into different software tools for dynamic system simulation. However, only a few take into account the thermal interactions between neighboring BHEs [16]. One of the first models—the Superposition Borehole Model (SBM)—was conceptualized by Eskilsson and Claesson [19]. It uses Thermal Resistance Models (TRM) for the representation of single BHEs. So-called "g-functions" are applied to factor in the interactions between neighboring BHEs in arrays with arbitrary geometric configurations. However, such functions have to be generated in advance by externally executed detailed numerical simulations. They solve the thermal response of a step-pulse for multiple line sources in a dimensionless form. Some methods have been developed to aggregate pulses further back in time, thus facilitating multi-year simulations with dynamic load conditions [20]. However, as transient storage operation conditions require sophisticated temporal superposition, the model is more suited for constant operation scenarios.

The most widespread BTES model is the duct ground storage model (DST) by Pahud and Hellström [11]. It reduces the global 3D thermal diffusion problem to a 2D problem assuming a radial symmetric storage geometry. As with the aforementioned SBM, the DST model also utilizes a TRM approach to represent single BHEs. The overall temperature inside the ground is obtained by the superposition of a local, a global, and a steady flux part. While the local and the global model are realized with finite difference models (FDM), the steady flux part is defined by analytical equations.

Both the SBM and the DST model have been implemented into *TRNSYS* [21], a software for dynamic simulations of thermal energy systems.

So far, the only BTES model that has been developed using the modeling language *Modelica*, is the Hybrid Step Response Model (HSRM) by Picard and Helsen [12]. For the representation of BHEs, the model uses a Thermal Resistance and Capacity Model (TRCM), as introduced by Bauer [22], increasing the short-time accuracy compared to TRM based models. Around each single BHE, a radial FDM is used for the local model. Moreover, the global temperature field is obtained using Javed's method [20], which is a simplified and more compact version of Claesson's approach. It analytically calculates the step response of multiple equal line sources. Temporal superposition of multiple pulses again renders the consideration of time-varying operation scenarios possible. As a result, the HSRM model facilitates accurate simulations of both short-term and long-term behavior of BTES systems with arbitrary designs. Nevertheless, the pre-calculation of the response functions for the global model are time-consuming. Consequently, the model is better suited for studies with a small number of different configurations. As a uniform temperature along all borehole walls is assumed, the applicability of the HSRM model is restricted to BTES systems with BHEs connected in parallel

Obviously, the existing models for simulation of BTES systems have certain drawbacks: Both the DST and SBM model disregard the thermal capacity of the backfilling inside the boreholes. Considering that the space between the pipes and the borehole wall—i.e., the backfilled space—yields the steepest thermal gradients, this imposes a serious limitation on the short-time accuracy of these models. Furthermore, there is no existing model that can simulate both the impact of different hydraulic circuitries as well as the resulting pressure losses. While parallel connection of BHEs is common for heat extraction boreholes, most BHE arrays for storage purposes show serial connection schemes. Therefore, disregarding serial connections as in the HSRM model poses a strong limitation for BTES applications. Moreover, the existing models assume homogeneous thermal properties inside the storage volume and do not allow for consideration of stratigraphic changes in these properties or of an upper BHE section with thermally insulating grout [23]. Additionally, there are some practical limitations of the models. For example, it is not possible to simulate two instances of the DST model simultaneously.

One general advantage of the modeling language *Modelica* is the possibility to create tool-independent models that can be used in different modeling and simulation environments. Even though *Modelica* standard conformity poses a challenging task for complex models, developers should try not to restrain the use of their model to a single software. Unfortunately, the HSRM does only work in the *Modelica* environment it was developed with.

To overcome these issues, a new open source *Modelica* toolbox for the Simulation of BTES systems, the *MoBTES* component library, has been developed. It is not restricted to a single simulation environment and has a modular structure, enabling modification of component type and modeling approaches. Important design features of BTES systems, like serial and parallel BHE connections, reversal of flow direction, pressure loss calculation, consideration of stratigraphic subsurface models, and partly insulated BHEs, are implemented.

## 2. Methods

### 2.1. MoBTES Modeling Approaches

To enable the efficient simulation of BTES systems in *Modelica* for both dynamic system simulations and large parameter studies, the component library *MoBTES* was created. It extensively utilizes object-orientation to allow for a high reusability of the BTES model components and an easy extensibility. It comprises components for the simulation of BHEs and BTES systems and uses components and interfaces from the *Modelica* standard libraries *Fluid Heat Flow* and *Heat Transfer* [4]. Generally, all models are built in accordance with the *Modelica Language Specification* version 3.4 [4], avoiding syntax and scripts specific to individual *Modelica* environments. Nevertheless, problems may occur since each environment handles the implementation of the *Modelica* language slightly different. The library

has been developed and optimized for user experience using *SimulationX* [24], but other software tools have been successfully tested as well. A short description of the library structure and the tested simulation environments can be found in Appendix A.

Analogous to the previously mentioned BTES modeling approaches, the model is subdivided into a global part, a local part, and a BHE part. In contrast to the actual shape of the storage under investigation, circular global, and local models are used, allowing for a reduction from 3D to 2D, by exploiting their symmetries. However, *MoBTES* offers the option to choose from circular, rectangular, and hexagonal layouts. The radii of the global and local models are calculated to result in volumes equivalent to those of the actual layout. The hypothesis that the size of the model volume is of higher importance than its shape is in line with Hellström [18] who concluded a detailed study on this matter.

Figure 1 shows the discretization of the modeled region into smaller volume elements that form the global model. The global model calculates heat flows on a large scale and therefor only considers the average temperature inside each volume element. Each global element, which is located inside the actual storage region, is connected to an element of the local model. This local element, in turn, is connected to a corresponding BHE element, such that it interconnects the BHE element with the global element. This setup of interfaces between the different sub-models links the borehole wall temperature and the average temperature inside the respective storage volume, i.e., the global element temperature. Exploiting the equation-based nature of *Modelica*, this allows for an independent mathematical description of the thermal processes within each sub-model.

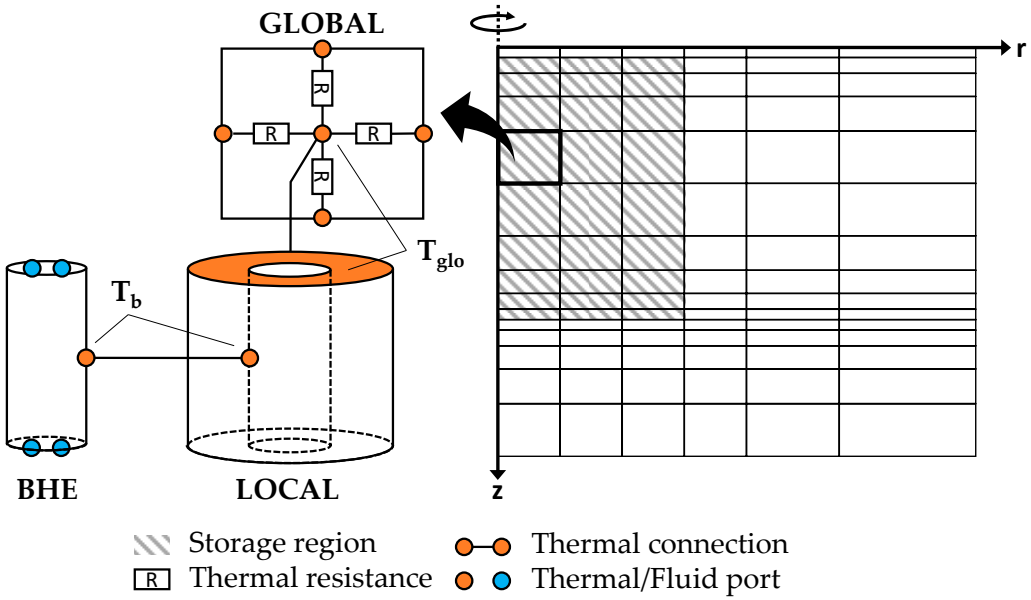


**Figure 1.** Mesh of a MoBTES model (**right**) and the fundamental connection scheme of the sub-models (**left**). The local element interconnects the global elements to their associated borehole heat exchanger (BHE) elements by giving a relation between the borehole wall temperature ($T_b$) and the mean volume temperature ($T_{glo}$).

The definition of interfaces between the sub-models together with *Modelica*'s object-oriented approach render the replacement of each sub-model possible and facilitate the utilization of different modeling approaches or component types. This enables the adaption of the model to the requirements of each application in terms of short- or long-term accuracy and computational effort. All currently available variants will be outlined in the following chapters.

#### 2.1.1. Borehole Heat Exchanger Models

The BHEs are divided vertically into segments that are connected by flow ports. *MoBTES* offers two interchangeable approaches to solve the heat transport problem inside the BHEs, both of which

have their advantages and disadvantages. As the default approach, a TRCM after Bauer [22] is deployed, which takes account of the thermal capacities of the grout and therefore achieves a more accurate reproduction of the transient short-time behavior. The second approach disregards the grout capacities in a TRM. Consequently, the degrees of freedom (DoF) and thus the computing time are reduced. Both approaches contain models for Single-U, Double-U, and Coaxial BHEs. A detailed definition of the models is given by Bauer [22,25].

### 2.1.2. Local Heat Transport Models

The main purpose of a local model is to link the borehole wall temperature $T_b$ of the BHE segment it is connected with, to the temperature of its corresponding global volume element $T_{glo}$, which is defined as the average temperature inside this ground volume. There are currently two different approaches for the local model implemented in *MoBTES*: one generally more suited for transient operation scenarios and the other one rather for more steady conditions like step-response studies. For the more transient case, an FDM is used to represent the radial symmetric process around a single BHE segment. The approach, which is already known from the DST or HSRM models [11,12], divides the local volume into concentric ring elements (see Figure 2a). Following Eskilson and Claesson's [19] guidelines for radial meshing, the three innermost elements have an equal thickness and succeeding elements grow by a constant factor. As defined by Equation (1), the global temperature $T_{glo}$ is calculated by the weighted average ring temperatures. $C_i$ and $T_i$ are the thermal capacity and temperature of a single ring element, respectively, and $C_{\mathrm{loc}}$ is the overall thermal capacity of the local volume.

$$T_{glo} = \sum_{i=1}^{n_{\mathrm{rings}}} \frac{C_i}{C_{\mathrm{loc}}} * T_i \tag{1}$$

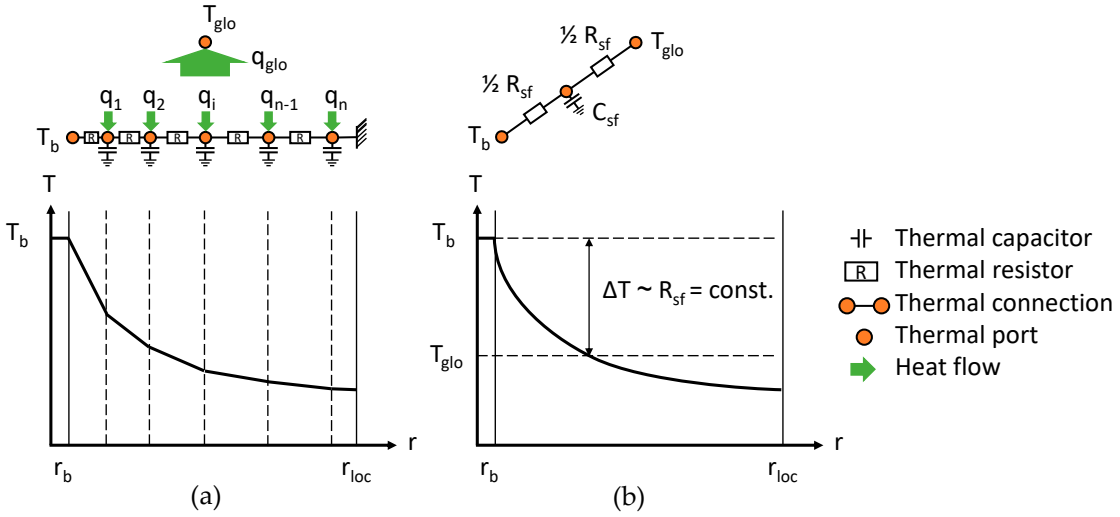


**Figure 2.** Local model concepts: (**a**) finite differences model and (**b**) steady flux model.

The heat flux $q_{glo}$ to or from a volume element is defined on the global level and distributed as $q_i$ among the n ring elements of the local model according to the weighting factors.

The second local model variant implemented in *MoBTES* is based on the steady flux part of the analytical solution for heat conduction inside a hollow cylinder with a fixed heat flow $Q_{\mathrm{sf}}$ at the inner boundary and no flow of heat over the outer boundary [26] (see Figure 2b). This steady flux profile describes the temperature gradient within the hollow cylinder after initial transient processes have subsided. Its shape is time-independent and can therefore be used to calculate the temperature difference between the borehole wall temperature $T_b$ and the average volume temperature $T_{glo}$. The

relation between the steady flux $Q_{sf}$ and this temperature difference can be expressed as a resistance $R_{sf}$. The DST model uses this resistance to calculate heat transport processes for long time-scales [11].

Carslaw and Jaeger analytically investigated the conduction of heat in a hollow cylinder for different boundary conditions [27]. Their result for the above-mentioned case of a fixed heat flow $Q_{sf}$ over the inner boundary and no flow of heat over the outer boundary is given by Equation (2) and can be used to obtain a solution for the local volume temperature profile. It depends on time and radius and consists of three terms. The first one only depends on the energy injected over time and gives an expression for the average volume temperature $T_m$ (Equation (3)). The second term defines a time-independent radial temperature profile $T_o$, which corresponds to the profile shape under steady flux conditions, where $R_0$ is the thermal resistance between the borehole wall radius $r_b$ and radius $r$, $r_{loc}$ the radius of the local volume and $\lambda$ the thermal conductivity inside the volume (Equation (4)).

$$T(r,t) = Q_{sf}\left(\frac{1}{C_{loc}}t + R_0(r) - \sum_{i=1}^{\infty} R_i(r)\, e^{-\frac{t}{\tau_i}}\right) \tag{2}$$

$$T_m(t) = \frac{Q_{sf}}{C_{loc}}t = \frac{Q_{sf}}{c\,\rho\,\pi({r_{loc}}^2 - {r_b}^2)}t \tag{3}$$

$$T_o(r) = Q_{sf}\,R_0(r) = \frac{Q_{sf}}{2\pi\,\lambda}\,\frac{{r_{loc}}^2}{{r_{loc}}^2 - {r_b}^2}\left(\ln\left(\frac{r_{loc}}{r}\right) - \frac{3}{4} + \frac{2r^2 - {r_b}^2}{4{r_{loc}}^2} + \frac{{r_b}^2}{{r_{loc}}^2 - {r_b}^2}\ln\left(\frac{r_{loc}}{r_b}\right)\right) \tag{4}$$

Finally, the third term describes the transition from the initially uniform temperature inside the hollow cylinder to the steady flux temperature profile. Its summands converge to zero with time. The speed of this process depends on the size of the respective time constants $\tau_i$ and is generally higher for summands with a higher index i. If this initial transition period is disregarded, Equations (5)–(8) can be used to obtain an expression for the steady flux resistance $R_{sf}$.

$$T(r_b,t) - T_m(t) = T_0(r_b) \tag{5}$$

$$= \frac{Q_{sf}}{2\pi\lambda}\left(\left(\frac{{r_{loc}}^2}{{r_{loc}}^2 - {r_b}^2}\right)^2 \ln\left(\frac{r_{loc}}{r_b}\right) - \frac{3{r_{loc}}^2 - {r_b}^2}{4({r_{loc}}^2 - {r_b}^2)}\right) \tag{6}$$

$$= \frac{Q_{sf}}{2\pi\lambda}\left(\ln\left(\frac{r_{loc}}{r_b}\right) - \frac{3}{4}\right),\ r_{loc} >> r_b \tag{7}$$

$$= Q_{sf}\,R_{sf} \tag{8}$$

Franke [28] introduced the idea of implementing a surrogate capacity $C_{sf}$ to this steady flux model to approximate the initial transient behavior until steady flux conditions prevail. Equation (9) gives the definition of this capacity, where $a$ is the thermal diffusivity of the local volume and $\tau_1$ the first and largest time constant of Equation (2). The resulting steady flux local model is depicted in Figure 2b. It was originally designed for dynamic optimization problems. Consequently, strong emphasis was put on computational speed.

$$C_{sf} = \frac{\tau_1}{R_{sf}} \simeq \frac{{r_{loc}}^2}{15\,a\,R_{sf}} \tag{9}$$

#### 2.1.3. Global Heat Transport Model

Most BTES systems exhibit an axial symmetry. This symmetry is exploited by the global model to reduce the 3D problem to a 2D FDM model with axes in the radial and vertical directions. The subsurface domain is discretized into rectangular elements. Each of these elements represents the cross section of a ring of the modeled region. The average element temperatures, which are derived from the local model, serve as input for the calculation of the global thermal diffusion process. Furthermore, Dirichlet boundary conditions are used to define temperatures at the outer model edges. Thereby,

the temperature at the model's ground surface boundary is either set to the average annual ambient temperature or to a time-varying temperature defined by an input. To ensure a sufficient size of the modeled region, while simultaneously maintaining a low number of DoF, the size of the global elements outside of the storage region increases by a defined growth factor following the scheme of Eskilsson and Claesson [19].

### 2.2. Model Validation

The individual validities as well as the limitations of the sub-model approaches are demonstrated and discussed in detail in the original literature [18,25,28]. Therefore, the validation of the *MoBTES* model focuses on the functional interaction of the sub-models. To assess the accuracy of results, a parameter study was carried out for a large range of parameters, in which the energy balances of *MoBTES* models are compared to those of detailed FEM models.

In a case study, monitoring data from an existing BTES system is used to test *MoBTES*' ability to accurately reproduce real-world applications. The relative deviations $\delta Q$ of the charged and discharged energy as well as the resulting energy balance are calculated according to Equation (10).

$$\delta Q = \frac{Q_{\text{model}} - Q_{\text{reference}}}{Q_{\text{reference}}} * 100\% \tag{10}$$

#### 2.2.1. Parameter Study

To evaluate the long-term accuracy of the proposed model for both local model variants (FDM and steady flux), a parameter study is carried out, in which the average annual amounts of charged and discharged energy are compared to detailed 3D simulations. These benchmark simulations are performed in *FEFLOW* [29], a commercial finite element software tool for the simulation of groundwater flow, and mass and heat transport in porous and fractured media, which is frequently used for the simulation of BTES applications [8,30–32]. An operation period of ten years is simulated. In each year, the storage is charged for six months with a constant inlet temperature of 80 °C, and afterwards is discharged for another six months with an inlet temperature of 20 °C. All BHEs are connected in parallel and the volume flow rate is set to 2 l/s per BHE. The investigated parameter range is given in Table 1.

**Table 1.** Parameter range for the 3D finite element method (FEM) benchmark models.

| Parameter | Range |
|---|---|
| Number of BHEs | 4, 7, 9, 16, 19, 25, 36, 37, 49, 61, 62, 64, 81, 91, 93, 100, 121, 127, 130, 144, 169, 173, 196 |
| BHE length | 50 m, 100 m |
| BHE spacing | 3 m, 5 m |
| BTES layout | circular, rectangular, hexagonal |
| Local model variants | steady flux, FDM with 10 capacity nodes |

Closely-packed and symmetric BTES designs of rectangular, circular, and hexagonal shapes of up to 196 BHEs are investigated (Figure 3). For each of the resulting layouts, models with a minimal axial spacing of 3 m and 5 m between the BHEs as well as lengths of 50 m and 100 m are created. Finally, a total of 99 corresponding benchmark simulations are carried out. Each of those benchmarks is compared to two *MoBTES* simulations, one using the steady flux local model, and the other using the FDM local model with 10 capacity nodes. Moreover, all models in this study utilize the TRM variant for Double-U BHEs, since FEFLOW does not provide a TRCM model. A full list of all benchmark and *MoBTES* models, their parametrization, and aggregated results can be found in the supplementary data (Table S1).

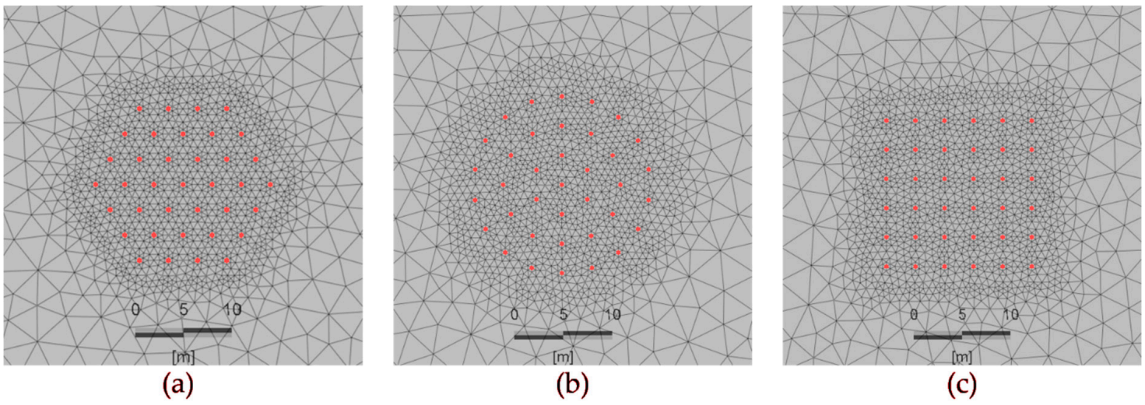


**Figure 3.** Top view on *FEFLOW* benchmark models with red markers for BHE positions: (**a**) hexagonal storage with 37 BHEs; (**b**) circular storage with 37 BHEs; (**c**) rectangular storage with 36 BHEs.

### 2.2.2. Case Study

To assess the predictive abilities of *MoBTES* concerning real storage operation, a BTES system installed in the Brædstrup solar district heating system (Denmark) [33] is simulated and the results are compared to monitoring data. The Brædstrup system consists of 48 BHEs with a length of 45 m each. Six BHEs are connected in series, resulting in eight strings of BHEs in parallel (see Figure 4). During charging operation, the flow through the BTES system is directed from the central BHEs to the peripheral BHEs. During discharging, the flow direction is reversed.

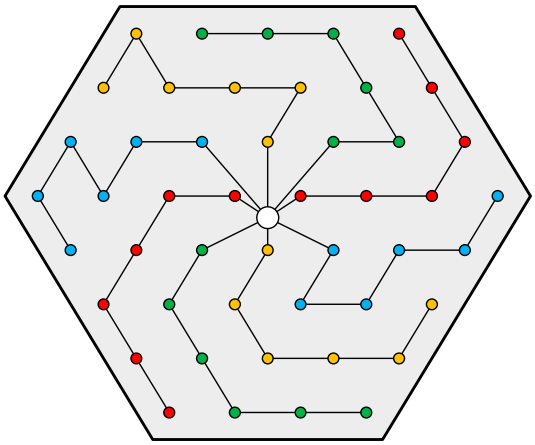

**Figure 4.** Brædstrup borehole thermal energy storage (BTES) system layout and serial BHE connections [33].

An important prerequisite for an accurate simulation of a real BTES system is good knowledge of the underground's thermal properties at the storage location. Tordrup et al. [31] used inverse modeling to determine thermal conductivity and volumetric heat capacity values for six geological layers at the storage site for a suitable model parametrization. Using monitoring data of the first 500 days of operation, they could reach an overall deviation between the energy balance of their fitted model and the monitoring data of 4.0%. The resulting average effective values for the thermal conductivity and the volumetric heat capacity of 1.72 W/(m K) and 1.96 MJ/(m$^3$ K), respectively, were used for the parametrization of the *MoBTES* model. However, this study has some important limitations which have to be kept in mind for the interpretation of the case study results. For example, adiabatic boundary conditions were set at all model boundaries to reduce the computational effort of the inverse modeling process. This is a major limitation, especially for the ground surface boundary, where thermal losses of the storage are usually highest.

In contrast to Tordrup et al. [31], who used data smoothed to daily values, this study exploits the full temporal resolution of 5 min from the raw monitoring data. Although the available data covers the time from the initial storage startup until the end of 2017, Tordrup et al.'s parameter estimation only utilized data of the first 500 days of operation. Therefore, the performance evaluation of the *MoBTES* model is primarily conducted for this period as well. Nevertheless, selected *MoBTES* models are simulated over the whole range of available data and compared to the monitored energy balance.

Figure 5 shows the measured inlet and outlet temperatures of the storage system during the considered time span. It indicates that during this time span, different operation strategies were tested: In 2012, the first year of operation, charging and discharging was performed in pulses with constant volume flow rates. In contrast to that, during the second charging period in 2013, the outlet temperatures were kept constant at defined temperature levels over longer periods, presumably by regulation of the volume flow. The presence of different operational strategies and the comparably good availability of data make the Brædstrup dataset a particularly suitable test case for the validation of *MoBTES*.

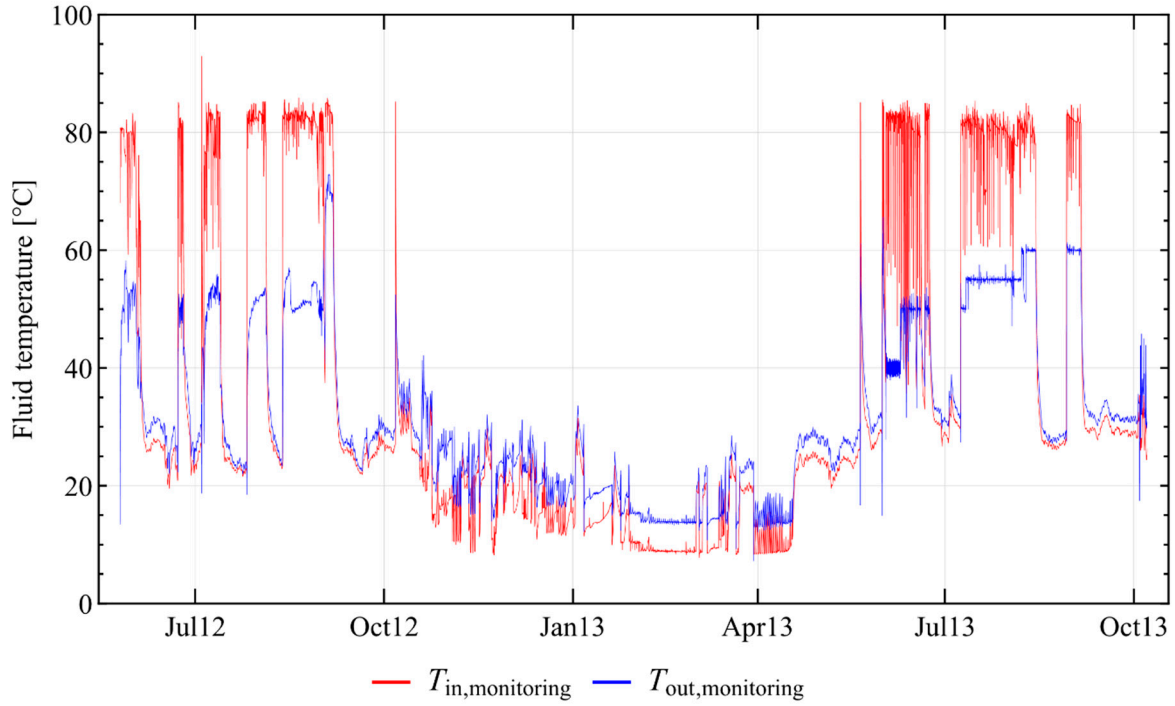


**Figure 5.** Measured inlet and outlet temperatures of the BTES system in Brædstrup during the first 500 days of operation.

For the comparison of the measurement data to the *MoBTES* models, all implemented modeling approaches are tested, using the monitored inlet temperature and volume flow rate time series as input. TRM and TRCM models are deployed for the BHE models and for the local model the steady flux and the FDM variants are compared. The FDM model's number of capacity nodes is varied between 2 and 16. Overall, a total of 20 simulations are carried out over the first 500 days of operation. Subsequently, the deviations between simulated and monitored values of the storage outlet temperature as well as the charged and discharged amount of energy are calculated for all models.

## 3. Results

### *3.1. Parameter Study Results*

Different BTES layouts and geometries are simulated using *MoBTES* with both the FDM as well as the steady flux local model. Subsequently, the amounts of charged and discharged heat are calculated

and compared to the results of the outcome of the respective *FEFLOW* benchmark models. Figure 6 shows the individual deviations of charged and discharged energy of all simulated *MoBTES* models. For both model variants, regression lines are depicted for the deviation in charging and discharging to illustrate the impact of the storage volume.

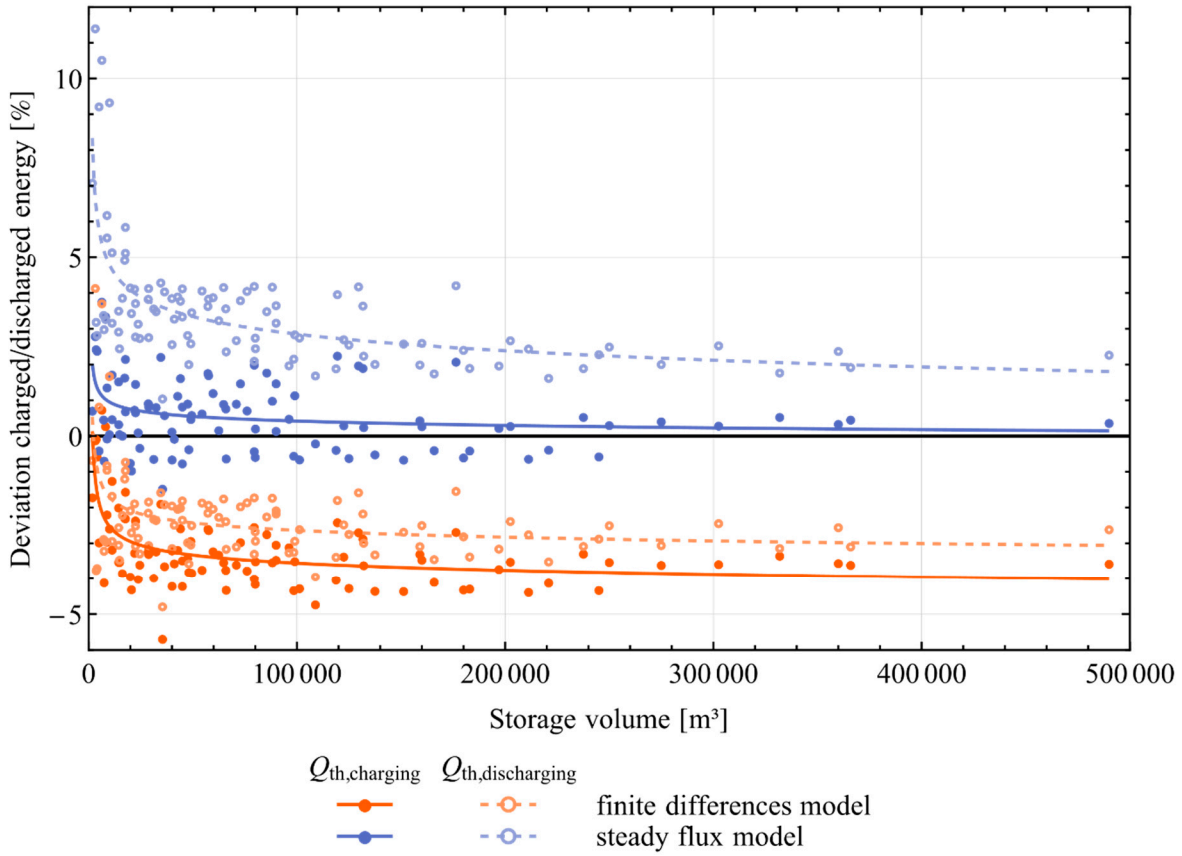


**Figure 6.** Relative deviation of charged and discharged thermal energy between *MoBTES* and *FEFLOW* for different storage system layouts.

Table 2 summarizes the mean results of the two local model variants. In comparison with the *FEFLOW* models, the FDM models underestimate the amount of charged energy by an average of −3.2% and discharged energy by an average of −2.3%. The similar magnitudes of deviation for both charging and discharging result in storage efficiencies close to those of the benchmark models. While the mean storage efficiency of all *FEFLOW* models is 60.9% the FDM *MoBTES* models yield an efficiency of 61.4%. In contrast to that, the deviations for charging and discharging differ significantly more for the steady flux models which achieve 62.5% storage efficiency on average. Underlying reason for this is a small deviation of +0.6% for charging in combination with an overestimation of +3.5% for the discharged energy amounts.

**Table 2.** Mean values of the *MoBTES* simulation results for both local model variants and deviation to *FEFLOW* benchmark models (standard deviation in brackets).

| Results | ***MoBTES*** **FDM** | ***MoBTES*** **Steady Flux Model** |
|---|---|---|
| Mean storage efficiency *MoBTES* | 61.4% | 62.5% |
| Mean deviation from *FEFLOW*: charged energy | −3.2% (±1.1%) | +0.6% (±1.0%) |
| Mean deviation from *FEFLOW*: discharged energy | −2.3% (±1.3%) | +3.5% (±1.7%) |
| Average computation time *MoBTES* | 751.8 s | 181.1 s |

On average, running an FDM model took 752 s, whereas the steady flux-based models required less than one-quarter of this time (181 s). Most of the computation time was consumed for the preprocessing, translation, and compilation of the *Modelica* models to C-code, whereas the actual simulations required only a fraction of it. The study was carried out using *SimulationX*, but for comparison, selected models were simulated in *Dymola* [34] and *OpenModelica* [35] as well. While *OpenModelica* yielded similar computation times as *SimulationX*, the model translation and compilation in *Dymola* took significantly less time resulting in much shorter overall computation times.

Figure 7 shows the impact of different parameters on the relative deviation between the charged and discharged energy amounts of *FEFLOW* and *MoBTES* FDM models. In accordance with Figure 6, the mean deviation in charging is larger than the deviation in discharging for all models utilizing an FDM local model. Additionally, it can be observed that the choice of layout seems to have an impact on the deviation, since there is a notable difference for circular, rectangular, and hexagonal layouts. Moreover, the deviation increases for more shallow systems and for larger BHE spacings.

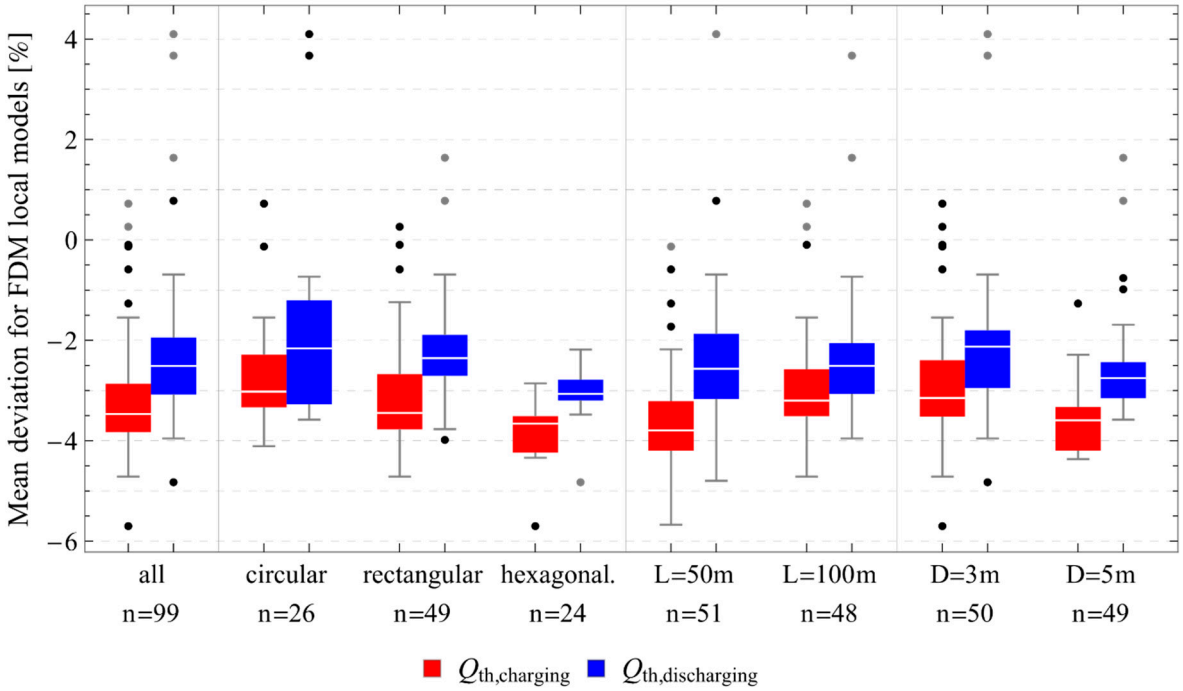


**Figure 7.** Impact of different parameters on the deviation of charged and discharged energy between *FEFLOW* and *MoBTES* models using an FDM local model (L = BHE length, D = minimal BHE distance).

Figure 8 illustrates the distribution of the deviations between *FEFLOW* and steady flux *MoBTES* models. During charging, the *MoBTES* models produce results very similar to *FEFLOW* and exhibit only few outliers. In contrast, the deviation is much larger during discharging and more outliers occur. The increased difference between relative deviations for charging and discharging leads to the higher discrepancy in storage efficiencies (cf. Table 2).

### 3.2. Case Study Results

For the case study, 20 *MoBTES* models with different modeling approaches and levels of discretization are simulated using monitoring data from the Bædstrup BTES inlet temperature as input. Subsequently, their outputs are compared to the outputs of the on-site measurements. One simulation of the considered 500-day-spanning monitoring data takes on average 12.3 min with models using the FDM approach for the local model. Compared to that, the steady flux approach reduces the computation time by more than 70% to only 3.5 min.

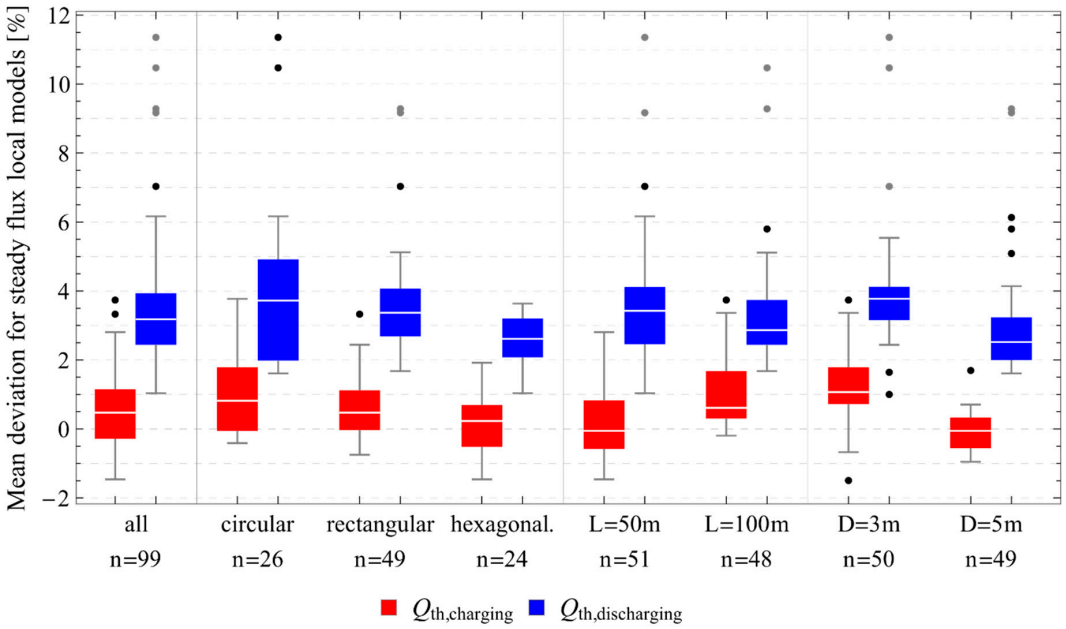


**Figure 8.** Impact of different parameters on the deviation of charged and discharged energy between *FEFLOW* and *MoBTES* models using a steady flux local model (L = BHE length, D = minimal BHE distance).

Figure 9 plots the computation times against the average temperature deviations for all individual simulation runs. In case of the FDM-based models, the computation time correlates with the level of discretization, i.e., the number of capacity nodes used. The steady flux models, which have only one capacity included, achieve a comparable computational speed to the FDM models with two capacities. This indicates that not only the absolute amount of DoFs determines the computational effort. Accordingly, model runs which utilize a TRCM BHE model do not generally take longer than their TRM counterparts, even though they have additional DoFs.

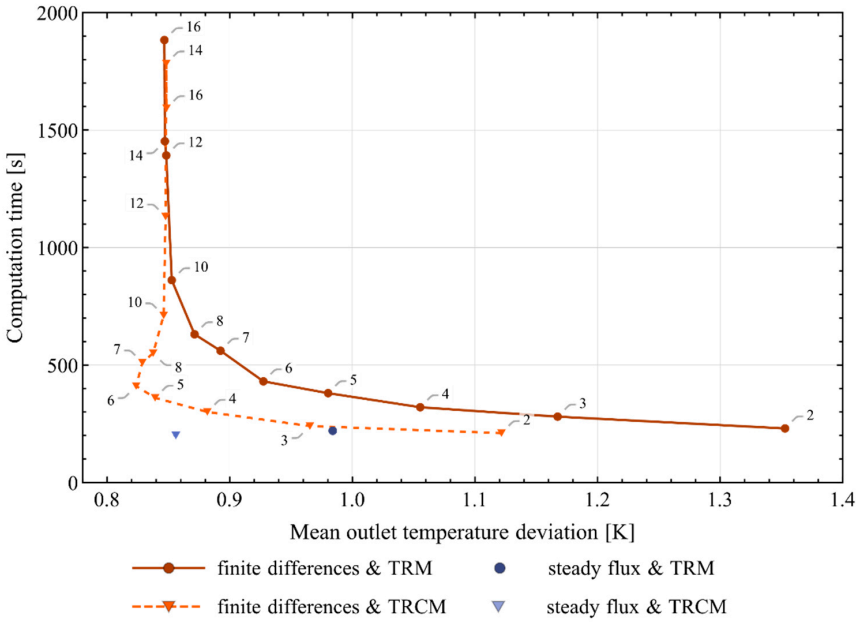


**Figure 9.** Computation time and mean deviation of the outlet temperature in comparison to the Brædstrup monitoring data for different local models. FDM models are labeled with their according number of used capacity nodes.

As a measure for the model accuracy, the mean outlet temperature deviation $\Delta T_{mean}$ is determined according to Equation (11), where $t_{sim}$ is the final simulation time and $\mathbb{1}(t)$ is an indicator function being 1 for times of storage operation and 0 otherwise:

$$\Delta T_{mean} = \frac{\int_0^{t_{sim}} \mathbb{1}(t) \left| T(t)_{outlet,monitoring} - T(t)_{outlet,MoBTES} \right| \mathrm{d}t}{\int_0^{t_{sim}} \mathbb{1}(t) \mathrm{d}t} \tag{11}$$

Regarding the outlet temperature deviation, models using a TRCM generally perform better than their counterparts with a TRM. Only for finer capacity node meshes both approaches' accuracies converge. Notably, a minimum in the deviation of the outlet temperature can be observed for the combination of TRCM models and FDM local models with six capacity nodes. A finer discretization does not improve the model's accuracy any further.

Figure 10 shows the deviation of the energy balance of the *MoBTES* models and the monitoring data. All models exhibit an underestimation of the energy balance by −3.2 to −8.4%. The lowest deviations can be observed for the models, which use a steady flux local model, showing an underestimation of the monitored energy balance of −3.2% for the model using a TRCM BHE model and −3.9% for the TRM variant, respectively. For the simulations utilizing FDM local models, a general trend towards lower deviations can be observed for an increase in the number of capacity nodes. Variants with six capacities or more exhibit an underestimation of the energy balance by approximately 6%. Regarding the BHE models, it can again be observed that models, which use the TRCM approach, show better accuracy in comparison to their TRM counterparts.

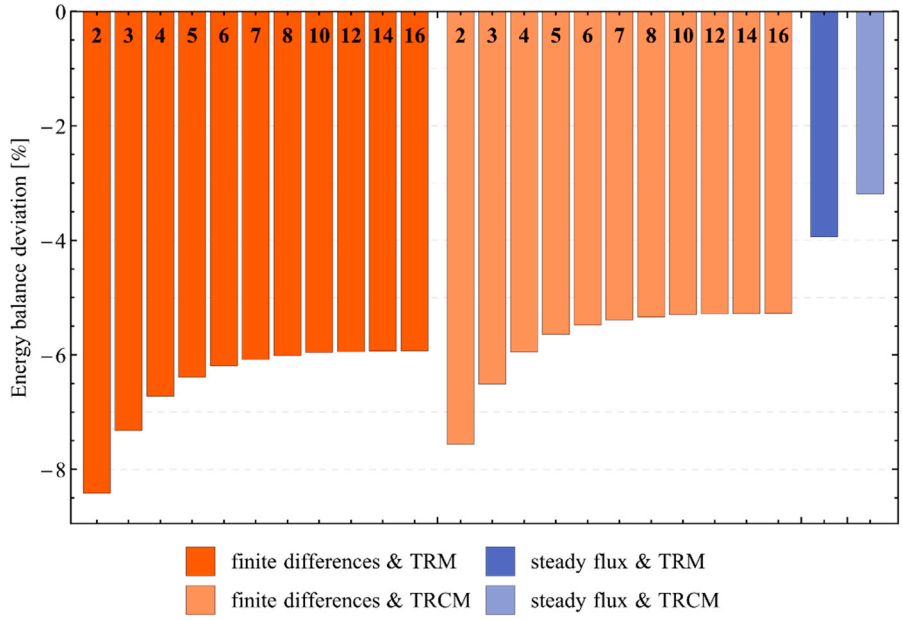


**Figure 10.** Relative deviation of the *MoBTES* models' energy balance in relation to the monitoring data after 500 simulated days (number of local model capacities on finite differences bars).

A more detailed insight into the model's short-time behavior can be gained by comparing the results of the different TRCM-based models to the monitored data over the first 24 h of BTES system operation (cf. Figure 11). At the initial startup of the system, the inlet temperature was kept relatively constant at a temperature of 80 °C, whereas the volume flow rate was adjusted over time. During the first twelve hours, models utilizing the FDM approach with two to five capacities or the steady flux model result in outlet temperatures above the monitored outlet temperature, whereas FDMs with seven or more capacities underestimate it. The model, which uses an FDM with six capacities, shows an almost perfect fit. It can be observed that the outlet temperature of the FDM variants converges to a

certain profile for an increasing number of capacity nodes. For the second half of the shown period, all models overestimate the outlet temperature, exhibiting smaller deviations for models with a finer discretization of the capacity.

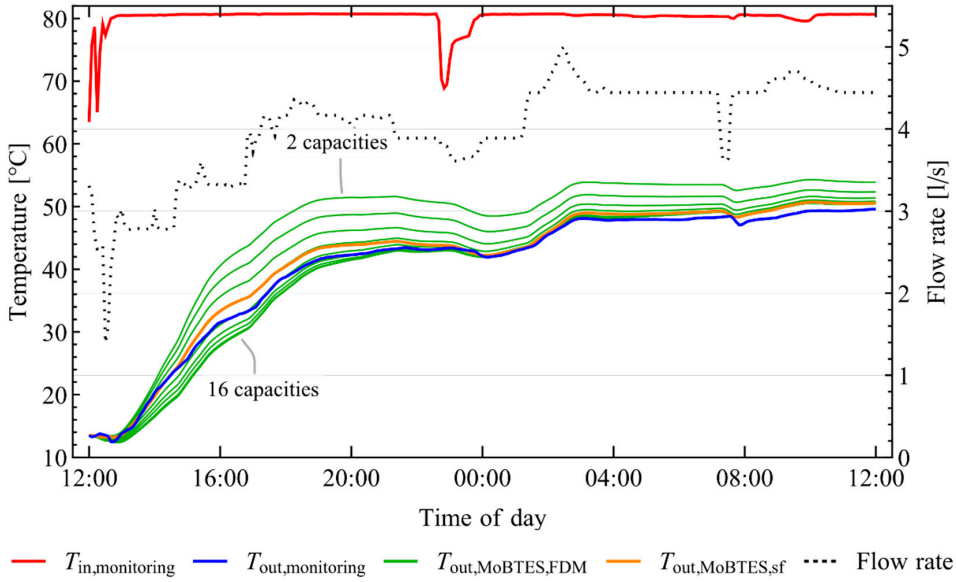


**Figure 11.** Comparison of monitored and simulated outlet temperatures for *MoBTES* models with Thermal Resistance and Capacity Model (TRCM) (FDM variants: number of capacity nodes increases from top to bottom).

To test the predictive abilities of *MoBTES* and the underlying parametrization of the case study over a larger time span, a steady flux model and an FDM model with six capacities (both using the TRCM BHE model) are simulated over the whole range of available monitoring data of 1680 days. Subsequently, the energy balance histories of the models are calculated and compared to the monitored energy balance history (Figure 12).

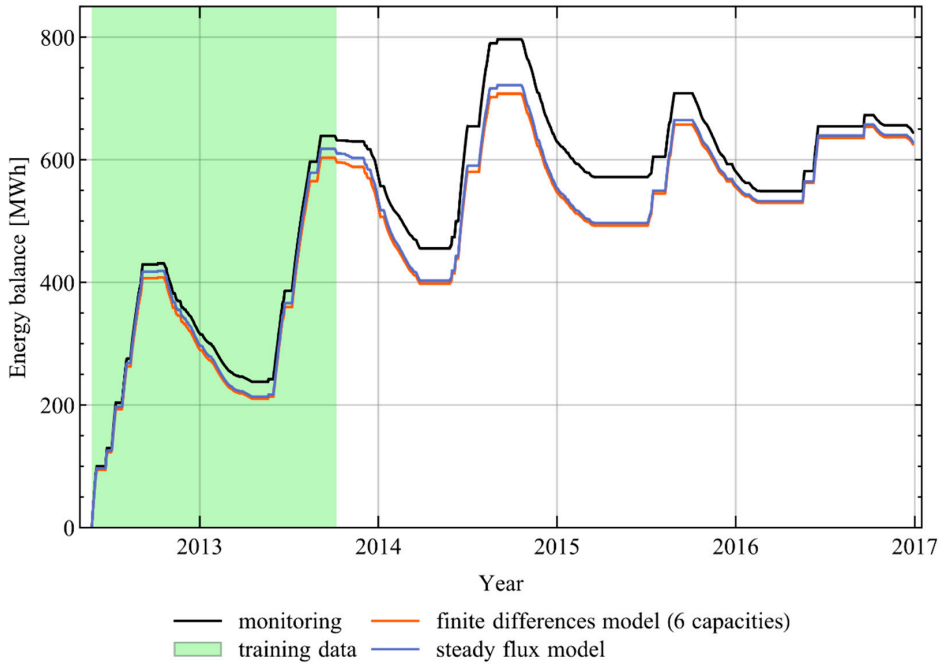


**Figure 12.** Energy balance from monitoring data and two selected models from startup until the end of the available data.

The final energy balance deviation after 1680 days amounts to −2.9% and −2.4% for the FDM approach and the steady flux approach, respectively. Surprisingly, these values are considerably lower than the deviations observed after 500 days of simulation (−5.5% and −3.2%). More important though is the maximum deviation which occurs during the summer of 2015 and amounts to −13.9% and −13.1%, respectively. The difference between the energy balances of the two *MoBTES* model variants is small in comparison to their deviation to the monitored data.

## 4. Discussion

### *4.1. Parameter Study*

The parameter study's main purpose is to compare *MoBTES* to an established model with well-defined parameters and thereby assess its ability to accurately predict the amount of charged and discharged thermal energy over a large parameter range. However, the *FEFLOW* models, which were chosen as benchmarks, also represent a simplification of realty and are prone to the effect of geological uncertainty. Consequently, *FEFLOW*'s actual accuracy in terms of simulating real BTES systems is limited. The comparison of *FEFLOW* and *MoBTES* should therefore be regarded as validation of the new model by numerical means.

The results presented in Section 3.1 show minor deviations between the charged and discharged amount of heat for all *MoBTES* models, except for very small BTES systems (cf. Figure 6). However, BTES systems consisting only of very few BHEs are not common, as storage efficiency generally increases with size, making those small systems inefficient. Therefore, the inaccuracy for small systems does not represent a major limitation of *MoBTES.* It is most likely caused by assumptions made for the modeling approaches of *MoBTES* local models. Figure 1 illustrates that the local models exchange thermal energy with the BHEs through the borehole walls and with the global model by extracting and injecting heat to their whole volume. As a consequence, no heat is exchanged via their outer boundaries. This poses a reasonable assumption for BHEs in the center of BTES systems. However, the error is larger for BHEs at the edge of the storage volume as they are not symmetrically surrounded by neighboring BHEs. The surface-to-volume ratio increases for small systems, hence leading to larger deviations. As a consequence, the minimal possible number of BHEs in *MoBTES* was limited to seven, to avoid excessive errors.

The overall magnitude of deviation for most models is in a low single-digit percentage range, which can be regarded as adequate. Accordingly, it is not possible to identify a local model approach as more accurate for simple step-response studies like the presented parameter study. However, additional information can be drawn from it. Although, the steady flux local models exhibit comparable magnitudes of deviation as the FDM variants, they clearly outperform them regarding the computational efficiency (cf. Table 2). Consequently, the steady flux model is preferable for large parameter studies with steady operation schemes.

Interestingly, the choice of the BTES layout seems to have an impact on the deviation for both local model variants (cf. Figures 7 and 8). Circular layouts tend to higher estimates in comparison to rectangular layouts, hexagonal resulting in the lowest estimates. There are several possible underlying reasons, which have to be discussed:

The first one concerns the overall shape of the BTES systems and the global models. We have to remember that *MoBTES* itself is a circular BTES model, and therefore the actual shapes of the benchmark models differ for rectangular and hexagonal layouts (cf. Figure 3). If this geometry transformation was the root cause for the observed layout impact, the circular models would have to perform best. This is true for the FDM variants, where the magnitude of deviation is smallest for circular arrangements, but not true for the steady flux variants, where the opposite is the case. Consequently, the model reduction approach of the global model has probably only a minor effect.

A second potential cause regards the shape of the local models. These have a circular cross section, whereas none of the areas around a single BHE is circular for the actual layouts. However, this

deviation in shape is considerably smaller for hexagonal cross-sections in comparison to rectangular ones. Again, the fact that hexagonal layouts perform best for the steady flux variants, while they exhibit the largest deviations for FDM variants contradicts the assumption that this might be the major cause for the impact of the choice of layout on the deviation.

A third potential cause for the observed impact of the storage layout on the deviation could be their diverging packing densities. Equal minimal BHE distances D lead to different radii of the local model $r_{loc}$ for rectangular, hexagonal, and circular layouts. Hexagonal layouts yield the highest packing density, resulting in smaller radii $r_{loc}$ for the same BHE distances D. Therefore, parameter study models with equal minimal BHE distance D, but varying storage layouts, result in different radii $r_{loc}$. If this would be the underlying reason, the observed impact would actually have to be related to the model volume, which is directly correlated to the BHE distance D and length L. Hexagonal layouts, which have the highest packing density, i.e., smaller storage volumes in average, yield in lower estimates of charged and discharged amounts of energy for both local model variants. However, the impact of BHE distance D and length L (cf. Figures 7 and 8) suggests that a potential correlation between deviation and storage volume should be reversed.

All effects, which are implied by the presented figures, are rather small and possibly not statistically significant. Nevertheless, some useful conclusions can be drawn by analyzing the difference in deviation between charging and discharging for the steady flux models (cf. Figure 8 There is a higher number of more pronounced outliers for discharging than for charging. Referring to Figure 6, these outliers can be connected to models of small BTES systems. This indicates that steady flux models with very small storage volumes exhibit the highest deviations from the *FEFLOW* benchmarks of all simulated *MoBTES* models. Therefore, FDM local models should be preferably applied for the simulation of small BTES systems.

As an overall result of the parameter study, it can be stated that *MoBTES* can be used for the simulation of simple BTES applications, as it produces results very close to those of detailed FEM models. Still, this is limited to certain applications. For example, *MoBTES* does not consider groundwater flow or BHE arrangements that strongly diverge from axisymmetric layouts. However, BTES systems are preferably built on sites with negligible groundwater flow to reduce convective losses. In addition to that, these systems should be constructed with a low surface-to-volume ratio to ensure an efficient performance. Due to these general rules for the construction of BTES systems, the aforementioned limitations do not pose a problem for most practical purposes. These general rules do not necessarily apply for regular BHE arrays, which are only used either for extraction or for injection of heat. This underlines the importance of using *MoBTES* for its original purpose of storage applications.

### *4.2. Case Study*

Design and operation of the Brædstrup system were investigated in great detail to achieve an accurate representation by the MoBTES models [31,33]. Nevertheless, there are still significant uncertainties left regarding the components' thermal properties. This has to be kept in mind in order to avoid overinterpretation when comparing the simulation results to the monitoring data. Independently, the case study is perfectly suited for a further comparison of the different *MoBTES* model variants in terms of efficiency and accuracy.

#### 4.2.1. Computational Effort and Mean Outlet Temperature Deviation

While the simulation of BTES systems using *MoBTES* reduces the computational effort in comparison to 3D FEM models by several orders of magnitude, there are significant differences between the different *MoBTES* approaches as well: computation times for the initial 500-day period range from 200 s to 1880 s (Figure 9). As expected, the specific computation time for the simulation of one year of storage operation is considerably higher compared to the parameter study described in Section 3.1. For example, the combination of steady flux local model and TRM BHE model takes 165.1 s per simulated year for the case study. In contrast, a comparable *MoBTES* model from the parameter

study takes only 20.6 s for one year. This can probably be attributed to generally smaller time steps in the case study due to a more transient operation, on the one hand, as well as a limitation of the maximum time step size to the resolution of the monitoring data of 5 min on the other hand.

Putting the computational time and the mean outlet temperature deviation of the different models in relation to each other (Figure 9) also unveils some interesting coherencies. As expected, the computational effort generally increases with the number of capacities of the local models. Consequently, the steady flux local models, which include only one capacity reach the lowest computation times. Comparing the temperature deviation of TRM-based and TRCM-based combinations strongly emphasizes the superiority of the TRCM approach. Both the FDM-TRM as well as the FDM-TRCM model combinations' mean outlet temperature deviations decrease with an increase in the number of capacities. However, for higher capacity numbers they seem to converge to a certain minimal value, which is a common outcome for grid refinement studies. However, for all models comprising less than ten capacities, the TRCM approach achieves in some cases significantly lower deviations than the comparable TRM models, while resulting in slightly lower computation times. As stated several times, the consideration of the grout's thermal capacity is of high importance. Discretization of meshes for numerical simulation should generally be refined at model areas with steep gradients and strong transient behavior. The temperatures within the boreholes of a BTES system fulfill both aspects, which explains the good performance of the *MoBTES* variants that use TRCM BHE models.

It seems that there is a good trade-off between the computational effort and the accuracy for models with six to eight capacities: these models gain a significant reduction in the temperature deviation while they experience only a minor increase in the computational time. Surprisingly, the deviation for FDM-TRCM model combinations even exhibits a minimum for six capacities, which might be explained by a closer look at the short time performance of the models (see Section 4.2.3). In terms of a good trade-off between computational speed and accuracy, the steady flux model combined with a TRCM model seems to be a serious alternative to the FDM based models.

#### 4.2.2. Comparison of Overall Energy Balance Deviations

Counterintuitively, the overall energy balance deviations (cf. Figure 10) of the models utilizing the steady flux approach even undercut that of the FDM based models. However, this finding does not contradict the observation that some of the FDM models perform better in terms of predicting the outlet temperature (cf. Figure 9). This is because of two reasons: First, the underlying energy balance is achieved by the summation of charged and discharged energy. Consequently, an error in charging can be compensated by an equally large error in discharging. In contrast to that, the temperature deviation considers only absolute deviation values, as defined by Equation (11). Second, the temperature deviation does not take the volume flow rate into account. Since the volume flow rate varies significantly over time, the simulated outlet temperature contributes to the energy balance with varying weights.

#### 4.2.3. Short Time Accuracy

The presented results are values integrated over the entire simulated time span. Therefore, they are mostly defined by the long-term accuracy of the model, whereas the short-time accuracy can be investigated best at times of strong changes in the operation of the BTES. The start-up phase of the storage represents such a sudden change in operation, which can be regarded as a step-pulse with a temperature raise of almost 70 K (cf. Figure 11). Moreover, the strong variation of the volume flow rate during that time span poses an additional difficulty for the reproduction of the transient operation behavior of the system. Most likely, the model with six capacities represents the best fit to the monitored outlet temperature by coincidence. However, this could explain the minimum in the mean outlet temperature deviation for this number of capacities (cf. Figure 9). In line with the results for the average outlet temperature deviation (cf. Figure 9), the steady flux model performs equally

well as the FDM model with five capacities. As expected, the difference between the model variants decreases over time.

#### 4.2.4. Comparison of Model Results and the Extended Monitoring Data

A successful comparison of the *MoBTES* models to the monitored data requires a good knowledge of the subsurface properties. For the Brædstrup case study, these key input parameters are gathered from a parameter estimation study conducted by Tordrup et al. [31]. With this parametrization, *MoBTES* underestimates the amount of energy after 500 days of operation by 3.2% to 6.5% disregarding models that use local FDM models with four or less capacities (cf. Figure 10). For comparison, the 3D FEM model by Tordrup et al. [31] with the best fit also resulted in an underestimation of the energy budget by 4%. This indicates that *MoBTES* is capable to reproduce the operation of the Brædstrup system during this period just as well as the 3D FEM model.

Regarding the energy balance history for the extended simulation period of 1680 days (cf. Figure 12) a maximum deviation of the *MoBTES* energy balance can be observed in 2015 before a trend reversal sets in resulting in a comparably low deviation by the end of the simulation period. The change in the model drift could indicate an insufficient size of the modeled region. However, this concern could be dispelled as a significant increase of the outer model boundaries did not result in any noticeable change in the models' energy balance.

When assessing the predictive capabilities of *MoBTES*, the limitations of the inverse modeling study by Tordrup et al. mentioned in Section 2.2.2 should be considered. Especially, the application of the adiabatic model boundaries represents an oversimplification as it corresponds to a perfect insulation on the ground surface. This is of little consequence during the initial storage operation when temperatures inside the storage volume and consequently the losses through the ground surface are naturally low. Therefore, this could explain both the good fit during the start-up period and the following increasing deviation.

The decline in the deviation towards the end of the simulation is an indication that the meaningfulness of an overall balance is limited, as different segments of the energy balance compensate each other. However, the use of the overall energy balance as evaluation value is due to the lack of more detailed data of the original simulations of Tordrup et al.

If an overall evaluation of the model quality is to be given, it must be considered that model input parameters, such as heat capacities and thermal conductivities of the soil and grout are subject to considerable uncertainties. Under this premise, the results of the FDM models with at least five capacities and the results of the steady-flux model are sufficiently accurate. As all models have some difficulties to accurately predict the storage behavior beyond the fitting period, the parameter estimation study should be repeated on the data foundation that is available now, taking thermal losses through the ground surface into account. As this goes clearly beyond the scope of this study, it should be considered as a future application of *MoBTES*.

## 5. Conclusions

The presented *MoBTES* model facilitates the deployment of different modeling approaches for its sub-models, allowing for an adaption to the numerical requirements of varying applications. The currently implemented variants are based on well-known and proven approaches, which exploit the physical characteristics of BTES systems. Consequently, the comparison of *MoBTES* to 3D FEM benchmark models and monitoring data from an existing plant reveals only minor deviations in their performance figures. While all variants are able to adequately reproduce the long-term system behavior, the right choice can significantly increase the computational efficiency or short-time accuracy. In addition to that, the presented model framework can be used as a test bed for new developed modeling approaches, provided they are compatible with the division of the model into a global, a local and a BHE sub-model. Other possible future applications of the developed open source *Modelica* library, could

be the rededication of the BHE models for non-storage applications or the realization of additional underground thermal energy storage technologies by reusing the available ground components.

In contrast to existing BHE models in *Modelica*, *MoBTES* is a dedicated BTES model and therefore should cover all relevant design features of such systems. Therefore, emphasis was put on the implementation of functionalities like serially connected BHEs, consideration of the stratigraphy at the storage site, flow reversal, hydraulic pressure loss, or partly insulated BHEs. To ensure an efficient operation, actual BTES systems are favorably build as compact arrays of thermally interacting BHEs on sites with negligible groundwater movement. Therefore, *MoBTES* only considers those cases and its accuracy might be impaired significantly for other applications.

The implemented model features allow for an accurate assessment of the impact of different designs on the storage performance, while maintaining a computational efficiency suitable for system simulation. Additionally, the flexibility of *MoBTES* enables the use of very fast models for extensive parameter studies or stochastic simulation. The versatile and multi-domain modeling approach of *Modelica*, allows for the integration of *MoBTES* into models of whole energy systems, including sector coupling and the combination with a wide range of other open source model libraries.

**Supplementary Materials:** The following are available online at http://www.mdpi.com/1996-1073/13/9/2327/s1, Table S1: Benchmark parameter study models and results. The MoBTES Modelica library, including an example package with the parameter study model, the case study model and all related parameters or datasets, is available online at https://github.com/JFormhals/MoBTES.

**Author Contributions:** This research was made collaboratively by all authors. Conceptualization was done by J.F., B.W., D.O.S., and I.S. Development of the methodology, software, data processing, formal analysis, and visualization was done by J.F. Validation was done by H.H., B.W., and J.F. Funding acquisition and supervision was done by D.O.S. and I.S. Review and editing was done by D.O.S., H.H., B.W., I.S., and J.F. All authors have read and agree to the published version of the manuscript.

**Funding:** This work was financially supported by the German Research Foundation (DFG) in the framework of the Excellence Initiative, Darmstadt Graduate School of Excellence Energy Science and Engineering (GSC 1070) and the European Research Development Fund (ERDF) by supporting the North-West Europe Interreg project DGE-Rollout.

**Acknowledgments:** The authors want to thank Brædstrup Fjernvaerme for sharing the monitoring data of the solar district heating plant in Brædstrup that was used for this work. Furthermore, the authors want to thank Morten Vang Bobach of Arcon-Sunmark and Jim Larsen of Brædstrup Fjernvaerme for sharing their detailed knowledge about the construction and operation of the BTES system.

**Conflicts of Interest:** The authors declare no conflicts of interest.

## Nomenclature

| | |
|---|---|
| BHE | borehole heat exchanger |
| BTES | borehole thermal energy storage |
| DoF | degrees of freedom |
| FDM | finite differences model |
| HSRM | hybrid step response model |
| MoBTES | Modelica borehole thermal energy storage model |
| SBM | superposition borehole model |
| TRCM | thermal resistance and capacity model |
| TRM | thermal resistance model |

## Symbols

| | | |
|---|---|---|
| a | thermal diffusivity | $m^2/s$ |
| c | gravimetric thermal capacity | $kg/m^3$ |
| C | thermal capacity | J/K |
| D | borehole spacing | m |
| L | Borehole length | m |
| q | specific heat flux | W/m |
| Q | Thermal energy | J |
| $\dot{Q}$ | heat flux | W |
| r | radius | m |
| R | thermal resistance | K/W |
| T | temperature | K |
| t | time | s |
| $\delta$ | relative deviation | - |
| $\rho$ | density | $kg/m^3$ |
| $\lambda$ | thermal conductivity | W/(m K) |
| $\tau$ | time constant | s |
| $\mathbb{1}$ | indicator function | - |

## Subscripts

| | |
|---|---|
| b | borehole wall |
| glo | global problem |
| loc | local problem |
| m | mean |
| min | minimum |
| sf | steady flux |
| sim | final simulation time |
| th | thermal |
| 0 | constant temperature profile under steady flux condition |

## Appendix A Modelica Library

The structure of the developed *Modelica* library can be seen in Figure A1. The main component is the *BTES* model, which has one fluid port each for inlet and outlet of the storage. An additional input is available if the user choses to define a time-varying ground surface temperature. All physical components, which are used to build the BTES model, are included in in the *Components* package. The *Components.Ground* package includes models for the global solution and the different local solutions, whereas the *Components.BoreholeHeatExchangers* package includes the Single-U, Double-U and Coaxial BHE models. The *Builder* package includes functions and enumerations which are needed for the assembly of the *BTES* model. All parameter sets which can be used in the BTES model are stored in the *Parameters* package as records. There are typical data records and the records of the examples shown in this work for the location, different soil types, the heat exchangers, grouts and heat carrier fluids. All components or parameter records that can be replaced by each other share common base classes. These base classes define all common properties, like interfaces or indispensable parameters, which is especially important for the replacement of the local, global, and BHE models. New implementations should inherit from the respective base class, to be in conformity with the *MoBTES* modeling approach. *MoBTES* version 1.0 has been successfully tested for *SimulationX* and *Dymola*.

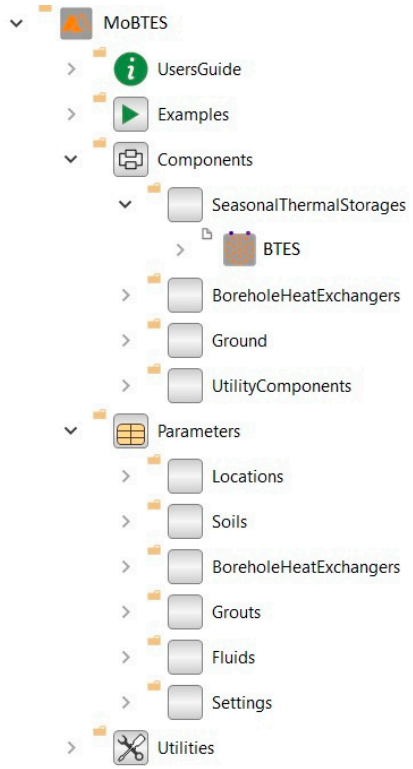


**Figure A1.** *MoBTES Modelica* library structure.

## References


1. Reuss, M. The use of borehole thermal energy storage (BTES) systems. In *Advances in Thermal Energy Storage Systems: Methods and Applications*; Elsevier: Cambridge, UK, 2015; pp. 117–147. ISBN 9781782420965.
2. Gehlin, S. Borehole thermal energy storage. In *Advances in Ground-Source Heat Pump Systems*; Elsevier: Duxford, UK, 2016; pp. 295–337.
3. Welsch, B.; Göllner-Völker, L.; Schulte, D.O.; Bär, K.; Sass, I.; Schebek, L. Environmental and economic assessment of borehole thermal energy storage in district heating systems. *Appl. Energy* **2018**, *216*, 73–90. [CrossRef]
4. Olsson, H. Modelica—A unified object-oriented language for physical systems modeling; Modelica Association. Available online: https://www.modelica.org/documents/ModelicaSpec34.pdf (accessed on 30 April 2020).
5. Schweiger, G.; Larsson, P.O.; Magnusson, F.; Lauenburg, P.; Velut, S. District heating and cooling systems—Framework for Modelica-based simulation and dynamic optimization. *Energy* **2017**, *137*, 566–578. [CrossRef]
6. Filonenko, K.; Howard, D.; Buck, J.; Veje, C. Comparison of two simulation tools for district heating applications. In Proceedings of the 9th International Conference on Energy Reliability REMOO-2019, Hong Kong, China, 16–18 April 2019.
7. Wetter, M. Haugstetter Modelica versus TRNSYS—A Comparison between an equation-based and a procedural modeling language for building energy simulation. *Proc. SimBuild* **2006**, *2*, 262–269.
8. Diersch, H.J.G.; Bauer, D.; Heidemann, W.; Rühaak, W.; Schätzl, P. Finite element modeling of borehole heat exchanger systems. Part 2. Numerical simulation. *Comput. Geosci.* **2011**, *37*, 1136–1147. [CrossRef]
9. Schulte, D.O.; Welsch, B.; Rühaak, W.; Bär, K.; Sass, I. BASIMO—Borehole Heat Exchanger Array Simulation and Optimization Tool. In Proceedings of the European Geosciences Union General Assembly 2017, Vienna, Austria, 23–28 April 2017.
10. Blocon. *Earth Energy Designer* (version 4); Windows; Blocon: Lund, Sweden, 2016.

11. Pahud, D.; Hellström, G. The new duct ground heat model for TRNSYS. In Proceedings of the Eurotherm Seminar nº49, Physical models for Thermal Energy Stores, Eindhoven, The Netherlands, 25–27 March 1996; pp. 127–136.
12. Picard, D.; Helsen, L. A New Hybrid Model For Borefield Heat Exchangers Performance Evaluation. In Proceedings of the 2014 Ashrae Annual Conference, Seattle, WA, USA, 28 June–2 July 2014; pp. 857–866.
13. Skarphagen, H.; Banks, D.; Frengstad, B.S.; Gether, H. Design Considerations for Borehole Thermal Energy Storage (BTES): A Review with Emphasis on Convective Heat Transfer. *Geofluids* **2019**, 1–26. [CrossRef]
14. Moradi, A.; Smits, K.M.; Lu, N.; McCartney, J.S. Heat Transfer in Unsaturated Soil with Application to Borehole Thermal Energy Storage. *Vadose Zone J.* **2016**, *15*. [CrossRef]
15. Picard, D. Modeling, Optimal Control and HVAC Design of Large Buildings using Ground Source Heat Pump Systems. Ph.D. Thesis, KU Leuven, Leuven, Belgium, 2017.
16. Lanahan, M.; Tabares-Velasco, P.C. Seasonal thermal-energy storage: A critical review on BTES systems, modeling, and system design for higher system efficiency. *Energies* **2017**, *10*, 743. [CrossRef]
17. Chio, S.; Miriaiiliosseinabadi, S. Simulation modeling of ground source heat pump systems for the performance analysis of residential buildings. In Proceedings of the BS 2013: 13th Conference of the International Building Performance Simulation Association, Chambéry, France, 26–28 August 2013; pp. 1960–1967.
18. Hellström, G. Ground Heat Storage: Thermal Analyses of Duct Storage Systems. Ph.D. Thesis, Lund University, Lund, Sweden, 1991.
19. Eskilson, P.; Claesson, J. Simulation model for thermally interacting heat extraction boreholes. *Numer. Heat Transf.* **1988**, *13*, 149–165. [CrossRef]
20. Javed, S. Thermal Modelling and Evaluation of Borehole Heat Transfer. Ph.D. Thesis, Chalmers University of Technology, Göteborg, Sweden, 2012.
21. Solar Energy Laboratory. *TRNSYS—A Transient System Simulation Program (Version 18)*; University of Wisconsin-Madison, Solar Energy Laboratory: Madison, WI, USA, 2017.
22. Bauer, D.; Heidemann, W.; Müller-Steinhagen, H.; Diersch, H.J.G. Thermal resistance and capacity models for borehole heat exchangers. *Int. J. Energy Res.* **2011**, *35*, 312–320. [CrossRef]
23. Schulte, D.O.; Welsch, B.; Boockmeyer, A.; Rühaak, W.; Bär, K.; Bauer, S.; Sass, I. Modelling Insulated Borehole Heat Exchangers. *Environ. Earth Sci.* **2016**, *75*, 910. [CrossRef]
24. ESI ITI. *SimulationX (Version 4.1)*; ESI ITI: Dresden, Germany, 2017.
25. Bauer, D. Zur thermischen Modellierung von Erdwärmesonden und Erdsonden-Wärmespeichern. Ph.D. Thesis, Universität Stuttgart, Stuttgart, Germany, 2012.
26. Claesson, J.; Eskilson, P. Conductive heat extraction to a deep borehole: Thermal analyses and dimensioning rules. *Energy* **1988**, *13*, 509–527. [CrossRef]
27. Carslaw, H.S.; Jaeger, J.C. Conduction of Heat in Solids. *Phys. Today* **1962**, *15*, 74–76. [CrossRef]
28. Franke, R. *Integrierte Dynamische Modellierung und Optimierung von Systemen mit Saisonaler Wärmespeicherung*; Fortschrittberichte VDI: Reihe 6, Energietechnik Nr. 394; VDI-Verlag: Düsseldorf, Germany, 1998; ISBN 3-18-339406-5.
29. DHI WASY. *FEFLOW* (version 7.1); Windows; DHI WASY: Berlin, Germany, 2017.
30. Mielke, P.; Bauer, D.; Homuth, S.; Götz, A.E.; Sass, I. Thermal effect of a borehole thermal energy store on the subsurface. *Geotherm. Energy* **2014**, *2*, 5. [CrossRef]
31. Tordrup, K.W.; Poulsen, S.E.; Bjørn, H. An improved method for upscaling borehole thermal energy storage using inverse finite element modelling. *Renew. Energy* **2017**, *105*, 13–21. [CrossRef]
32. Homuth, S.; Mikisek, P.; Götz, A.E.; Sass, I. Geothermische Langzeitmodellierung eines solargekoppelten Erdsonden-Wärmespeichers in Crailsheim. In Proceedings of the Der Geothermiekongress 2011, Bochum, Germany, 15–17 November 2011.
33. Sørensen, P.A.; Larsen, J.; Thøgersen, L.; Dannemand Andersen, J.; Østergaard, C.; Schmidt, T. Boreholes in Brædstrup. *Final Rep.* **2013**.

34. Dassault Systemes. *Dymola—Dynamic Modeling Laboratory* (version 2020); Windows; Dassault Systèmes AB: Lund, Sweden, 2020.
35. Fritzson, P.; Aronsson, P.; Lundvall, H.; Nyström, K.; Pop, A.; Saldamli, L.; Broman, D. The OpenModelica Modeling, Simulation, and Development Environment. In Proceedings of the 46th Conference on Simulation and Modelling of the Scandinavian Simulation Society (SIMS2005), Trondheim, Norway, 13–14 October 2005; pp. 83–90.

## Appendix B – Optimized layouts of borehole thermal energy storage systems in 4th generation grids

Published as:

**Hemmatabady H**, Formhals J, Welsch B, Schulte DO and Sass I (2020): Optimized layouts of borehole thermal energy storage systems in 4th generation grids, *Energies,* no. 17, p. 4405, doi: /10.3390/en13174405.

energies

MDPI

Article

# Optimized Layouts of Borehole Thermal Energy Storage Systems in 4th Generation Grids

**Hoofar Hemmatabady [1,2,*], Julian Formhals [1,2], Bastian Welsch [1,2], Daniel Otto Schulte [1] and Ingo Sass [1,2]**

[1] Geothermal Science and Technology, Technical University of Darmstadt, Schnittspahnstraße 9, 64287 Darmstadt, Germany; formhals@geo.tu-darmstadt.de (J.F.); welsch@geo.tu-darmstadt.de (B.W.); daniel.schulte@gast.tu-darmstadt.de (D.O.S.); sass@geo.tu-darmstadt.de (I.S.)

[2] Graduate School of Excellence Energy Science and Engineering, Technical University of Darmstadt, Otto-Berndt-Str. 3, 64287 Darmstadt, Germany

* Correspondence: hemmatabady@geo.tu-darmstadt.de

Received: 31 July 2020; Accepted: 19 August 2020; Published: 26 August 2020


**Abstract:** Borehole thermal energy storage (BTES) systems are a viable option to meet the increasing cooling demand and to increase the sustainability of low-temperature district heating and cooling (DHC) grids. They are able to store the rejected heat of cooling cycles on a seasonal basis and deliver this heat during the heating season. However, their efficient practical implementation requires a thorough analysis from technical, economic and environmental points of view. In this comparative study, a dynamic exergoeconomic assessment is adopted to evaluate various options for integrating such a storage system into 4th generation DHC grids in heating dominated regions. For this purpose, different layouts are modeled and parameterized. Multi-objective optimization is conducted, varying the most important design variables in order to maximize exergetic efficiency and to minimize levelized cost of energy (LCOE). A comparison of the optimal designs of the different layouts reveals that passive cooling together with maximizing the heating temperature shift, accomplished by a heat pump, lead to optimal designs. Component-wise exergy and cost analysis of the most efficient designs highlights that heat pumps are responsible for the highest share in inefficiency while the installation of BTES has a high impact in the LCOE. BTES and buffer storage tanks have the lowest exergy destruction for all layouts and increasing the BTES volume results in more efficient DHC grids.

**Keywords:** district heating and cooling; borehole thermal energy storage; dynamic exergoeconomic method; TRNSYS; MATLAB; coupling; multi-objective optimization

## 1. Introduction

In European households, heating accounts for 78% of the total final energy use. Cooling of buildings still has a fairly small share in the energy use, but the demand during summer months is continuously rising due to climate change [1]. It is estimated that by 2025 the installed cooling capacity in Europe is likely to be 55–60% higher than in 2010 [2]. Therefore, simultaneous supply of heating and cooling needs to be considered as an important part of the future energy supply system.

By 2050, more than 80% of European residents are expected to live in urban areas [3]. This trend increases the benefits of district energy systems, which tend to be more economic for densely populated regions [4]. District heating and cooling (DHC) systems can be environmentally beneficial and pave the way toward the sustainable energy supply, if they are applied appropriately [4,5].

The 4th generation district heating (DH) concept specifies some prerequisites that need to be met for the proper application of DH systems and the fulfillment of their role in a future sustainable energy economy. The most important ones are the implementation of low-temperature DH networks,

the ability to recycle heat from low-temperature sources such as solar and geothermal heat and the implementation as an integrated part of smart energy systems [6]. A future 4th generation district cooling (DC) system can be defined as a system more interactive with the electricity, DH and gas grids [6]. Overall, a 4th generation DHC grid can be considered as a low-temperature interactive energy grid for supplying heating and cooling demands.

Every cooling process involves the rejection of excess heat to a heat sink. Lower sink temperatures generally result in a more efficient system operation. As the temperature of the ground during cooling seasons is lower and more stable than the ambient temperature, it can be used as an efficient heat sink by utilizing borehole heat exchangers (BHEs). In addition, arrays of BHEs are suitable thermal energy storage systems for waste heat and fluctuating renewable energy sources [7]. Such borehole thermal energy storage (BTES) systems exploit the high heat capacity of the underground to store large quantities of heat on a seasonal basis in the geological environment [8]. The results of analyzing the influence of design parameters on energetic performance of medium deep BTES systems showed that they can have a very high efficiency of more than 80% in large-scale applications [7,9–11].

Aforementioned benefits of BTES systems and the increasing trend of installing cooling capacity in Europe, makes the utilization of BTES-assisted 4th generation DHC grids an interesting concept for future energy supply. These benefits have been already proven by several projects (e.g., [12–14]). A review of some of these projects can be found in [15]. However, there are not enough guidelines for designing BTES systems in DHC grids. An efficient implementation of this concept requires more detailed assessments and system design from technical, economic and environmental points of view. A BTES should not be regarded in isolation, but merely as one component within a district heating and cooling network [8,16,17]. Therefore, a method needs to be selected that evaluates the optimal integration of BTES systems into DHC grids considering their interaction with other components.

An energy carrier's exergy is defined by its potential to interact with its environment [18], namely the availability of energy. Exergoeconomics is the branch of engineering that combines exergy analysis and economic principles. It can provide information to a system designer which are not available through conventional energy analysis and economic evaluations, but crucial to the design and operation of a cost-effective system [18]. Moreover, increasing exergy efficiency leads to reduced environmental impacts and a higher sustainability [19]. For environmental evaluation of BTES and energy systems, Life Cycle Assessment (LCA) has been proven to be a useful tool [20,21]. However, LCA lacks thermodynamic assessment [19]. Therefore, the exergoeconomic analysis method can be considered as a method which takes technical, economic and environmental aspects into consideration. Moreover, by adding $CO_2$ emission costs to the total costs, economic effects of direct environmental emissions can be considered as well.

Exergy analysis of an installed BTES system for heating and cooling applications was done by Kizilkan and Dincer [22,23]. These studies specify that a significant energy saving can be done by determining the exergy destruction of the whole system and its components. However, they have mainly used a static approach, which is suitable for high-temperature systems., e.g., power generation systems. When a system's operating temperature is close to the reference state, e.g., heating and cooling systems, the utilization of a dynamic approach is necessary [24].

In this study, a dynamic exergoeconomic assessment approach including $CO_2$ emission costs is adapted to BTES systems to render a comprehensive technical, economic and environmental assessment of their implementation into 4th generation DHC grids. The approach is presented on the example of a generic case study. After giving a general overview on this case study, different system layouts and scenarios are specified. Moreover, mathematical optimization is done for each scenario using the outputs of the exergoeconomic assessment approach as objective functions, varying the most sensitive system parameters. Finally, the results are compared and discussed.

## 2. Case Study Setup

For the case study, a notional district located in Frankfurt, Germany is chosen. Frankfurt is located in a heating-dominated region with a low cooling demand, which is mainly caused from the commercial and industrial sectors. It is assumed to consist of 100 single family houses, 100 multifamily houses and 50 office buildings. After designing 3D thermal zone models of each building type, load profiles are calculated in TRNBuild [25]. Boundary conditions are based on standard libraries for building construction types of renovated buildings [26], schedules (e.g., occupation) [27] and regime types (e.g., heating and cooling set point temperature) [27]. The weather data from Frankfurt airport is taken from Meteonorm data [28].

Figure 1 shows the calculated load profile. The total annual heating and cooling demands of the DHC grid are 8.47 GWh and 1.05 GWh, respectively, with more than 70% of the cooling demand for the office buildings. Supply and return temperatures ($T_{sup}$, $T_{ret}$) of the grid are 6 °C and 12 °C for active and 18 °C and 22 °C for passive cooling. In accordance to the 4th generation DH concept, supply and return temperatures are set to 45 °C and 35 °C during the heating season [29].

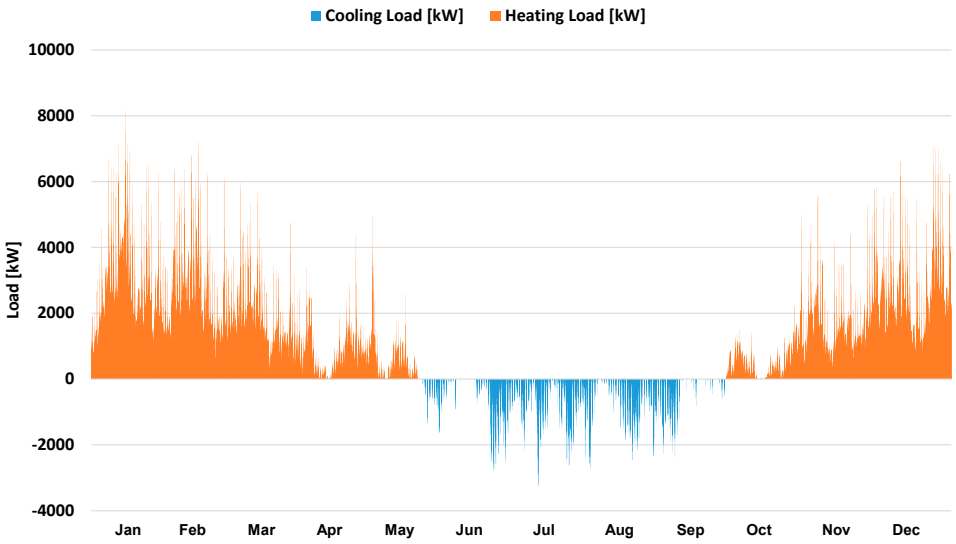


**Figure 1.** District heating and cooling (DHC) load profile.

## 3. System Design Scenarios

Four generally different designs of the case district's heating and cooling system shall be evaluated. The proposed scenarios are summarized in Table 1. All scenarios comprise a BTES system which is discharged by a heat pump (HP). Furthermore, the systems contain one or two gas boilers (GB) to cover heat demands which are not covered by the BTES system. Moreover, all scenarios include a buffer storage tank (BST) which is needed to lower the size of the BTES system, to maximize the total load supply from the ground loop and to operate the HPs more steadily by smoothening the load demands. The four scenarios generally differ by their approach of cooling (active or passive) and by the connection of the BTES system and the GB (serial or parallel). All four systems have their own characteristics during heating and cooling operation, respectively, which shall be outlined in the following.

**Table 1.** The proposed scenarios.

| Scenario | Cooling | GB | HPs | BST |
|---|---|---|---|---|
| ActSer | Active | Serial | Single stage | Cooling/Heating |
| ActPar | Active | Parallel | Double stage | Cooling/Heating |
| PasSer | Passive | Serial | Single stage | Cooling/Heating |
| PasPar | Passive | Parallel | Double stage | Cooling/Heating |

### 3.1. Cooling Operation

The DHC is located in a heating-dominated region. The two general cooling approaches are

- Active Cooling (Scenarios ActSer and ActPar): The total cooling load is supplied actively by heat pumps, which use the BTES as their heat sink (Figure 2) and
- Passive Cooling (Scenarios PasSer and PasPar): The total cooling load is supplied passively by the BTES using heat exchangers (HEX), which separate load and sink side (Figure 3).

The BTES temperature difference is taken as 5 K for active and 3 K for passive scenarios. The nominal BTES side flow rate of the HP, as well as the connected pump, are specified accordingly and at a BTES side temperature of 15 °C. The pump is turned on or off by a thermostat, which monitors the BST supply temperature.

In the active scenarios, either a single stage HP covers the whole cooling demand (ActSer), or each double stage HP module covers it partially (ActPar). Double stage HPs are selected for ActPar scenario, because of their more efficient operation in partial cooling mode. The nominal load side flow rate of the HP, as well as that of the connected pump, are selected according to the design supply and return temperatures. The BST thermostat turns on or off the pump and its flow rate is regulated considering the HP output capacity. For passive scenarios, the same on/off strategy operates the pump and the regulation is done considering the energy balance equation of the HEX.

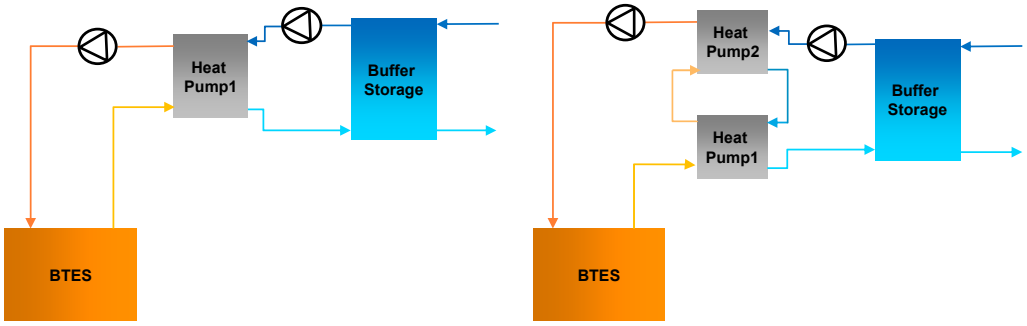


**Figure 2.** System layouts of the active cooling scenarios: ActPar (left) and ActSer (right).

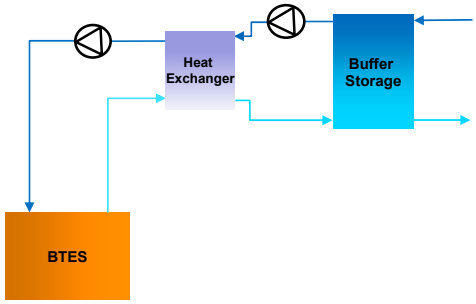


**Figure 3.** System layout of the passive cooling scenarios (PasSer and PasPar).

### 3.2. Heating Operation

The scenarios in heating mode are defined to compare the effect of the temperature shift and the maximum corresponding heating load that can be supplied efficiently by the ground loop. The design temperature difference of the BTES for heating mode is suggested to be between 3–5 K by some geothermal HP manufacturers [30]. In some practical applications this is taken as approx. 4 K [14,31]. 4 K can hardly be achieved for serially-connected HPs at full load performance (according to the manufacturer's data [32]). Therefore, to have similar boundary conditions for all scenarios, it is taken as 5 K for this study. The nominal flow rate of the HP on the source side and the connected pump are specified to meet the temperature difference at a source side temperature of 10 °C. The pump is

controlled by the BST on/off thermostat. On the load side, lower temperature shifts increase the COP of the HP but result in a lower BST efficiency [33] and a higher power consumption of the circulating pumps. Consequently, the serial and parallel scenarios are proposed to assess partial and full grid temperature shift by the ground loop, respectively. Like active cooling scenarios, the load side pump is turned on or off by the BST thermostat and its flow rate is regulated considering the HP output capacity.

#### 3.2.1. Serial Scenarios

In serial mode (Figure 4) the HP consists of single stage modules, which heat the return water temperature from the bottom of the BST up to a specific set point temperature. The supplementary boiler GB2, which is connected to the BST in series, provides the additional heat up to the grid supply temperature of 45 °C. The maximum volume flow rate from the grid, which is sent from the diverter to the BST, is specified regarding the selected HP capacity for its continuous daily operation during the peak heating day. On the load side, the overall heat pump capacity ($Cap_{HP}$), the temperature shift of the BST ($\Delta T_{BST}$) and the volume of the BST ($Vol_{BST}$) are selected using an optimization approach. Consequently, as the case study is located in a heating-dominated region, GB1 supplies the rest of the overall heating demand, which cannot be supplied by the HP and GB2 optimally.

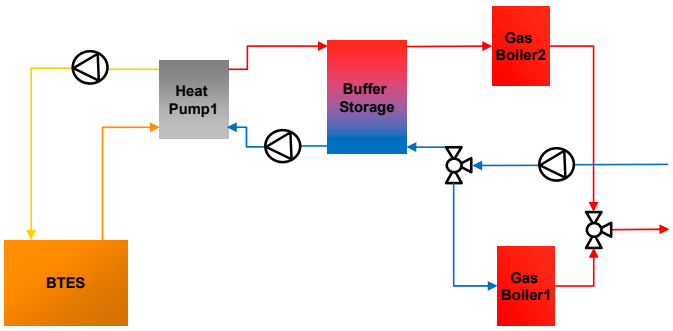


**Figure 4.** System layout of serial heating scenarios.

#### 3.2.2. Parallel Scenarios

The system layout for parallel scenarios is shown in Figure 5. Two serially-connected HPs heat the return fluid from the BST up to the grid supply temperature. The amount of heat which cannot be supplied by the ground loop will be supplied by the gas boiler, which is in parallel operation with the HPs. On the load side, the maximum amount of the return fluid which is sent to the BST, $Cap_{HP}$ and $Vol_{BST}$ are specified with the same strategy as the serial scenario and $\Delta T_{BST}$ is fixed to the grid temperature shift.

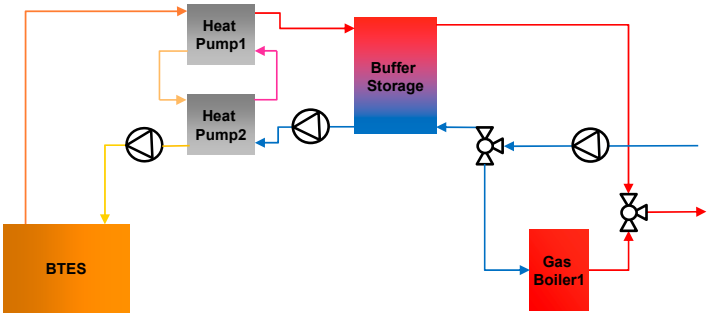


**Figure 5.** System layout of parallel heating scenarios.

A reference scenario is designed based on energetically-efficient conventional systems. In this reference case, the total heating demand is supplied by condensing GBs with a high energetic efficiency of 95% [34] and the whole cooling demand is covered by air-source HPs with a seasonal COP of 4 [35].

## 4. Evaluation Criterion

### *4.1. Exergy Analysis*

As mentioned earlier, exergy is defined as a system's potential to interact with its environment. For thermal systems, this corresponds to the temperature difference between the heat carrier medium and a predefined reference temperature. A variation of the reference temperature does not affect the results of an exergy analysis significantly for systems with higher operating temperatures (e.g., power plants). In contrast, when operation temperatures of a system are close to the reference temperature (e.g., in heating and cooling systems), the results of an exergy analysis strongly depends on the definition of the reference environment [36]. The reference temperature for a steady-state exergy analysis must be chosen as a fixed temperature, such as the seasonal mean temperature or annual mean temperature. For the dynamic analysis, however, several possible reference temperatures like the indoor air temperature, the undisturbed ground temperature and the outdoor temperature are discussed [36]. In this study, the outdoor temperature is considered as the reference temperature. Thermal exergy of a fluid, which can be used for exergy calculations in heating and cooling systems [24], can be calculated using Equation (1). $T_0$ is the reference temperature and is taken as the ambient temperature in this study.

$$\dot{E} = \dot{m} c_p \times ((T - T_0) - T_0 \ln \frac{T}{T_0}) \quad (1)$$

The exergetic efficiency ($\eta_{exergy}$) of a system is the ratio of the output exergy rate ($\dot{E}_{out}$) to the exergy rate of the expended resources ($\dot{E}_{in}$) to generate this output. By integrating $\dot{E}_{in}$ and $\dot{E}_{out}$ into each time step over a system's lifetime ($n_{end}$), its overall average $\eta_{exergy}$ can be calculated (Equation (2)).

$$\eta_{exergy} = \frac{\sum_{n=0}^{n_{end}} \dot{E}_{out,n}}{\sum_{n=0}^{n_{end}} \dot{E}_{in,n}} \times 100\% \quad (2)$$

Dynamic exergy calculation of $\dot{E}_{out}$ and $\dot{E}_{in}$ for the whole system in heating load (HL) and cooling load (CL) supply can be calculated using Equations (3) and (4), respectively.

$$\dot{E}_{out,\,HL} = \begin{cases} \dot{E}_{sply} - \dot{E}_{rtn} & T_0 \le T_{ret} \\ \dot{E}_{sply} & T_{ret} < T_0 \le T_{sup} \\ 0 & T_0 \ge T_{sup} \end{cases} \quad \dot{E}_{in,HL} = \dot{E}_{elec} + \dot{E}_{gas} + \dot{E}_{BTES} \quad (3)$$

$$\dot{E}_{out,\,CL} = \begin{cases} \dot{E}_{sup} - \dot{E}_{ret} & T_0 \ge T_{ret} \\ \dot{E}_{sup} & T_{sup} \le T_0 < T_{ret} \\ 0 & T_0 \le T_{sup} \end{cases} \quad \dot{E}_{in,CL} = \dot{E}_{elec} + \dot{E}_{gas} - \dot{E}_{BTES} \quad (4)$$

where $\dot{E}_{BTES}$ is the exergy which is stored in or extracted from the BTES system during heating and cooling seasons, it can be calculate using Equation (5). $T_b$ denotes the temperature on the boundary where heat transfer ($\dot{Q}_{BTES}$) occurs [9]. As BTES is considered as a component in the DHC grid, it is taken as the average storage temperature.

$$\dot{E}_{BTES} = \dot{Q}_{BTES} \times (1 - \frac{T_0}{T_b}) \quad (5)$$

$\dot{E}_{gas}$, the chemical exergy of natural gas, can be calculated by Equation (6) [37] using the lower heating value (LHV) of natural gas.

$$\dot{E}_{gas} \approx 1.04 \times LHV \quad (6)$$

### 4.2. Economic Analysis

The total expenditures to generate the output consists of capital investment costs ($\dot{C}_{IC}$), maintenance costs ($\dot{C}_{MC}$), fuel costs ($\dot{C}_{f}$) and environmental costs ($\dot{C}_{env}$). By dividing the net present value of the total cost by the discounted total energy output, levelized cost of energy (LCOE) can be calculated using Equation (7) [38]. The system lifetime ($n_{end}$) and the discount rate (i) are assumed to be 30 years and 3%, respectively.

$$\mathrm{LCOE} = \frac{\sum_{n=0}^{n_{end}} \left( \dot{C}_{IC,\,n} + \dot{C}_{MC,\,n} + \dot{C}_{f,n} + \dot{C}_{env,n} \right) \cdot (1+i)^{-n}}{\sum_{n=0}^{n_{end}} \dot{Q}_{out,n} \, (1+i)^{-n}} \times 100\% \tag{7}$$

Investment cost (IC) and maintenance cost (MC) functions of the main components are listed in Table 2. After summing up electricity consumptions ($f_{elec}$) as well as gas consumptions ($f_{gas}$) in each time step over the system lifetime for each simulation, fuel and environmental costs are calculated using Equations (8) and (9). Electricity and gas costs ($c_{elec}$ and $c_{gas}$), Global Warming Potential as a result of the consumption of electricity and gas ($GWP_{elec}$ and $GWP_{gas}$) and the emission costs ($c_{CO2}$) as a function of the assessment year are calculated as given in Table 3.

$$\dot{C}_{f,n} = f_{elec,\,n} c_{elec,n} + f_{gas,\,n} c_{gas,n} \tag{8}$$

$$\dot{C}_{env,n} = f_{elec,\,n} c_{CO2,n} GWP_{elec,n} + f_{gas,\,n} c_{CO2,\,n} GWP_{gas,n} \tag{9}$$

**Table 2.** Cost function of different components.

| Component | Investment Cost Function (€) | Maintenance (€/yr.) | Reference |
|---|---|---|---|
| BTES | $65 \times L_{BHE}$ | - | [39] |
| Property | $75.05 \times A_{Property}$ | - | [40] |
| HP | $(2053.8 \cdot Cap_{HP}{}^{-0.348}) \times Cap_{HP}$ | $0.0075 \times C_{IC}$ | [41] |
| BST | $(130 + 11{,}680 \cdot Vol_{BST}{}^{-0.5545}) \times Vol_{BST}$ | - | [42] |
| GB | $(11{,}418.60 + 64.6115 \cdot Cap_{GB}{}^{0.7978}) \times f_{GB}$ [a] | $0.02 \times C_{IC}$ | [43] |

[a] $f_{GB} = 1.0818 - 8.2898 \cdot 10^{-7}\ Cap_{GB}$.

**Table 3.** Fuel costs, CO2 costs and GWP.

| Parameter | Cost Function 2020–2030 | Cost Function 2030–2050 | Reference |
|---|---|---|---|
| $C_{elec,n}$(€/kWh) | $0.002364n + 0.131$ | $-0.0005n + 0.1625$ | [44,45] |
| $C_{gas,n}$(€/kWh) | $0.00216n + 0.0268$ | $0.00321n + 0.04702$ | [44,45] |
| $c_{CO2,n}$(€/tCO2) | $-0.2083n^2 + 9.072n + 5.553$ | 80 | [46] |
| $GWP_{elec,n}$(tCO2/kWh) | $(-20.99n + 423.89) \times 10^{-6}$ | $(-8.595n + 287.55) \times 10^{-6}$ | [47] |
| $GWP_{gas,n}$(tCO2/kWh) | $250 \times 10^{-6}$ | $250 \times 10^{-6}$ | [48] |

### 4.3. Exergoeconomic Analysis

In every technoeconomic evaluation, the aim is to minimize cost and to maximize the efficiency. Therefore, the two objective functions, Equations (2) and (7), need to be optimized simultaneously. Setup and boundaries of the optimization variables and technical constraints are summarized in Table 4.

$$\begin{array}{ll} \max & \eta_{exergy} \\ \min & \mathrm{LCOE} \end{array}$$

**Table 4.** Ranges of optimization variables and constraints.

| Subject to | Reason |
|---|---|
| $30\ m \leq L_{BHE} \leq 400\ m$ | Length range of shallow BHEs [49] |
| $30 \leq N_{BHE} \leq 1200$ | Heat transfer range of BHEs (W/m), corresponds to $L_{BHE}$ |
| $2\ m \leq S_{BHE} \leq 25\ m$ | Maximum available surface area |
| $50\ kW \leq Cap_{HP} \leq 8150\ kW$ | Minimum capacity of each HP module/Maximum heating load |
| $25\ m^3 \leq Vol_{BST} \leq 10{,}000\ m^3$ | HP min. running time/continuous HP operation in peak load |
| $3\ K \leq \Delta T_{BST}$ [b] $\leq 10\ K$ | Minimum temperature shift of HPs/Grid temperature shift |
| **Constraints** | **Reason** |
| $Rey_{BHE} \geq 2300$ | Minimum Reynolds number for turbulent flow in BHEs |
| $T_{BHE,in} \geq -5\ °C$ | Minimum peak load BHE inlet temperature [49] |

[b] For ActSer and PasSer scenarios.

## 5. Computational Model

The proposed system layouts are modeled and parameterized in TRNSYS 18 [50]. MATLAB [51] is coupled with TRNSYS for multi-objective optimization utilizing the non-dominated sorting genetic algorithm (NSGA II) [52] toolbox.

### *5.1. Multi-Objective Optimization*

The mentioned objective functions and constraints (Section 4.3) are specified in MATLAB. Initial guesses from MATLAB are written into a text file, which is read by TRNSYS. The corresponding values of the objective functions and constrains are calculated in TRNSYS and written into another text file, which is read by MATLAB. The coupling happens once at the beginning and once at the end of each simulation. The algorithm initially tries to find the points, which do not violate the constraints, and assesses the objectives afterwards. This procedure is repeated for each scenario until the best Pareto front, which is the loci of the most optimal solutions, is selected. Figure 6 illustrates the computational model.

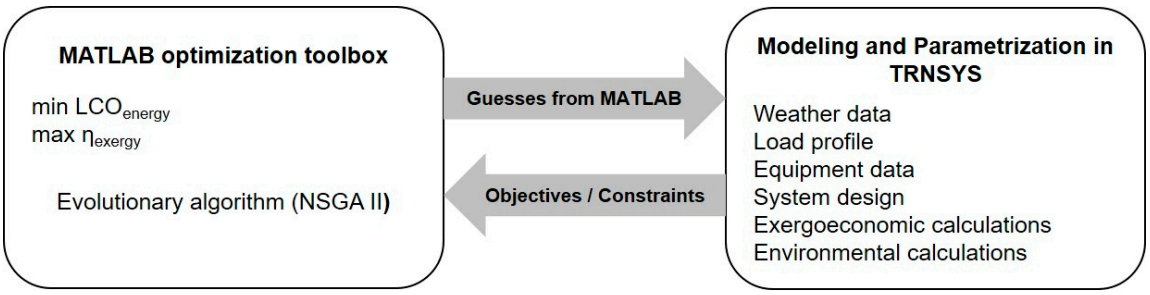


**Figure 6.** Computational model.

### *5.2. System Simulation*

The calculated load profile, as shown Figure 1, is given as a time series to TRNSYS simulation studio. Type 557, which is based on a duct storage model [53], is used for BTES modeling. It can be used to simulate thermally interacting BHEs within a cylindrical storage volume. The validity of Type 557 has already been proven in many practical projects (e.g., [54]). Design parameters (Table 5) are based on standard libraries [49] and location-specific parameters are chosen according to experimental data [55]. The BST is modelled with type 534, which divides the tank's volume into different stratified layers and solves the energy balance equation to calculate a time-dependent temperature change of the fluid inside the tank at different levels. It has also been used for the simulation and validation of similar studies [56–58]. The loss coefficient (Table 5) is based on the data from a manufacturer [59]

and matches practical investigations [54,56]. Types 927 and 1221 are used for simulating single- and double-stage HPs, respectively. According to inlet source- and load-side temperatures and flow rates, output capacity and power consumption of HPs are calculated based on the provided catalog files. The catalogs are chosen so that they can be representative of the operation of common HPs on the market [32,60]. The chosen catalogs are transformed into external files with normalized values, which are read by the HP types and a parametric study was conducted to check the compatibility of the provided files and the original manufacturers' catalogs. Type 700 was used to model the GBs, which are assumed to be condensing gas boilers with a high energetic efficiency of around 95% [34]. Important parameters of the other components including heat exchangers, pumps and thermostats were mainly selected based on manufacturer [30] or experimental [54] data and are illustrated in Table 5.

**Table 5.** Main TRNSYS parameters.

| Component | Parameter | Value | Component | Parameter | Value |
|---|---|---|---|---|---|
| **BTES Type 557** | BHE type | 2U | **HP Type 1221** [c] | 1st stage cooling capacity | 102.9 kW |
| | Boreholes in series | 6 | | 2nd stage cooling capacity | 56.1 kW |
| | Borehole radius | 0.065 m | | 1st stage cooling power | 22.9 kW |
| | Pipe outer/inner radius | 0.016/0.0131 m | | 2nd stage cooling power | 10.2 kW |
| | Pipe thermal conductivity | 0.38 W/m.K | | 1st stage heating capacity | 86.9 kW |
| | BTES thermal conductivity | 2.6 W/m.K | | 2nd stage heating capacity | 49.8 kW |
| | BTES heat capacity | 2080 kJ/m$^3$.K | | 1st stage heating power | 28.9 kW |
| | Grout thermal conductivity | 2 W/m.K | | 2nd stage heating power | 15.1 kW |
| | Fluid specific heat (EG 25%) | 3.811 kJ/kg.K | | | |
| **BST Type 534** | Number of tank nodes | 30 | **HP Type 927** [c] | Cooling capacity | 59.8 kW |
| | Number of ports | 4 | | Cooling power | 13 kW |
| | Aspect ratio | 2.5 | | Heating capacity | 50.6 kW |
| | Loss Coefficient | 0.15 W/m$^2$.K | | Heating power | 18 kW |
| **Pump Type 110** | Total pump efficiency | 60% | **Boiler Type 700** | Efficiency | 95% |
| **Thermostat 106, 113** | Dead band temperature | 0.5 K | **HEX Type 91** | Effectiveness | 0.895 |

[c] Values at rated conditions of the catalog and differ from normalization values.

## 6. Results

Figure 7 displays the area assessed by the optimization algorithm, including points that violate the constraints. As it is expected, the algorithm initially tries to find a minimum, where increasing the efficiency decreases the cost. From that point on, a further increase in efficiency results in higher costs and the algorithm searches for the loci of the points with maximum efficiencies and minimum costs.

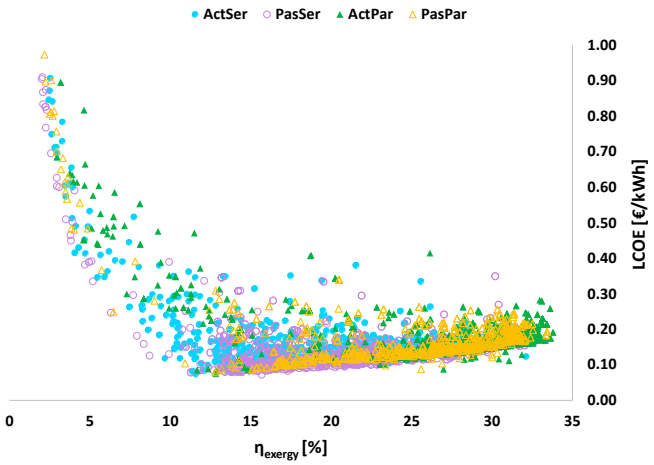


**Figure 7.** The assessed area by the optimization algorithm to find a minimum for each scenario.

### *6.1. Pareto Efficient Solutions*

Figure 8 shows the local evaluations by the algorithm for finding the points which do not violate the constraints. The non-dominated points for each scenario are located on a Pareto front, which is closest to the bottom right corner (Figures 8 and 9). On the Pareto fronts LCOE ranges from aimately 8 to 20 ct/kWh and $\eta_{exergy}$ from 14 to 35%. For the reference scenario those numbers are 6.5 ct/kWh and 12%, respectively.

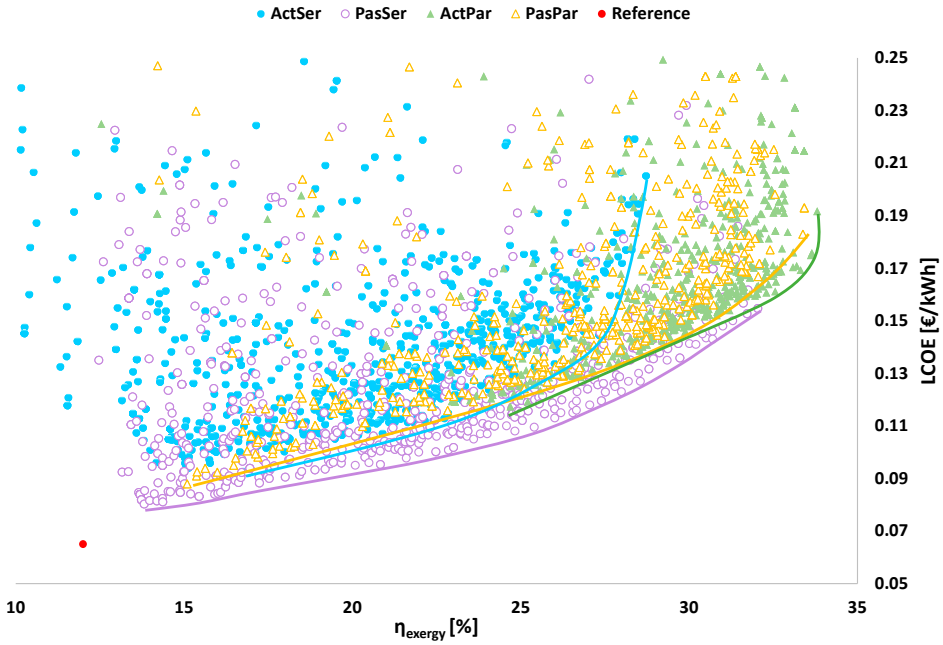


**Figure 8.** Results of local evaluations by the algorithm.

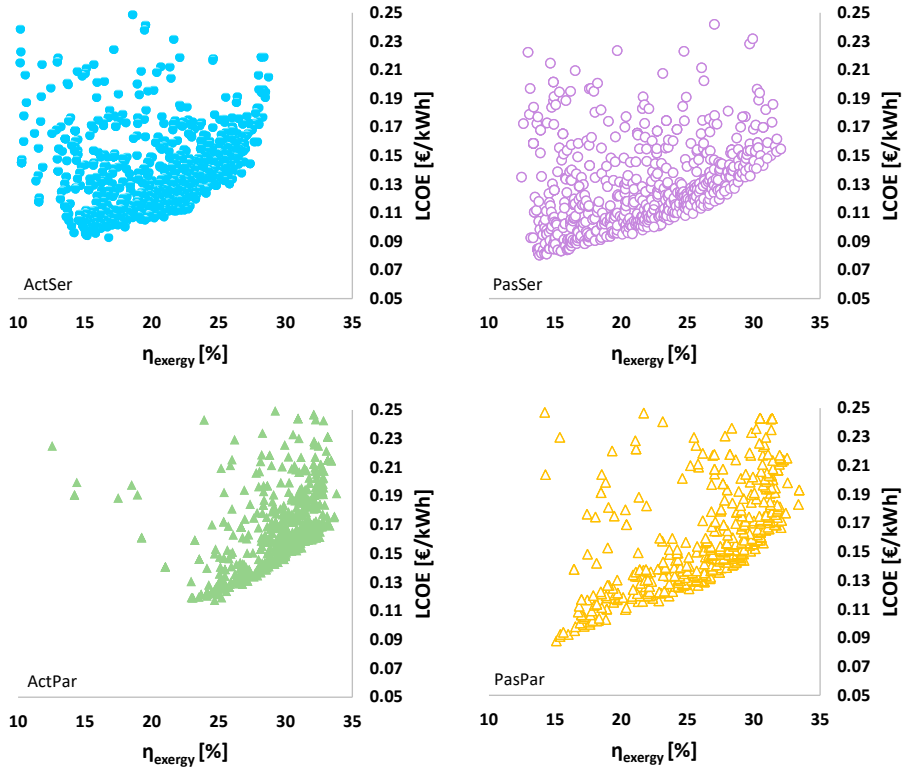


**Figure 9.** Results of local evaluations by the algorithm.

When HPs are designed to cover the whole $\Delta T_{BST}$ i.e., in the serial scenarios, supplying cooling load passively (PasSer) leads to more economical and more efficient designs. This means designs with equal efficiency have lower costs and designs with equal costs are more efficient for the PasSer scenario than for the ActSer scenario. Especially, when it comes to efficiencies higher than approx. 27%, costs for the ActSer scenario show a much steeper increase than the other scenarios.

In contrast, when double stage HPs are connected serially and cover almost half of $\Delta T_{BST}$ i.e., in the parallel scenarios, active cooling (ActPar) is superior to passive cooling (PasPar) for designs with efficiencies higher than approx. 25%. However, for less efficient designs, passive cooling becomes more economical again than active cooling.

When comparing the serial with the parallel connection of HP and GB in heating operation, it is obvious that the parallel scenarios generally are able to reach higher efficiencies than their parallel counterparts with equal cooling mode, while the serial systems are generally advantageous when lower efficiencies are in demand as they reach lower costs.

However, the serial scenario with passive cooling (PasSer) also reaches exergetic efficiencies up to 32% and thus shows the most economical designs for a wide efficiency range, except for the highly efficient design points with exergetic efficiencies over 32%. Here, ActPar scenario becomes beneficial, as it reaches efficiencies up to almost 34%.

The ranges of the selected optimized variables for each scenario are given in Table 6. Scattering plots showing the distribution of the volume of BTES ($Vol_{BTES}$) and $Cap_{HP}$ on the pareto front of each scenario and their effect on the objective functions are illustrated in Figure 10. $Vol_{BTES}$ (Equation (10) [53]) is selected because it gives a relation for three of the main optimization variables including $N_{BHE}$, $L_{BHE}$ and $S_{BHE}$. Consequently, by choosing the mentioned variables from the optimized ranges in Table 6, an optimum design point with a corresponding HP capacity can be selected using Figure 10. Although there are exceptions, it can be generally implied that the increase in $Vol_{BTES}$ as well as $Cap_{HP}$ results in more efficient, but more expensive, design points. Figure 11a shows $Vol_{BTES}$ for the local search of the ActSer scenario and its effect on the objective functions. $\eta_{exergy}$ and LCOE have their optimum values in the middle ranges of the chosen boundaries. Moreover, a higher $\Delta T_{BST}$ (Figure 11b) mainly results in a more efficient and more economical design, with $\eta_{exergy}$ showing a higher sensitivity. The objective functions of the other serial scenario, PasSer, have approx. the same sensitivity to $Vol_{BTES}$ and $\Delta T_{BST}$.

$$Vol_{BTES} = \pi \times N_{BHE} \times L_{BHE} \times (0.525 \times S_{BHE})^2 \quad (10)$$

**Table 6.** Ranges of the optimized solutions on the Pareto fronts.

| Scenario | $L_{BHE}$ [m] | $N_{BHE}$ | $S_{BHE}$ [m] | $Cap_{HP}$ [kW] | $Vol_{BST}$ [$m^3$] | $\Delta T_{BST}$ [K] |
|---|---|---|---|---|---|---|
| ActSer | 95–155 | 294–1194 | 10.7–15.1 | 1264–4400 | 917–6847 | 7.9–9.1 |
| ActPar | 156–200 | 426–924 | 11.4–15 | 2175–4349 | 1260–5630 | - |
| PasSer | 143–169 | 222–1026 | 7.3–11.6 | 809–4097 | 795–6356 | 6.7–9.8 |
| PasPar | 159–224 | 174–1008 | 11.3–14 | 759–4046 | 1459–7045 | - |

For further analysis of the scenarios, three characteristic Pareto efficient designs (further referred to as Characteristic Designs) are chosen for each scenario. These include the most economical, the most efficient and a compromise solution, which is the closest to the corner (Figures 8 and 9). Table 7 lists their most important design parameters as well as the corresponding $\eta_{exergy}$ and LCOE. Bold lines show the most economical and the most efficient layouts overall, which belong to PasSer and ActPar scenarios. The economical, the compromise and the most efficient layouts of each scenario are referred to with ECO, COMP and EFF respectively.

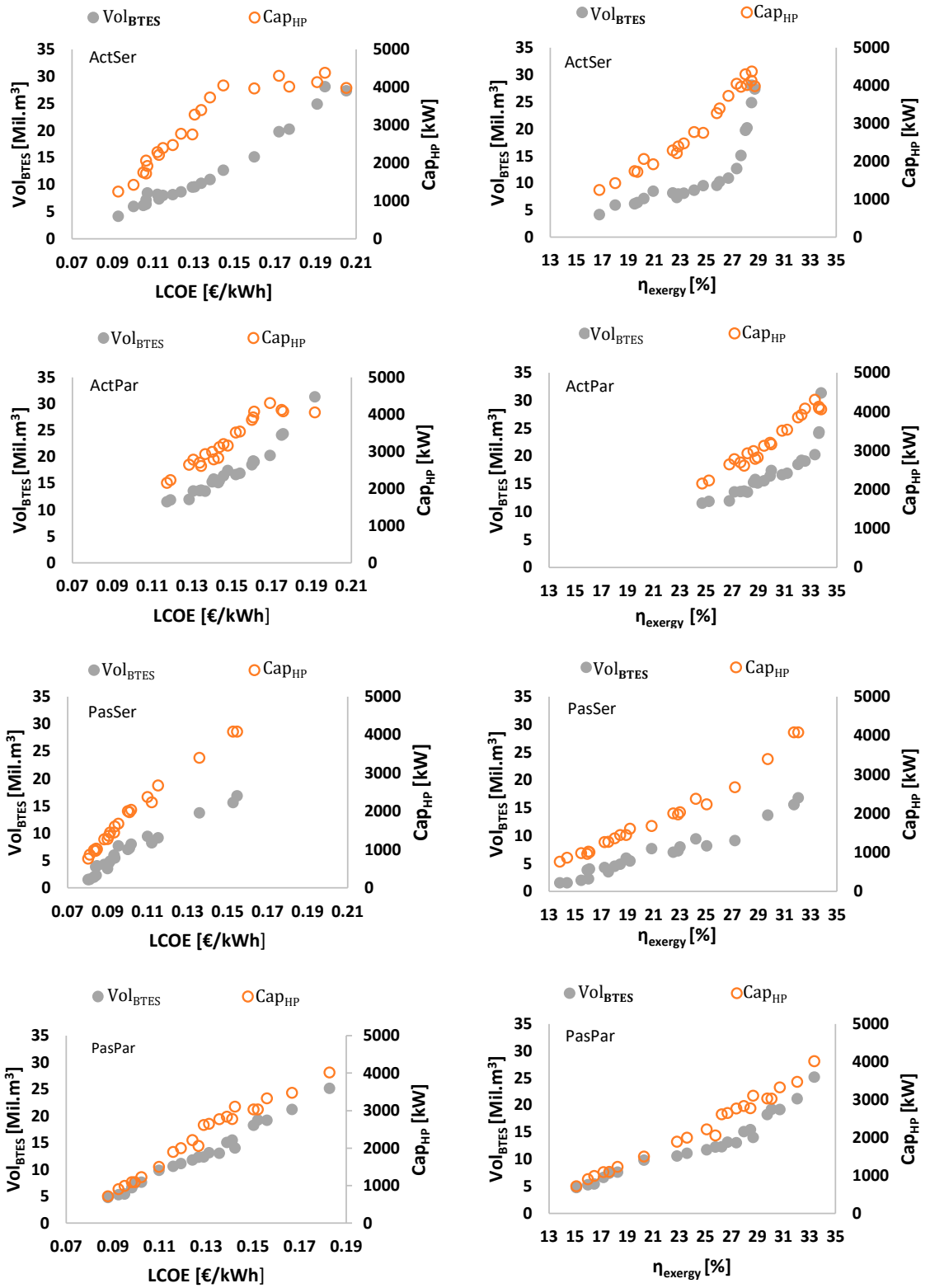


**Figure 10.** Scattering of the decision variables on the Pareto fronts of ActSer, ActPar, PasSer and PasPar scenarios.

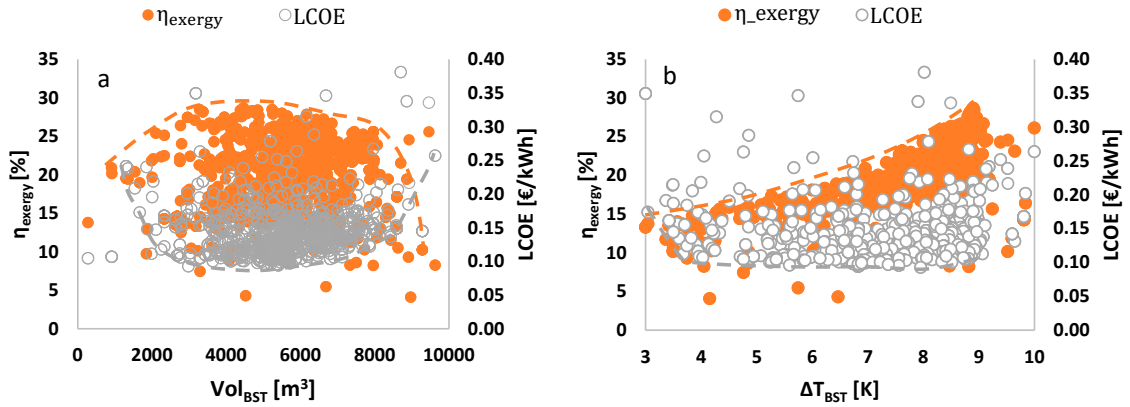


**Figure 11.** Local search for finding optimum ranges of (**a**) $Vol_{BTES}$ and (**b**) $\Delta T_{BST}$ of ActSer scenario.

**Table 7.** The economic, the compromise and the efficient system designs of each scenario.

| Scenario | | LCOE [ct/kWh] | $\eta_{exergy}$ [%] | $L_{BHE}$ [m] | $N_{BHE}$ | $S_{BHE}$ [m] | $Cap_{HP}$ [kW] | $Vol_{BST}$ [$m^3$] | $\Delta T_{BST}$ [K] |
|---|---|---|---|---|---|---|---|---|---|
| ActSer | Economical | 9.27 | 16.77 | 112 | 294 | 12.0 | 1264 | 2989 | 7.95 |
| | Compromise | 12.37 | 24.05 | 116 | 702 | 11.0 | 2782 | 4646 | 8.59 |
| | Most efficient | 19.45 | 28.49 | 136 | 1036 | 15.1 | 4400 | 3281 | 8.91 |
| ActPar | Economical | 11.73 | 24.69 | 190 | 426 | 12.8 | 2175 | 1260 | - |
| | Compromise | 14.37 | 29.42 | 170 | 660 | 12.6 | 3136 | 5420 | - |
| | Most efficient | 19.16 | 33.80 | 175 | 918 | 15.0 | 4097 | 4307 | - |
| PasSer | Economical | 8.02 | 13.81 | 145 | 222 | 7.4 | 809 | 3556 | 6.68 |
| | Compromise | 10.00 | 22.47 | 143 | 480 | 10.9 | 2007 | 3008 | 9.50 |
| | Most efficient | 15.47 | 32.04 | 153 | 942 | 11.6 | 4097 | 4658 | 9.65 |
| PasPar | Economical | 8.79 | 15.10 | 185 | 174 | 12.9 | 758 | 4186 | - |
| | Compromise | 12.66 | 25.78 | 164 | 636 | 11.6 | 2073 | 4007 | - |
| | Most efficient | 18.29 | 33.38 | 162 | 1008 | 13.3 | 4046 | 5128 | - |

### *6.2. Scenario Analysis*

To gain deeper insight into the coherencies of the results and the differences for the four scenarios, the component-wise exergy destruction and loss (Figure 12) and composition of *LCOE* (Figures 13–16) for all 12 Characteristic Designs (cf. Section 6.1.) as well as for the reference case are presented and discussed in the following sections.

#### 6.2.1. Reference Case

As mentioned earlier, for the reference scenario the total heating demand is supposed to be supplied by condensing GBs and the cooling demand by air-source HPs. Therefore, it has one design point and not a pareto front. Despite high energetic efficiency, condensing GBs have a very low exergetic efficiency as natural gas with its high exergy content is converted to generate low exergy heat [18]. The calculated $\eta_{exergy}$ of the condensing GBs and the air-source HPs are 11% and 21%, respectively. Consequently, the calculated overall average $\eta_{exergy}$ is 12% and its corresponding exergy destruction is 240 GWh/30yrs. Moreover, using the cost functions in Tables 2 and 3, the LCOE of the reference scenario is 6.5 ct/kWh. The largest exergy destruction belongs to the most economical design from PasSer scenario and is 197 GWh/30yrs (Figure 12), which is almost 22% lower than the reference case. However, its LCOE is 23.5% higher.

#### 6.2.2. ActSer–Active Cooling and Serial Heating

The total exergy destruction is reduced significantly by moving from the economical to the most efficient point (Figure 12). For the economical design, the highest exergy destruction is from the GBs

followed by the HP. For the compromise solution, these are almost balanced and for the most efficient design, the HP dominates exergy destruction. Exergy destruction of the BST and the BTES show the lowest number compared to the other system components.

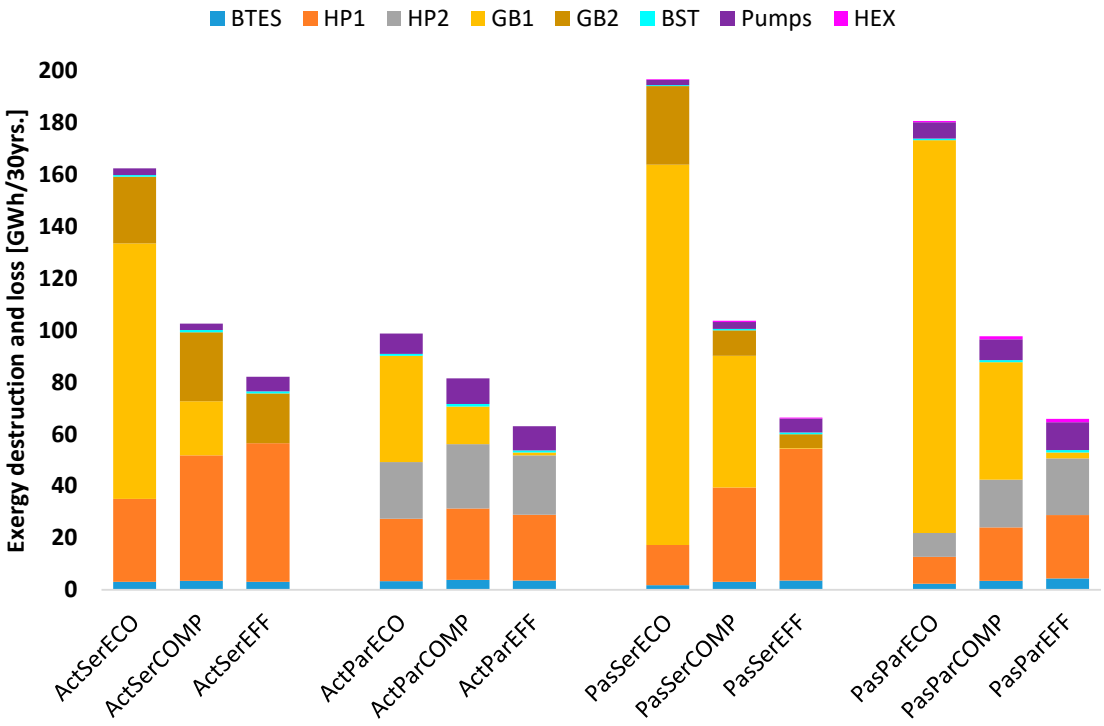


**Figure 12.** Component-wise exergy destruction and loss for the economical (ECO), the compromise (COMP) and the most efficient (EFF) designs in Table 7.

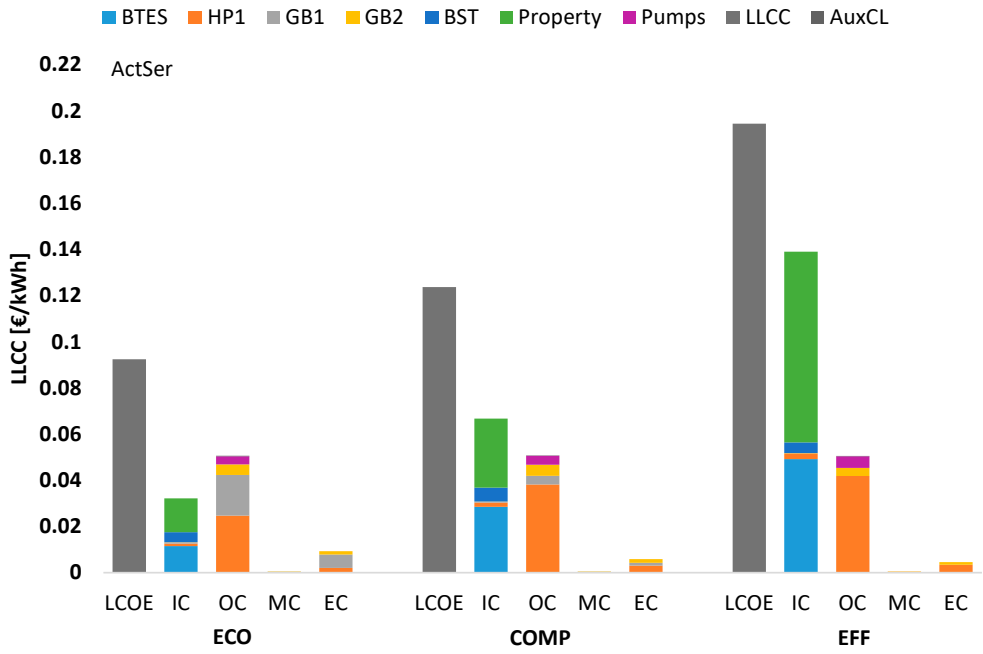


**Figure 13.** Total and component-wise Levelized Life Cycle Cost (LCOE) of ActSer scenario; LCOE is the summation of Initial Cost (IC), Operational Cost (OC), Maintenance Cost (MC) and Emission Cost (EC) for the economical (ECO), the compromise (COMP) and the most efficient (EFF) designs.

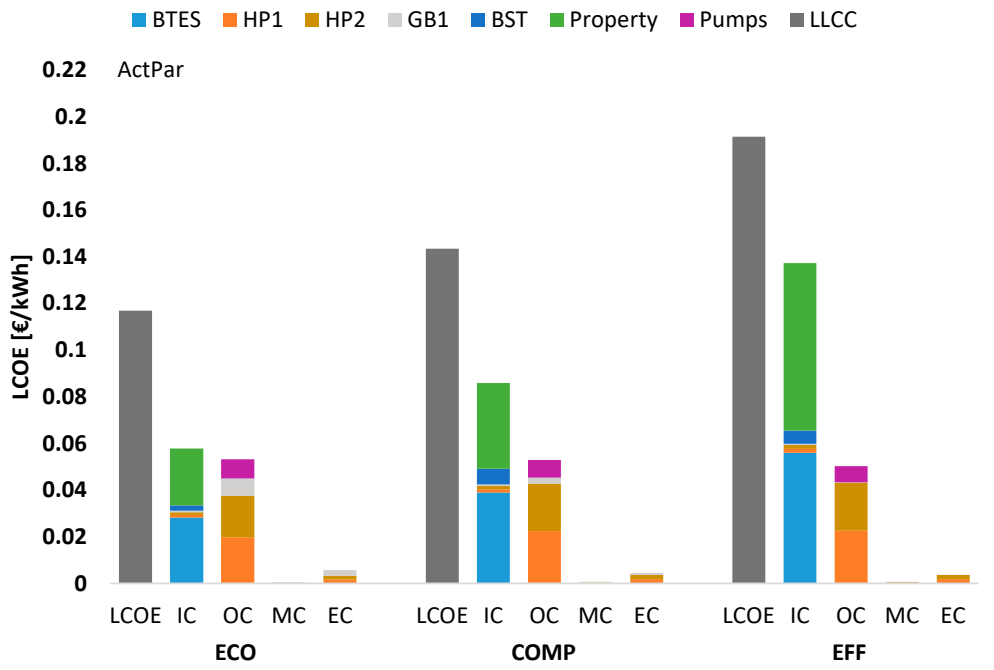


**Figure 14.** Total and component-wise Levelized Life Cycle Cost (LCOE) of ActPar scenario; LCOE is the summation of Initial Cost (IC), Operational Cost (OC), Maintenance Cost (MC) and Emission Cost (EC) for the economical (ECO), the compromise (COMP) and the most efficient (EFF) designs.

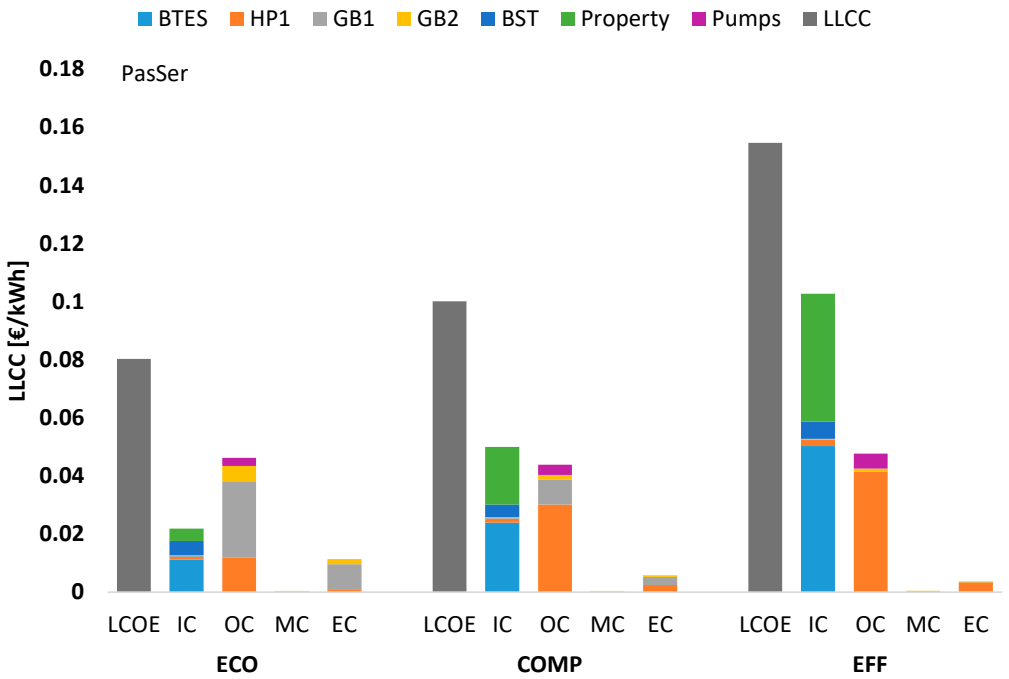


**Figure 15.** Total and component-wise Levelized Life Cycle Cost (LCOE) of PasSer scenario; LCOE is the summation of Initial Cost (IC), Operational Cost (OC), Maintenance Cost (MC) and Emission Cost (EC) for the economical (ECO), the compromise (COMP) and the most efficient (EFF) designs.

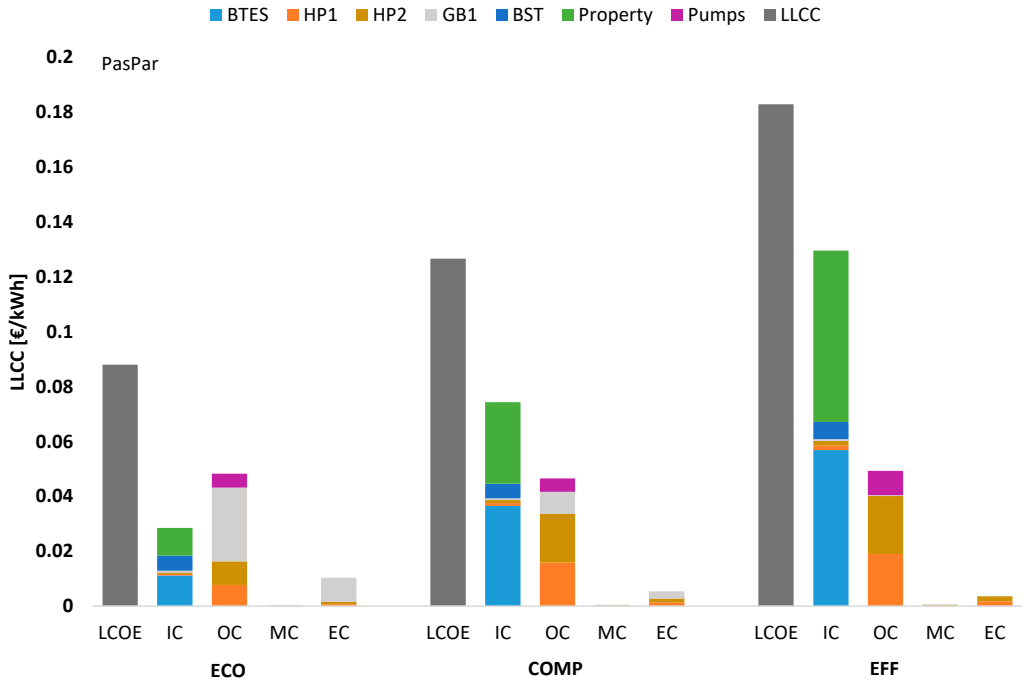


**Figure 16.** Total and component-wise Levelized Life Cycle Cost (LCOE) of PasPar scenario; LCOE is the summation of Initial Cost (IC), Operational Cost (OC), Maintenance Cost (MC) and Emission Cost (EC) for the economical (ECO), the compromise (COMP) and the most efficient (EFF) designs.

Figure 13 shows the LCOE of the Characteristic Designs for the ActSer scenario. For the economical design ICs are lower than OCs. This relation is reversed for the most efficient and compromise designs. It is almost three times higher for the most efficient design. GBs have the lowest share in ICs, even for the economical layout. The largest share is either from the BTES or from the property, which is used for installing the BTES. Combined, they make up more than 94% of the ICs of the most efficient layout. The OCs remain almost the same for all designs, with HPs being the major part for the compromise and the most efficient designs. The power consumption of the pumps is mainly required to circulate the fluid inside the BTES and increases with its size. However, it also depends on $N_{BHE}$, which specifies the design pressure drop that the pump is required to meet. MCs are very low in comparison to the other costs and increase slightly from the economical to the most efficient design point. This is mainly due to the increased HP capacity. The highest ECs can be observed for the economical design and originates from the high share of the GB.

### 6.2.3. ActPar–Active Cooling and Parallel Heating

ActPar scenario comprises the most efficient layout among all the layouts (Figure 8, Table 7). Like for the other scenarios, the most efficient layout has the lowest share of GBs for covering the peak demand and the highest share of HPs in heating load supply. In heating mode, entering temperatures on the BTES side of HP1 are higher than HP2 with lower load side temperatures. In cooling mode, HP1 has lower BTES side and load side temperatures. As HP2 has lower exergy destruction in heating and cooling modes, it can be concluded that the load side temperature has more effect on the exergetic performance of the HPs in the proposed system layout (Figure 12). Increased flow rates are required to maintain the same design temperature difference on both sides of the HPs in comparison to the other scenarios. This results in higher power consumption of the circulating pumps and the associated exergy destruction. Like previous scenarios, the exergy destruction of the BST and the BTES are the lowest in comparison to the other components.

As shown in Figure 14, ICs are higher than OCs for all three Characteristic Designs. The BTES and the property have the highest shares in ICs, followed by the BST. HPs contribute to a high percentage

of OCs, which increases from the economical to the most efficient one because of larger HP capacities. The higher power consumption of the circulating pumps also results in their higher share in OCs, which increases for higher efficiencies. Like previous scenarios, MCs increase and ECs decrease from the economical to the most efficient design.

#### 6.2.4. PasSer–Passive Cooling and Serial Heating

PasSer scenario shows the most economical and least efficient design point of all Characteristic Designs (Table 7). As shown in Figure 12, the highest exergy destruction results from the GBs followed by the HP. Here, due to the passive cooling strategy, the exergy destruction of the HP in cooling mode is omitted and that of the HEX is added, which is the lowest among other components. Overall, HEX, BST and BTES show the lowest share in exergy destruction.

As for the ActSer scenario, OCs remain almost the same for the three design options. ICs are lower than OCs for the economical layout and more than double for the most efficient one. The largest share of ICs is either from the BTES or from the land use, except for the economical design, for which the property costs are much lower than the ICs of the BTES due to the lowest spacing. Like for the ActSer scenario, MCs are negligible and increase with efficiency. The highest ECs can be observed for the economical point and decrease for more efficient systems.

#### 6.2.5. PasPar–Passive Cooling and Parallel Heating

As for all scenarios, the most economical layout has the highest exergy destruction, which decreases from the economical to the most efficient solution (Figure 12). The exergy destruction of the HP in cooling mode is replaced with that of the HEX and increases for larger BTES volumes due to higher flow rates. In accordance with the ActPar scenario, the overall exergy destruction of HP1 is higher than HP2, which implies the importance of load side temperature. The relatively high flow rates of the pumps result in a high share of the overall exergy destruction, which increases from the economical to the most efficient design.

Total and component-wise LCOE of the PasPar scenario are illustrated in Figure 16. The economical layout has a high share of GB in heating load supply. Therefore, the OCs and ECs as a result of gas consumption are approx. 55% and 12% of the LCOE, respectively. The most efficient solution has the largest number of BHEs and the largest spacing of all Characteristic Designs. Consequently, the ICs are the dominating part of the LCOE with a share of above 65%, which is again caused by high costs of the BTES and the associated property. MCs are a minor share and increase from the economical to the most efficient design. ECs make up almost 12% of the LCOE of the economical layout and decrease with increasing efficiency.

### *6.3. Sensitivity Analysis*

#### 6.3.1. Variation of Initial Costs and Energy Costs

In a one-at-a-time sensitivity analysis, effects of 20% variation in ICs and OCs on the LCOE of the Characteristic Designs (cf. Section 6.1.) are assessed (Figure 17). Changing the ICs has a stronger effect than changing OCs for the most efficient designs (gray lines). In contrast to that, the OCs show a higher impact on the LCOE for the economical layouts. By reducing OCs and ICs of the economical point of PasSer scenario by 20%, its LCOE decreases to 7.0 ct/kWh and 7.6 ct/kWh, respectively. Moreover, the influence of varying OCs on LCOE of different scenarios is almost the same for all of the chosen points of each scenario. This is different from varying ICs, which has a higher influence on more efficient layouts with larger BTES volumes and smaller GB capacities.

#### 6.3.2. Changing Heat Pump Type

As mentioned earlier, HPs contribute to a high percentage of exergy destruction and LCOE. In the previous parts of the study, a commonly used standard heat pump type was considered. However,

to capture the effects of increasing HP efficiencies, the HPs of the active scenarios are replaced by a more efficient HP type [61] with a 20% higher nominal COP (Figure 18). As expected, total exergetic efficiency increases and LCOE decreases by using a more efficient HP. This is more pronounced for the most efficient scenarios because of their higher contribution of HPs. For the most efficient point of ActPar scenario, the overall exergetic efficiency increases by 11.2% and the cost decreases by 2.9%. Therefore, using HPs with higher COPs has a larger effect on the exergetic efficiency than on the cost.

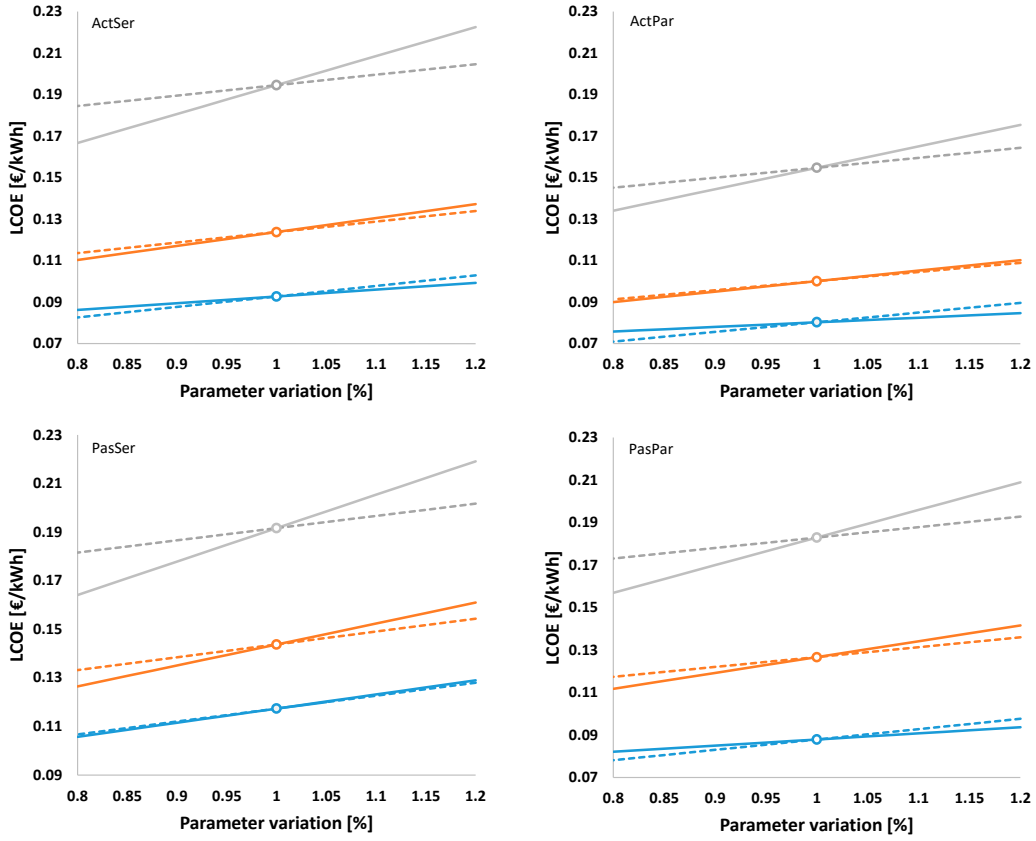


**Figure 17.** Effect of varying ICs (solid lines) and OCs (dash lines) for the economical (blue), the compromise (orange) and the most efficient (gray) designs of ActSer, ActPar, PasSer and PasPar.

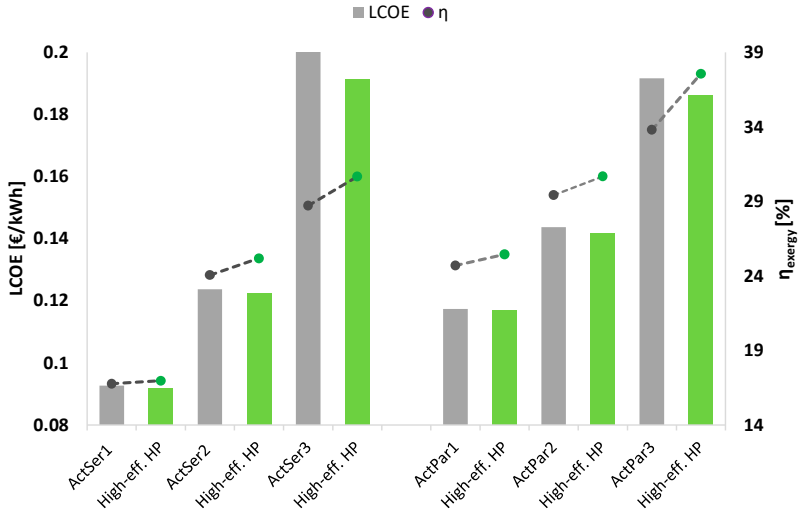


**Figure 18.** Effects of changing HP on LCOE and $\eta_{exergy}$ on the economical (1), the compromise (2) and the most efficient (3) designs of the active scenarios.

### *6.4. Exergy and Global Warming Potential*

Reducing environmental impacts plays a major role in global transition to renewable energies. As mentioned earlier, the LCA method lacks thermodynamic assessment. Moreover, increasing exergy efficiency reduces environmental impacts [19]. To have a rough estimation of how they are related to each other, GWPs of the evaluated system layouts were calculated parallel to the optimization procedure in each simulation run. To assess GWPs, the GWPs associated with electricity and gas consumption are calculated based on the functions in Table 3. The GWP as a result of the production of each system component ($GWP_{prod,n}$) is calculated using available online data [20,62]. Finally, Equation (11) was used for the calculation of each component's GWP and then summed up for the overall GWP of each system layout.

$$GWP = \sum_{n=0}^{n_{end}} GWP_{elec,n} + GWP_{gas,n} + GWP_{prod,n} \quad (11)$$

Results of calculating GWP for different design points of the scenarios and their corresponding exergetic efficiency are illustrated in Figure 19. As expected, an increase in exergetic efficiency leads to a decrease in environmental impacts. This trend can be expressed by a function. Therefore, the exergoeconomic optimization results in system layouts with lower GWP by taking thermodynamic inefficiencies into consideration.

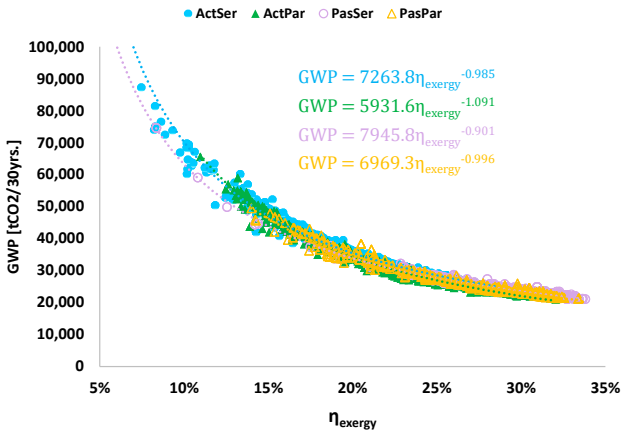


**Figure 19.** Relation between $\eta_{exergy}$ and GWP.

## 7. Discussion

### *7.1. Limitations*

On the one hand, a generic study of a complex system requires many simplifications and assumptions, which has its own drawbacks and may cause uncertainties. On the other hand, implementing too much detail is computationally expensive and may lead to unexpected results, which can prevent the definition of generic rules and guidelines. A proper approach can be conducting a generic study which is followed by detailed assessments, when it comes to practical applications. The following simplifications and assumptions were considered in this study:

- Load scenarios were calculated based on German standards for renovated buildings. Results of this study can provide design guidelines for buildings with different performances as long as they have the same temperature ranges and similar functionalities. The definition of the DHC grid temperature levels were based on the target return temperatures of low-temperature grids. However, due to simplification, the DHC grid configuration and the associated costs and exergy destruction rates are not considered in this study. Future studies, which assess different building types and grid configurations, and consider DHC pipes and circulation pumps as main components of BTES-assisted DHC grids are required for more comprehensive analysis.

- To set up an optimization algorithm according to real HP data within a wide range, it is assumed that the selected HP consists of a number of HP modules with similar performances. However, there is a maximum limit for the number of HP modules to avoid technical issues in practice. Moreover, according to an inquiry from a HP manufacturer, large-scale HPs can be ordered with desired technical specifications which are easily compatible with part-load applications.
- It is assumed that GBs cover the load which cannot be supplied by the ground loop, without considering the effect of part-load ratio on its performance. However, modulating GBs mainly have a minimum turn-down ratio, which specifies the minimum acceptable part-load ratio. For a more detailed assessment the boiler and the combustion efficiencies need to be provided as a function of entering liquid temperature and device part-load ratio.
- The selected BST volume by the optimization algorithm is allocated to one tank with an aspect ratio (the ratio of height to diameter) of 2.5, according to an estimation regarding an efficient design as well as the maximum acceptable tank height for large-scale applications. Splitting the selected volume into multiple tank units with different aspect ratios can be considered as a future study.
- The project lifetime is considered to be 30 years. Approx. 2000 evaluations, each taking around 20 min, were required for the initial convergence of the optimization algorithm. Consequently, a time step of one hour was considered for the simulations. However, a more detailed assessment required shorter time steps down to a few minutes, which also enables an application of more exact control strategies. The optimization always results in better solutions with shorter time steps and a larger number of evaluations.
- The heat transfer mechanism of the BTES is considered to be conductive. It is also assumed that BTES is installed in the ground with a uniform thermal conductivity and heat capacity. However, in real geothermal applications convective heat transfer might exist and ground thermal characteristics might not be uniform. Moreover, there are always regional limitations for the implementation of large-scale geothermal projects, e.g., unfavorable subsurface conditions or restrictions due to groundwater protection.
- The IC functions (Table 2) are based on the available literature, which are mainly defined by having data from real projects in a specific range. However, due to the large ranges of the optimization boundaries, it is assumed that extrapolation is acceptable. Regarding OCs (Table 3), energy cost functions are specified by the predicted costs from the economic studies for the years 2030 and 2050 and assuming a linear interpolation between the available data points. Similar assumptions have been made for the environmental emissions and the associated costs. Consequently, cost functions are subject to large uncertainties and the sensitivity analysis was done with the purpose of lowering these uncertainties.

### *7.2. Discussion of Results*

The PasSer scenario shows the most economical designs for a wide efficiency range of up to 32%. This can be explained by the passive cooling strategy, which leads to an omission of HPs that are usually responsible for significant amounts of exergy destruction and high OCs. Moreover, lower pumping power, due to covering the whole heating temperature shift in serial scenarios, overcompensates higher COPs in parallel scenarios because of lower temperature shifts by HPs.

For the highly efficient designs with exergetic efficiencies over 32%, ActPar scenarios show the best results. Large values for both $Cap_{HP}$ and $Vol_{BTES}$ are needed to reach such high exergetic efficiencies. Consequently, higher COPs of HPs in parallel scenarios have a larger impact and overcompensate lower power consumption of circulation pumps in serial scenarios. However, in cooling mode, a higher power consumption of the pumps due to the lower temperature shift on BTES side has a slightly higher share in inefficiencies and losses.

For the serial scenarios (Figure 11), higher $\Delta T_{BST}$ mainly results in a more efficient and more economical design, with $\eta_{exergy}$ showing a higher sensitivity. This indicates that the improved

performance of the BST, due to better stratification and less mixing losses, overcompensates the lower COPs of the HPs due to higher temperature shifts. Therefore, the algorithm favors scenarios with higher values for $\Delta T_{BST}$.

The optimization of the serial layouts leads to the maximum possible temperature shift of the grid by the HPs, which makes them similar to the HPs in parallel scenarios. However, due to weaker performance of HPs for covering high temperature shifts, $\eta_{exergy}$ does not exceed 28.5% with a LCOE of 19.45 ct/kWh for ActSer scenario. This corresponds to a layout in which GB1 is omitted and the supplementary load is supplied by GB2 serially. A Pareto efficient design point of the ActPar scenario with the same $\eta_{exergy}$ has an LCOE of 13.86 ct/kWh. Therefore, to move towards more economical points in the serial scenarios, both GBs are required, and a splitter sends the fluid to either the HPs and GB2 or to the GB1. The GB1 has a share between 0 and 49% of the total heating demand on the Pareto front of the ActSer scenario. Similarly, for the PasSer scenario, the point with the highest $\eta_{exergy}$ of 32% has LCOE of 15.5 ct/kWh with the highest share of HPs and GB2. Reducing this share on the Pareto front results in more economical and less efficient points with an increased share of GB1 up to 60%.

As mentioned earlier, HPs contribute to a high share of exergy destruction as well as OCs, especially for the most efficient scenarios. For the same design, two HPs, each of which cover parts of the heat demand, have lower exergy destruction and power consumption than one HP covering all of it. However, the pumping power that is required for circulating the fluid on both sides of the serially-connected HPs as well as the associated exergy destruction and OCs are much higher. Therefore, a suitable HP for integrating BTES systems is the one that can provide the highest temperature change with the lowest power consumption as well as the minimum possible flow rates.

The design flow rate also has a high influence on heat transfer characteristics on the BTES side. Higher flow rates lead to better convective heat transfer from the circulating fluid to the ground. Therefore, definition of the optimum flow rate on the BTES side and the characteristics of the most efficient corresponding HP is proposed as a future study.

As indicated in Figure 9, an increase of $Vol_{BTES}$ yields in a higher $\eta_{exergy}$ as well as higher LCOE. $L_{BHE}$ and $S_{BHE}$ are mainly selected from the middle ranges of the specified boundaries by the optimization algorithm, with maximum amounts of 220 m and 15 m, respectively. $N_{BHE}$ has the widest range which varies between 15% and 85% of the maximum boundary from the most economical to the most efficient point. Therefore, it can be implied that $N_{BHE}$ has the highest influence on the objective functions. The number of BHEs in series has a high effect on the distribution of BHEs in a BTES with a specific volume, the flow rate per BHE and the circulating pump's power. In this study it was taken as 6, like for many installed BTES systems [63]. Therefore, for a future study, taking it as an additional optimization variable could result in more efficient design points.

Cooling-based BTES systems recover the rejected heat from cooling cycles seasonally for an efficient design. In heating-dominated regions, the amount of extracted heat is much more than the stored heat and the dominating mechanism equals that of conventional geothermal HPs. Consequently, similar cost incentives to geothermal HPs in the household sector [64] need to be considered for DHC grids of such regions, in order to be more cost-competitive with fossil-based systems with low exergetic efficiencies and high GWPs.

## 8. Conclusions

A dynamic exergoeconomic optimization method is used for detailed evaluation of the proposed layouts for integrating BTES systems into 4th generation DHC grids in heating-dominated regions. Based on the results of this study, the following general conclusions can be drawn:

- In cooling mode, passive strategy yields to a high share of the optimized designs from the most economical up to highly efficient ones. Active cooling with serially-connected heat pumps results in a small share of the optimized designs, which are the most efficient but the most expensive ones.
- In heating mode, maximizing the heating temperature shift by single HPs and supplying the remaining shift up to the grid supply temperature by serially-connected GBs yields to a high

percentage of the optimized designs. However, in the most economical design, the maximum 40% of the overall heating share are supplied by this configuration and the rest is met by parallel-operating GBs. The share increases up to 100% for more efficient designs.

- The most efficient but most expensive designs are resulted from covering nearly the overall heating demand on the grid temperature shift by serially-connected HPs and supplying only the peak loads by GBs.
- Larger BTES volumes and corresponding HP capacities mainly result in more efficient designs with higher costs. However, less efficient and more economical designs have higher capacities of GBs. The highest share of exergy destruction comes from HPs for the most efficient and from GBs for the least efficient designs. BTES, BST and HEX have the lowest exergy destruction for all Pareto efficient layouts.
- For the most efficient designs ICs significantly exceed OCs. While the largest share of ICs arises either from the BTES itself or from the property, which is used for building it, the highest share in OCs originates from the HPs. Nevertheless, for the most economical designs, OCs usually exceed ICs. For all layouts, ECs decrease from the most economical to the most efficient designs while MCs increase.
- GWPs decrease with increasing exergetic efficiency and their relation can be expressed with a function. Therefore, by conducting exergoeconomic analysis, thermodynamic inefficiencies as well as environmental impacts are improved. By considering GWPs and LCOE as objective functions and comparing the results with the optimized results of this study, further relations between LCA and exergoeconomic analysis and their application for optimization problems can be specified.

The results of this study can be used to design 4th generation DHC grids and to assess the transition of old generation to low-temperature grids utilizing BTES systems. In future, the same method will be used for the evaluation of integrating BTES systems into 4th generation solar DHC grids.

**Author Contributions:** Conceptualization, H.H., J.F., B.W., D.O.S. and I.S.; methodology, H.H; original draft preparation, H.H.; review and editing, B.W., J.F., I.S., D.O.S. and H.H.; visualization, H.H.; supervision, D.O.S., B.W. and I.S.; funding acquisition, I.S. All authors have read and agreed to the published version of the manuscript.

**Funding:** This work was financially supported by the German Research Foundation (DFG) in the framework of the Excellence Initiative, Darmstadt Graduate School of Excellence Energy Science and Engineering (GSC 1070) and the Open Access Publishing Fund of Technical University of Darmstadt.

**Conflicts of Interest:** The authors declare no conflict of interest.

## Nomenclature

| | |
|---|---|
| ActSet | active serial |
| ActPar | active parallel |
| BHE | borehole heat exchanger |
| BST | buffer storage tank |
| BTES | borehole thermal energy storage |
| COMP | compromise |
| DC | district cooling |
| DH | district heating |
| DHC | district heating and cooling |
| ECO | economical |
| EFF | efficient |
| GB | gas boiler |
| HP | heat pump |
| NSGA | non-dominated sorting genetic algorithm |
| PasSer | passive serial |
| PasPar | passive parallel |

**Symbols**

| | | |
|---|---|---|
| A | area | $m^2$ |
| c | specific heat capacity | kJ/(kg K) |
| c | specific cost | €/$tCO^2$, €/kWh |
| $\dot{C}$ | cost rate | €/yr. |
| Cap | capacity | kW |
| EC | emission cost | €/kWh |
| $\dot{E}$ | thermal exergy rate | kW |
| GWP | global warming potential | $CO^2$/kWh |
| i | discount rate | % |
| IC | initial cost | €/kWh |
| L | length | m |
| LHV | lower heating value | kW |
| LCOE | levelized cost of energy | €/kWh |
| $\dot{m}$ | flow rate | kg/s |
| MC | maintenance cost | €/kWh |
| OC | operational cost | €/kWh |
| n | year | |
| N | number | |
| Rey | Reynolds number | |
| S | spacing | m |
| T | temperature | °C |
| Vol | Volume | $m^3$ |
| f | fuel consumption | kWh |
| $\dot{Q}$ | heat flux | kW |
| η | efficiency | % |

**Subscripts**

| | |
|---|---|
| BHE | borehole heat exchanger |
| BST | buffer storage tank |
| BTES | borehole thermal energy storage |
| CL | cooling load |
| elec | electricity |
| env | environmental |
| f | fuel |
| HL | heating load |
| IC | initial cost |
| MC | maintenance cost |
| prod | production |
| ret | return |
| sup | supply |
| 0 | reference |
| b | boundary |

## References


1. Fleiter, T.; Steinbach, J.; Ragwitz, M.; Dengler, J.; Köhler, B.; Reitze, F.; Tuille, F.; Hartner, M.; Kranzl, L.; Forthuber, S. *Mapping and Analyses of the Current and Future (2020–2030) Heating/Cooling Fuel Deployment (Fossil/Renewables)*; European Commission, Directorate-General for Energy: Brussel, Belgium, 2016.
2. Werner, S. European space cooling demands. *Energy* **2016**, *110*, 148–156. [CrossRef]
3. United Nations Department of Economics and Social Affairs, Population Division. *World Urbanization Prospects: The 2014 Revision*; United Nations Department of Economics and Social Affairs, Population Division: New York, NY, USA, 2015; p. 41.
4. Rezaie, B.; Rosen, M.A. District heating and cooling: Review of technology and potential enhancements. *Appl. Energy* **2012**, *93*, 2–10. [CrossRef]
5. Werner, S. International review of district heating and cooling. *Energy* **2017**, *137*, 617–631. [CrossRef]

6. Lund, H.; Werner, S.; Wiltshire, R.; Svendsen, S.; Thorsen, J.E.; Hvelplund, F.; Mathiesen, B.V. 4th Generation District Heating (4GDH): Integrating smart thermal grids into future sustainable energy systems. *Energy* **2014**, *68*, 1–11. [CrossRef]
7. Schulte, D.O.; Rühaak, W.; Oladyshkin, S.; Welsch, B.; Sass, I. Optimization of medium-deep borehole thermal energy storage systems. *Energy Technol.* **2016**, *4*, 104–113. [CrossRef]
8. Skarphagen, H.; Banks, D.; Frengstad, B.S.; Gether, H. Design considerations for Borehole Thermal Energy Storage (BTES): A review with emphasis on convective heat transfer. *Geofluids* **2019**, *2019*, 4961781. [CrossRef]
9. Welsch, B.; Ruehaak, W.; Schulte, D.O.; Baer, K.; Sass, I. Characteristics of medium deep borehole thermal energy storage. *Int. J. Energy Res.* **2016**, *40*, 1855–1868. [CrossRef]
10. Schulte, D.O.; Welsch, B.; Boockmeyer, A.; Rühaak, W.; Bär, K.; Bauer, S.; Sass, I. Modeling insulated borehole heat exchangers. *Environ. Earth Sci.* **2016**, *75*, 910. [CrossRef]
11. Bär, K.; Rühaak, W.; Welsch, B.; Schulte, D.; Homuth, S.; Sass, I. Seasonal high temperature heat storage with medium deep borehole heat exchangers. *Energy Procedia* **2015**, *76*, 351–360. [CrossRef]
12. Sibbitt, B.; McClenahan, D.; Djebbar, R.; Thornton, J.; Wong, B.; Carriere, J.; Kokko, J. The performance of a high solar fraction seasonal storage district heating system–five years of operation. *Energy Procedia* **2012**, *30*, 856–865. [CrossRef]
13. Bauer, D.; Marx, R.; Nußbicker-Lux, J.; Ochs, F.; Heidemann, W.; Müller-Steinhagen, H. German central solar heating plants with seasonal heat storage. *Sol. Energy* **2010**, *84*, 612–623. [CrossRef]
14. Dincer, I.; Rosen, M. A unique borehole thermal storage system at University of Ontario Institute of Technology. In *Thermal Energy Storage for Sustainable Energy Consumption*; Springer: Dordrecht, The Netherlands, 2007; pp. 221–228.
15. Lanahan, M.; Tabares-Velasco, P.C. Seasonal thermal-energy storage: A critical review on BTES systems, modeling, and system design for higher system efficiency. *Energies* **2017**, *10*, 743. [CrossRef]
16. Formhals, J.; Hemmatabady, H.; Welsch, B.; Schulte, D.O.; Sass, I. A modelica toolbox for the simulation of borehole thermal energy storage systems. *Energies* **2020**, *13*, 2327. [CrossRef]
17. Welsch, B.; Rühaak, W.; Schulte, D.O.; Formhals, J.; Bär, K.; Sass, I. Co-simulation of geothermal applications and HVAC systems. *Energy Procedia* **2017**, *125*, 345–352. [CrossRef]
18. Bejan, A.; Tsatsaronis, G.; Moran, M.J. *Thermal Design and Optimization*; John Wiley & Sons: New York, NY, USA, 1995.
19. Nuss, P. *Life Cycle Assessment Handbook: A Guide for Environmentally Sustainable Products*; Curran, A.M., Ed.; John Wiley & Sons, Inc.: Hoboken, NJ, USA; Scrivener Publishing LLC: Salem, MA, USA, 2015.
20. Welsch, B.; Göllner-Völker, L.; Schulte, D.O.; Bär, K.; Sass, I.; Schebek, L. Environmental and economic assessment of borehole thermal energy storage in district heating systems. *Appl. Energy* **2018**, *216*, 73–90. [CrossRef]
21. Karasu, H.; Dincer, I. Life cycle assessment of integrated thermal energy storage systems in buildings: A case study in Canada. *Energy Build.* **2020**, *217*, 109940. [CrossRef]
22. Kizilkan, O.; Dincer, I. Borehole thermal energy storage system for heating applications: Thermodynamic performance assessment. *Energy Convers. Manag.* **2015**, *90*, 53–61. [CrossRef]
23. Kizilkan, O.; Dincer, I. Exergy analysis of borehole thermal energy storage system for building cooling applications. *Energy Build.* **2012**, *49*, 568–574. [CrossRef]
24. Sayadi, S.; Tsatsaronis, G.; Morosuk, T. Dynamic exergetic assessment of heating and cooling systems in a complex building. *Energy Convers. Manag.* **2019**, *183*, 561–576. [CrossRef]
25. Klein, S.; Beckman, W.; Mitchell, J.; Duffie, J.; Duffie, N.; Freeman, T.; Mitchell, J.; Braun, J.; Evans, B.; Kummer, J. *Trnsys 18—Volume 6 Multizone Building Modeling with Type 56 and Trnbuild*; Solar Energy Laboratory, University of Wisconsin: Madison, WI, USA, 2017; p. 199.
26. DIN4108. *Thermal Protection and Energy Economy in Buildings-Part 2: Minimum Requirements to Thermal Insulation*; Beuth Verlag: Berlin, Germany, 2013.
27. Merkblatt, S. *Raumnutzungsdaten für die Energie-und Gebäudetechnik*; SIA: Zürich, Switzerland, 2015.
28. Meteotest. Meteonorm: Irradiation Data for Every Place on Earth. Available online: http://www.meteonorm.com/ (accessed on 12 August 2020).
29. Nussbaumer, T. *Planungshandbuch Fernwärme*; EnergieSchweiz, Bundesamt für Energie: Bern, Switzerland, 2017.
30. Viessmann GmbH. Available online: www.viessmann.de (accessed on 12 August 2020).

31. Gautschi, T. *Anergienetze in Betrieb*; Städtische Wärmewende: Wien, Austria, 2015.
32. Waterfurnace Co. Available online: https://www.waterfurnace.com/commercial/products/water-source-geothermal-heat-pumps/ (accessed on 12 August 2020).
33. Karim, A.; Burnett, A.; Fawzia, S. Investigation of stratified thermal storage tank performance for heating and cooling applications. *Energies* **2018**, *11*, 1049. [CrossRef]
34. Viessmann GmbH. Available online: https://www.viessmann.de/de/wohngebaeude/gasheizung/vitocrossal.html (accessed on 12 August 2020).
35. Viessmann GmbH. Available online: https://www.viessmann.de/de/wohngebaeude/hybridheizung/gas-hybridgeraete/vitocal-250-s.html (accessed on 12 August 2020).
36. Sayadi, S.; Tsatsaronisb, G.; Morosuk, T. A New Approach for Applying Dynamic Exergy Analysis and Exergoeconomics to a Building Envelope. Available online: https://pdfs.semanticscholar.org/e5d6/e5929d68b7d153f590d8d8e113ee1e86993b.pdf (accessed on 24 August 2020).
37. Bargel, S. Entwicklung eines exergiebasierten Analysemodells zum umfassenden Technologievergleich von Wärmeversorgungssystemen unter Berücksichtigung des Einflusses einer veränderlichen Außentemperatur. Ph.D. Thesis, Ruhr-Universität Bochum, Universitätsbibliothek, Bochum, Germany, 2011.
38. Short, W.; Packey, D.J.; Holt, T. *A Manual for the Economic Evaluation of Energy Efficiency and Renewable Energy Technologies*; National Renewable Energy Lab.: Golden, CO, USA, 1995.
39. Luo, J.; Rohn, J.; Bayer, M.; Priess, A. Thermal performance and economic evaluation of double U-tube borehole heat exchanger with three different borehole diameters. *Energy Build.* **2013**, *67*, 217–224. [CrossRef]
40. Statistisches Bundesamt. Available online: https://www.destatis.de/DE/Home/_inhalt.html (accessed on 12 August 2020).
41. Croteau, R.; Gosselin, L. Correlations for cost of ground-source heat pumps and for the effect of temperature on their performance. *Int. J. Energy Res.* **2015**, *39*, 433–438. [CrossRef]
42. Mauthner, F.; Herkel, S. Technology and Demonstrators-Technical Report Subtask C–Part C1-C1: Classification and Benchmarking of Solar Thermal Systems in Urban Environments. Available online: http://task52.iea-shc.org/data/sites/1/publications/IEA-SHC-Task52-STC1-Classification-and-benchmarking-Report-2016-03-31.pdf (accessed on 24 August 2020).
43. Gebhardt, M.; Kohl, H.; Steinrötter, T. *Preisatlas, Ableitung von Kostenfunktionen für Komponenten der rationellen Energienutzung*; Institut für Energie und Umwelttechnik eV (IUTA): Duisburg-Rheinhausen, Germany, 2002; pp. 1–356.
44. Bundesamt, S. Preise–Daten zur Energiepreisentwicklung. Available online: https://www.destatis.de/DE/Themen/Wirtschaft/Preise/Publikationen/Energiepreise/energiepreisentwicklung-pdf-5619001.pdf?__blob=publicationFile (accessed on 24 August 2020).
45. Schlesinger, M.; Hofer, P.; Kemmler, A.; Kirchner, A.; Koziel, S.; Ley, A.; Piégsa, A.; Seefeldt, F.; Straßburg, S.; Weinert, K. Entwicklung der Energiemarkte-Energiereferenzprognose: Studie im Auftrag des Bundesministeriums für Wirtschaft und Technologie. Available online: https://www.bmwi.de/Redaktion/DE/Publikationen/Studien/entwicklung-der-energiemaerkte-energiereferenzprognose-endbericht.html (accessed on 24 August 2020).
46. German Federal Government. *German Federal Government (2019): Climate Action Programme 2030*; German Federal Government: Berlin, Germany, 2019.
47. Fritsche, U.R.; Greß, H.-W. *Der nicht erneuerbare kumulierte Energieverbrauch und THG-Emissionen des deutschen Strommix im Jahr 2016 sowie Ausblicke auf 2020 bis 2050*; Internationales Institut für Nachhaltigkeitsanalysen und-strategien GmbH (IINAS): Darmstadt, Germany, 2018.
48. *IINAS (2017): GEMIS-Globales Emissions-Modell Integrierter Systeme-Model and Database*; International Institute for Sustainability Analysis and Strategy: Darmstadt, Germany, 2017.
49. VDI. *VDI 4640 Thermal Use of the Underground. VDI-Gesellschaft Energie und Umwelt (GEU)*; Beuth Verlag: Berlin, Germany, 2019.
50. Klein, S.; Beckman, W.; Mitchell, J.; Duffie, J.; Duffie, N.; Freeman, T.; Mitchell, J.; Braun, J.; Evans, B.; Kummer, J. *TRNSYS 18–A TRaNsient System Simulation Program, User Manual*; Solar Energy Laboratory, University of Wisconsin-Madison: Madison, WI, USA, 2017.
51. *MATLAB. 9.2.0.556344 (R2017a)*, The MathWorks Inc.: Natick, MA, USA, 2017.
52. Deb, K.; Pratap, A.; Agarwal, S.; Meyarivan, T. A fast and elitist multiobjective genetic algorithm: NSGA-II. *IEEE Trans. Evol. Comput.* **2002**, *6*, 182–197. [CrossRef]

53. Hellstrom, G. Ground Heat Storage: Thermal Analyses of Duct Storage Systems. Ph.D. Thesis, Lund University, Lund, Sweden, 1991.
54. Mesquita, L.; McClenahan, D.; Thornton, J.; Carriere, J.; Wong, B. Drake Landing Solar Community: 10 Years of Operation. In Proceedings of the ISES Conference Proceedings, Abu Dhabi, UAE, 11 February 2017; pp. 1–12.
55. Bär, K.; Arndt, D.; Fritsche, J.-G.; Götz, A.E.; Kracht, M.; Hoppe, A.; Sass, I. 3D-Modellierung der tiefengeothermischen Potenziale von Hessen–Eingangsdaten und Potenzialausweisung [3D modelling of the deep geothermal potential of the Federal State of Hesse (Germany)–input data and identifi cation of potential. *Z. Dtsch. Ges. Geowiss.* **2011**, *162*, 371–388.
56. Renaldi, R.; Friedrich, D. Techno-economic analysis of a solar district heating system with seasonal thermal storage in the UK. *Appl. Energy* **2019**, *236*, 388–400. [CrossRef]
57. Allard, Y.; Kummert, M.; Bernier, M.; Moreau, A. Intermodel comparison and experimental validation of electrical water heater models in TRNSYS. In Proceedings of the Building Simulation, Sydney, Australia, 14 November 2011; pp. 688–695.
58. Baldwin, C.; Cruickshank, C.A. Using TRNSYS types 4, 60, and 534 to model residential cold thermal storage using water and water/glycol solutions. In Proceedings of the IBPSA-Canada's eSim Conference, Hamilton, ON, Canada, 3–6 May 2016; pp. 335–348.
59. LIPP GmbH. Available online: https://www.lipp-system.de/tanks/thermal-storage-tanks (accessed on 12 August 2020).
60. Trane Co. Available online: https://www.trane.com/commercial/north-america/us/en/products-systems/equipment/unitary/water-source-heat-pumps.html (accessed on 12 August 2020).
61. Viessmann GmbH. Available online: https://www.viessmann.de/de/wohngebaeude/waermepumpe/sole-wasser-waermepumpen/vitocal-350-g.html (accessed on 12 August 2020).
62. Ökobaudat–Sustainable Construction Information Portal. Available online: https://www.oekobaudat.de/OEKOBAU.DAT/ (accessed on 12 August 2020).
63. Miedaner, O.; Mangold, D.; Sørensen, P.A. Borehole thermal energy storage systems in Germany and Denmark-Construction and operation experiences. In Proceedings of the 13th International Conference on Energy Storage, Beijing, China, 19–21 May 2015; pp. 1–8.
64. BMWi-This Is How Germans Heat Their Homes. Available online: https://www.bmwi-energiewende.de/EWD/Redaktion/EN/Newsletter/2015/09/Meldung/infografik-heizsysteme.html (accessed on 12 August 2020).


## Appendix C – Strategies for a transition towards a solar district heating grid with integrated seasonal geothermal energy storage

Published as:

Formhals J, Feike F, **Hemmatabady H**, Welsch B, Sass I (2021): Strategies for a transition towards a solar district heating grid with integrated seasonal geothermal energy storage, *Energy, 228, p.120662,* doi: /10.1016/j.energy.2021.120662

Energy 228 (2021) 120662

Contents lists available at ScienceDirect

Energy

journal homepage: www.elsevier.com/locate/energy

# Strategies for a transition towards a solar district heating grid with integrated seasonal geothermal energy storage

Julian Formhals [a, b, *], Frederik Feike [b, c], Hoofar Hemmatabady [a, b], Bastian Welsch [a, b], Ingo Sass [a, b]

[a] Geothermal Science and Technology, Technical University of Darmstadt, 64287, Darmstadt, Schnittspahnstraße 9, Germany
[b] Graduate School of Excellence Energy Science and Engineering, Technical University of Darmstadt, 64287, Darmstadt, Otto-Berndt-Str. 3, Germany
[c] Institute for Technical Thermodynamics, Technical University of Darmstadt, 64287, Darmstadt, Alarich-Weiss-Str. 10, Germany

ARTICLE INFO

*Article history:*
Received 1 December 2020
Received in revised form
12 March 2021
Accepted 14 April 2021
Available online 19 April 2021

*Keywords:*
4GDH
Solar district heating
Borehole thermal energy storage
Transition strategies
Modelica
Life cycle assessment

ABSTRACT

District heating plays a key role in achieving the TU Darmstadt's emission reduction target for 2050. A combination of efficiency measures, integration of solar thermal collectors, waste heat utilization and seasonal storage is being considered to achieve these targets. However, the existing campus building infrastructure does not allow for an efficient immediate transition to a low-temperature solar district heating grid. Therefore, a stepwise transition with a successive reduction of the grid temperatures is investigated. Dynamic system simulations serve to compare transition strategies until 2050 with regard to their environmental performance and economic efficiency. The proposed strategies differ in dimensions of components as well as the timing of construction or decommissioning. Results indicate that the emission reduction target can be met most economically by a strategy with a gradual construction of 42,000 $m^2$ of solar thermal collectors and a seasonal storage consisting of 37 boreholes of 750 m each, accompanied by a concurrent scaling-down of the existing CHP capacity. Compared to a strategy with an immediate construction of a full-sized system, the levelized cost of heat can be reduced from 7.6 ct/kWh to 6.3 ct/kWh, as projected renovation rates, energy prices and emission factors are taken into account better.



## 1. Introduction

Recent studies suggest district heating (DH) as a viable option for supplying large amounts of renewable energy for space heating [1]. Particularly fourth generation district heating (4GDH) systems [2], which operate on supply temperatures down to 50 °C or lower, facilitate the efficient integration of renewable energies [3,4] and waste heat sources [5]. However, a prerequisite for the rollout of 4GDH is a building stock suitable for low temperature heating [6]. Slow replacement and renovation rates of existing buildings impede a fast transition toward this technology [7]. Transition strategies specially tailored to existing building and grid infrastructure [8,9], as well as the utilization of locally available renewable and waste heat potentials [10], can help to overcome these hurdles.

The Technical University of Darmstadt is currently investigating concepts to reduce its energy demand [11], in order to support national targets for global warming potential (GWP) reduction [12]. Even though several synergy and efficiency related measures can bring the university one step closer to its emission saving goals, it has become evident that a large-scale integration of renewable heat sources is imperative [11,13].

Solar district heating (SDH) [14] with underground thermal energy storage (UTES) [15] has proven to be a promising technology in this context. Although solar thermal systems on their own have a very high potential to provide the annual required thermal energy, they have the inherent drawback of their heat supply not corresponding to the temporal course of the heat demand. This mismatch can be overcome by storing excess heat for periods of several months into UTES systems [16]. Borehole thermal energy storage (BTES) systems are a common type of UTES, as they are comparably cheap and site requirements are low [17]. Arrays of borehole heat exchangers (BHE) are used to access the underground's vast thermal capacity for sensible heat storage [18].

* Corresponding author. Geothermal Science and Technology, Technical University of Darmstadt, 64287, Darmstadt, Schnittspahnstraße 9, Germany.
*E-mail address:* julian.formhals@tu-darmstadt.de (J. Formhals).

https://doi.org/10.1016/j.energy.2021.120662
0360-5442/

The amount of discharged energy from such systems increases for lower discharge temperatures [19] and is usually raised to grid supply temperatures by heat pumps (HP), whose efficiency in turn depends to a large extent on the temperature raise they must provide. Consequently, the efficiency of BTES-assisted systems is highest for systems with low supply temperatures [21,51], i.e. 4GDH systems. A novel concept of BTES are medium deep (MD-BTES) systems, which consist of fewer BHEs of several hundred meters of length [19]. They have the advantage over conventional shallow systems of a much smaller thermal impact on shallow groundwater resources [22]. Moreover, MD-BTES systems utilize naturally higher undisturbed ground temperatures in larger depths. Consequently, they can be operated efficiently on higher temperature levels than their shallow counterparts [23].

A transformation into a campus SDH system with an integrated MD-BTES seems to be a promising option to achieve the university's emission reduction targets. However, such a transformation can be performed in several ways and at different rates. Which strategy is the most favorable in terms of costs and emissions strongly depends on local conditions and is still unclear at this stage.

### 1.1. State of the art and scope

A general definition of the concept of 4GDH and its advantages over systems of the 3rd generation (3GDH) is given by Lund et al. [2]. Sorknæs et al. [4] investigate the transition to a 100% renewable municipal energy system and find it beneficial both from an economic as well as an energetic point of view. Their scenario comprises a transition towards 4GDH, including solar thermal collectors (STC) and seasonal storage. Welsch et al. [24] conduct a life cycle assessment of different combinations of STC, BTES and combined heat and power (CHP). They identify a combined utilization of those technologies as most efficient solution. This result is supported by Elhashmi et al. [25], who investigate the integration of STCs and BTES into an existing DH system and find a combined system to be superior as well. Rämä et al. [26] investigate the integration of HPs or STCs into an existing 3GDH system over the period of 2014–2030 in three steps. Different combinations of technologies are compared, for integration into 3GDH or 4GDH, respectively. They conclude that an integration of HPs is most favorable in the existing 3GDH system, but STCs could be profitable as well, if grid temperatures were lowered. Several further studies assess the integration of renewable energies into DH systems on different temperature levels and conclude that a transition to 4GDH seems to be favorable [3,27–29]. However, all those studies compare 3GDH to 4GDH in a static manner, in which the transition process itself is excluded. Volkova et al. [6] evaluate the process dynamics of a transition towards 4GDH and identify retrofitting of consumer equipment as a main barrier. Accordingly, Oltmanns [13] focuses on identifying buildings which impede transition of the *Lichtwiese* DH system most. He states that these should be improved first, as they provide the highest leverage, while buildings with a lower impact should be renovated in the upcoming decades. Hence, a gradual transition is to be expected. Studies investigating such a process should therefore take long-term projections of expected renovation rates, required grid temperatures and energy prices into account.

This study presents a new methodology, which facilitates the assessment of strategies for the transition of an existing 3GDH system towards 4GDH. It considers a step-wise integration of STC, MD-BTES and waste heat sources. Strategies for integrating new components and decommissioning existing infrastructure are compared by energetic, economic and environmental means. The time frame of the study extends from 2025 to 2050 and is divided into three periods, enabling changes in the system design at the start of each period. Dynamic system simulations are carried out to assess the DH system performance, using long-term projections for energy prices, weather conditions and EFs. To account for high uncertainties in projected prices, a sensitivity analysis is appended.

### 1.2. Campus Lichtwiese district heating grid

The *Lichtwiese* is located on an old airfield on the outskirts of Darmstadt and one of four main campuses of the university. It comprises 40 buildings, consisting of offices, lecture halls, laboratories, large test halls, a library and a cafeteria, with a net floor area of about 150,000 $m^2$. The annual heat demand is approximately 25 GWh, which corresponds to 43% of the university's overall heat demand. Most of the campus was erected in the seventies and several of its buildings are under monumental protection, complicating energetic refurbishment. Since the *Lichtwiese* still has large open space, it is currently the main expansion area of the university, resulting in brisk construction work in recent years. A DH grid of 3.8 km length is supplying heat from a central CHP plant (Fig. 1), located on site. It consists of three CHP units with a total thermal power of 7 $MW_{th}$ and six gas boilers of 9.3 $MW_{th}$ each, providing heat to all university buildings. Grid supply temperatures range from 80 to 110 °C, depending on the ambient temperature, and the return temperature is 60 °C.

A recent study examined the present potential for reducing the temperature level of the grid. The authors concluded, that the current building stock would allow for a reduction of grid temperatures by at least 10 K [50]. The project *EnEff:Stadt Campus Lichtwiese*, which is currently running in its second phase, has identified components of the grid, which are most critical for further lowering of the grid temperature level down to temperatures of a 4GDH system [11]. As one of the first practical implementations from this project, waste heat from a high-performance computer (HPC) is fed into the return line of the grid by a heat pump [5]. In 2017, a cooling grid was constructed to cope with the increasing cooling demand on the campus. It is fed by three compression and one absorption chiller with a combined cooling power of 3 $MW_{th}$. However, the cooling grid is outside of the scope of this study and should be considered in future studies.

In order to achieve the German national climate protection goals, the university aims to reduce the specific GWP by 80% until 2050 compared to the level of 1990. As part of this plan, the area-specific final energy demand is to be reduced by 50% compared to 2015 [11]. Considering the aforementioned campus building stock, this might be an ambitious goal, but initial studies have deemed it feasible [11]. However, the campus net floor area is projected to double until 2050. Consequently, the total heat demand is expected to remain approximately constant.

As a complement to the *EnEff* project, the upcoming project *SKEWS* includes the construction of a MD-BTES demonstrator on campus [31]. It will consist of four BHEs, each 750 m deep, using the crystalline bedrock as heat storage medium, which is located only a few tens of meters below ground surface. A thermal insulation of the upper BHE sections shall preserve potential aquifers and lower thermal losses [32,55].

## 2. Methods

The study examines the period from 2025 to 2050, which is divided into three transition stages. Within each stage, the grid temperature range and system design are fixed. Different transition strategies are compared to identify the most economical way to satisfy the university's emission saving goals.

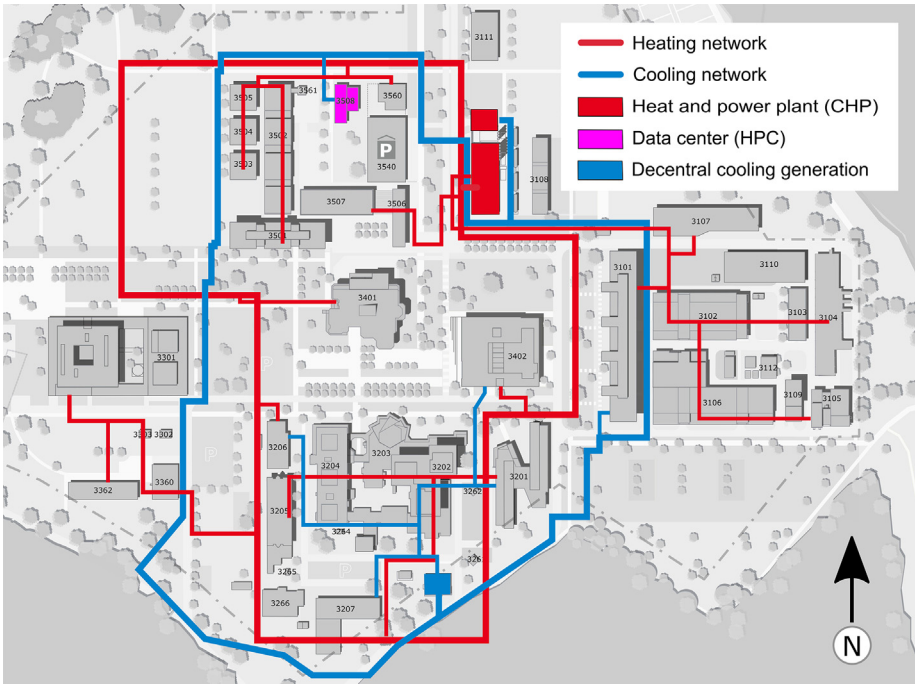


**Fig. 1.** TU Darmstadt campus Lichtwiese district heating and cooling network in 2018 (changed after [13]).

### 2.1. Study design

Five strategies are defined, which differ in final dimensioning of the renewable system components as well as the timing of construction and decommissioning of components. Additionally, a reference scenario is used for comparison to status quo.

#### 2.1.1. Assumptions and boundary conditions

It is assumed that the grid supply temperatures will decrease stage by stage from the current level of 80–110 °C to 50–60 °C (Table 1). Correspondingly, the return temperatures are expected to decrease from 60 °C down to 30 °C. Moreover, the amount of waste heat output from HPC cooling is expected to double. Projections of the net heated floor area suggest a continuation of the vigorous construction activities on campus in recent years, resulting in a doubling to 300,000 $m^2$. A regression analysis of the current weather dependent heat demand has predicted a lowering of the final heat demand, due to the impact of climate change, from 24.9 GWh to 22.7 GWh. The increase in net heated floor area is assumed to be compensated by efficiency related measures.

#### 2.1.2. Energy saving goals

In accordance with national climate protection goals, the university's goals use the year 1990 as a reference [11]. This makes an exact calculation of the reference EF difficult, as information on heat supply and demand for this period is incomplete. According to the envisaged reduction pathway, the EF in 2025 should amount to 50% of its 1990 value, which already constitutes a significant reduction. And there is no doubt that the university has already been able to significantly reduce its EF during this period through measures such as increased deployment of CHP and new buildings with a significantly lower specific heat demand. Therefore, for the purposes of this study, it is assumed that the 2025 energy saving goals will be achieved and further reductions are specified in relation to that year. Table 2 shows the resulting target EFs for each transition stage. The energy saving goals are considered satisfied if the system attains an average EF equal to or lower than that of the saving goals pathway of 85.3 $g_{CO2\text{-}equiv}$/kWh.

#### 2.1.3. Definition of transition strategies

The construction and decommissioning of the system components is classified into five transition levels, where level 0 corresponds to the current status and level IV to the most advanced state (see Fig. 2). For the STC area, a reference value is indicated (i.e. 100%), which is varied from 50% to 200% in a parametric study.

Approximately 43% of the university's final heat demand can be attributed to campus *Lichtwiese*. Consequently, the same share of the overall thermal power of the CHP units can be assigned to the *Lichtwiese*, which amounts to 3 $MW_{th}$.

The BHEs of the MD-BTES are planned in a hexagonal arrangement, limiting the possible number of BHEs to 19 or 37. While systems with only seven BHEs are considered inefficient, the next larger arrangement of 61 BHEs is excluded in advance as being oversized.

As mentioned in chapter 2.1.1, the HPC cooling capacity is expected to double. The flow temperature range of the existing HPC

**Table 1**
Assumptions for the three transition stages.

| Parameter | Status quo | Stage I | Stage II | Stage III |
|---|---|---|---|---|
| Period | 2021 | 2025–2030 | 2030–2040 | 2040–2050 |
| Grid supply temperature level | 80–110 °C | 70–100 °C | 60–80 °C | 50–60 °C |
| Grid return temperature | 60 °C | 50 °C | 40 °C | 30 °C |
| HPC cooling power | 350 $kW_{th}$ | 350 $kW_{th}$ | 500 $kW_{th}$ | 700 $kW_{th}$ |

**Table 2**
Energy saving goals for the end of each transition stage used for this study.

| Target/Projection | Unit | Status quo | Stage I | Stage II | Stage III |
|---|---|---|---|---|---|
| Net heated floor area | [$m^2$] | 150,000 | 180,000 | 240,000 | 300,000 |
| Total final heat demand | [GWh/a] | 24.9 | 24.9 | 22.7 | 22.7 |
| Specific final heat demand | [kWh/($m^2$ a)] | 165.3 | 133.3 | 91.4 | 73.1 |
| Specific EF compared to 2025[a] | [%] | 100 | 86 | 60 | 40 |
| Specific EF | [$g_{CO2\text{-}equiv}$/kWh] | 125.7[b] | 108.1 | 75.4 | 50.3 |

[a] Hanson et al. [13].
[b] Reference scenario simulation result.

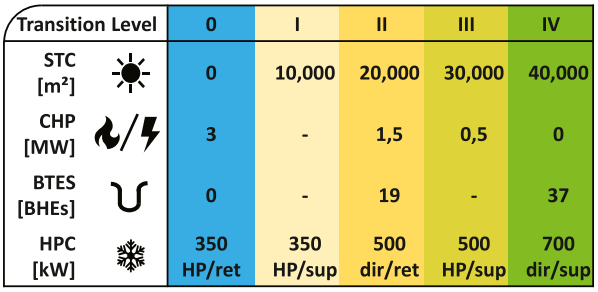


**Fig. 2.** Transition levels of system components ("-": level not used/defined).

high temperature cooling is 45–50 °C. Currently the waste heat is fed into the return line of the grid by a HP (*HP/ret*). With the assumed lowering of the grid temperatures, a direct feed into the return line (*dir/ret*), a supply line feed by HP (*HP/sup*) or direct feed into the supply line (*dir/sup*) become viable options.

Fig. 3 shows the planned transition levels of each of the DH components during the three transition stages for each proposed strategy. The *Immediate* strategy is characterized by maximum deployment of renewable energies and decommissioning of all CHP units in transition stage I. A bit less abrupt, but still aiming at a fast transition, the *Progressive* scenario starts with the implementation of SDH in stage I, but keeps the existing CHP units running during this stage. To avoid costs for repeated construction work, the *Step* scenario maintains the existing system design until 2030 and implements the final SDH system in one step. In contrast to the first two scenarios, the *Step* scenario does not require a HP for the HPC in addition to the currently existing one, since waste heat continues to be fed into the return line of the grid during transition stage II. To take the step-wise lowering of the grid temperatures into account, the *Gradual* scenario expands the STC field and the MD-BTES accordingly. At the same time the CHP capacity is reduced step-wise down to level III. The Conservative scenario keeps the system unchanged in stage I and results in the smallest SDH system (i.e. STC and BTES). Additionally, a *Reference* scenario is defined for comparison, using only CHP, gas boilers and waste heat utilization with their dimensions corresponding to the existing infrastructure (level 0). In contrast to the five transition strategies, grid temperatures are left unchanged from the current level.

For each proposed strategy, the reference STC field size is varied between 50% and 200% in steps of 10% in relation to the area given in Fig. 2. Thus, including the *Reference* scenario, a total of 81 systems is investigated.

## 2.2. Model implementation

The system is modeled with *Modelica* [34] and simulation runs are carried out using *SimulationX* [35] as simulation environment. Dynamic simulations of the thermo-hydraulic system are carried out over the period of 25 years. Within each stage the component

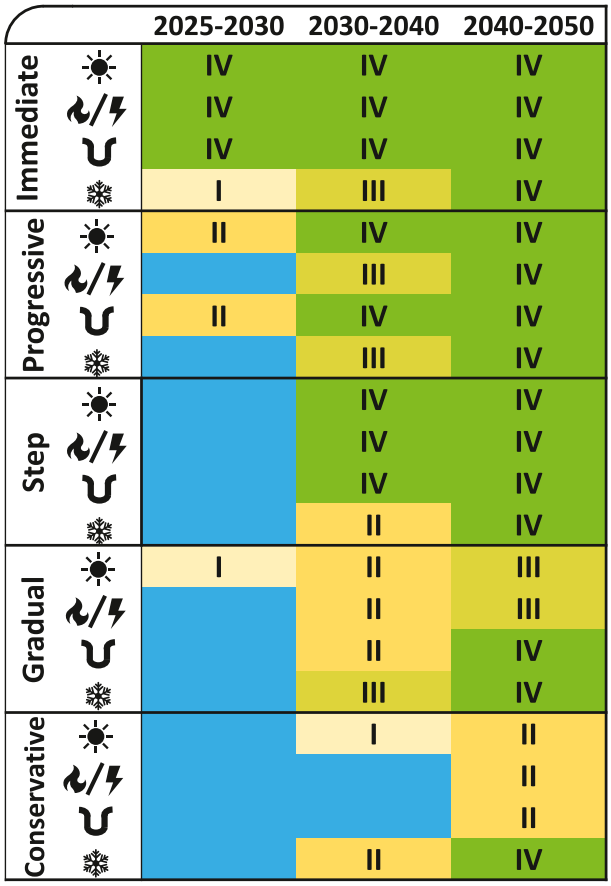


**Fig. 3.** Component transition levels within each transition stage for the defined strategies.

dimensions, DH grid conditions and ambient conditions are adapted according to the scenario design.

### 2.2.1. Model library, model components and their setup

The DH system was modeled using the in-house developed *MoSDH* (Modelica Solar District Heating) library (Fig. 4). *MoSDH* is based on low level components of the *Modelica Standard Library*'s *Thermal* package. The defining variables for DH system simulations with *MoSDH* are fluid temperature (i.e., enthalpy), pressure and mass flow rate. Heat transfer and pressure loss calculations are mostly based on the *VDI Heat Atlas* [36].

In the following sections the components of the library and their specific setup for this study are described.

Solar Thermal: The flat plate collector model uses a quadratic loss term for efficiency calculation and the isotropic sky model after Liu and Jordan [37,38]. It considers multiple collector modules connected in parallel and in series as well as mutual shadowing of

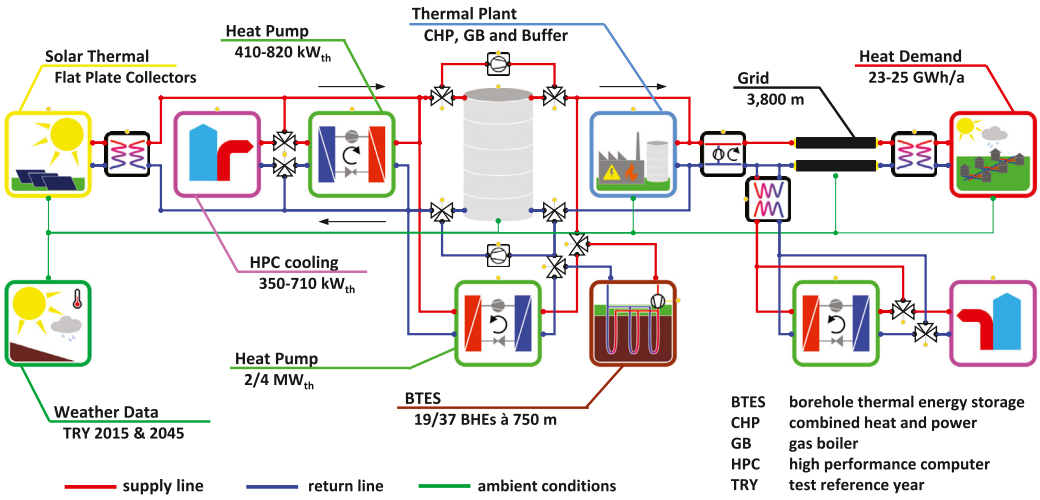


**Fig. 4.** Model of the SDH system in Modelica.

collector rows. Efficiency parameters are obtained from data sheets of large-scale STCs [52]. Validation was carried out against an established model from *TRNSYS* [40] for the locations Tehran, Sydney and Reykjavik. The deviation of the annual solar yield was below 5% for all locations.

Weather: The weather component reads hourly ambient temperature as well as direct and diffuse solar irradiation data from text files. Test reference years (TRY) for the campus location are used from the German Weather Service [41]. For transition stage I the *TRY 2015* is used, which represents a typical year derived from measured data during the period from 1995 to 2012. At the start of transition stage II, the weather data switches to *TRY 2045,* which constitutes a typical year for climate projections in the period from 2031 to 2060. Average ambient temperatures and annual solar irradiation amount to 10.6 °C and 1085 kWh/m$^2$ for *TRY 2015* as well as 11.3 °C and 1162 kWh/m$^2$ for TRY 2045, respectively.

BTES: A BTES consisting of 19 or 37 BHEs of 750 m in a hexagonal layout is modeled using the *MoBTES* model. The design of the modeled coaxial BHEs was carried out according to the planned demonstrator, where the upper section is thermally insulated by the use of a backfill material with low thermal conductivity [31]. A detailed description of the *MoBTES* model and its validation can be found in Formhals et al. [42].

Buffer storage: The model consists of several volume elements to account for thermal stratification. It was developed in the course of a master thesis and validated against an existing model [43]. Since the volume of the buffer storage tank should be adapted according to the size of the STC aperture area, its size is defined by a ratio of 0.25 $m^3_{buffer}/m^2_{collector}$.

Thermal power plant: This model combines a CHP model with several units and a gas boiler for auxiliary heating. In both models, the fuel consumption is derived from efficiency curves. In addition to that, the CHP model uses a curve for its power to heat ratio. For the underlying case study, data sheets of the existing components at campus *Lichtwiese* are used. According to the existing system at campus *Lichtwiese*, a smaller buffer storage with a volume of 125 m$^3$ is used to increase the running times of the CHP units.

Heat pumps: The HPs are modeled using efficiency maps for the maximum heating power and the coefficient of performance, which are derived from manufacturer datasheets of high temperature HP [53]. Since the availability for high temperature HPs data in the required heating power range is limited, the maximum heating power was scaled. This was done under the assumption that larger HPs have an efficiency at least as high as smaller units.

Grid: The campus DH grid has a length of approximately 3.8 km, represented by two segmented pipes of this length, one for the supply and one for the return line. Since the weighted average diameter of the campus grid is close to the diameter of a DN250 DH pipe [54], the pipe model was parametrized accordingly. The pre-insulated pipes are modeled by reusing sub-models from the *MoBTES* model: DH pipe segments are represented by BHE segments. Moreover, the ground surrounding the pipes is modeled by a thermal resistance and capacity model, which was initially implemented to consider the heat transport in the immediate vicinity of BHE segments. The thermal resistance between this circular region and the ground surface is derived from the *VDI Heat Atlas* [36].

Heat Demand: In accordance with the simplified representation of the campus DH grid, the demand side is combined into one consumer. The heat load curve was generated by applying a regression model, derived by monitoring data over the period between November 2016 and July 2019, on the used TRY datasets [13].

### 2.2.2. Control strategy

The control strategy is based on system states, which define respective component behaviors. Transitions between states are triggered by conditional expressions. According to the active state, components receive set values for thermal power, supply temperature or mass flow rate via a central bus system. STC, HPC and BTES are activated and deactivated in the given order depending on the state of charge of the buffer storage tank. The single HPC in the grid is represented by two separate model blocks, one of which is connected to the supply line of the grid and the other to the return line. As in the existing system, HPC cooling is only fed into the grid during the heating period, while cooling fans are used in summer [5].

In summer operation heat is transferred to the BTES, if the buffer's state of charge exceeds a certain threshold. During heating season, the BTES is discharged into the buffer storage directly or via HP. Discharging is enabled if half of the buffer storage volume is below the reference grid temperature, which is the case almost all winter and carries on until BTES flow temperatures fall below 10 °C.

The thermal plant satisfies the heat demand, which cannot be covered by the SDH system. CHP units are switched on and off according to the charging state of the small buffer. If CHP units are active, a direct feed can be used to bypass the buffer. If the required

heat demand exceeds the limits of the CHP and the buffer, the gas boiler covers the residual load. The temperatures that enter the grid are regulated according to a heating curve, which relates the supply temperature to the 24 h average ambient temperature. Up to a certain level, the temperature level of the heat supplied by the SDH part is raised by mixing with volume flow from the thermal plant, if necessary.

### 2.3. Analysis

An economic and environmental assessment of the systems under investigation is carried out after Mauthner et al. [14] and Welsch et al. [24]. It is expected that both the energy prices and the EF of the electricity purchased from the grid will change over time, as assumed in the *EVO* scenario by Welsch et al. [24]. For this reason, the *EVO* scenario was applied in this study as well. To account for uncertainties in fuel and investment costs, a sensitivity analysis is carried out for selected systems.

#### 2.3.1. Economic assessment

A common figure for comparing the economic efficiency of thermal energy systems is the LCOH (Equation (1)) [46]. To allow for an annual resolution of costs, attributed to the heat delivered over the span of one year $Q_a$, the concept of annuities $A$ is used [47]. In this concept, repayments of an initial investment are evenly distributed over its lifetime of $n$ years. Functions and data for investment costs $I_0$, annual maintenance costs $M_a$, fuel costs $F_a$, revenues $R_a$ and expected lifetimes $a_{life}$ for the system components are adopted from Mauthner et al. [14] and Welsch et al. [24]. For each of the components, annuities $AN$ are calculated by multiplying the initial investment costs by the annuity factor $AF$ [48] (Equation (2)). An interest rate $r$ of 3% was assumed. Residual values of existing components are factored in by their age and expected remaining lifetime. Annuities are paid accordingly. In the case of early decommissioned components (e.g., existing CHP units), no resale was considered. Investment costs were further repaid over the remaining depreciation period, but no further maintenance costs were charged.

$$\mathrm{LCOH}_a = \frac{AN + M_a + F_a - R_a}{Q_a} \tag{1}$$

$$AN = I_0\ \mathrm{AF} = I_0 \frac{(1+r)^{a_{\mathrm{life}}} r}{(1+r)^{a_{\mathrm{life}}} - 1} \tag{2}$$

#### 2.3.2. Environmental assessment

The environmental impact of the delivered heat $Q_{th}$ was calculated using an LCA approach, taking into account emissions caused by operation ($GWP_{op}$) and production ($GWP_{prod}$). In the case of CHP, the production of electricity was included in the evaluation, to avoid allocation of emissions. As a result, the economic and environmental differences of the investigated systems due to a change in produced electricity, are considered as well. The total EF of each system was calculated according to Equation (3), where $i$ stands for the different components of the system [24]. However, in order to allow for a comparison between annual EFs and energy saving goals, Equation (3) had to be adapted. Emissions attributed to the production of components are distributed evenly over the lifetime $a_{life}$ of each component as given in Equation (4).

$$\mathrm{EF} = \frac{\mathrm{GWP}}{Q_{\mathrm{th,tot}}} = \frac{1}{Q_{\mathrm{th,tot}}} \sum_{i=1}^{n} \left(\mathrm{GWP}_{\mathrm{prod},i} + \sum_{a=1}^{a_{\mathrm{life}}} \mathrm{GWP}_{a,\mathrm{op},i}\right) \tag{3}$$

$$\mathrm{EF}_a = \frac{\mathrm{GWP}_a}{Q_{\mathrm{th},a}} = \frac{1}{Q_{\mathrm{th},a}} \sum_{i=1}^{n} \left(\frac{\mathrm{GWP}_{\mathrm{prod},i}}{a_{\mathrm{life}}} + \mathrm{GWP}_{a,\mathrm{op},i}\right) \tag{4}$$

#### 2.3.3. System performance figures

Equation (5) defines the solar fraction of a system, where the amount of energy stored into the BTES $Q_{BTES,charged}$ is subtracted from the overall energy supplied by the STC field $Q_{solar}$ to achieve the direct delivered solar energy. The amount of energy discharged from the storage $Q_{BTES,discharged}$ is included into the solar fraction. The storage utilization factor $\eta_{BTES}$ is defined by Equation (6).

$$f_s = \frac{Q_{solar} - Q_{BTES,charged} + Q_{BTES,discharged}}{Q_{grid,feed}} \tag{5}$$

$$\eta_{BTES} = \frac{Q_{BTES,discharged}}{Q_{BTES,charged}} \tag{6}$$

### 2.4. Limitations

Due to the necessity of several simplifications and assumptions, the presented study has certain limitations that should be kept in mind. In accordance with the mentioned *EnEff* project, the focus of this study was put on a single campus of the university. Even though a separate supply of heat is generally possible and the different campus grids are already operating on various temperature levels, technical and economical interdependencies of the connected grids are strong. This could result both in synergetic as well as adverse effects. Furthermore, the district cooling grid of the university was not within the system boundaries of this study. A coupling of the two grids will most certainly be implemented in the future and improve energetic efficiency. The assumed measures and costs for the conversion of the DH grid into a 4GDH, especially concerning consumers and distribution, need to be considered as a part of separate studies. Another limitation concerns the underlying input data for the development of energy prices and climate as well as the used cost relations, since these are subject to significant uncertainties. Moreover, the design of the study introduces several simplifications, using discrete system transition stages, a limited number of parameter variations and a fixed set of technologies. This was caused by numerical limitations on the one hand, and the case study character of the study on the other hand, focusing on a certain system and a certain possible technology. A widening of this scope would have been hard to handle as thoroughly as the presented work.

## 3. Results

### 3.1. Parameter study

#### 3.1.1. Annual supplied thermal energy

As expected, in each transition scenario the amount of directly provided solar thermal energy increases with an increase in the STC field size (Fig. 5). The BTES system covers up to 38.5% of the total heat demand. It can be observed that this share increases with STC size up to a maximum and decreases hereafter, which is in line with the feed-in order mentioned in Chapter 2.2.2. Accordingly, the

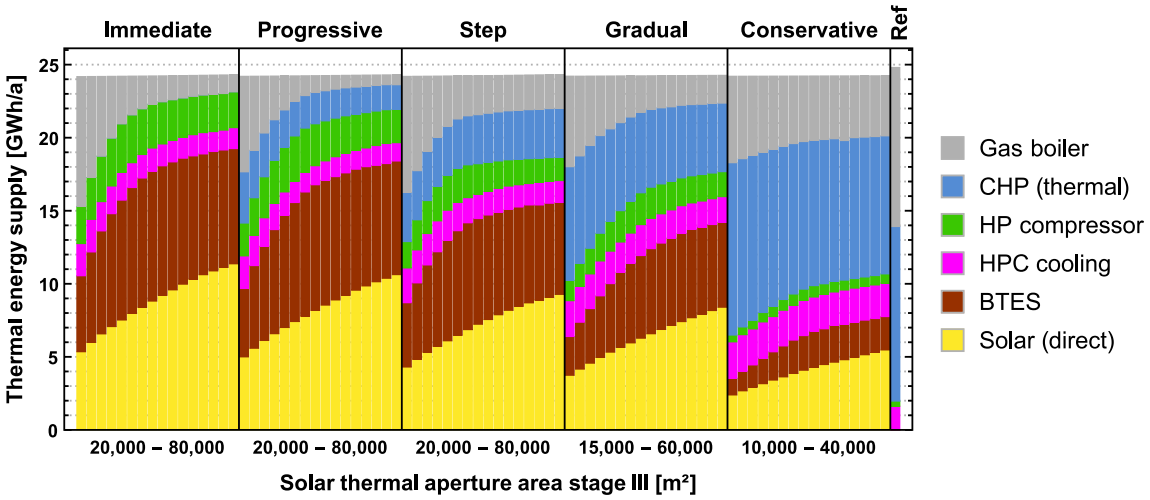


**Fig. 5.** Average annual thermal energy supply of each simulated system. Direct solar delivery is calculated by subtracting the energy stored into the BTES from the total solar production.

amount of HPC waste heat, reduces for systems with high solar shares, since priority is given to STCs. An early integration of BTES into the grid generally results in higher demands of electricity, since the HPs need to raise discharged energy to higher temperatures (*Immediate* & *Progressive*). Finally, the share of CHP increases for slow transition strategies and almost reaches the level of the *Reference* system for *Conservative* strategies. The *Reference* system yields a CHP share of 51.7%, which is close to the actual share of 55% in 2018 [13]. This deviation can be partly explained by the integration of HPC cooling, which was only installed in 2021.

### 3.1.2. Economic and environmental performance

Even without further modifications, the existing heating system can reach a comparatively low EF at moderate heating costs (*Referece* scenario, Fig. 6). This can be attributed to the high share of CHP, which leads to considerable enhancements in the GWP balance due to emission credits for the replacement of grid electricity with CHP electricity.

Within each strategy, an increase of the STC area results in a lowering of the EF. Below a certain point however, further reductions lead to a disproportional increase in the LCOH. Counterintuitively, it is not the *Immediate* but the *Progressive* strategy that provides the system design with the lowest overall EF. In contrast, the overall lowest LCOH is obtained by the *Conservative* strategy, which cannot compete with the other strategies in terms of emission reduction. Among the other four strategies that gain similarly low EFs, the *Gradual* strategy achieves the lowest LCOH. Most importantly, both the *Conservative*, as well as the *Gradual* strategy are even more economic than the *Reference* scenario.

### 3.1.3. Selection of efficient system designs

Table 3 specifies several performance figures for three characteristic system designs per transition strategy: the ones with the lowest EF, lowest LCOH and lowest LCOH that attains the EF target.

The solar yield of all characteristic systems lies in the range of 306–518 kWh/(m$^2$ a), which is plausible for SDH systems [14]. It generally decreases for systems with larger aperture areas indicating a saturation effect. Furthermore, the solar fraction $f_{sol}$ varies between 27.9% for the $LCOH_{min}$ *Conservative* scenario and 83.3% for the $EF_{min}$ *Immediate* scenario system. The storage utilization $\eta_{BTES}$

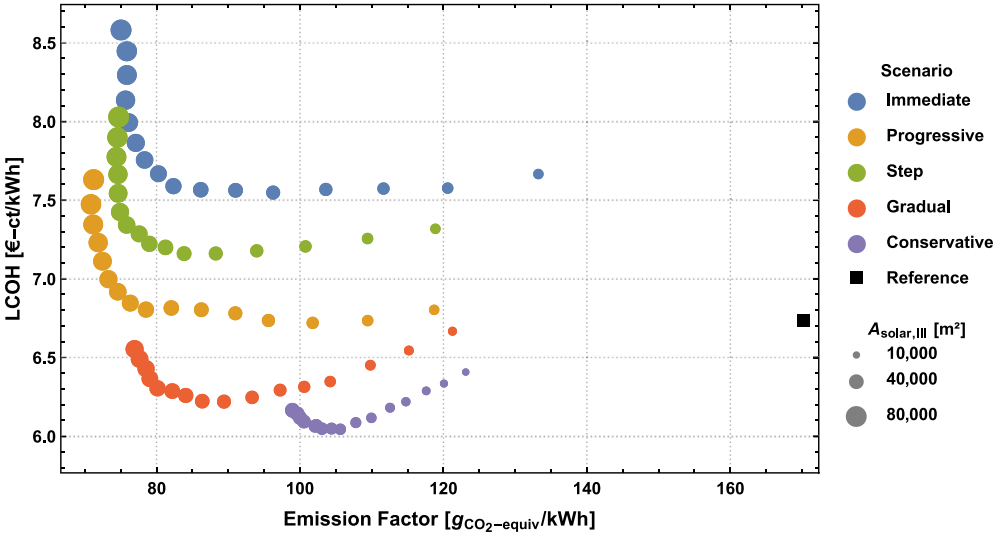


**Fig. 6.** LCOH and EF for the systems under investigation.

of the characteristic systems reaches a maximum of 92.4%. For the comparison of the total GWP from 2025 to 2050, it should be considered that the *Reference* system already includes a reduction of the specific heat demand in 2050 by 50%. Consequently, the actual GWP of a completely unchanged DH system would be significantly higher.

Apparently, none of the system designs which use the *Conservative* transition strategy reaches the target EF. In contrast, several of the selected system designs of the four more ambitious strategies do so. An abrupt transformation of the *Lichtwiese* into an SDH system however, as represented by the *Immediate* scenario, is not advisable under the given circumstances as well. Those systems result in higher LCOHs, particularly in comparison to the *Gradual* and *Progressive* transition strategies, without a significant additional emission reduction. For further analysis, the $EF_{target}$ systems of each scenario are selected. In the case of the *Conservative* scenario the $EF_{min}$ system is chosen instead.

With an LCOH of 6.3 ct/kWh, the most economic system to reach the target EF belongs to the *Gradual* strategy. Even for an increase of all energy prices and investment costs by 20%, it would result in an LCOH below the expected value of the *Immediate* system (cf. Table 3 *Cost variation*).

Fig. 7 depicts the composition of the specific costs per transition phase of the selected systems as well as the revenues from the sale of excess electricity to the grid. The composition of the LCOH for the *Immediate* system reveals that the integration of a BTES in Phase I results in a high LCOH, if the HP's electricity demand is not covered by self-production of the CHP.

The *Gradual* system, which does not use a BTES within stage I and reduces the CHP capacity beginning from stage II onwards, results in a total LCOH which is 0.5 ct/kWh lower than for the second most economic system (*Progressive*). This cost advantage can be attributed mostly to transition stage II (cf. Fig. 7). While the *Progressive* strategy comprises a simultaneous full-scale integration of an SDH system with integrated BTES and the phase out of CHP technology in stage II, the CHP units maintain half capacity for the *Gradual* strategy. Consequently, there is still enough self-produced cogenerated electricity available to supply circulation pumps and HPs.

However, since the economic and environmental performance of the CHP is projected to continuously decrease, a successive increase of STC area and BTES capacity within stage II and III, with a simultaneous reduction of the CHP capacity down to minimum, as included in the *Gradual* strategy, is advisable.

According to the results of the study, a reasonable transition strategy for the *Lichtwiese* campus could be as follows: The STC area should be enlarged from 14,000 $m^2$ in 2025 to 28,000 $m^2$ in 2030, and to a final size of 42,000 $m^2$ in 2040. At the same time, the CHP capacity should be reduced from 3 $MW_{th}$, to 1.5 $MW_{th}$ and finally to 0.5 $MW_{th}$. An expansion to the maximum sized MD-BTES with 37 BHEs is recommended in 2040, with an initial size of 19 BHEs in 2030.

These findings, however, assume that no subsidies are considered, as they are difficult to predict. Current subsidies could favor earlier construction as they significantly reduce investment costs of BTES systems and STCs [24].

### 3.1.4. Energy saving goals

Fig. 8 shows emission targets as well as the temporal development of the annual EFs for the selected systems in relation to the emissions of the *Reference* scenario in 2025. It is quite clear, that the *Reference* system loses attractiveness over time. As already pointed out by Welsch et al. [24], a decrease in the EF of grid electricity is very likely, due to a higher share of renewables in the future. Subsequently, emission credits caused by the substitution of grid electricity with CHP electricity, will diminish. Accordingly, EFs increase within all transition stages in which CHP is used. As a result, the target trajectory is exceeded by all systems before 2030. In addition to that, the *Immediate* scenario system, which does not use CHP at all, even starts with an EF higher than the *Reference* case, highlighting the currently prevailing advantage of the CHP technology. While the *Immediate*, *Progressive*, *Step* and *Gradual* scenario systems surpass the cumulated emission reduction goal, they narrowly miss the final target value in 2050.

Overall, the development of specific emissions over time illustrates that CHP is an efficient technology for several years to come, not only from an economic but also from an ecological perspective. The investigated transition scenarios comprise cost-effective ways to reduce the total emissions of DH systems. However, the final emission target in 2050 was missed, even for systems with a large SDH dimensioning (cf. Fig. 8). This indicates the importance of the integration of additional renewable technologies or the expansion of waste heat utilization. Latter one should be a feasible option, since projections of the waste heat potential were very

**Table 3**
Performance figures for the most economic system that attains the EF target, the system with the lowest EF and the system with the lowest LCOH within each transition strategy.

| Scenario | System | Final $A_{solar}$ [$m^2$] | Solar yield [kWh/($m^2$a)] | Solar fraction $f_s$ [%] | BTES utilization $\eta_{BTES}$ [%] | Total GWP [$t_{CO2}$] | Total EF [$g_{CO2}$/kWh] | Final EF [$g_{CO2}$/kWh] | Total LCOH [ct/kWh] | 20% cost variation [ct/kWh] | Final LCOH [ct/kWh] |
|---|---|---|---|---|---|---|---|---|---|---|---|
| Reference | – | 0 | 0 | 0 | 0 | 98,301 | 170.2 | 188.8 | 6.7 | 5.4–8.1 | 7.3 |
| Immediate | $EF_{target}$ | 48,000 | 431 | 76.6 | 74.9 | 47,601 | 82.4 | 58. | 7.6 | 6.1–9.1 | 6.9 |
| | $EF_{min}$ | 80,000 | 306 | 83.3 | 60.2 | 43,392 | 75.1 | 56.6 | 8.6 | 6.9–10.3 | 8.1 |
| | $LCOH_{min}$ | 36,000 | 475 | 68.0 | 85.7 | 55,615 | 96.2 | 71.1 | 7.6 | 6.0–9.1 | 6.9 |
| Progressive | $EF_{target}$ | 48,000 | 449 | 72.6 | 77.7 | 45,386 | 78.5 | 60.4 | 6.8 | 5.5–8.2 | 6.5 |
| | $EF_{min}$ | 76,000 | 349 | 78.9 | 61.2 | 40,935 | 70.8 | 57.3 | 7.5 | 6.0–9.0 | 7.5 |
| | $LCOH_{min}$ | 28,000 | 518 | 54.4 | 92.4 | 58,811 | 101.8 | 89.8 | 6.7 | 5.4–8.1 | 6.5 |
| Step | $EF_{target}$ | 40,000 | 476 | 59.0 | 81.6 | 48,459 | 83.9 | 62.6 | 7.2 | 5.7–8.6 | 6.7 |
| | $EF_{min}$ | 72,000 | 348 | 66.6 | 58.2 | 43,011 | 74.4 | 57.2 | 7.8 | 6.2–9.3 | 7.8 |
| | $LCOH_{min}$ | 36,000 | 494 | 56.1 | 84.7 | 50,987 | 88.2 | 67.9 | 7.2 | 5.7–8.6 | 6.7 |
| Gradual | $EF_{target}$ | 42,000 | 452 | 55.3 | 79.4 | 48,584 | 84.1 | 62.7 | 6.3 | 5.0–7.5 | 6.4 |
| | $EF_{min}$ | 60,000 | 396 | 61.5 | 60.9 | 44,441 | 76.9 | 56.7 | 6.6 | 5.3–7.9 | 6.9 |
| | $LCOH_{min}$ | 36,000 | 474 | 51.6 | 85.7 | 51,653 | 89.4 | 70.1 | 6.2 | 5.0–7.5 | 6.3 |
| Conservative | $EF_{target}$ | – | – | – | – | | – | – | – | – | – |
| | $EF_{min}$ | 40,000 | 364 | 33.5 | 56.7 | 57,185 | 99.0 | 75.4 | 6.2 | 4.9–7.4 | 6.0 |
| | $LCOH_{min}$ | 24,000 | 438 | 27.9 | 87.1 | 61,020 | 105.6 | 84.7 | 6.1 | 4.8–7.3 | 5.8 |
| **Target** | | | | | | **50,135** | **85.3** | **50.3** | | | |

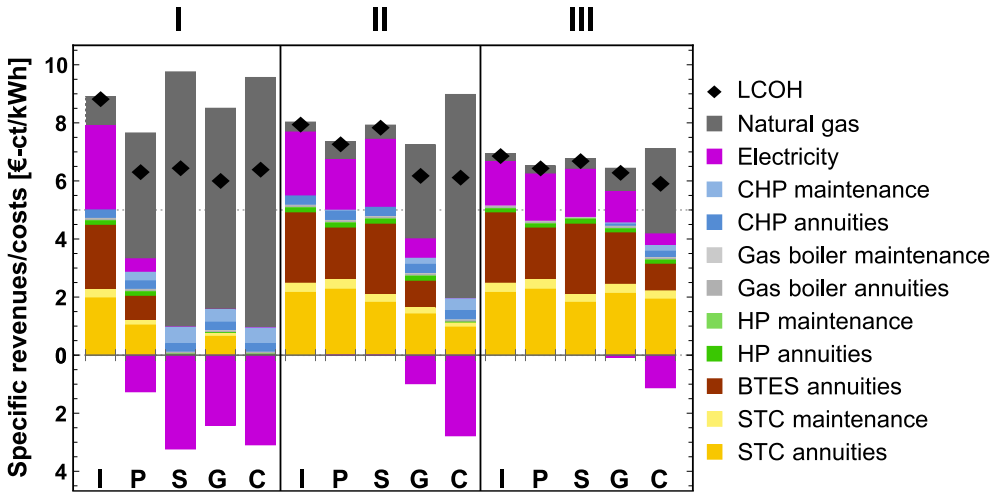


**Fig. 7.** Specific revenues (bottom) and costs (top) for the $EF_{target}$ system of *Immediate* (I), *Progressive* (P), *Step* (S) and *Gradual* (G) transition strategies and the $EF_{min}$ system of *Conservative* (C) allocated to the different transition stages.

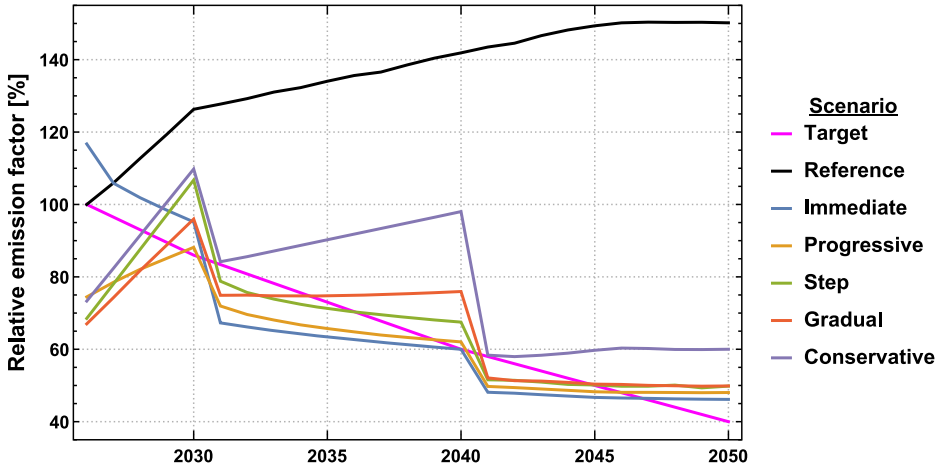


**Fig. 8.** Relative annual emission factor of the $EF_{min}$ system for the *Conservative* scenario and $EF_{target}$ systems else.

conservative. The remaining emissions in 2050 are mostly due to gas consumption of boiler and CHP units, which could be reduced by the utilization of biomass. However, a total carbon-neutrality in 2050 seems hard to attain. For one thing, the used LCA approach considers emissions during production phase, which cannot be avoided completely and would have to be compensated by carbon sinks. Secondly, the used projections do not anticipate carbon neutrality of the grid electricity in 2050. Nevertheless, if this goal were to be achieved, it would contribute significantly to the goal of a carbon-neutral campus DH system.

### 3.2. Sensitivity analysis

Both the energy prices as well as the investment costs are varied for the selected system designs (cf. Table 3) in order to assess the sensitivity of the heat costs incurred to changes in the economic input data (Fig. 9). It can be observed that the *Reference* and *Conservative* scenarios, which have the highest share of CHP heat, are especially sensitive to changes in energy prices. For scenarios with an increasing share of SDH, the sensitivity shifts from a high impact of energy prices towards a high impact of investment costs, which is due to the generally high investment costs of STC and BTES.

## 4. Conclusion

The presented study investigates different strategies and technological pathways for the transition of an existing campus district heating grid towards a low-temperature SDH system. It emphasizes the importance of considering the projected development of existing infrastructure and boundary conditions. If such temporal developments are excluded during system engineering, it can lead to considerably higher costs. In contrast, a dynamic study design, as presented in this study, allows economic and ecological advantages of certain technologies at certain transition phases to be identified and included in the planning process. While studies of 4GDH systems with fixed system design make a compelling point for the utilization of 4GDH in general, operators of existing DH systems could argue that a transition of their system is not possible due to practical reasons. The presented study demonstrates the feasibility of a step-wise transition of such a system, which comprises several old buildings under monumental protection and a relatively new CHP plant. Hence, the proposed methodology of numerical simulations with dynamic boundary conditions and system design represents a reasonable extension to existing approaches. However, due to the higher computational effort of such a transient simulation approach, it does not provide the ability of a completely

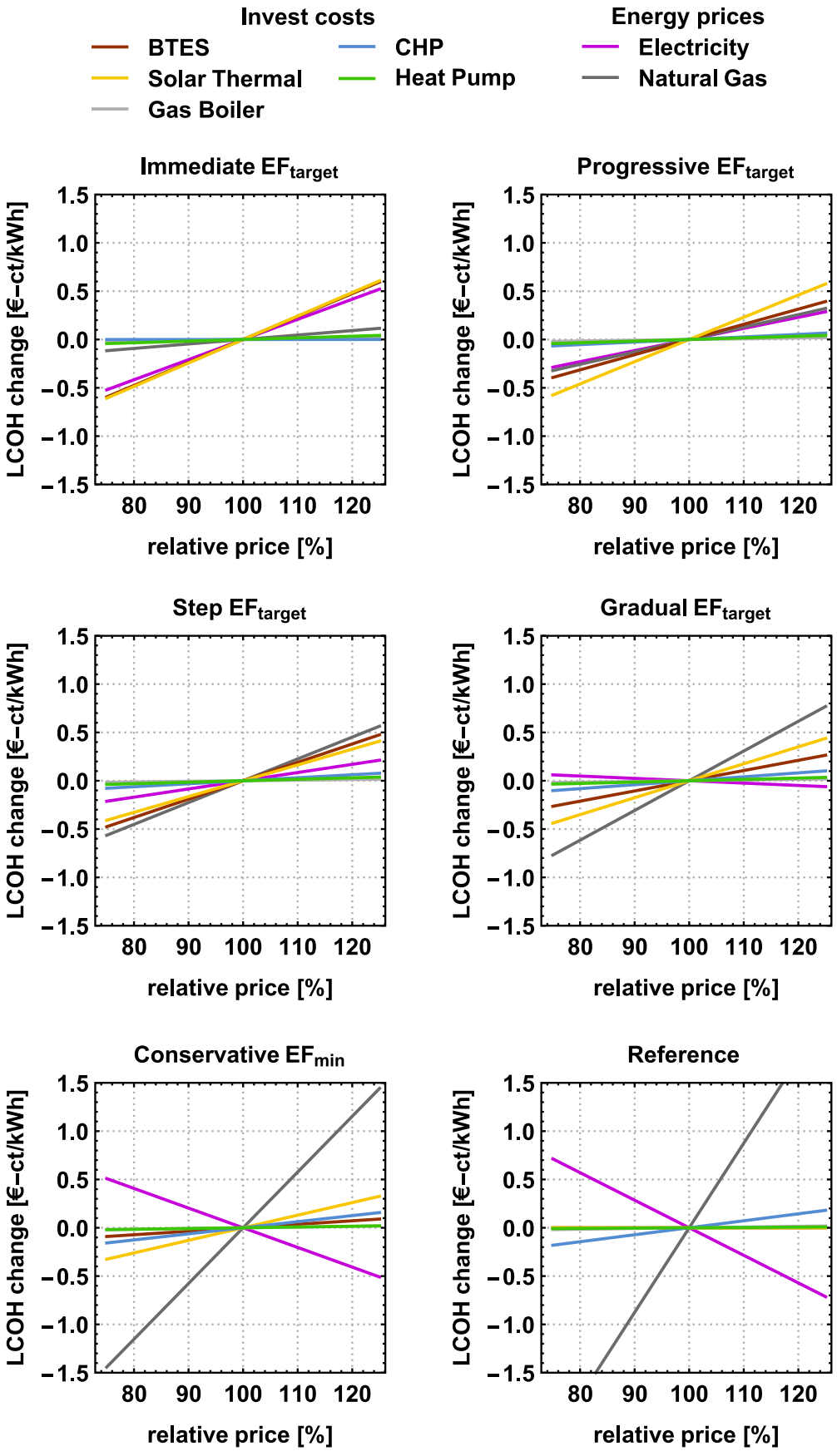


**Fig. 9.** Variation of energy prices and invest costs for the selected systems.

technology-open analysis, as it can be achieved e.g., by energy budget tools [49]. Nevertheless, the developed model library efficiently exploits the possibilities of equation-based modeling with *Modelica* and facilitates a detailed representation of specific existing systems.

The approach was used to conduct a parametric study, which demonstrates that MD-BTES systems facilitate high solar fractions and thus enable the provision of a significant share of renewable energies in the heat demand of SDH systems. In the case study of the campus *Lichtwiese* DH grid, the BTES-assisted systems under consideration appear to be very promising options for taking a major step towards achieving the TU Darmstadt's emission reduction targets. Even LCOHs below the reference case are possible, but for a definite conclusion costs of transition measures, such as adjustments to building heating systems and the grid, should be included.

Furthermore, results indicate that unambitious transition strategies similar to the *Conservative* scenario will ultimately fail to attain the emission targets. However, an abrupt transformation of the *Lichtwiese* into a SDH system, as represented by the *Immediate* scenario, is also not advisable under the given circumstances. Such hasty transitions result in higher LCOH, compared to *Gradual* and *Progressive* transition strategies, without achieving any significant additional emission reductions.

Consequently, in the case of the *Lichtwiese* DH system, it is advisable to gradually integrate SDH from 2025 with a final STC area of 42,000 $m^2$ and an MD-BTES consisting of 37 BHEs. The existing CHP units are to be operated at full capacity until 2030 and afterwards reduced in steps to a final capacity of 500 kW in 2040.

While cumulative emission saving goals in 2050 could be satisfied by the proposed systems, the final target in 2050 is missed narrowly and carbon-neutrality cannot be achieved. Consequently, future studies should include additional measures like a switch from natural gas to biomass combustion or power-to-heat technology. Furthermore, necessary transformation measures on the consumer side and subsidies should be considered and included in cost calculation. Finally, the proposed concept of MD-BTES, which so far has only been evaluated numerically, should be validated by experimental data, to verify the identified energetic and economic potentials.

## Declaration of competing interest

The authors declare that they have no known competing financial interests or personal relationships that could have appeared to influence the work reported in this paper.

## Nomenclature

| | |
|---|---|
| 3GDH | Third generation district heating |
| 4GDH | Fourth generation district heating |
| BHE | borehole heat exchanger |
| BTES | borehole thermal energy storage |
| CHP | combined heat and power |
| DH | district heating |
| EF | emission factor |
| GB | gas boiler |
| GWP | global warming potential |
| HP | heat pump |
| HPC | high-performance computer |
| LCOH | levelized cost of heat |
| MD | medium deep |
| SDH | solar district heating |
| STC | solar thermal collector |
| TRY | test reference year |
| UTES | underground thermal energy storage |

*Symbols*

| | |
|---|---|
| A | Area $m^2$ |
| AN | Annuities € |
| AF | Annuity factor |
| F | Fuel costs € |
| f | Fraction % |
| M | Maintenance costs € |
| I | Investment costs € |
| Q | Thermal energy J |
| r | Interest rate % |
| R | Revenues € |
| η | Efficiency/utilization rate % |

*Subscripts*

| | |
|---|---|
| a | Index of specific year |
| i | Index of a specific component |
| life | Component lifetime |
| min | Minimum |
| op | Concerning component operation |
| prod | Concerning component production |
| sol | Solar |
| th | Thermal |
| tot | Total |

## Author contribution

Julian Formhals: Conceptualization, Methodology, Software, Validation, Formal analysis, Investigation, Data curation, Writing – original draft, Visualization, Frederik Feike: Conceptualization, Validation, Investigation, Data curation, Writing – review & editing, Hoofar Hemmatabady: Conceptualization, Validation, Investigation, Writing – review & editing, Bastian Welsch: Conceptualization, Methodology, Investigation, Writing – review & editing, Supervision, Project administration, Ingo Sass: Conceptualization, Resources, Writing – review & editing, Supervision, Project administration, Funding acquisition

## Funding

This work was financially supported by the European Regional Development Fund (ERDF) by supporting the North-West Europe Interreg project *DGE-Rollout* (NWE 892), the German Federal Ministry of Economic Affairs and Energy (BMWi) in the project *EnEff:-Stadt Campus Lichtwiese II* (03ET1638) as well as the German Research Foundation (DFG) in the framework of the Excellence Initiative, *Darmstadt Graduate School of Excellence Energy Science and Engineering* (GSC 1070).

## References

[1] Connolly D, Lund H, Mathiesen BV, Werner S, Möller B, Persson U, et al. Heat Roadmap Europe: combining district heating with heat savings to decarbonise the EU energy system. Energy Pol 2014;65:475–89. https://doi.org/10.1016/j.enpol.2013.10.035.

[2] Lund H, Werner S, Wiltshire R, Svendsen S, Thorsen JE, Hvelplund F, et al. 4th Generation District Heating (4GDH). Integrating smart thermal grids into future sustainable energy systems. Energy 2014;68:1–11. https://doi.org/10.1016/j.energy.2014.02.089.

[3] Averfalk H, Werner S. Economic benefits of fourth generation district heating. Energy 2020;193. https://doi.org/10.1016/j.energy.2019.116727.

[4] Sorknæs P, Østergaard PA, Thellufsen JZ, Lund H, Nielsen S, Djørup S, et al. The benefits of 4th generation district heating in a 100% renewable energy system. Energy 2020;213. https://doi.org/10.1016/j.energy.2020.119030.

[5] Oltmanns J, Sauerwein D, Dammel F, Stephan P, Kuhn C. Potential for waste heat utilization of hot-water-cooled data centers: a case study. Energy Sci Eng 2020;8:1793–810. https://doi.org/10.1002/ese3.633.

[6] Volkova A, Mašatin V, Siirde A. Methodology for evaluating the transition

process dynamics towards 4th generation district heating networks. Energy 2018;150. https://doi.org/10.1016/j.energy.2018.02.123.
[7] Esser A, Dunne A, Meeusen T, Quaschning S, Wegge D, Hermelink A, et al. Comprehensive study of building energy renovation activities and the uptake of nearly zero-energy buildings in the EU. Brussel, Belgium. European Commission; 2019.
[8] Volkova A, Krupenski I, Ledvanov A, Hlebnikov A, Lepiksaar K, Latõšov E, et al. Energy cascade connection of a low-temperature district heating network to the return line of a high-temperature district heating network. Energy 2020;198. https://doi.org/10.1016/j.energy.2020.117304.
[9] Kleinertz B, Brühl G, Veitengruber F, Pellinger C, Roon S Von. Transformation of an existing into a fourth generation heating network. Energy Procedia 2018;149. https://doi.org/10.1016/j.egypro.2018.08.212.
[10] Pelda J, Stelter F, Holler S. Potential of integrating industrial waste heat and solar thermal energy into district heating networks in Germany. Energy 2020;203. https://doi.org/10.1016/j.energy.2020.117812.
[11] Hanson J, Plößer T, Maihöfner D, Kuhn C, Sauerwein D, Stein T, et al. EnEff: Stadt Campus Lichtwiese : energieeffiziente Weiterentwicklung des Campus Lichtwiese durch intelligente Systemvernetzung (Abschlussbericht zum Fkz: 03ET1356 A). Darmstadt, Germany. Technical University of Darmstadt; 2019.
[12] BMUB. Climate Action Plan 2050 - principles and goals of the German govenment's climate policy. Berlin. Federal Ministry for the Environment, Nature Conservation, Building and Nuclear Safety (BMUB); 2016.
[13] Oltmanns J. Analysis and Improvement of an existing university district energy system. Technical University of Darmstadt; 2021. https://doi.org/10.26083/tuprints-00017367.
[14] Mauthner F, Herkel S. Task 52 - solar heat and energy economics in Urban Environments - technical Report Subtask C1 - technology and demonstrators. Solar Heating and Cooling Programme. Gleisdorf, Austria: International Energy Agency; 2016.
[15] Reed AL, Novelli AP, Doran KL, Ge S, Lu N, McCartney JS. Solar district heating with underground thermal energy storage: pathways to commercial viability in North America. Renew Energy 2018;126:1–13. https://doi.org/10.1016/j.renene.2018.03.019.
[16] Sibbitt B, McClenahan D, Djebbar R, Thornton J, Wong B, Carriere J, et al. The performance of a high solar fraction seasonal storage district heating system–five years of operation. Energy Procedia 2012;30:856–65. https://doi.org/10.1016/j.egypro.2012.11.097.
[17] Mangold D, Miedaner O, Tziggili EP, Schmidt T, Unterberger M, Zeh B. Technisch-wirtschaftliche Analyse und Weiterentwicklung der solaren Langzeit-Wärmespeicherung. Stuttgart. Stuttgart: Solites - Steinbeis Research Institute for Solar and Sustainable Thermal Energy Systems; 2012.
[18] Gehlin S. Borehole thermal energy storage. In: Rees S, editor. Adv. Ground-source heat pump syst. Elsevier; 2016. p. 295–327.
[19] Welsch B, Rühaak W, Schulte DO, Bär K, Sass I. Characteristics of medium deep borehole thermal energy storage. Int J Energy Res 2016;40:1855–68. https://doi.org/10.1002/er.3570.
[21] Gabrielli P, Acquilino A, Siri S, Bracco S, Sansavini G, Mazzotti M. Optimization of low-carbon multi-energy systems with seasonal geothermal energy storage: the Anergy Grid of ETH Zurich. Energy Convers Manag X 2020;8. https://doi.org/10.1016/j.ecmx.2020.100052.
[22] Welsch B. Technical, environmental and economic assessment of medium deep borehole thermal energy storage systems, Dissertation. Darmstadt: Technical University of Darmstadt; 2019.
[23] Sass I, Heldmann C-D, Lehr C. Erschließung eines Marmorkarstvorkommens als mitteltiefer Erdwärmesondenspeicher im Tuxertal, Tirol. Grundwasser 2016;21:137–45.
[24] Welsch B, Göllner-Völker L, Schulte DO, Bär K, Sass I, Schebek L. Environmental and economic assessment of borehole thermal energy storage in district heating systems. Appl Energy 2018;216:73–90. https://doi.org/10.1016/j.apenergy.2018.02.011.
[25] Elhashmi R, Hallinan KP, Chiasson AD. Low-energy opportunity for multi-family residences: a review and simulation-based study of a solar borehole thermal energy storage system. Energy 2020;204. https://doi.org/10.1016/j.energy.2020.117870.
[26] Rämä M, Wahlroos M. Introduction of new decentralised renewable heat supply in an existing district heating system. Energy 2018;154. https://doi.org/10.1016/j.energy.2018.03.105.
[27] Hemmatabady H, Formhals J, Welsch B, Schulte DO, Sass I. Optimized layouts of borehole thermal energy storage systems in 4th generation grids. Energies 2020;13. https://doi.org/10.3390/en13174405.
[28] Rehman H ur, Hirvonen J, Jokisalo J, Kosonen R, Sirén K. EU emission targets of 2050: costs and CO2 emissions comparison of three different solar and heat pump-based community-level district heating systems in nordic conditions. Energies 2020;13. https://doi.org/10.3390/en13164167.
[29] Behzadi A, Arabkoohsar A. Comparative performance assessment of a novel cogeneration solar-driven building energy system integrating with various district heating designs. Energy Convers Manag 2020:220. https://doi.org/10.1016/j.enconman.2020.113101.
[31] Sass I, Bär K, Schulte DO, Welsch B, Formhals J, Hornich W, et al. SKEWS (Solargekoppelter kristalliner Erdwärmesondenspeicher): Wärmespeicherprojekt der TU Darmstadt am Campus Lichtwiese. Darmstadt: 11 Tiefengeothermie-Forum; 2016.
[32] Schulte DO, Welsch B, Boockmeyer A, Rühaak W, Bär K, Bauer S, et al. Modeling insulated borehole heat exchangers. Environ Earth Sci 2016;75:910. https://doi.org/10.1007/s12665-016-5638-x.
[34] Modelica, Modelica Association. Version 3.4 [Software]. 2017. Available from: https://modelica.org/.
[35] SimulationX. Version 4.1 [Software]. ESI ITI; 2020. Available from: https://www.simulationx.de/.
[36] Kabelac S, Kind M, Martin H, Mewes D, Schaber K, Stephan P. VDI Heat Atlas. In: VDI e V. 11th. Berlin, Heidelberg, Germany: Springer-Verlag; 2013. 978-3-540-77876-9.
[37] Duffie JA, Beckman WA. Solar Engineering of Thermal Processes. In: Solar Energy Laboratory University of Wisconsin-Madison. 4th. New Jersey: John Wiley & Sons, Inc.; 2013. ISBN 978-0-470-87366-3.
[38] Liu BYH, Jordan RC. The long-term average performance of flat-plate solar-energy collectors. Sol Energy 1963;7. https://doi.org/10.1016/0038-092x(63)90006-9.
[40] TRNSYS. Version 18 [Software]. Thermal Energy System Specialists; 2020. Available from: http://www.trnsys.com.
[41] BBR. Updated and enhanced test reference years (TRY) of Germany for medium and extreme weather conditions. Germany: Federal Office for Building and Regional Planning (BBR); 2017.
[42] Formhals J, Hemmatabady H, Welsch B, Schulte DO, Sass I. A modelica toolbox for the simulation of borehole thermal energy storage systems. Energies 2020;13. https://doi.org/10.3390/en13092327.
[43] Kirschstein X. Modelling, simulation and analysis of the integration of seasonal underground thermal energy storages into Campus Lichtwiese district heating grid, Master thesis. Darmstadt: Technical University of Darmstadt; 2020.
[46] Louvet Y, Fischer S, Furbo S, Giovanetti F, Köhl M, Mauthner F, et al. Task 54 - price reduction in solar thermal systems - LCOH for solar thermal Applications. Solar Heating and Cooling Programme. International Energy Agency; 2017.
[47] Fish JCL. Engineering economics: first principles. second ed. New York: McGraw-Hill; 1923.
[48] Whitman DL, Terry R. Fundamentals of engineering economics and decision analysis. Barrett SF, editor. Synthesis lectures on engineering, vol. 18. Williston, VT, USA: Morgan & Claypool; 2012. https://doi.org/10.2200/S00410ED1V01Y201203ENG018.
[49] Lund H. The EnergyPLAN energy system Analysis model. Renewable Energy Systems. 2nd. London: Academic Press; 2014. p. 53–78. ISBN: 9780124095953.
[50] Oltmanns J, Freystein M, Dammel F, Stephan P. Improving the operation of a district heating and a district cooling network. Energy Procedia 2018;149:539–48. https://doi.org/10.1016/j.egypro.2018.08.218.
[51] Formhals J, Welsch B, Schulte DO, Sass I. Effects of the district heating supply temperature on the efficiency of borehole thermal energy storage systems. 3rd international conference on smart energy systems and 4th generation district heating 2017.
[52] Solar Collector Factsheet - Arcon-Sunmark HT-SolarBoost 35/10. 2018. Accessed 20 April 2021.
[53] Planungsanleitung VITOCAL 350-HT PRO. 2019. Accessed 20 April 2021.
[54] Isoplus - Design manual rigid compound systems. 2020. Accessed 20 April 2021.
[55] Welsch B, Schulte DO, Rühaak W, Bär K, Sass I. Thermal impact of medium deep borehole thermal energy storage on the shallow subsurface. Vienna: European Geosciences Union General Assembly; 2017.

## Appendix D – AI-based enviro-economic optimization of solar-coupled and standalone geothermal systems for heating and cooling

Published as:

**Hemmatabady H**, Welsch B, Formhals J and Sass I (2021): AI-based enviro-economic optimization of solar-coupled and standalone geothermal systems for heating and cooling, Applied Energy, 311, 118652, doi:/10.1016/j.apenergy.2022.118652

Applied Energy 311 (2022) 118652

Contents lists available at ScienceDirect

Applied Energy

journal homepage: www.elsevier.com/locate/apenergy

# AI-based enviro-economic optimization of solar-coupled and standalone geothermal systems for heating and cooling

Hoofar Hemmatabady *, Bastian Welsch, Julian Formhals, Ingo Sass

*Geothermal Science and Technology, Technical University of Darmstadt, Schnittspahnstraße 9, 64287 Darmstadt, Germany*
*Graduate School of Excellence Energy Science and Engineering, Technical University of Darmstadt, Otto-Berndt-Str. 3, 64287 Darmstadt, Germany*

## HIGHLIGHTS

- Long-term enviro-economic optimizations of shallow geothermal layouts are conducted.
- Solar-coupled layouts with heat pumps are the most favorable option for heating.
- Standalone layouts are reasonable options for combined heating and cooling.
- The combination of ANN and multi-objective optimization methods is an accurate approach.

## ARTICLE INFO

*Keywords:*
District heating and cooling
Borehole thermal energy storage
Environ-economic method
Artificial neural network
TRNSYS
Multi-objective optimization

## ABSTRACT

Borehole heat exchanger (BHE) arrays represent a key technology for the future provision of sustainable building heating and cooling energy. They are either used as pure geothermal systems only extracting heating energy from the subsurface or they are also used to store excess heat from solar thermal collectors or waste heat from cooling applications in summer. The diversity of the systems makes it difficult to identify the optimal system in terms of emission reduction and economic efficiency. In this study, we assess the most relevant BHE system layouts for heating-only as well as combined heating and cooling purposes using dynamic simulations of the overall heating system in combination with an enviro-economic analysis method. The assessment routine is used in a multi-objective optimization approach to minimize the different system layouts' emission factor (EF) and their levelized cost of energy (LCOE). In order to cope with the high computational cost of the required long-term considerations, an artificial neural network (ANN) has been used to generate a proxy model in an intermediate step of the multi-objective optimization procedure. This approach delivers reliable optimization results, which reveal, that the lowest emissions for heating and cooling systems are realized by solar-assisted layouts. Comparison with a fossil-based reference layout shows that the most economical BHE layout accomplishes a 60% reduction in the EF with a moderate increase in the LCOE of only 13%. If, however, emission penalty costs are taken into account, the evaluated layouts also become economically advantageous compared to fossil-based systems.

## 1. Introduction

Climate change is a serious issue that the world is confronted with. Greenhouse gases (GHG) emitted by energy use from fossil fuels are the main reason for climate change [1]. In Europe, buildings require 40% of the overall energy and emit 36% of the GHG [2]. Heating and hot water consume 79% of the final energy demand in European households [3]. Cooling of buildings still has small share, but the demand is expected to increase considerably as the climate warms on average [4]. It is estimated that by 2025 the installed cooling capacity in Europe is likely to be 55–60% higher than in 2010 [5]. Statistics show that approximately 75% of heating and cooling is generated from fossil fuels [6]. Consequently, simultaneous supply of heating and cooling with higher sustainability needs to be considered as an important part of future energy systems.

By 2050, more than 80% of European residents are expected to live in urban areas [7]. This trend increases the benefits of district energy

* Corresponding author at: Geothermal Science and Technology, Technical University of Darmstadt, Schnittspahnstraße 9, 64287 Darmstadt, Germany.
*E-mail addresses:* hemmatabady@geo.tu-darmstadt.de (H. Hemmatabady), welsch@geo.tu-darmstadt.de (B. Welsch), formhals@geo.tu-darmstadt.de (J. Formhals), sass@geo.tu-darmstadt.de (I. Sass).

https://doi.org/10.1016/j.apenergy.2022.118652
Received 11 June 2021; Received in revised form 5 December 2021; Accepted 25 January 2022
Available online 4 February 2022

**Nomenclature**

| | |
|---|---|
| ANN | artificial neural network |
| ASHP | air-source heat pump |
| BHE | borehole heat exchanger |
| BST | buffer storage tank |
| BTES | borehole thermal energy storage |
| COMP | compromise |
| DC | district cooling |
| DH | district heating |
| DHC | district heating and cooling |
| Eco | economical |
| EF | emission factor |
| Env | environmentally-friendly |
| GB | gas boiler |
| GHG | greenhouse gases |
| GSHP | ground-source heat pump |
| HEX | heat exchanger |
| HP | heat pump |
| LCA | life cycle assessment |
| LCC | life cycle cost |
| LCOE | levelized cost of energy |
| NG | natural gas |
| NSGA | non-dominated sorting genetic algorithm |
| Op | operation |
| STC | solar thermal collector |

*Symbols*

| | |
|---|---|
| A | area of solar collector $m^2$ |
| a | year |
| $a_0$ | intercept efficiency |
| $a_1$ | efficiency slope kJ/hr.$m^2$.K |
| $a_2$ | efficiency curvature kJ/hr.$m^2$.$K^2$ |
| Cap | capacity kW |
| f | fuel consumption kWh |
| GWP | global warming potential g CO2 eq /kWh |
| i | component number |
| I | incident radiation on solar collectors kJ/hr.$m^2$ |
| IC | initial cost €/kWh |
| L | Length m |
| LCC | the present value of total life cycle cost € |
| LCOE | levelized cost of energy €/kWh |
| MC | maintenance cost €/kWh |
| n | number of systems components |
| N | number |
| OC | operational cost €/kWh |
| Q | thermal out put kWh |
| r | discount rate % |
| T | Temperature °C |
| Vol | Volume $m^3$ |
| $\dot{Q}$ | heat flux kW |
| η | Efficiency % |

*Subscripts*

| | |
|---|---|
| BHE | borehole heat exchanger |
| BST | buffer storage tank |
| BTES | borehole thermal energy storage |
| CL | cooling load |
| Elec | electricity |
| F | fuel |
| GB | gas boiler |
| HP | heat pump |
| IC | initial cost |
| MC NG | maintenance cost natural gas |
| Prod | production |
| ret | return |
| sup | supply |
| tot | total |

systems, which tend to be more economic for densely populated regions [8]. 4th generation district heating (4GDH) networks, with supply temperatures of less than 50 °C, are suitable for recycling heat from low-temperature sources such as solar and geothermal [9]. A future district cooling (DC) system, can be defined as a system more interactive with the electricity, DH and gas grids [9]. Overall, a 4th generation DHC grid can be considered as an interactive low-temperature energy grid to satisfy both heating and cooling demands [9,10]. The significant share of heating in final energy demand of European households as well as the increasing trend towards smart energy systems has made district heating (DH) a viable option for future energy supply [7,11].

As one of the main renewable energy sources, solar energy can have a major contribution in sustainable heating supply. Flat plate solar thermal collectors (STC), which are the most common type for heating applications, operate more efficiently at lower temperature levels [12]. Therefore, they are suitable options for low-temperature DH networks. However, the temporal mismatch between solar thermal supply and heat demand is a major drawback of such systems. To overcome this problem, seasonal energy storage technologies are essential. They can also be utilized in cooling cycles, where the rejected waste heat is stored seasonally for further use in the heating season.

Thermal energy storage (TES) technologies can be categorized to sensible, latent and chemical heat storage, from which chemical and latent TES solutions are not competitive for large-scale (district) applications [13]. Only some sensible heat storage technologies are appropriate for large-scale TES, which can be classified to large aboveground water tanks and underground TES (UTES) systems [14]. The most common types of UTES systems include tank TES, pit TES, aquifer TES and borehole TES (BTES) [15,16]. The main concentration of this study is on shallow BTES systems, with depths usually less than 100 m, but partly also in excess of 200 m [17]. BHEs with depths of more than 400 m are not dealt with shallow geothermal standards [17]. BTES systems exploit the high underground thermal capacity, to store large quantities of fluctuating renewable or waste energy on a seasonal basis [18,19]. In general, a BTES system consists of an array of boreholes, each fitted with a BHE, which is a closed-loop pipe system placed in a borehole. The number of BHEs, their radial distance and their length define the size of the storage [20]. The BHEs are backfilled with a cement-based grouting material, which stabilizes the borehole, provides hydraulic sealing and improves thermal contact with the underground. The heat transfer process starts by circulating a heat transfer fluid (usually a water-glycol mixture) in the pipes [21].

The high efficiency of BTES systems, especially in lower temperature levels [22,23], makes them a promising option for integration into low-temperature solar DH networks, to fill the temporal mismatch between solar thermal supply and heat demand. Moreover, BTES systems can be utilized to shift the excess heat from cooling seasons to be used in heating seasons for combined heating and cooling applications. The underground has higher/lower temperatures in heating/cooling seasons, compared to the ambient temperature. Higher source temperatures lead to more efficient operation of heating cycles. On the other hand, lower sink temperatures result in enhanced performance of cooling cycles. Consequently, in addition to its utilization for TES on a long-term basis, the underground is an efficient heat source/sink of conventional ground-source HP (GSHP) systems for heating-/cooling-only purposes.

Various implementation projects have already proven the

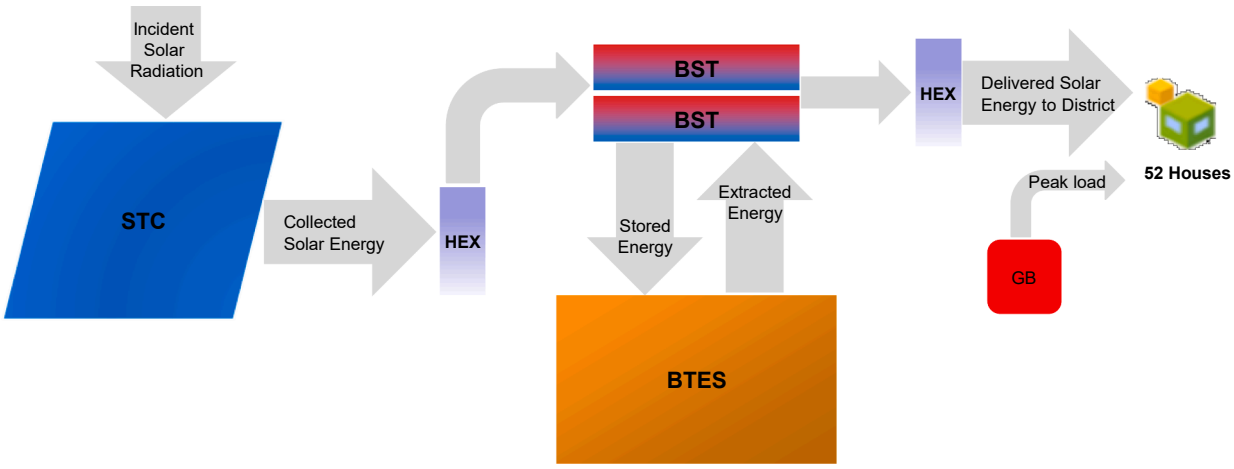


**Fig. 1.** Energy flow diagram of the reference case, modified after [33].

practicability of geothermal heating and cooling systems, for examples refer to [24,25]. However, the main issue that may lead to reduced efficiency of these systems is their inappropriate design and dimensioning considering their interaction with other components of the energy system. An exemplary system in Germany, consists of a BTES that is charged by STCs and discharged by a HP, which are connected to two buffer storage tanks (BSTs) [26,27]. The low HP capacity of this system led to its inefficient operation and caused a large capacity of the BTES to be remained unused as it is discharged less than planned [27]. Moreover, stagnation occurred in STCs due to smaller dimensions of the BTES, BST and HP, compared with design values [27]. A BTES should not be regarded in isolation, but merely as one component within a district heating and cooling network [18]. Guidelines are required for design and optimization of the BTES systems in DHC networks, considering their integration with other system components.

Considering the experience from demonstration and pilot projects, different configurations of BTES-assisted systems represent viable options. These need to be evaluated from a technical, economic and environmental point of view in order to increase their share in a sustainable thermal load supply. With this goal in mind, many studies have been conducted in recent years. Life cycle assessment (LCA) studies demonstrate that the integration of BTES systems yields a large reduction in global warming potential (GWP) [28,29]. Furthermore, the results of a parametric study on a BTES-assisted solar DH system show that, besides reducing GWP, they are economically more favorable than GSHPs [30]. Multi-objective optimization to simultaneously minimize the life cycle cost (LCC) and CO2 emissions of a BTES-assisted central heating system in different cold climate locations depicts its viability [31]. Moreover, the results of energetic and LCC analysis of a small-scale BTES-assisted solar DH system for several locations in the UK show the technical feasibility of these systems. However, encouraging financial policies are required for a faster rollout [32].

Nevertheless, none of the aforementioned and other similar studies have compared possible layouts of BTES-assisted systems for heating as well as cooling from environmental and economic points of view. In addition, as the operation of BTES systems and their temperature level are strongly dependent on the stored and extracted energy as well as the number of charging and discharging cycles, they should be evaluated on a long-term basis such as the project life time. Since such a long-term assessment entails high computational costs, though, optimization approaches for minimizing GWP and LCC are mainly based either on simplified parametric studies or on multi-objective optimizations with a limited number of variables or simulation years. This in turn is associated with lower accuracies. Moreover, due to computational costs the optimizations are mainly conducted with a limited number of evaluations, which rarely leads to final convergence of optimization algorithms. Therefore, an optimization study for comparing possible heating and cooling layouts of the BTES systems to specify decisive optimization variables, with less restrictions to the number of the variables, is needed. This should be done during project lifetime with unlimited number of evaluations until real convergence of the optimization problem.

In this study, solar-assisted and standalone geothermal layouts for heating as well as combined heating and cooling applications are compared using an environ-economic analysis method to minimize emission factor (EF) and Levelized Cost of Energy (LCOE). Initially, a model of a well-known reference system from Canada [33] is created, which is validated against real operational data. Subsequently, the boundary conditions are adapted to a case study in Germany. Based on the reference scenario and other studies, alternative layouts and their control strategies are then proposed. For modeling the different system layouts, the Software TRNSYS [34] is used. To evaluate the proposed designs, a combination of artificial neural network (ANN) and multi-objective optimization methods is utilized for predicting and minimizing the objective functions in MATLAB [35]. The ANN approach is required to reduce the optimization time. It is used as an intermediate stage to predict and validate the objective functions after initial evaluations of the objectives by a genetic algorithm. This leads to higher accuracy of the predicted functions for the optimization purposes with less input data, in comparison with similar studies which normally utilize uniform distribution functions to generate data in the evaluated space, e.g. [36]. As the final stage of the computational procedure, the validated objective functions are optimized until the final convergence of the optimization algorithm. Finally, a sensitivity analysis is conducted to assess the effect of changing cost functions.

Optimization results of this study define dimensions of the most important components of geothermal layouts by taking their required long-term evaluations into consideration. Utilizing the proposed computational model, it is assured that the results are converged to the best solutions. Consequently, design guidelines for geothermal systems, considering their transient interaction with other system components during project lifetime can be presented, which has not been done so far.

## 2. Reference case selection and validation

The selected reference case, Fig. 1, is the BTES system in Drake Landing Solar Community [37]. In summer, nearly 2,300 $m^2$ roof-mounted flat plate STCs store solar energy in 144 single U-tube borehole heat exchangers (BHE) with a length of 35 m each. During winter operation, the recovered energy from the BTES and the collected energy from the STCs provide most of the required heating load for 52 single-family homes, supported only by a gas boiler (GB) to supply peak

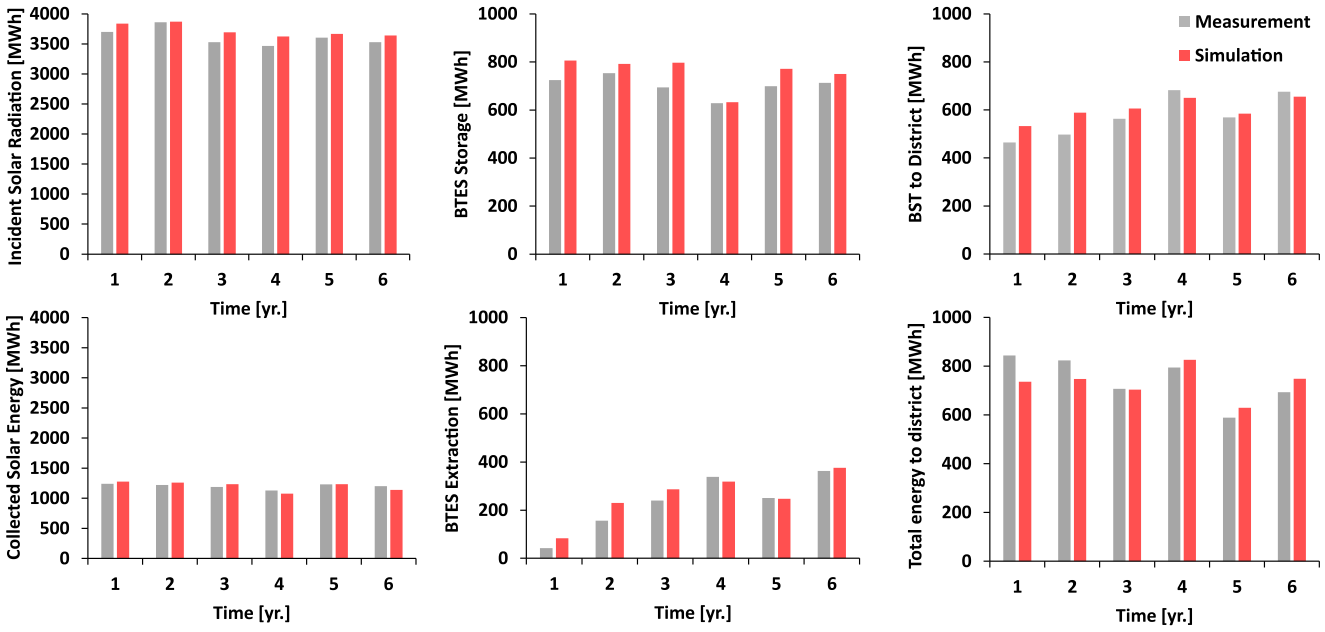


**Fig. 2.** Simulation results (orange) vs. measurement data (blue) of the reference case.

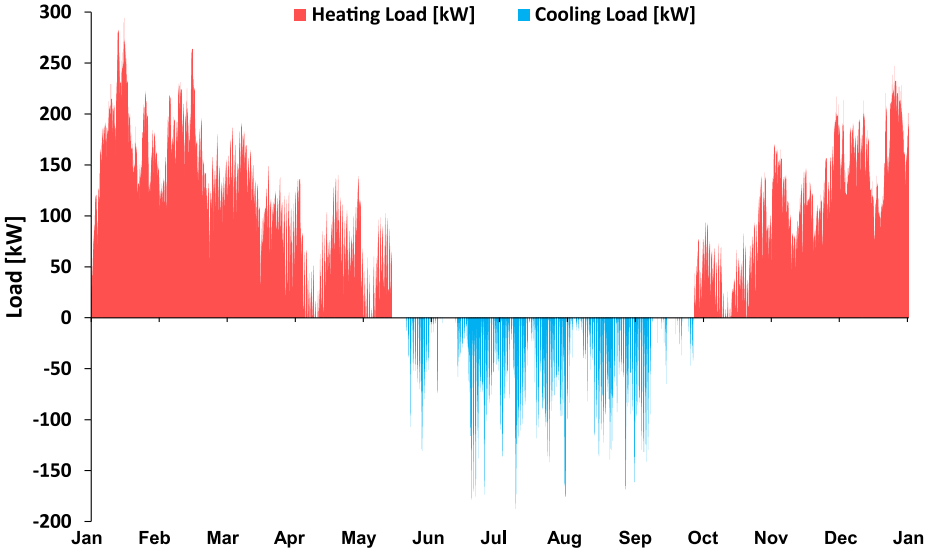


**Fig. 3.** District load profile.

demand. Two horizontal BSTs, each having a volume of 120 $m^3$, are used for diurnal storage of solar energy and the thermal connection of solar, ground and district loops. Two heat exchangers (HEXs) separate solar and district loops from BSTs and ground loop.

In case of the validation of reference model, data from the annual report [33], calibrated parameter values from the designers [38–40], a regression model for calculating load profile as a function of ambient temperature [40] and the weather data of 6 years of operation [41] serve as model inputs. Fig. 2 shows the simulation results in TRNSYS against the measured numbers as given in the annual report. It can be seen that the simulation can represent the performance of the system in operation. The deviations between the measurement and the simulation results are mainly due to differences in the operational strategies used in the simulation (cf. Chapter 4.1.1.) in comparison with the ones applied in reality [33,42]. Moreover, to enhance system's performance, modifications have been implemented to the system during years of operation [33]. Overall, it can be concluded that the system can be used as a validated reference case for a generic study to compare different layouts of geothermal systems.

## 3. Case study

### 3.1. Case study setup

A notional urban quarter in Frankfurt, Germany, consisting of 31 single-family homes and 4 office buildings is considered in a generic case study. Load profiles of each building topology are calculated using 3D thermal zone models in TRNBuild, taking into account weather data from Frankfurt [10,43,44]. Construction materials, occupation schedules and set point temperatures are based on standard libraries [44,45].

Fig. 3 shows the total calculated load profile of the quarter. The overall annual heating and cooling demands are 523 MWh and 62 MWh, respectively, with most of the cooling demand attributed to the office buildings. In heating mode, the supply temperature ($T_{sup}$) to the

**Table 1**
The proposed scenarios for heating-only mode.

| Scenario | Heating | Cooling | STC | GHE | BST | GB |
|---|---|---|---|---|---|---|
| H1 | Passive (BTES) | — | Flat plate | 2U-tube | Vertical | Peak |
| H2 | Active (BTES) | — | Flat plate | 2U-tube | Vertical | Peak |
| H3 | Active (GSHP) | — | — | 2U-tube | Vertical | Peak |

**Table 2**
The proposed scenarios for combined heating and cooling mode.

| Scenario | Heating | Cooling | STC | GHE | BST | GB |
|---|---|---|---|---|---|---|
| HC1 | Passive (BTES) | Active (ASHP) | Flat plate | 2U-tube | Vertical | Peak |
| HC2 | Active (BTES) | Active (ASHP) | Flat plate | 2U-tube | Vertical | Peak |
| HC3 | Active (BTES) | Passive (BTES) | — | 2U-tube | Vertical | Peak |

buildings is a function of the ambient temperature with gliding-constant operation [30] and minimum and maximum values of 37 °C and 41 °C, respectively. The return temperature ($T_{ret}$) is approximately 7 °C lower. These values are compatible with the temperature level of low-energy buildings, 4GDH grids and the reference case. In cooling mode, $T_{sup}$ and $T_{ret}$ are 18 °C and 22 °C, respectively, which are reasonable values for passive geothermal cooling operation [46].

### 3.2. Adapting the reference case to the case study

In a next step, the validated reference case model is adapted to the case study. This includes the adjustment of different location-dependent parameters such as the solar irradiation and BTES thermophysical properties. Moreover, the reference BHE type is replaced by double U-tube BHEs, which are the most popular type of BHEs in Germany [21]. Furthermore, the horizontal BSTs from the reference system are substituted by vertical BSTs, which are commonly used in central solar heating plants in Germany [26]. The main advantage of vertical BSTs is reduced mixing and heat loss due to smaller relative contact area between water temperature layers. This advantage is more in tanks with higher aspect ratios [33], which can be reached easier by using two (multiple) BSTs, especially when there is a limitation for maximum allowable installation heights. Moreover, using two (multiple) BSTs, as the center of a thermal plant, ensures more sustainable and consistent load supply. Therefore, in this study, as in the reference case and other similar plants like [47], two BSTs are considered. Definition of the optimum number and length of the BHEs and volume of the BSTs is part of this study.

## 4. System design scenarios

Two different operational scenarios are considered: heating-only mode (H) and combined heating and cooling mode (HC). For each of these, three different system designs are compared.

In heating-only mode (Table 1), two system layouts (H1 and H2) contain a BTES systems, which is charged by STCs during summer season. In winter, system H1 supplies the heating load passively without the use of HPs, while system H2 uses HPs. The third system option H3 represents a conventional GSHP system without storage or regeneration.

In combined heating and cooling mode (Table 2), the solar-assisted BTES systems (HC1 and HC2) are heated up by STCs during the summer seasons as well. Therefore, they cannot be used as heat sink for cooling purposes efficiently. In both cases, the cooling load is supplied by an air-source HP (ASHP). As for the heating-only scenario, the heating load in winter is either provided without (H1) or with (H2) HPs. Again, the third system layout (HC3) lacks STCs. Instead, the rejected waste heat from the cooling cycle is passively stored in the BTES system, which renders the air-source heat pump obsolete. When the BTES temperature is not low enough for passive cooling load supply, HPs meet the load actively. In the heating season, the BTES is once more discharged actively with the use of the HPs.

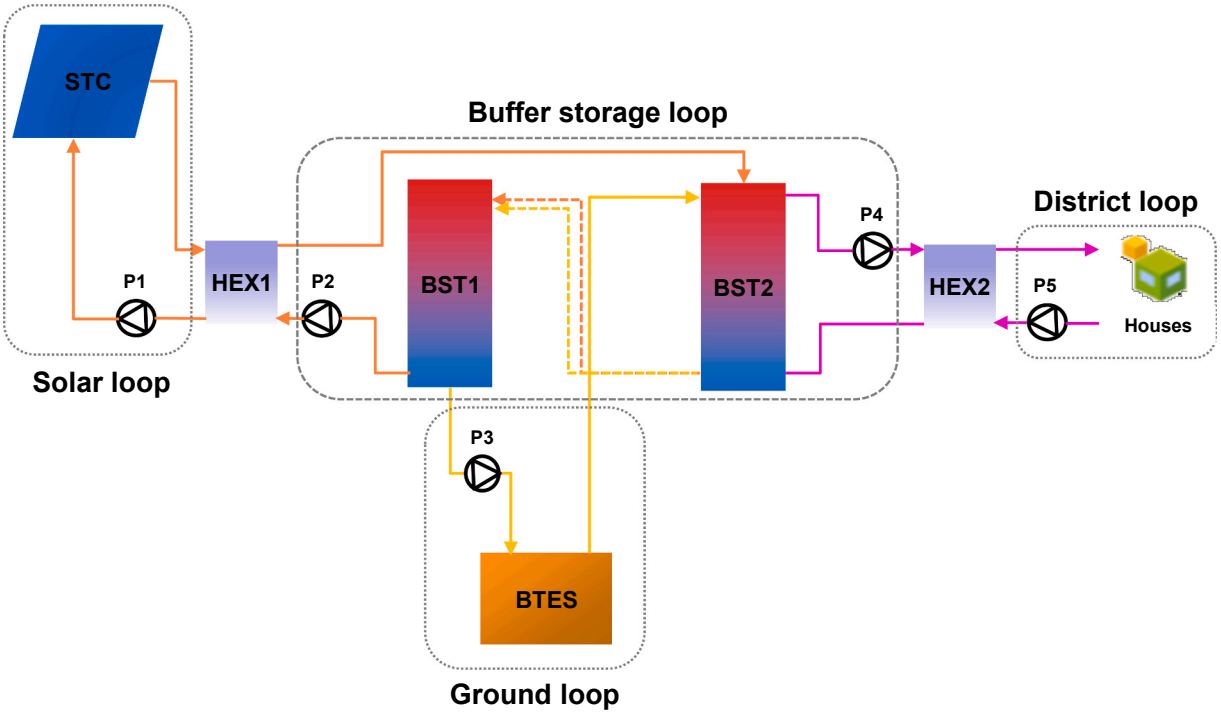


**Fig. 4.** System layout of the passive heating (BTES).

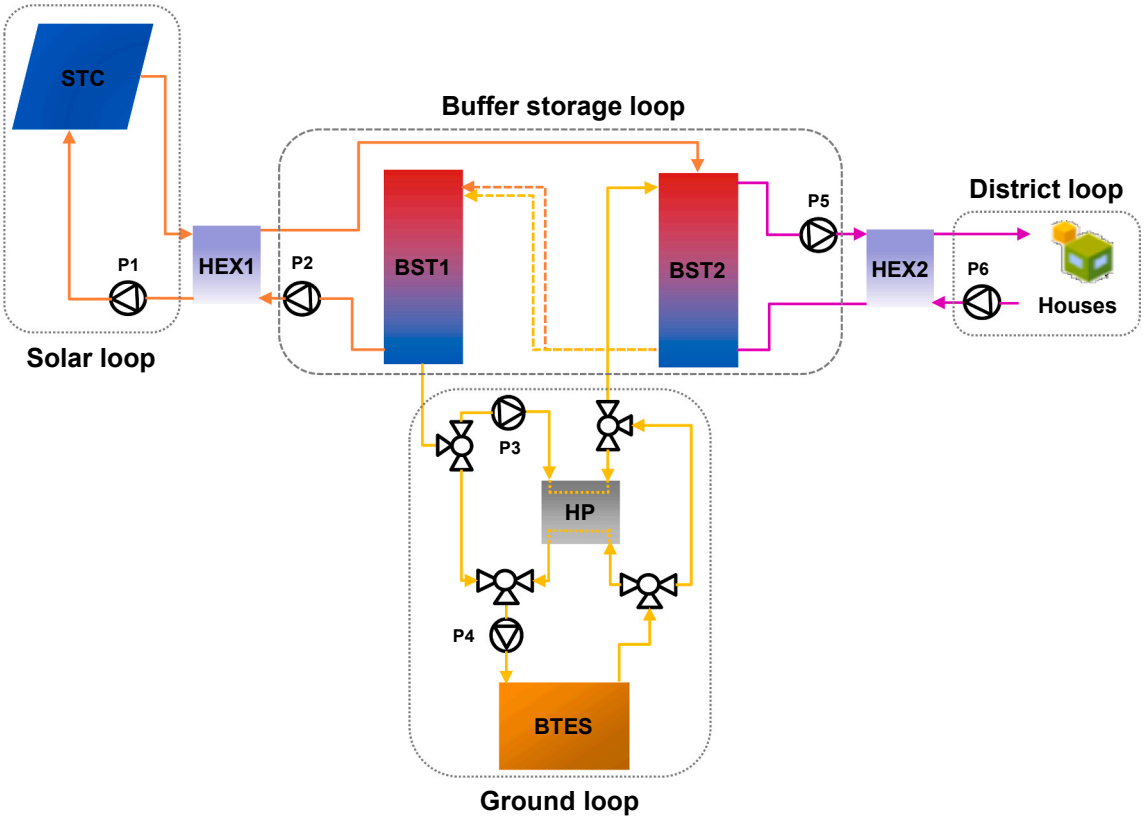


**Fig. 5.** System layout of the active heating (BTES).

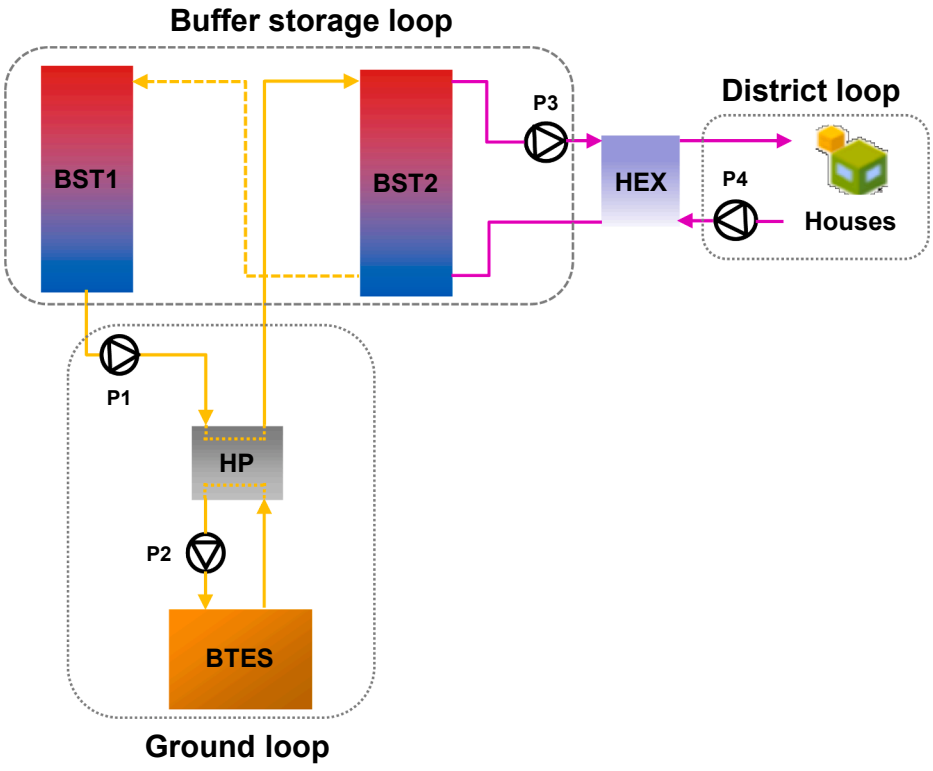


**Fig. 6.** System layout of the active heating (GSHP).

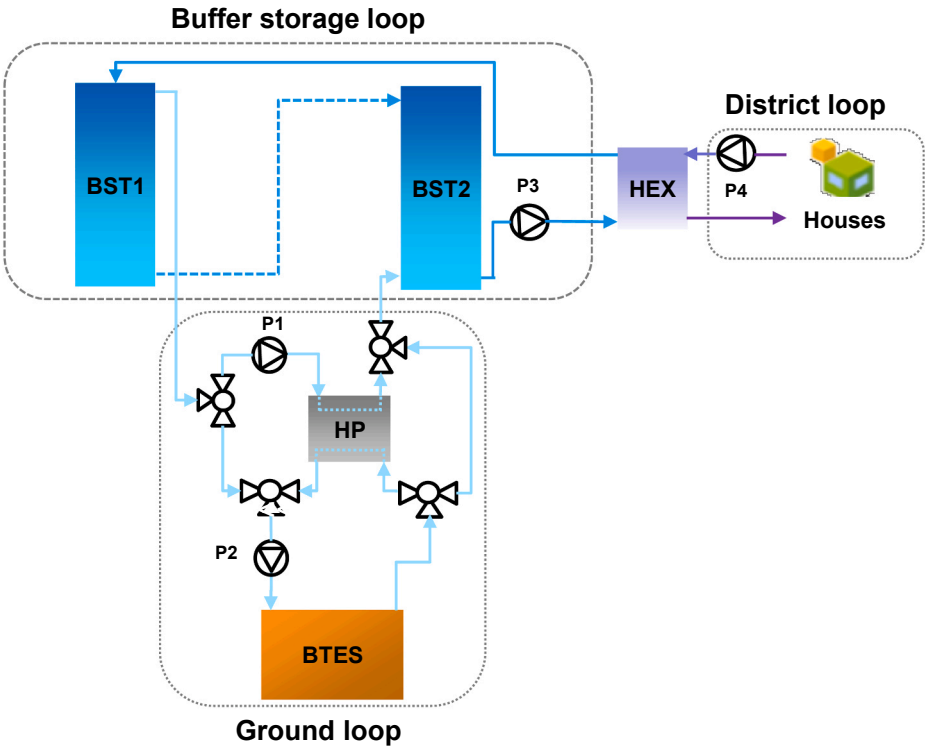


**Fig. 7.** System layout of the BTES in cooling mode.

### 4.1. Heating operation

#### 4.1.1. Passive heating (BTES)

A simplified representation of system layout H1 in discharging mode is illustrated in Fig. 4. During summer operation, the collected solar energy is delivered to the BSTs via the solar loop HEX (HEX1). The control strategy is adapted from [48]. A variable-speed STC pump (P1) is activated by a differential controller, which monitors the outlet temperature of the STCs, the top temperature of the warmer BST and the bottom temperature of the colder BST. The design temperature difference (ΔT) of STCs is taken as 15 K [42]. The variable-speed pump that delivers the solar energy to the BSTs (P2) has the same flow rate as the solar loop pump, with the nominal flow rate slightly lower than the solar loop, as in the reference case [42].

Charging of the BTES is controlled by a differential controller, which monitors the temperature difference ΔT between the BTES center and the top of the warmer BST (BST2). Similarly, ΔT between the BTES center and the bottom of the colder BST (BST1) is used for BTES discharging control. In both modes, a high limit cut-out prevents the BTES and BST2 from overheating. A supplementary charging mode is also possible in parallel with the discharging mode, especially during transition seasons, when the solar yield exceeds the heating demand.

Another variable-speed pump (P4) is placed in the loop that delivers BSTs energy to the district HEX (HEX2). Its flow rate is controlled by the HEX's energy balance equation and the supply temperature in the district loop $T_{sup}$ so that the fluid of the district loop is heated up to set point. The variable-speed pump of the district loop (P5) is also controlled to meet the district design ΔT (cf. Chapter 3.1.).

#### 4.1.2. Active heating (BTES)

For the H2 layout (Fig. 5) the control strategies of solar, buffer storage and district loops are the same as for H1. A HP, which is chosen based on the operational data from a manufacturer [49], discharges the BTES actively and is bypassed when the BTES temperature is high enough to supply the load passively. The HP and the BTES pumps (P3 and P4) start working when the BSTs are not hot enough to supply the demand. For this purpose, the ΔT between the district $T_{sup}$ and the bottom of the colder BST (BST1) is monitored as the dead band for filling the BSTs. Moreover, the top of the warmer BST (BST2) is monitored as high limit cut-out. The flow rate on the load side of the HP is modulated considering its capacity and the design ΔT of the BST side of the district HEX.

#### 4.1.3. Active heating (Geothermal)

In the H3 scenario (Fig. 6) a GSHP actively supplies the heating load. The control strategies of the buffer storage and the district loops are similar to the H1 layout. For the BTES loop, the control strategy is similar to the active mode of the H2 layout, where the temperatures of the district and the BSTs are monitored to control the filling level of tanks. The load side flow rate of the GSHP is also modulated considering its capacity and the design ΔT of the BST side of the district HEX.

### 4.2. Cooling operation

In the combined heating and cooling scenarios, the operational data of the ASHP used for cooling in the layouts HC1 and HC2 is selected based on a manufacturer's catalog [50]. The control strategy for the BTES when used as the heat sink for passive cooling in layout HC3 (Fig. 7) is set by a differential controller. It monitors ΔT between the BTES center and the top of the BST1, which is the entering node of the return fluid from the district loop HEX. Active cooling mode is activated as soon as the passive cooling controller turns off due to high BTES temperatures and the $T_{sup}$ of the district exceeds the design value.

## 5. Evaluation criterion

### 5.1. Environmental analysis

For the environmental assessment of the proposed system layouts their EF is calculated by dividing their overall GWP by total thermal

**Table 3**
Objective functions and optimization variables.

| Objective functions | Definition |
|---|---|
| min EF | Emission Factor |
| min LCOE | Levelized Cost of Energy |
| **Subject to** | |
| $30\ m \leq L_{BHE} \leq 400\ m$ | Length of BHEs |
| $6 \leq N_{BHE} \leq 300$ | Number of BHEs |
| $56.6\ kW \leq Cap_{HP}{}^{a} \leq 300\ kW$ | Capacity of HP |
| $13.57\ m^2 \leq A_{STC} \leq 5000\ m^2$ | Are of STCs |
| $10\ m^3 \leq Vol_{BST} \leq 1000\ m^3$ | Volume of BSTs |

[a] for active scenarios.

**Table 4**
Main TRNSYS parameters.

| Component | Parameter | Value | Component | Parameter | Value |
|---|---|---|---|---|---|
| **BTES** | BHE type | 2U | **STC** | Fluid specific heat | 3.798 kJ/(kg·K) |
| **Type 557** | Boreholes in series | 3,6 | **Type 1a** | Efficiency mode | 2 |
| | Borehole radius | 0.065 m | | Tested flow rate | 25 l/min |
| | Pipe outer/inner radius | 0.016/0.013 m | | Intercept efficiency | 0.778 |
| | BTES thermal conductivity | 2.6 W/(m·K) | | Efficiency curvature | 0 |
| | BTES heat capacity | 2080 kJ/(m³·K) | | | |
| | Grout thermal conductivity | 2 W/(m·K) | **HEX** | | |
| | Fluid specific heat | 4.182 kJ/(kg·K) | **Type 91** | Effectiveness | 0.80 |
| | | | **Type 512** | Effectiveness | 0.95 |
| **BST** | Number of tank nodes | 30 | | | |
| **Type 534** | Number of ports | 4 | **HP** | Rated heating capacity | 56.6 kW |
| | Aspect ratio | 3.916 | **Type 927c** | Rated power | 13.2 kW |
| | Loss coefficient | 0.15 W/(m²·K) | | Rated cooling capacity | 43.4 kW |
| **Pump** | Total pump efficiency | 60% | **Boiler** | Efficiency | 95% |
| **Type 110** | | | **Type 700** | | |

[c] Values at entering load-side and source-side temperatures of 30 °C and 0 °C [36].

output ($Q_{tot}$), Eq. (1) [28]. The overall GWP is calculated using Eq. (2). It adds up the GWP associated with the production of n system components ($GWP_{Prod,i}$), cf. Table A1, and the GWP associated with the emissions caused during the operation of the evaluated layout ($GWP_{Op,a}$) for the whole project lifetime ($a_{life}$). $Q_{tot}$ is the summation of thermal output at each year ($Q_a$) during project lifetime.

$$EF = \frac{GWP}{Q_{tot}} \tag{1}$$

$$GWP = \sum_{i=1}^{n} GWP_{Prod,i} + \sum_{a=1}^{a_{life}} GWP_{Op,a} \tag{2}$$

After calculating the yearly consumption of electricity ($f_{elec,a}$) and natural gas ($f_{gas,a}$), $GWP_{Op,a}$ can be calculated using Eq. (3). The EFs associated with electricity and natural gas consumption as functions of the assessment year ($EF_{elec,a}$ and $EF_{gas,a}$) are calculated based on available data for Germany as given by IINAS [51,52]. They are projected into the future using the evolutionary scenario by Welsch et al. [28], Table A.2.

$$GWP_{Op,a} = f_{elec,a}EF_{elec,a} + f_{gas,a}EF_{gas,a} \tag{3}$$

### 5.2. Economic analysis

The economics of the various system layouts are compared on the basis of the achieved LCOE. These can be calculated by dividing the present value of total LCC of an overall system layout by the discounted total energy using Eq. (4) [53]. $C_{IC,a}$ are the capital investment costs, $C_{MC,a}$ are the maintenance costs and $C_{F,a}$ are fuel costs. $a_{life}$ and the discount rate (r) are assumed as 30 years and 3%, respectively.

$$LCOE = \frac{\sum_{a=1}^{a_{life}} (C_{IC,a} + C_{MC,a} + C_{F,a}) \cdot (1+r)^{-a}}{\sum_{a=1}^{a_{life}} Q_a (1+r)^{-a}} \tag{4}$$

Investment cost (IC) and maintenance cost (MC) of the main components are based on benchmark functions, c.f. Tables A.3. Based on the annual consumption values $f_{elec,a}$ and $f_{gas,a}$, $C_{F,a}$ is calculated using Eq. (5). Electricity and natural gas costs are defined as functions of the assessment year ($c_{elec,a}$ and $c_{gas,a}$) by linearly projecting the estimated values by economic reports, cf. Table A.4 and Table A.5.

$$C_{F,a} = f_{elec,a}c_{elec,a} + f_{gas,a}c_{gas,a} \tag{5}$$

### 5.3. Enviro-economic optimization

The aim of an enviro-economic optimization is to simultaneously minimize the LCOE and the EF. However, both target functions compete with each other. Systems with a lower EF usually cost more. Therefore, multi-objective optimization is required to find the best solutions for both. The objective functions, optimization variables and their boundaries are listed in Table 3. The optimization variables are chosen to define dimensions of important components of a geothermal layout, including BTES ($L_{BHE}$ and $N_{BHE}$), HP ($Cap_{HP}$), STCs ($A_{STC}$) and BSTs ($Vol_{BST}$).

## 6. Computational model

### 6.1. Modeling and simulation

In the following section, the main components (TRNSYS types) used for the modeling of the proposed layouts are discussed. Moreover, the most important parameters of each type can be found in Table 4.

Type 1a is used for the simulation of STCs, which is based on a quadratic efficiency performance model (Eq. (6)) [34] for the calculation of STC efficiency $\eta_{STC}$. Coefficients $a_0$, $a_1$ and $a_2$ are obtained from standardized collector performance tests, $\Delta T$ is the difference between the mean fluid temperature and ambient temperature and I is the incident radiation on STCs. Initial values for the validation of the reference case were taken from benchmark values given in [54].

$$\eta_{STC} = a_0 - a_1\frac{\Delta T}{I} - a_2\frac{(\Delta T)^2}{I} \tag{6}$$

The BTES is modeled using the duct storage model (Type 557) [55]. As mentioned in Chapter 3.2., double U-tube BHEs are chosen. The BHE-related design parameters, e.g. pipe material and dimensions, are selected based on standard libraries [46] and location-specific parameters. Furthermore, the storage thermal conductivity and heat capacity are taken from experimental data [56].

Type 534 is used for the modelling of the BST. It divides the tank into a series of isothermal layers to account for stratification. The number of layers is chosen in accordance with benchmark studies [39] and a manual refinement study. Data from a manufacturer [57] and installed

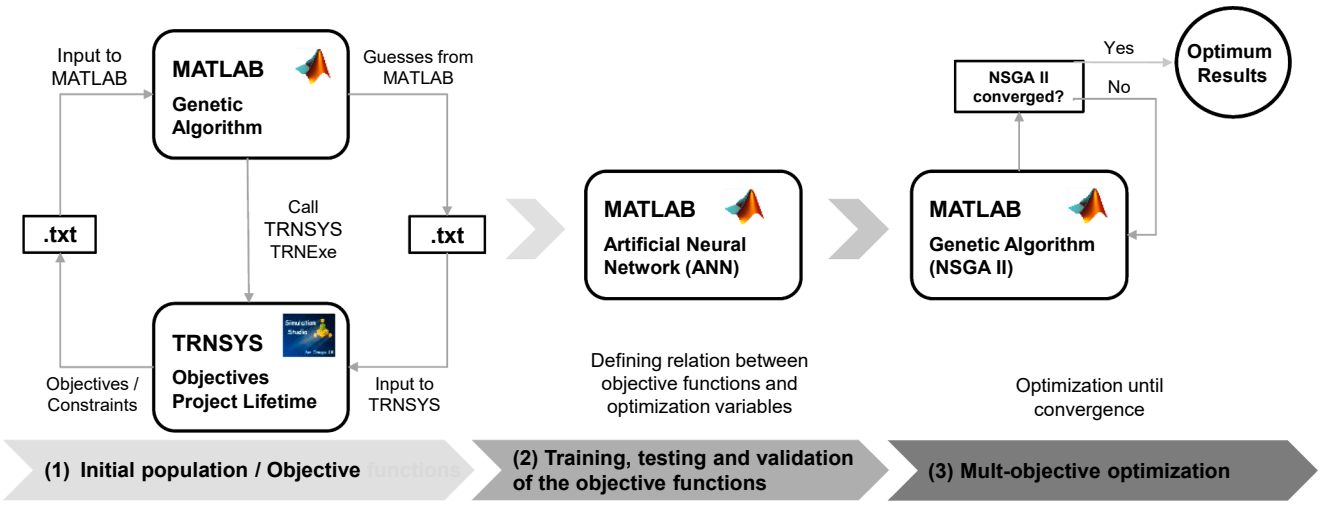


**Fig. 8.** Optimization procedure.

systems (e.g. [58]) are used for specifying loss coefficient and aspect ratio.

Type 927 is used for simulating HPs. It works based on interpolation with four independent variables: Output capacity, corresponding outlet source and load side temperatures as well as flow rates are read based on inlet temperatures and flow rates from a provided catalog file [49]. After preparing the catalog data files, their validity was checked against the manufacturers' catalogs at various operating conditions.

Peak demands are covered by a condensing GB with an energetic efficiency of 95% [59]. It is modelled using Type 700.

The HEX of the solar loop is modelled by Type 91b. The district HEX is modelled by Type 512, which sends a control signal to the variable-speed pump on the BST side according to the required $T_{sup}$. The effectiveness of the HEXs is chosen from the benchmark values in [33]. Moreover, as Type 512 is just capable of controlling the set-point temperature on the cold-side of the HEX, as required for the heating mode, the HEX type is improved and adapted to control the operation of the variable speed pump in cooling mode using the Fortran compiler inside TRNSYS.

Several variable speed pumps are used to force the flow in the different fluid loops. These are modeled with Type 110.

Finally, to implement the control strategies discussed in Chapter 4, the controllers of STCs, BSTs and BTES are modelled with a differential controller with hysteresis (Type 2b), while for controlling the operation of the GB a simple aquastat (Type 106) is used. More details about Type 2b function can be found in Appendix B.

### 6.2. *Coupling multi-objective optimization and system simulation*

The general optimization procedure for a system layout is illustrated in Fig. 8. It is divided into three sequential stages. In the first stage, an initial direct optimization based on TRNSYS system simulations is performed. Such a direct optimization method is suitable, when the simulation time is low and convergence of the optimization can be reached fast. However, since simulating the operation of geothermal-based heating and cooling systems is computationally intensive, it is not possible to achieve convergence of the direct optimization approach in an acceptable time frame. For this reason, the optimization is terminated after a certain acceptable duration before the final convergence is reached. The results gained so far are then used in the second stage to create a proxy model, which approximates the shape of the objective function in the region defined by the parameter boundaries. In the third stage, the proxy model is used to minimize LCOE and EF in a multi-objective optimization.

As the creation of the proxy model requires a much smaller computational effort than the numerous simulations of the TRNSYS model, this approach is much more time efficient. Comparable approaches have already been presented for geothermal applications and have proven to facilitate optimization for systems that are too complex for direct optimization [19].

#### 6.2.1. *Initial direct optimization*

For the direct optimization, TRNSYS is coupled with MATLAB, which allows for the utilization of the available MATLAB optimization tools. Genetic algorithm is used, which is a common method for nonlinear optimization [60]. Estimates of the algorithm for the systems design parameters under consideration are written to a text file, from which they are read by TRNSYS as input parameters for the system simulations. After a 30-year simulation is finished, the resulting LCOE and EF of 30-year simulations in TRNSYS are sent back and evaluated by the optimization algorithm in MATLAB.

#### 6.2.2. *Training, testing and validation of the proxy model*

The results from the first stage direct optimization are given as input data to the artificial neural network toolbox in MATLAB, which is used here to create the proxy model. ANNs are powerful tools to identify input–output relations of nonlinear and complex systems [61]. Application of ANNs for modeling and performance predication of energy systems has already been proven by other studies [36,62]. Sample points are used for training, testing and validation of the output as a function of inputs. The sample points can be chosen randomly by uniform distribution functions that generate data points in the evaluated space. In this study, to increase the accuracy and further reduce the computational effort, the sample points are chosen based on the study's objective to minimize LCOE and EF, defined in the initial optimization in the first stage.

The Levenberg-Marquardt algorithm [63] is used as training algorithm as it resulted in lower estimation errors for the proxy model. In specifying the proxy model, the first step is defining the percentage of the fed data that are used for training, testing and validation of the ANN. Thereafter, number of hidden layers and their hidden neurons, which are used to specify relation between input data and outputs, need to be defined. Finally, the training procedure starts and the regression value R is calculated, which measures the correlation between outputs of the ANN proxy models and the actual simulation results. An R value of 1 means a close match between the guessed values and the actual values. It is calculated by the overall mean of training, testing and validation R values of the ANN, which are taken as 70%, 15% and 15% of the fed data respectively. Neural networks consist of at least 3 layers, the input layer, a hidden layer and the output layer [35]. Some adjustments, e.g.

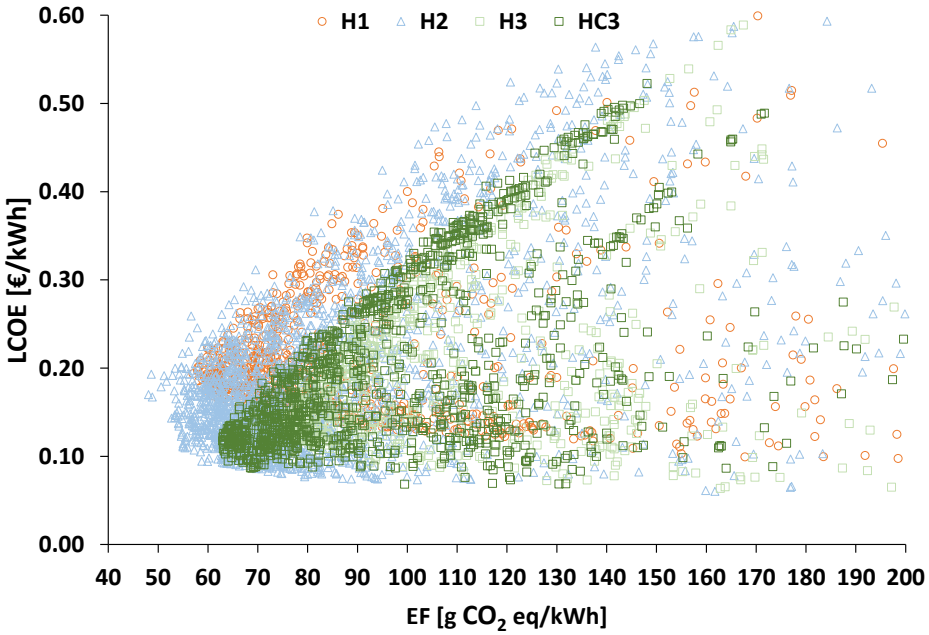


**Fig. 9.** Initial search by genetic algorithm to train the ANN.

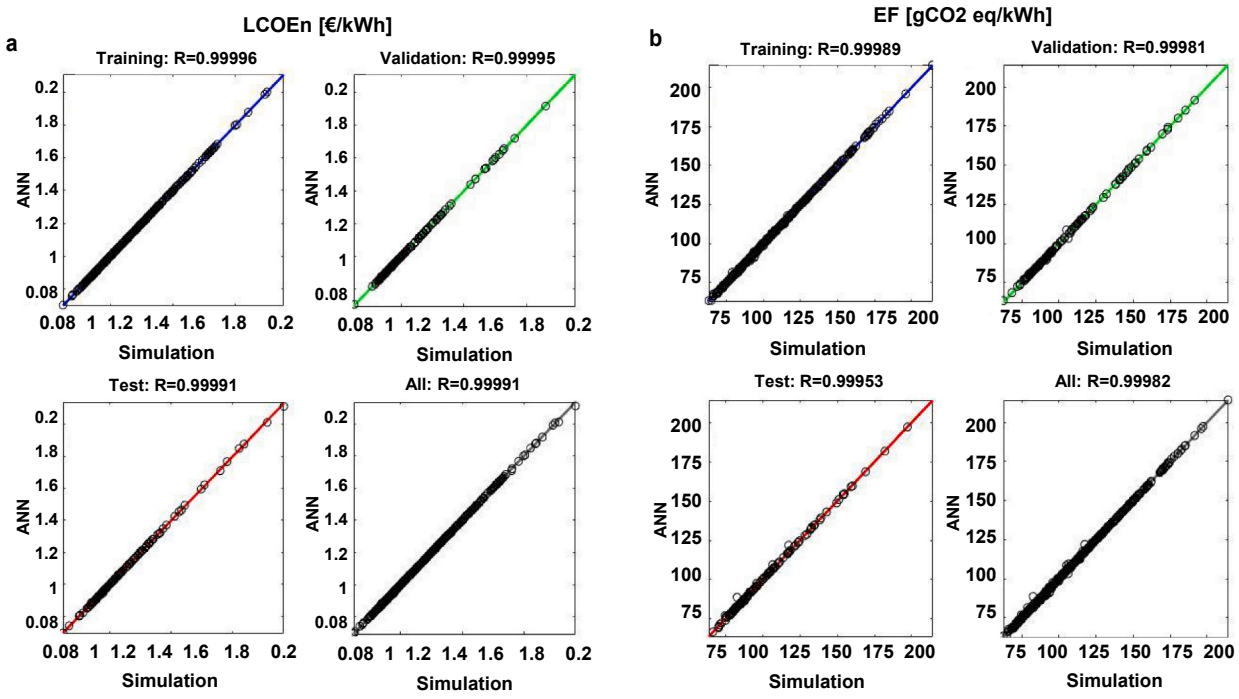


**Fig. 10.** Estimation error of the ANN for Scenario H1: LCOE (left), EF (right).

increasing the number of hidden layers, may be required to improve the accuracy. Multiple layers of neurons with nonlinear transfer functions allow the network to learn nonlinear relationships between input and output vectors [35]. The number of hidden layers is chosen as 1, which has 10–15 hidden neurons, depending on the investigated layout. The aforementioned numbers are chosen by running the training algorithm several times with different numbers of input data for each layout to have the lowest estimation errors (cf. Chapter 6.2.3). In this study, nearly 5% of the data is also used for validation after the proxy model is trained and the selected results of the last stage of the optimization are again compared with simulation results.

### 6.2.3. *Verification of the objective functions*

Fig. 9 shows the results of EF and LCOE for all conducted optimization iterations during the direct optimization carried out in the first stage of the optimization procedure (Fig. 8). The algorithm generally seeks in the entire parameter space, increasing the search density at loci where it comes closer to the objective of the optimization, i.e. minimum EF and LCOE.

Fig. 10 illustrates the estimation error exemplary for the H1 scenario. As it can be seen in the figure, the overall R value is 0.99996 for predicting LCOE and 0.99982 for EF, which proves the accuracy of the utilized method for estimating the objective functions. The required

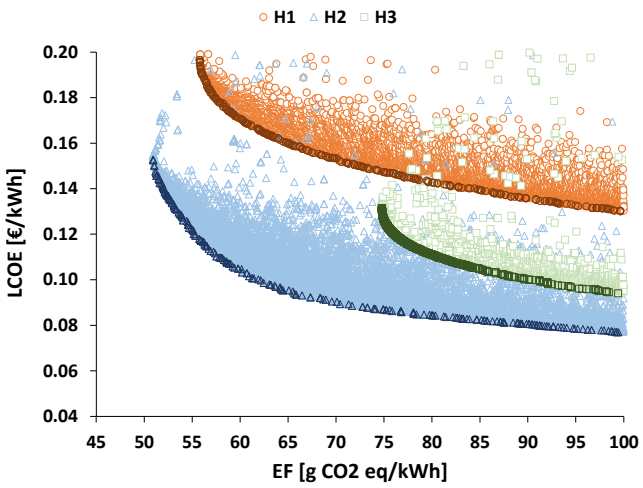


**Fig. 11.** Optimization results of scenarios H1, H2 and H3.

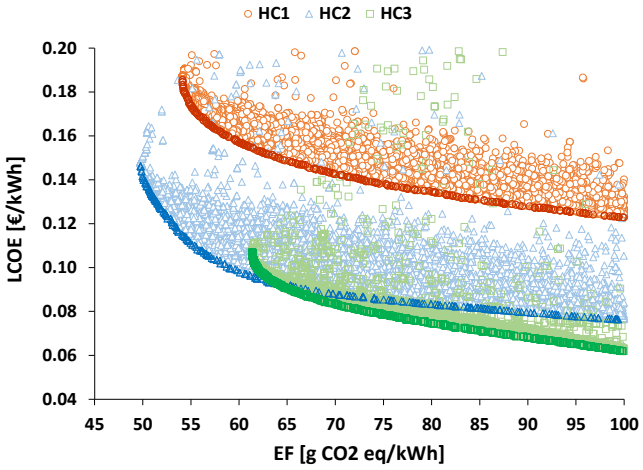


**Fig. 12.** Optimization results of scenarios HC1, HC2 and.

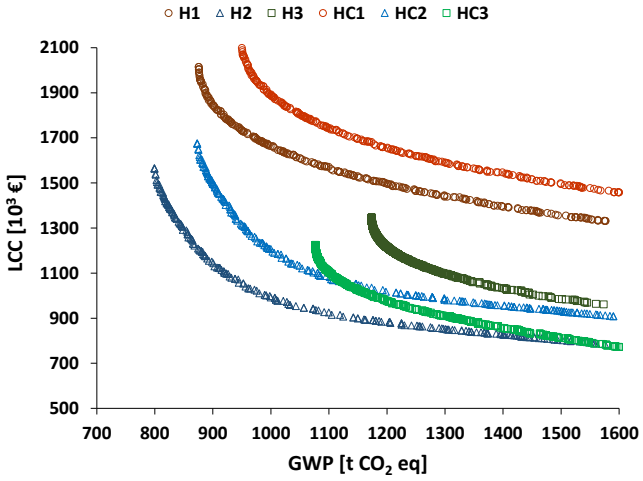


**Fig. 13.** Optimization results of all layouts.

number of evaluations for reaching low estimation errors is dependent on the layout and the number of optimization variables. Larger numbers of variables require more data for training. Consequently, the H2 scenario with 5 optimization variables required approximately 2000 runs, while the H1 and H3 scenarios which have 4 optimization variables required 1400 and 1200 points.

#### 6.2.4. Final multi-Objective optimization

Finally, in the third stage, the trained and validated proxy models are given to the non-dominated sorting genetic algorithm (NSGA II) [64] toolbox in MATLAB. The multi-objective optimization continues until the algorithm converges. The number of evaluations in this stage depends on the optimization settings. However, due to the application of the proxy model, the optimization algorithm converges within a few minutes, even for strict tolerance settings. Table C1 shows the most important NSGA II optimization settings that are used in this study, which are mainly based on recommended settings in MATLAB considering the optimization problem and number of optimization variables [65]. Results of the final multi-objective optimization of each layout specify values of the optimization variables and are located on a Pareto front, which is locus of the points with the lowest amounts of EF and LCOE. Moreover, characteristic designs on the Pareto front are selected and their component-wise EF and LCOE are discussed. Finally, a sensitivity analysis is done to consider the effects of uncertainties on the characteristic points.

## 7. Results and discussion

### 7.1. Pareto efficient solutions

After verification of the objective functions, the final stage of the computational model is conducted using the NSGA II algorithm to identify Pareto efficient solutions of each scenario, closest to the bottom left corner. Assuming a maximum of 2000 simulations for training of the ANN, and 20,000 points for the final convergence of NSGA II, the proposed computational model can reduce the computational time by approximately 90% in the present case.

Fig. 11 presents the results for the three heating-only system layouts (H1–H3). Among these, H2 (i.e. the layout with seasonal storage and active discharging via an HP) shows the best results. Moreover, for the solutions with equal EFs, H3 (i.e. the GSHP layout without storage) results in much lower LCOEs than the scenario with passive discharging of the BTES (H1). However, in terms of EF reductions, both layouts utilizing STCs and seasonal storage (H1 and H2) outperform H3 by a wide margin.

For HC1 and HC2 (i.e. the layouts including seasonal storage of solar energy and cooling via an ASHP), no separate training simulations are carried out, as the ASHPs are simulated using the same boundary conditions (Chapter 3.1 and Chapter 4.2). Moreover, it is assumed that there is no interaction between ASHPs and other system components. The calculated EF and LCOE for the ASHPs are 40 g CO2 eq and 0.0912 € per kWh of cooling load supply. The overall EF and LCOE per kWh of the combined heating and cooling load (Fig. 12) for HC1 and HC2 are then calculated using the results of H1 and H2. However, for HC3 (i.e. the layout using the BTES as heat sink for cooling), a separate optimization is carried out.

A comparison of the optimization results of the three HC layouts reveals that HC3 achieves the lowest LCOE for EFs of more than approximately 65 g CO2 eq/kWh. However, like for the heating-only scenarios, system 3 without STCs cannot reach EF values as low as in the solar-assisted layouts HC1 and HC2. Again, the systems with active discharging of the BTES via HP (HC2) outperform the passive layouts (HC1) in terms of EF slightly and in terms of LCOE significantly.

Finally, the heating-only scenarios and the combined heating and cooling scenarios shall be compared: For the solar-assisted layouts (H1/H2 and HC1/HC2) the specific cost and emissions per kWh of provided energy (i.e. LCOE and EF) decrease when cooling is included (Fig. 11 vs. Fig. 12). This is mainly attributed to the fact, that significantly more use energy is delivered in the cooling scenarios and that the generation of cooling energy with ASHP is comparably efficient. However, when

**Table 5**
Ranges of the optimized solutions on the Pareto fronts.

| Scenario | $A_{STC}$ [$m^2$] | $L_{BHE}$ [m] | $N_{BHE}$ | $Cap_{HP}$ [kW] | $Vol_{BST}$ [$m^3$] |
|---|---|---|---|---|---|
| H1 (HC1) | 2080–2650 | 50–65 | 42–66 | | 310–690 |
| H2 (HC2) | 410–1260 | 30–85 | 30–66 | 113.2 | 30–490 |
| H3 | — | 65–170 | 42–63 | 169.8 | 95–165 |
| HC3 | — | 100–220 | 21–33 | 113.2 | 70–100 |

regarding cumulative energy costs and emissions (i.e. LCC and GWP, Fig. 13) it becomes obvious that cooling in this cases causes additional costs as well as additional emissions. In contrast to that, for the standalone scenarios (H3 and HC3), cooling improves both the specific and the cumulative evaluation criteria. This highlights the advantage of recharging the underground to supply both heating and cooling load in comparison with conventional GSHP systems for heating-only purposes.

If, as a reference, it is assumed that the heating load was supplied by GBs and the cooling load by the ASHPs, the overall EF and LCOE would be roughly 250 g CO2 eq/kWh and 0.046 €/kWh. Therefore, the investigated layouts can decrease the EF by 79%, while they increase the LCOE by more than 44%, even though increasing gas and electricity costs are considered. However, it should be mentioned that the existing national subsidies to support renewable energies as well as the CO2 emission costs have not been included in LCOE calculations so far. These are evaluated in Chapter 6.4.

The range of the optimized variables on the Pareto front of each scenario is given in Table 5. As mentioned earlier, HC1 and HC2 are the

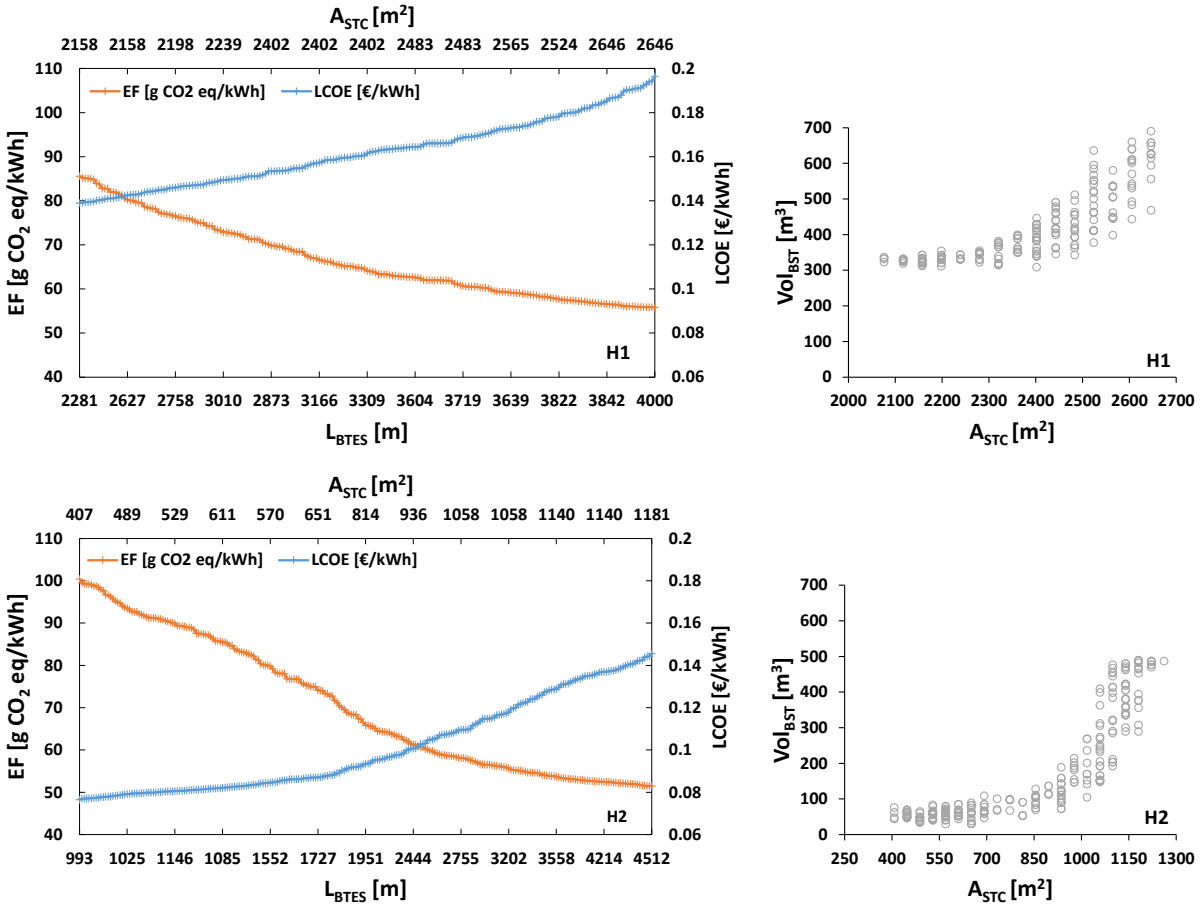


**Fig. 14.** Range of the optimization variables on the Pareto fronts of the solar-assisted scenarios.

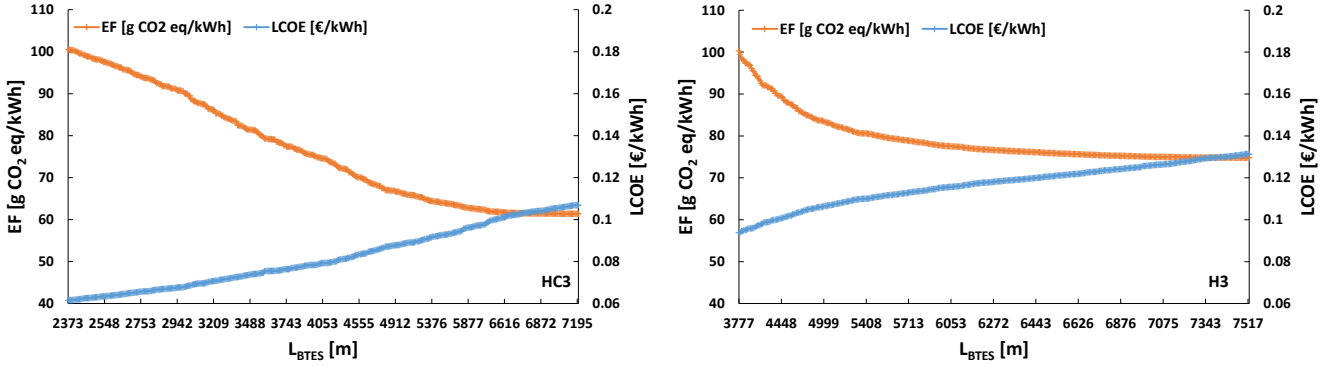


**Fig. 15.** Range of the optimization variables on the Pareto fronts of the standalone scenarios.

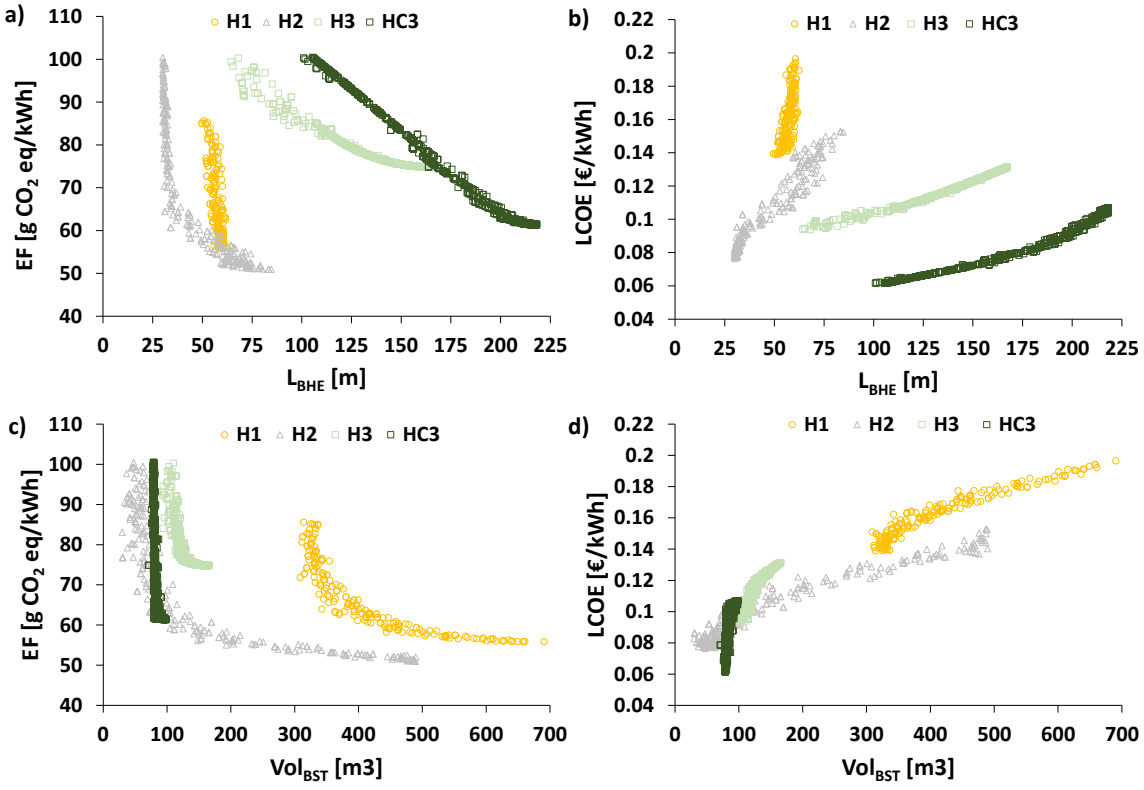


**Fig. 16.** Change in EF and LCOE with $L_{BHE}$ (a and b) and with $Vol_{BST}$ (c and d) for the optimized layouts on the Pareto front.

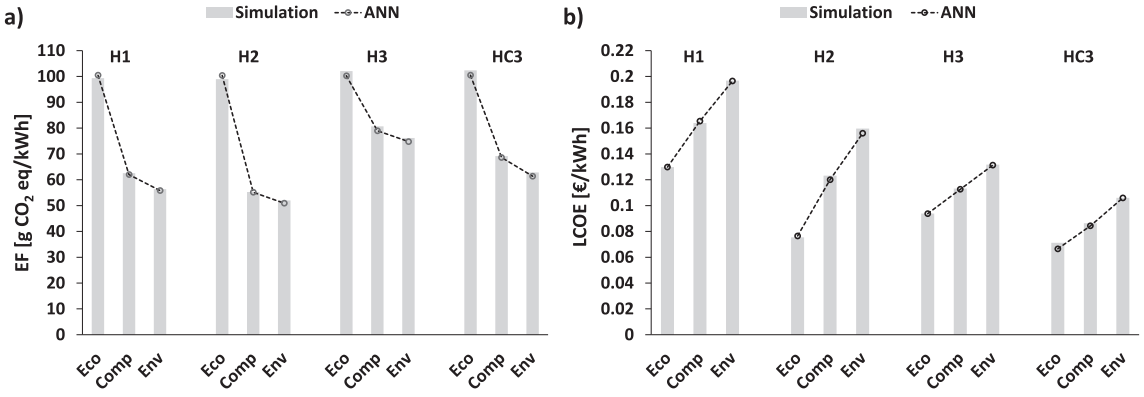


**Fig. 17.** Simulation vs. ANN results of EF (a) and LCOE (b) for the characteristic designs H1-H3 and HC3.

results of adding an ASHP to H1 and H2 to supply the cooling demand. Therefore, the ranges of their optimized variables are the same. For the solar-assisted scenarios, supplying the heating load passively results in larger STC areas, which requires also larger BTES and BST for seasonal and diurnal storage of the collected solar energy. The H3 and HC3 scenarios result in higher lengths than the other scenarios which is favorable because it leads to lower surface areas as larger amounts of spacing are recommended for more efficient operations of the standalone scenarios [10,46]. The H3 scenario results in lower source temperatures for the HP in comparison with the HC3 scenario, as the ground is only discharged. Hence, higher HP capacities are required to supply the same heating demand. This also results in larger $Vol_{BST}$ for scenario H3. It should be mentioned that the capacities of the HPs on Table 5 are nominal numbers. The real capacities are dependent on the ground-side temperatures, which vary for different scenarios and simulation time.

The relation between the optimized variables of the sample points on the Pareto fronts and their corresponding outputs is shown in Figs. 14 and 15. As it is expected, for all scenarios the EF decreases and LCOE increases by increasing the total drilling length ($L_{BTES} = L_{BHE}N_{BHE}$) for installing double U-tube BHEs. Similarly, an increase in $A_{STC}$ decreases EF and increases LCOE. Figs. 14 and 15 can be used to determine an optimal layout of the STC and the BTES, depending on a project's constraints and the envisaged layout, by choosing a value for the objectives. For a chosen total drilling length $L_{BTES}$, optimal ratios for $L_{BHE}$ and $N_{BHE}$ can be derived from Table 3, considering that higher $L_{BHE}$ results in lower EF and higher LCOE (cf. Fig. 16). Likewise, higher $Vol_{BST}$ also results in lower EF and higher LCOE for the solar-assisted scenarios. On the other hand, for the standalone scenarios $Vol_{BST}$ is mainly related to the HP capacity and remains within a limited boundary for different designs on the Pareto front. The more nonlinear behavior of the objective functions with changing $L_{BHE}$ in H1 and H2 is the result of the influence of STCs on the objectives.

For further analysis, three characteristic designs on the Pareto front of each layout are chosen. These include the most economical the most

**Table 6**
The economical, the compromise and the ecological system designs of each scenario.

| Scenario | | LCOE [ct/kWh] | GWP [gCO2/kWh] | $L_{BHE}$ [m] | $N_{BHE}$ | $Cap_{HP,nom}$ [kW] | $A_{STC}$ [$m^2$] | $Vol_{BST}$ [$m^3$] |
|---|---|---|---|---|---|---|---|---|
| H1 (HC1) | Economical | 12.98 (12.57) | 99 (93) | 50 | 42 | | 1954 | 308 |
| | Compromise | 16.39 (15.62) | 62 (60) | 58 | 60 | | 2443 | 419 |
| | Environmental | 19.67 (18.56) | 56 (55) | 61 | 66 | | 2646 | 690 |
| H2 (HC2) | Economical | 7.54 (7.65) | 99 (93) | 30 | 36 | 113.2 | 407 | 47 |
| | Compromise | 12.32 (11.92) | 55 (54) | 62 | 60 | 113.2 | 1058 | 239 |
| | Environmental | 15.96 (15.19) | 52 (51) | 83 | 60 | 113.2 | 1221 | 487 |
| H3 | Economical | 9.38 | 102 | 68 | 57 | 169.8 | – | 109 |
| | Compromise | 11.32 | 81 | 127 | 45 | 169.8 | – | 116 |
| | Environmental | 13.17 | 76 | 167 | 45 | 168.8 | – | 165 |
| HC3 | Economical | 7.12 | 102 | 105 | 24 | 113.2 | – | 79 |
| | Compromise | 8.63 | 69 | 184 | 27 | 113.2 | – | 79 |
| | Environmental | 10.60 | 63 | 218 | 33 | 113.2 | – | 98 |

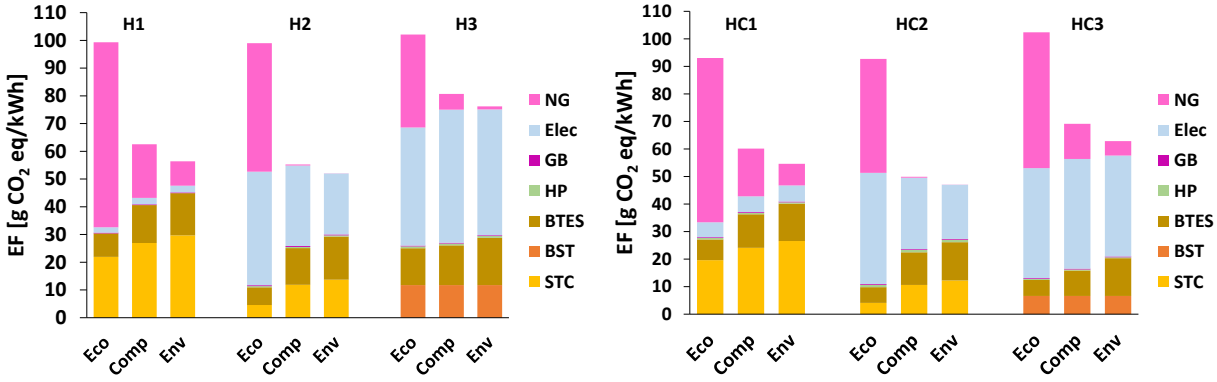


**Fig. 18.** Component-wise EF of the characteristic designs of Table 4.

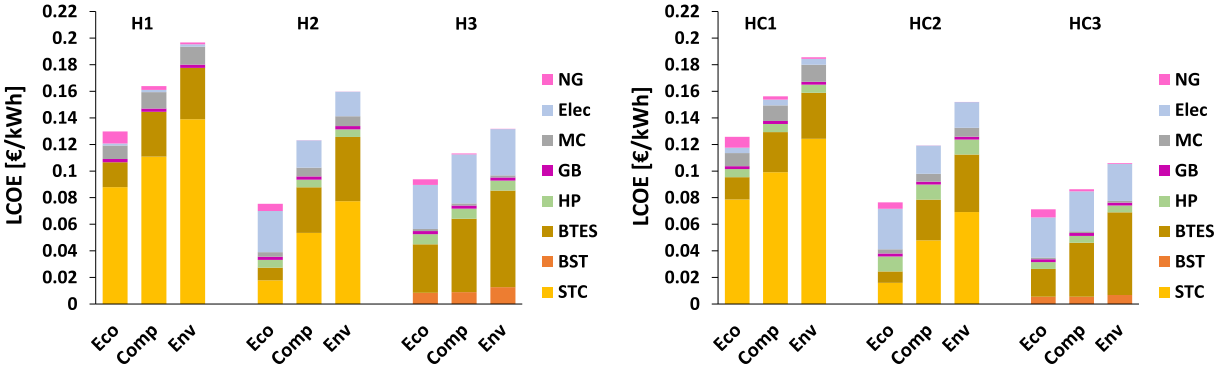


**Fig. 19.** Component-wise LCOE of the characteristic designs of Table 4.

environmentally-friendly and the compromise solutions. The compromise solution is the point with the minimum distance from the notional ideal point with the lowest possible EF and LCOE resulted from the optimization algorithm. These points are simulated with the TRNSYS models. The results are then compared with the outputs from the ANN, for the scenarios which were trained and optimized (H1-H3 and HC3, cf. Chapter 6.2). As illustrated in Fig. 17, the simulation results closely match the outputs from the ANN proxy model, which again proves the validity of the ANN method for predicting the objective functions. As not separate training was conducted for HC1 and HC2 scenarios. The simulation results of the characteristic designs and their corresponding optimized variables are given in Table 6 as well. The HC3 scenario yields the lowest LCOE and scenario HC2 has the lowest EF among the combined heating and cooling scenarios, while H2 always gives the best results for both objectives for the heating scenarios.

### 7.2. Environmental and economic analysis

To gain deeper insight into the coherencies of the results, the composition of EF and LCOE for the characteristic designs of Table 6 is shown in Figs. 18 and 19. For all scenarios, the overall EF and the EF during the operational phase decrease while the emissions during the production phase increase from the economical to the ecological designs. This is the result of more efficient operation of the layouts with higher renewable share and consequently higher LCOE. Adding ASHPs to the solar-assisted scenarios to supply cooling demand increases the IC, the overall electricity consumption, and the associated EF during the production and the operation of ASHPs. However, a comparison of H1 with HC1 and H2 with HC2 reveals that the overall specific values slightly decrease. Finally, for the standalone scenarios, utilizing the underground to supply both heating and cooling reduces both LCOE and EF considerably.

For H1 and HC1 layouts, STCs (including their diurnal BSTs) and

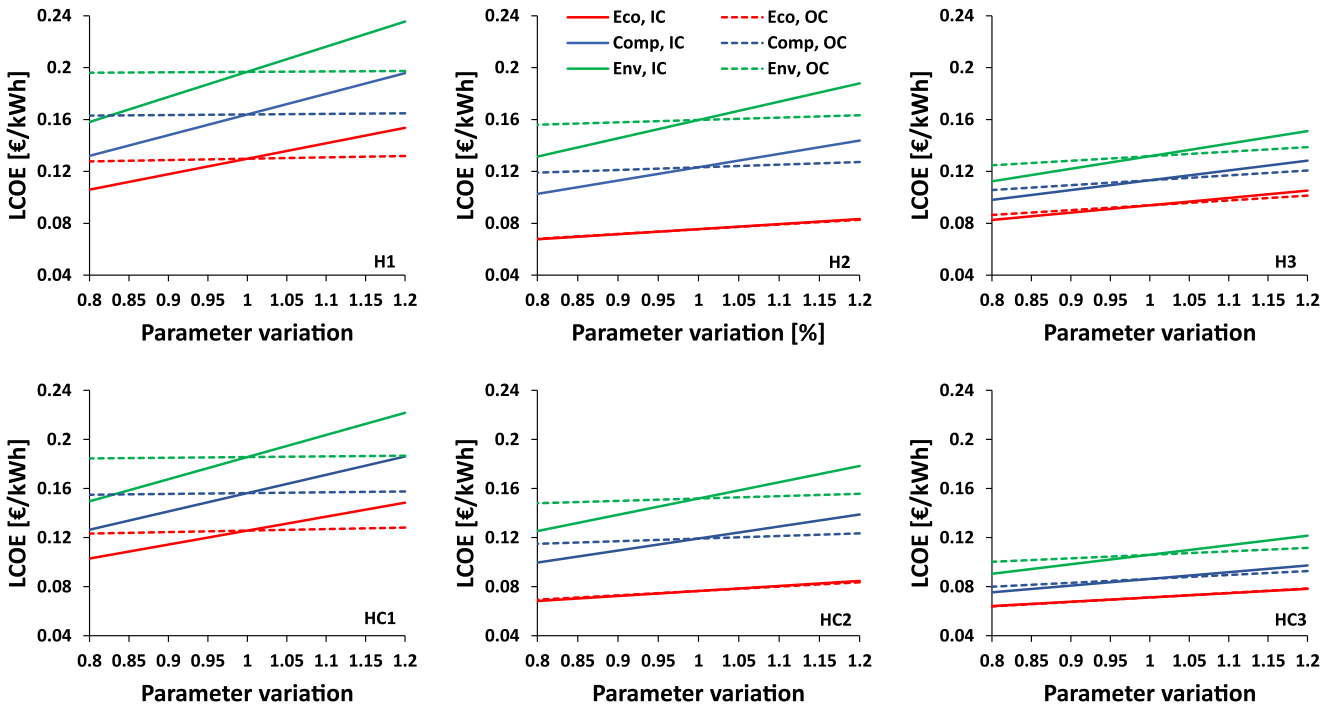


**Fig. 20.** Effect of varying initial costs (IC) and operational costs (OC) for the designs of Table 4.

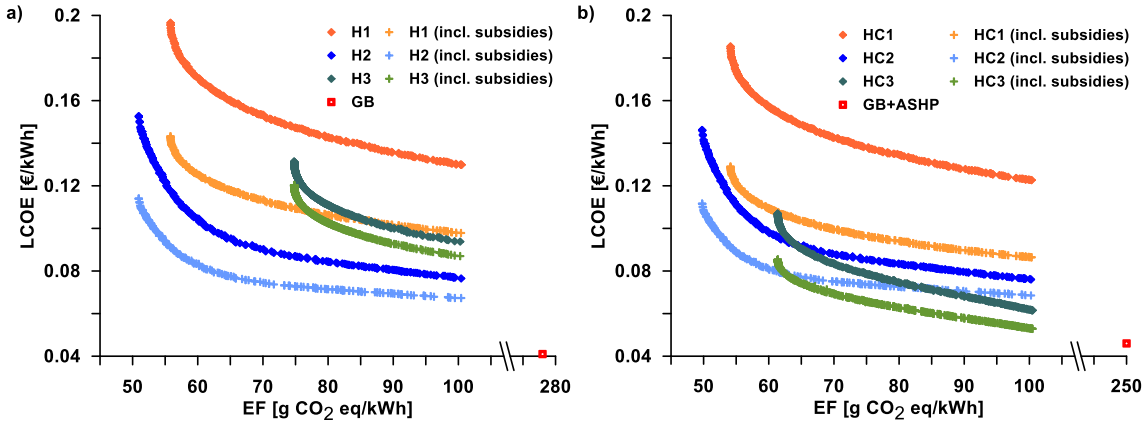


**Fig. 21.** Influence of considering national subsidies on the Pareto fronts of a) Heating and b) Heating and cooling layouts.

BTES have the highest shares in both EF and LCOE for the Env and Comp systems. In contrast to this, emissions from natural gas (NG) have the major share in the overall EF for the Eco system. This is the consequence of smaller BTES dimensions which results in higher NG consumption not only during the initial charging years, but also after the temperature of the BTES has reached its appropriate limit for passive load supply.

In H2 and HC2 layouts, the electricity consumption by the HPs has an important share in the EF as well as in the LCOE, which decreases from the economical to the ecological layouts due to more efficient operation of larger systems. STCs and BTES have major shares in both objectives, which are, however, comparatively lower than in the passive scenarios. This demonstrates the importance of utilizing efficient HPs for improving the performance of solar-assisted BTES systems, which almost leads to the omission of the GB operation for the compromise and the ecological solutions. Even when comparing active and passive BTES discharging for the most economical scenarios, the integration of a HP also results in a lower share of GB. But, the high electricity demand of the HP almost completely cancels out the reduction in EF due to lower gas consumption, resulting in an almost equal total EF as in the passive scenarios. In terms of LCOE, however, the active scenarios perform significantly better than the passive ones.

For the standalone layouts without solar system (H3 and HC3), the heating-only layout H3 has significantly lower gas consumptions than the combined heating and cooling equivalent HC3. However, emissions savings due to a lower gas consumption are equalized (Eco design) or even overshot again (Comp and Env designs) by two effects: on the one hand H3 has a higher electricity consumption of HPs due to the lower source temperatures especially after a few years of heat extraction and, on the other hand, in H3 the BTES system and BST are generally larger, which adds significant amounts of emission in the production phase. The combined heating and cooling load supply in HC3 increases the efficiency of the BTES due to recharging of the underground, which results in lower $L_{BTES}$ and consequently reduces its impact on both objectives.

### 7.3. Sensitivity analysis

#### 7.3.1. Effect of varying initial and energy costs

In a sensitivity analysis, effects of 20% variation in IC and OC on

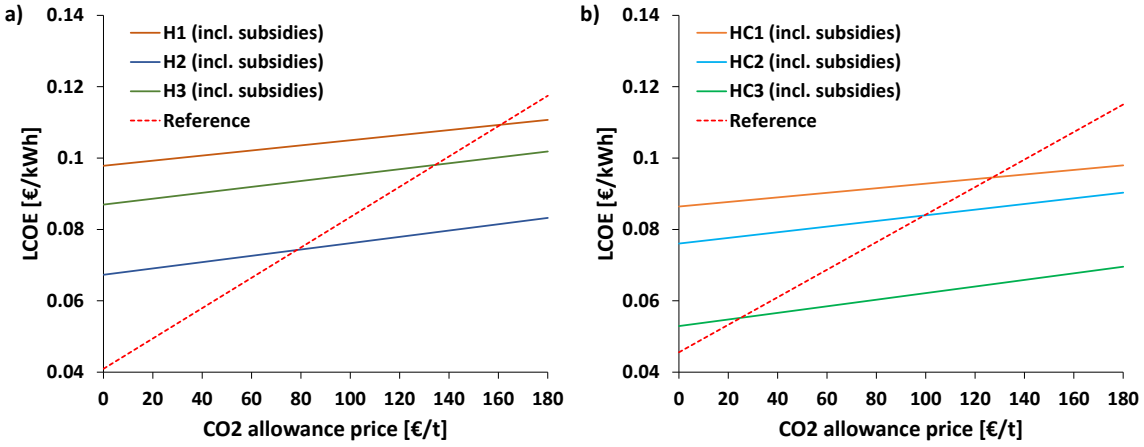


**Fig. 22.** Influence of considering national subsidies and emission costs on the economical designs of a) Heating and b) Heating and cooling layouts.

the LCOE of the characteristic designs of Table 6 are assessed (Fig. 20).

Varying the IC has a stronger effect than OC for the ecological and the compromise layouts. For the economical layouts, the impact of changing the OC is approximately similar to changing the IC, except for the passive scenarios. By reducing OC and IC of the economical point of HC3 scenario by 20%, its LCOE decreases from 7.12 to 6.42 ct/kWh and 6.39 ct/kWh, respectively, which corresponds to a reduction of 9.8 and 10.2%. For the different characteristic points of each layout, varying the IC has a smaller influence on more economical solutions, which are characterized by generally lower IC due to smaller $L_{BTES}$ and $A_{STC}$.

While the influence of varying OC is rather small for all systems, it can be observed that passive systems (H1&HC1) are especially robust to changes in fuel costs. Since the gas price is still comparably low, even with the considered rise over time, it generally makes up only a minor share in the overall costs of all the systems (cf. Fig. 19). Layouts, including a heat pump, suffer slightly more from changes in the OC as the electricity price is higher than the gas price. However, as the Comp and Env solutions of these layouts also comprise large production cost for BTES and solar, the impact of changing IC is still much larger than that of changing the OC.

### 7.3.2. National subsidies

As already explained, the investigated layouts reduce the EF substantially in comparison with conventional fossil-based systems. However, EF reduction is also associated with an increase in LCOE, which is mainly due to IC of STCs and BTES. One option to make renewable energy systems competitive to conventional ones is to financially support such systems by subsidies. In Germany, subsidies are currently paid by the government for the installation of solar thermal collectors, heat storage facilities and efficient heat pump [66]. The influence of considering these national subsidies on the Pareto fronts of the optimized layouts is illustrated in Fig. 21.

It must be mentioned that due to time constraints, the subsidies were not already included in a separate optimization study, but were added later to the existing optimized layouts. It is expected that the inclusion of the subsidies would also change the optimal layouts, leading to even better system designs than presented here.

As all layouts comprise components that receive subsidies, all Pareto fronts are shifted downwards to lower LCOE. These include the subsidies that are considered for solar thermal collectors, heat storage facilities and efficient heat pumps. The cost reduction decreases for the systems with higher EFs. Moreover, the solar-assisted scenarios take the most advantage of subsidies. Consequently, the passive layouts having the largest STC areas exhibit the highest reduction in LCOE of all.

After implementing the national subsidies, a layout with an EF of 100 g CO2 eq/kWh results in a LCOE of 0.052 €/kWh for the HC3 scenario. Therefore, compared with the reference layout with a EF and LCOE of 250 g CO2 eq/kWh and 0.046 €/kWh (cf. chapter 6.2) an increase of 13% in LCOE results in a reduction of 60% in EF. Overall, it can be concluded that national subsidies pave the way towards the utilization of the environmental benefits of geothermal layouts even on small-scale by making them more economically attractive. However, to reach the lowest EFs for easily-implementable small-scale systems, more supports are needed.

### 7.3.3. National subsidies and emission costs

Other than environmental effects of using fossil fuels, penalty costs that need to be paid for emitting environmental pollutants further decrease the economic attractiveness of fossil-based systems and will be a major barrier for their further application. Fig. 22 shows the influence of considering CO2 emission costs as well as national subsidies on the economical designs of the layouts. As the cheapest design of HC scenarios, HC3 is preferred to the reference case by considering a CO2 emission cost of only 30 €/t. This means 60% EF reduction with the same LCOE. For the most economical layout of the heating-only scenarios, an emission cost of approx. 80 €/t is required to have the same LCOE as fossil-based systems. It needs to be mentioned that having more environmentally-friendly solutions is associated with higher costs and the supporting policies are required to support these systems economically. Overall, it can be concluded that the simultaneous consideration of the national subsidies and the emission cost will make small-scale geothermal layouts economically comparable with fossil-based energy systems.

## 7.4. Limitations and future work

A generic study of a complex system requires simplifications and assumptions, which has its own drawbacks and may cause uncertainties. It has been tried to lower the uncertainties by choosing a system in operation as the reference case and simulating and validating the simulation against experimental results. In this part, the considered assumptions and simplifications as well as the proposed future works are explained.

- ANN is utilized as a proxy model for estimating the objective functions and convergence of the optimization with larger numbers of evaluations. However, estimation is always associated with uncertainties. Nevertheless, efforts were made to control these uncertainties by checking the functions from the training algorithm as well as by post-simulation of the selected final points. These measures have shown that the approach via the proxy model is very accurate.
- For the project lifetime of 30 years, every simulation with a time step of 1 h takes around 40 min. Moreover, an appropriate training of

ANN with low estimation errors, requires between 1,000 to 2,000 evaluations depending on the layout and number of variables. In dynamic simulation of energy systems, shorter time steps always result in more exact results but longer simulations, which is impracticable due to computation limits in this study.

- These computational limitations make it necessary to keep certain boundary conditions fixed. The results might for example be strongly dependent on system size and local climate conditions. The notional system located in Germany identifies optimal system layouts for central European locations and comparable regions. However, the presented methodology can generally be applied to any location and climate.
- The selected STC module has a gross area of 13.57 $m^2$. It is assumed that three STC modules are in series and, for pump selection, the pressure loss inside STCs is calculated accordingly. However, the number of STCs in series or parallel is dependent on the available area for installing the collectors and requires separate analyses considering the project site specifications.
- It is assumed that the BTES is installed in the ground with a uniform thermal conductivity and heat capacity and the only heat transfer mechanism is conductive. However, in real applications convective heat transfer might exist and ground thermal characteristics might not be uniform.
- For the calculation of OC, the energy cost functions taken from the economic studies are mainly based on predictions assuming that a linear interpolation between the available data points is acceptable. The IC functions are based on the available literature and are mainly defined by having data from real projects in a specific range. Consequently, cost functions are subject to uncertainties. The sensitivity analysis in chapter 6.4.1 is done with the purpose of considering these uncertainties.
- It is assumed that GBs cover the load that cannot be supplied by solar and/or ground loop, which is typical in many existing district heating grids. Using biomass boilers for peak load supply will result in further EF reduction. However, for a comparison with bio-fueled systems, other environmental impacts such as land consumption and fine particulate air pollution must be considered as well. Therefore, environmental and economic assessment of combined biomass boilers and the geothermal layouts is suggested as a future work.
- As mentioned earlier, for the solar-assisted HC scenarios (HC1 and HC2), BTES systems are heated up by STCs during the summer seasons and cannot be used as an efficient heat sink for cooling purposes. The utilization of two BTES systems, one for the storage of solar energy and the other for the rejection of the waste heat from cooling cycles, and possible configurations for performance improvement of the combined model is suggested as a future work.
- Although enviro-economic evaluations are initially used by decision-makers to evaluate a renewable energy project, they lack thermodynamic assessment [67]. Therefore, in practical applications, an enviro-economical optimization needs to be supplemented by a detailed thermo-economic assessment method to define the parameters which are kept constant during the optimization.

## 8. Conclusion

A combination of direct optimization, an ANN proxy and the NSGA II method is utilized for enviro-economic multi-objective optimization of solar-assisted and standalone geothermal layouts for heating as well as combined heating and cooling applications. The initial design and control strategies are adapted from a validated reference case to a notional case study in Germany. The following conclusions can be drawn from the results of this study:

- Utilizing the ANN as a mid-stage in the optimization procedure results in a proper verification and validation of the objective functions in several steps and is recommended for long-term evaluation of geothermal applications.
- For heating applications, active load supply by the solar-assisted geothermal layouts results in the lowest LCOE and EF, and passive load supply leads to the most expensive solutions. The lowest EFs can only be reached by solar-assisted scenarios. Moreover, the standalone scenario without solar is only suggested if higher EFs are acceptable and utilizing STCs is not possible.
- The utilization of BTES for the seasonal storage of the waste heat from cooling cycle leads to the most economical layouts, which still reach reasonably low EFs. However, like in the heating-only scenarios, reaching the lowest EFs is merely possible by utilizing STCs.
- When comparing heating-only scenarios and combined heating and cooling scenarios, it is found that in the case of solar-assisted systems, the inclusion of cooling with an ASHP slightly reduces the EF and LCOE. However, the GWP and LCC increase. Consequently, in these cases, the comfort gain from cooling comes at a cost to consumers and causes additional emissions. In contrast, for the standalone scenarios without solar collectors, the inclusion of cooling results in a real cost reduction for the consumer and a reduction in emissions.
- Increasing the total drilling length or the area of STCs decreases the EF and increases LCOE. The relation between the optimized variables and the outputs of the multi-objective optimization from this study can be used by designers for an initial evaluation of system's dimensions and its effect on the enviro-economic objectives (Table 5 and Figs. 14-16).
- In the passive solar-assisted layout, STCs and BTES have the highest shares in both EF and LCOE. In contrast, in the active design, the electricity consumption of the HPs has important shares in both objectives.
- Utilizing efficient HPs for improving the performance of solar-assisted BTES systems leads to much smaller dimensions of STCs and BTES in comparison to passive systems. This almost leads to the omission of the GB operation in the compromise and the ecological solutions.
- The geothermal standalone heating-only layouts result in the highest EF and larger $L_{BTES}$, which increases the LCOE significantly. Recharging of the underground with waste heat in combined heating and cooling results in lower $L_{BTES}$ and thus a lower impact on both the objectives.
- National subsidies can increase the economic attractiveness of the proposed layouts. By considering national subsidies, a 60% decrease in EF can be achieved if an increase in the LCOE of only 13% is accepted for the most economical layout compared to a fossil-based reference case. However, to reach the lowest EFs more supporting policies are needed.
- Considering CO2 emission costs in addition to the national subsidies can make the geothermal layouts economically more attractive than the fossil-based reference layout while decreasing EFs substantially.

## Funding

This work was financially supported by the German Research Foundation (DFG) in the framework of the Excellence Initiative, Darmstadt Graduate School of Excellence Energy Science and Engineering (GSC 1070).

*CRediT authorship contribution statement*

**Hoofar Hemmatabady:** Conceptualization, Methodology, Investigation, Visualization, Writing. **Bastian Welsch:** Conceptualization, Supervision, Visualization, Writing. **Julian Formhals:** Conceptualization, Investigation, Writing. **Ingo Sass:** Conceptualization, Supervision, Funding acquisition.

## Declaration of Competing Interest

The authors declare that they have no known competing financial interests or personal relationships that could have appeared to influence the work reported in this paper.

## Appendix A. Calculations of costs and emissions

See Tables A.1–A.5.

**Table A.1**
Emissions caused during the production of each system component ($GWP_{Prod,i}$).

| Component | $GWP_{Prod,i}$ (kg CO2 eq) | Reference |
|---|---|---|
| BTES | $(4.105 \times L_{BHE} + 63.25 \times t_{drill}{}^{a}) \times N_{BHE}$ | [28] |
| HP | $58.5 \times Cap_{HP}$ | [68] |
| STC & BST | $176 \times A_{STC}$ | [28] |
| GB | $78.1 \times Cap_{GB}{}^{0.729}$ | [69] |

a $t_{drill} = 19.8 \times (2.71828^{0.0036 \times L_{BHE}})$.

**Table A.2**
EF associated with electricity ($EF_{elec,a}$) and natural gas ($EF_{gas,a}$) consumption as function of the operation year.

| Parameter | 2020–2030 | 2030–2050 | Reference |
|---|---|---|---|
| $EF_{elec,a}$(kgCO2/kWh) | $(-20.99a + 423.89) \times 10^{-3}$ | $(-8.595a + 287.55) \times 10^{-3}$ | [51] |
| $EF_{gas,a}$(kgCO2/kWh) | $250 \times 10^{-3}$ | $250 \times 10^{-3}$ | [52] |

**Table A.3**
Investment and maintenance cost functions of different components.

| Component | Investment cost (€) | Maintenance cost (€/yr.) | Reference |
|---|---|---|---|
| BTES | $65 \times L_{BHE}$ | – | [70] |
| HP | $(2053.8 \times Cap_{HP}{}^{-0.348}) \times Cap_{HP}$ | $0.0075 \times C_{IC}$ | [71] |
| STC | $(335 \times A_{STC}) + 7500$ | $0.0075 \times C_{IC}$ | [54,72] |
| BST | $\left(403.5 \times Vol_{BST}{}^{-0.4676} + 750\right) \times Vol_{BST}$ | – | [54] |
| GB | $(11418.60 + 64.6115 \times Cap_{GB}{}^{0.7978}) \times f_{GB}{}^{a}$ | $0.02 \times C_{IC}$ | [69] |

a $f_{GB} = 1.0818 - (8.2898 \times 10^{-7} \times Cap_{GB})$.

**Table A.4**
Electricity cost ($c_{elec,a}$) as function of the operation year.

| Parameter | 2020–2026 | 2027–2011 | 2012–2050 | Reference |
|---|---|---|---|---|
| $c_{elec,n}$(€/kWh) | 0.00302n + 0.1304 | −0.003356n + 0.1686 | −0.00042n + 0.1363 | [73,74] |

**Table A.5**
Natural gas cost ($c_{gas,a}$) as function of the operation year.

| Parameter | 2020–2030 | 2030–2050 | Reference |
|---|---|---|---|
| $c_{gas,n}$(€/kWh) | 0.000432n + 0.0285 | 0.000212n + 0.03095 | [73,74] |

## Appendix B. TRNSYS models

In this part different TRNSYS layouts and their control strategies are explained and discussed. Initially, main TRNSYS components that are used for modelling the proposed layout are shown (cf. Table B.1.1). Moreover, mathematical description of the main controllers is explained (cf. Table B.1.2). Finally, TRNSYS models of the layouts and their control parameters are discussed.).

**Table B.1.1**
Main TRNSYS components.

| | | |
|---|---|---|
| Variable Speed Pump<br>  <br>Type110 | Flow Diverter<br>  <br>Type11f | Flow Mixer<br>  <br>Type11h |
| Heat Exchangers<br>Constant Effectiveness<br>  <br>Type91 | Heat Exchanger<br>Hot-side Modulation<br>  <br>Type512 | |
| Ground Heat Exchangers<br>  <br>Type557a | Buried Horizontal<br>Single-pipe Systems<br>  <br>Type952 | |
| GSHP<br>  <br>Type927 | ASHP<br>  <br>Type118 | |
| Solar Thermal Collectors<br>  <br>Type1a | Buffer Storage Tank<br>  <br>Type534 | |
| Differential Controller<br>  <br>Type2b | Aquastat<br>   <br>Type106 Type113 | |
| Weather Data<br>  <br>Type15 | Load<br>   <br>Type9c Type682 | |

### *B.1. TRNSYS components (Types)*

As the main control strategies of the layouts are specified by differential controllers (Type 2b), the controller function is discussed in this part. To give a hysteresis effect, the controller is normally used with the output control signal ($\gamma_o$) connected to the input control signal ($\gamma_i$) [34]. Table B.1.2 shows the controller function and how it defines $\gamma_o$ based on $\gamma_i$. If the controller is already on ($\gamma_i = 1$), it remains on ($\gamma_o = 1$) if the difference between upper input temperature ($T_H$) and lower input temperature ($T_L$) is greater than or equal to lower dead band temperature difference ($\Delta T_L$), otherwise it will be switched off ($\gamma_o = 0$). If the controller is already off ($\gamma_i = 0$), it remains off ($\gamma_o = 0$) if the difference between $T_H$ and $T_L$ is lower than the upper dead band temperature difference ($\Delta T_H$), otherwise it will be switched on ($\gamma_o = 1$). Regardless of the value of $\gamma_i$, the controller switches off ($\gamma_o = 0$), if temperature for high limit monitoring ($T_{in}$) is higher than maximum input temperature ($T_{max}$).

### B.2. TRNSYS model of passive heating (BTES)

TRNSYS model of H1 scenario is shown in Fig. B.2.1 As it can be seen in the figure, there are mainly four loops in the model including solar loop (SL), buffer storage loop (BSL), ground loop (GL) and district loop (DL). The solar energy that is collected in the SL is transferred to the BSL for diurnal storage. In charging mode, the energy is delivered from the BSL to the GL, to be stored in the BTES. In discharging mode, the stored energy in the BTES is then extracted and delivered from the GL to the BSL. The extracted energy from the BTES together with the collected solar energy in the SL is then transferred from the BSL to the DL to supply the heating demand.

STCs (Type1a) collect the solar energy and transfer it to the return fluid, from the underground pipes (Type952) of the solar loop (SL). The circulation is done by a variable-speed pump, P-SL, (Type 110), which is activated using a differential controller (Type2b). The controller functions are specified using Table B.1.2 with the values of the monitored temperatures, $\Delta T_L$, $\Delta T_H$ and $T_{max}$ from Table B.2.1. Moreover, its flow rate is controlled so that a design $\Delta T$ of 15 K for STCs is assured [42]. Using the SL HEX (Type 91b), the collected solar energy is transferred to the fluid from the bottom of the colder BST (BST2) on the BST side. The is done by another variable-speed pump, P-BST-SL, with the same flow rate as P-SL [42]. The temperature of the fluid is then increased and delivered to the top of the warmer BST (BST1), until the circulating pumps on both sides are turned off by the SL differential controller.

The return fluid from the BTES is diverted using flow diverter (Type 11f) to the bottom of the colder BST in the charging mode or to the top of the warmer BST in discharging mode. In charging mode, the stored solar energy in the BSTs is transferred to the BTES. This is done by the ground loop pump, P-GL, which is controlled by two differential controllers, one for heating and one for non-heating seasons, cf. Table B12 and Table B.2.1. In charging mode of the non-heating seasons, the controller turns off the pump when the BSTs do not contain enough energy or the BTES reaches its maximum temperature limit. In charging mode of the heating seasons, the controller turns on the pump when the bottom temperature of the colder BST (BST2) exceeds the design supply temperature on the load side. These strategies are specified by upper and lower dead band as well as maximum input temperatures, cf. Table B.3. In discharging mode, the BSTs are filled by P-GL, which is controlled by a differential controller considering the temperature level of the BTES center and BSTs, cf. Table B.1.2 and Table B.2.1.

In heating seasons, the collected energy in the BSTs, from the BTES and the STCs, is delivered to the DL using P-BST-DL. It is a variable-speed pump that is controlled by a control signal, which is an output of the district loop HEX (Type 512). It assures that the supply temperature in the district loop $T_{sup}$ is heated up to its set point. On the load side, P-DL circulates the fluid in the underground pipes (Type952) of the DL. Its flow rate is controlled considering the heat demand of the cased study (given as input to the model by Type 9c) to meet design $\Delta T$ of the DL. Moreover, a GB (Type 700) assures that the fluid is heated up to its set point temperature before it is delivered to the final consumer. It is controlled by a simple aquastat (Type 106), which turns on the GB considering the outlet temperature of the district HEX and the design $T_{sup}$ of the grid. Finally, Type 683 represents the simplified final consumer.

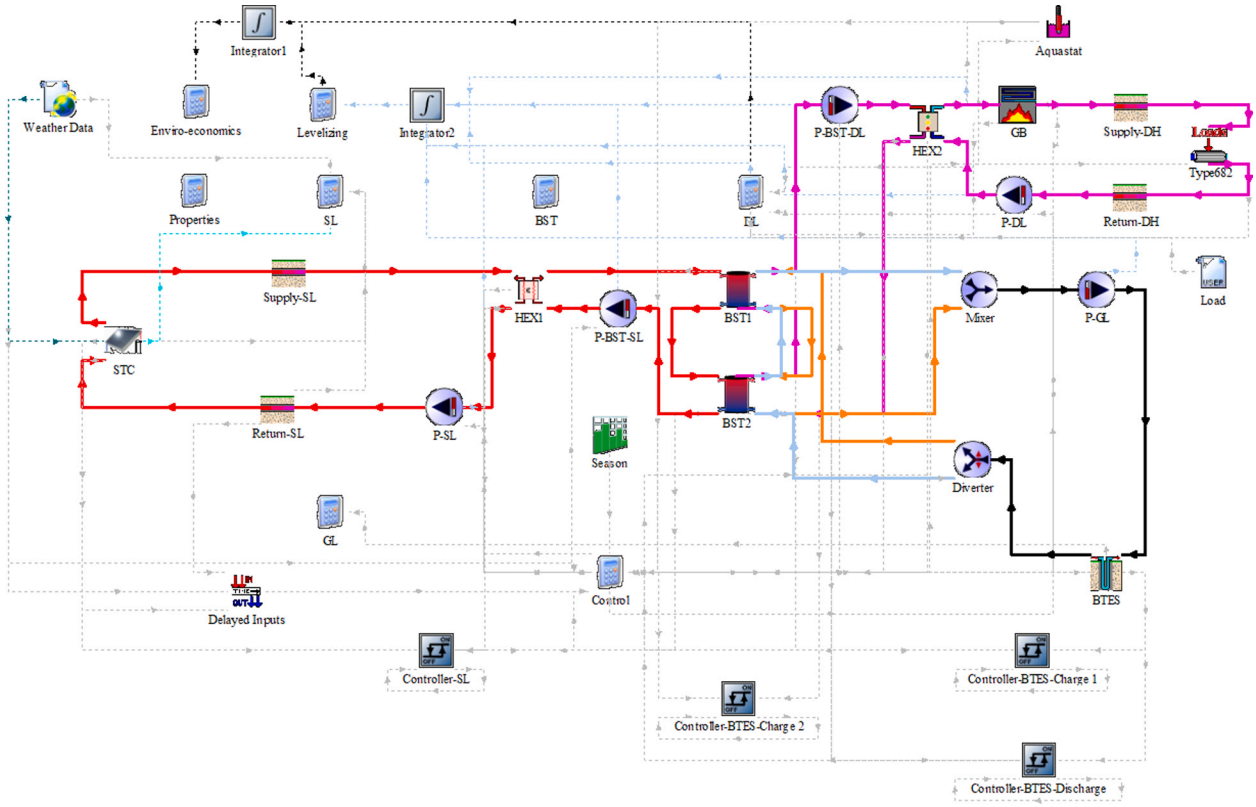


**Fig. B.2.1.** TRNSYS model of H1 scenario.

**Table B.1.2**
Differential controller (Type 2b) controller function [34].

| |
|---|
| If the controller was previously on ($\gamma_i = 1$) |
| If $\Delta T_L \leq (T_H - T_L)$ then $\gamma_o = 1$ |
| If $\Delta T_L > (T_H - T_L)$ then $\gamma_o = 0$ |
| If the controller was previously off ($\gamma_i = 0$) |
| If $\Delta T_H \leq (T_H - T_L)$ then $\gamma_o = 1$ |
| If $\Delta T_H > (T_H - T_L)$ then $\gamma_o = 0$ |
| If $T_{in} > T_{max}$ then $\gamma_o = 0$ |

**Table B.2.1**
Controller parameters of type 2b for the solar loop and BTES (charge and discharge) (slightly modified after [48]).

| | |
|---|---|
| Solar loop controller | $\Delta T_L = 2, \Delta T_H = 10, T_{max} = 90^{\circ}C$<br>$T_H$ : outlet temperature of STCs<br>$T_L$ : bottom temperature of the colder BST (BST2)<br>$T_{in}$ : top temperature of the warmer BST (BST1) |
| BTES controller (charge)<br>non-heating seasons | $\Delta T_L = 3, \Delta T_H = 10, T_{max} = 90^{\circ}C$<br>$T_H$ : top temperature of the warmer BST (BST1)<br>$T_L$ : average soil temperature near boreholes (center)<br>$T_{in}$ : average storage temperature |
| BTES controller (charge)<br>heating seasons | $\Delta T_L = 2, \Delta T_H = 10, T_{max} =$ toptemperatureofBST1<br>$T_H$ : load-side supply temperature<br>$T_L$ : bottom temperature of the colder BST (BST2)<br>$T_{in}$ : average soil temperature near boreholes (center) |
| BTES controller (passive discharge)<br>heating seasons | $\Delta T_L = 3, \Delta T_H = 10, T_{max} = 45^{\circ}C$<br>$T_H$ : average soil temperature near boreholes (center)<br>$T_L$ : bottom temperature of the colder BST (BST2)<br>$T_{in}$ : top temperature of the warmer BST (BST1) |

## *B.3. TRNSYS model of active heating (BTES)*

TRNSYS model of H2 scenario is shown in Fig. B.3.1. The control strategies of the GL in charging mode, the SL, the BSL and the DL are the same as H1, cf. Chapter B2. For the GL in discharging mode, a HP (Type 927), based on a manufacturer's data [49], discharges the BTES actively when its temperature is not high enough for direct heating load supply. This is done by an active discharge controller, which can be switched on only when the passive discharge controller is off. It monitors the load-side supply temperature $T_{sup}$ and compares it with the bottom temperature of the colder BST (BST2), cf. Table B.3.1. When $T_{sup}$ falls below the designed value, specified by $\Delta T_H$ and $\Delta T_L$, the controller sends the return fluid from the bottom of BST2 to the HP using diverter1 and the return fluid from the BTES to the HP using diverter2. Moreover, it switches on the HP as well as its source- and load-side circulation pumps (P-GL and P-HP). P-HP is also modulated considering HP's capacity to assure a $\Delta T$ of 7 K.

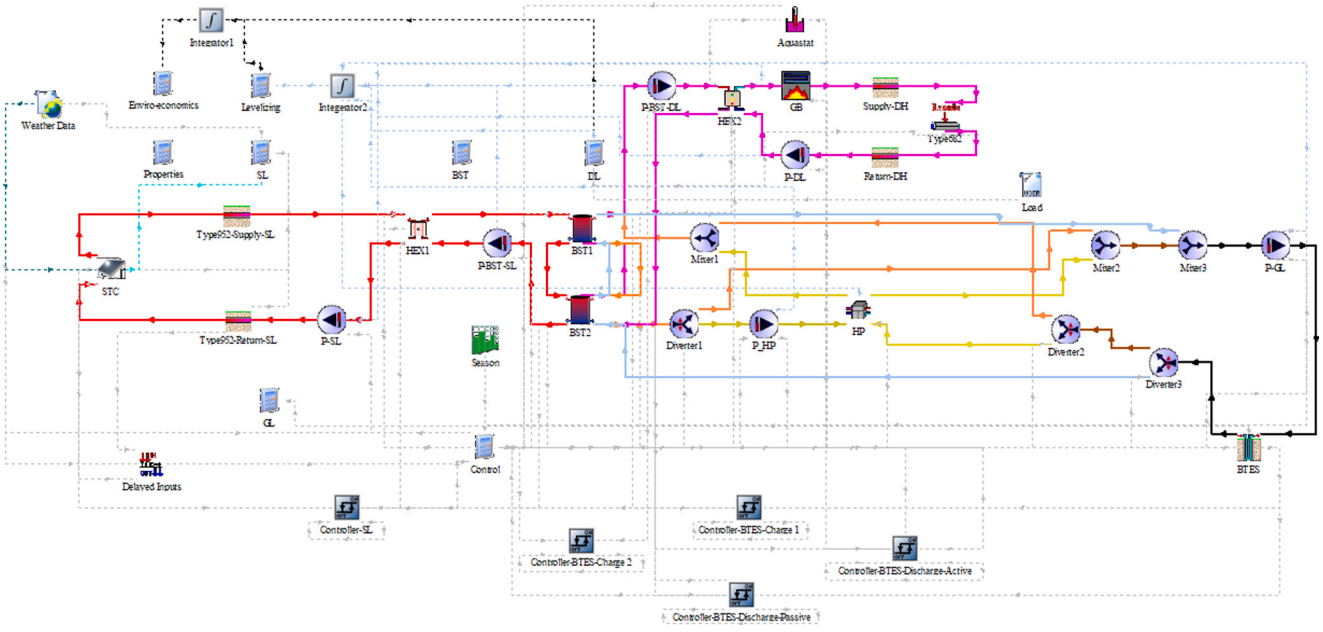


**Fig. B.3.1.** TRNSYS model of H2 scenario.

**Table B.3.1**
Controller parameters of type 2b for the ground loop in active discharge mode.

| | |
|---|---|
| BTES controller (active discharge)<br>heating seasons | $\Delta T_L = 2, \Delta T_H = 6, T_{max} = 45^{\circ}C$<br>$T_H$ : load-side supply temperature<br>$T_L$ : bottom temperature of the colder BST (BST2)<br>$T_{in}$ : top temperature of the warmer BST (BST1) |

## B.4. TRNSYS model of active heating (GSHP)

TRNSYS model of H3 scenario is shown in Fig. B.4.1. The underground, without charging or regeneration, is utilized as an efficient heat source for the GSHPs. The control strategy is of the differential controller of the GL is similar to the active mode of H2 scenario, cf. Table B.3.1, which switches on the HP, P-HP and P-GL. P-HP is also modulated considering HP's capacity to assure a design ΔT of 7 K. Like previous scenarios, P-BST-DL, is controlled by output control signals from the district loop HEX (Type 512) to assure that the DL design $T_{sup}$ is met. The GB, which is turned on or off by an aquastat supplies the load that cannot be delivered by the BSTs.

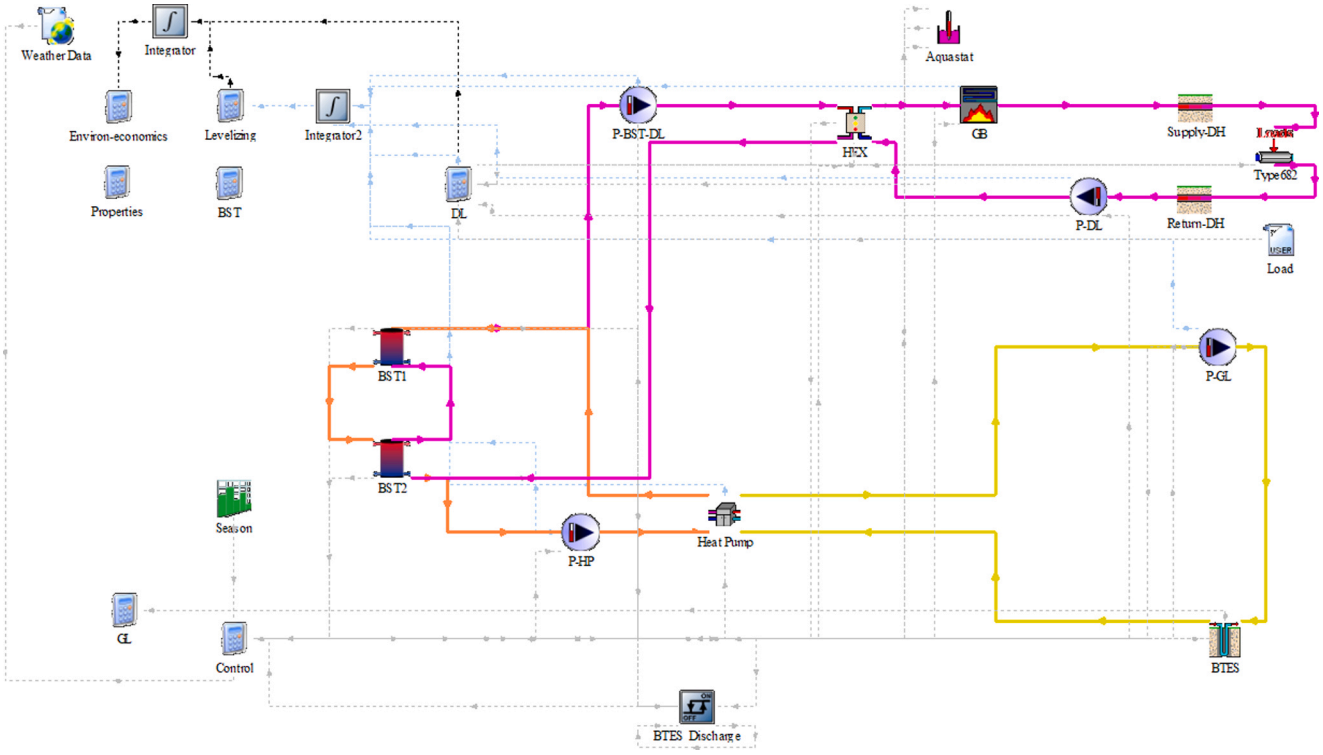


**Fig. B.4.1.** TRNSYS model of H3 scenario.

## B.5. TRNSYS model of passive cooling (BTES)

TRNSYS model of HC3 scenario is shown in Fig. B.5.1.. The heating load is supplied actively with the same strategy as H3. Controller parameters of the GL differential controller in active heating and passive cooling modes can be found Table B.5.1. In cooling season, the return fluid from the underground district pipes (Type 952) is delivered to the HEX-CL (based on Type 512 adapted to cooling operation, cf. Chapter 6.1). The output control signal of the HEX controls the operation of P-BST-DL so that the design load-side $T_{sup}$ of 18 °C is assured. The cold fluid from bottom of BST2 is delivered to HEX-CL through diverter3, which has one control value in each season. This results in an increase in its temperature when it leaves the HEX. It then enters the top of the BST1, from where it is directly transferred through diverter1 to the GL, for passive cooling, or to the HP, for active cooling. The active cooling occurs when the passive discharge controller is off and district $T_{sup}$ exceeds 18 °C. When the active cooling is activated, it turns on the HP and P-HP, which is modulated to supply the design cooling ΔT. Active or passive cooling strategy on the GL side is defined by diverter4, which diverts the return fluid from the GL to the bottom of BST2 or to the source side of the HP. As the load profile shows (Fig. 3), switching between heating and cooling is done once per year. Therefore, the BSTs are cooled down with the same cooling strategy, before the start of the cooling season.

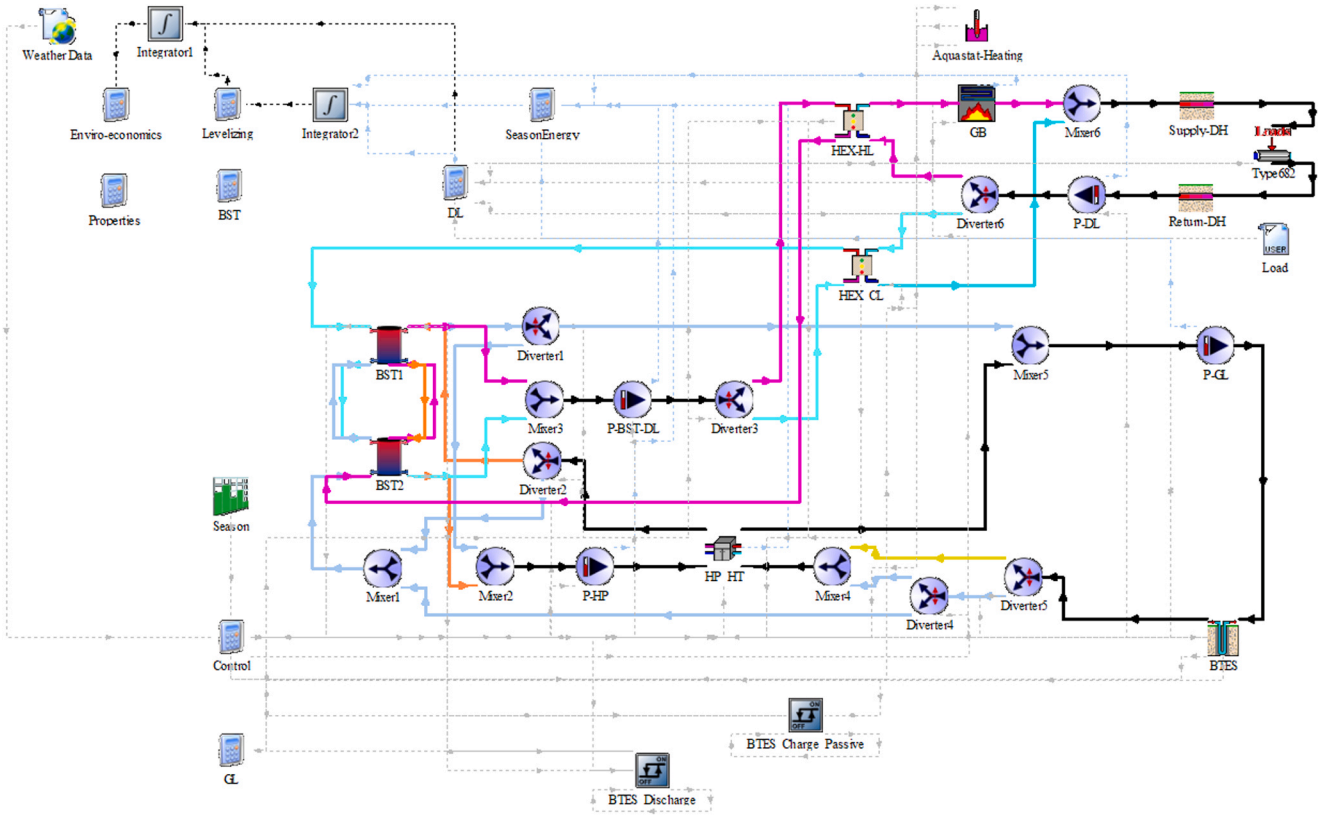


**Fig. B.5.1.** TRNSYS model of HC3 scenario.

**Table B.5.1**
Controller parameters of type 2b for the BTES in charge and discharge mode.

| | |
|---|---|
| BTES controller (passive charge)<br>cooling seasons | $\Delta T_L = 1, \Delta T_H = 4, T_{max} = 22^{\circ}C$<br>$T_H$ : top temperature of the warmer BST (BST1)<br>$T_L$ : average soil temperature near boreholes (edges)<br>$T_{in}$ : average soil temperature near boreholes (edges) |
| BTES controller (active discharge)<br>heating seasons | $\Delta T_L = 2, \Delta T_H = 6, T_{max} = 45^{\circ}C$<br>$T_H$ : load-side supply temperature<br>$T_L$ : bottom temperature of the colder BST (BST2)<br>$T_{in}$ : top temperature of the warmer BST (BST1) |

## *B.6. TRNSYS model of ASHP*

TRNSYS model of ASHPs is shown in Fig. B.6.1. Two ASHPs (Type 118) are considered to supply the cooling demand of a single family house and an office building locally. The calculations are then expanded to the number of each building type, cf. chapter 3.1. The operational data of the ASHPs are selected based on a manufacturer's catalog [50] and given as an input file to Type 118. The HPs are inverter type that use a variable-speed compressor to meet the design temperature at each time step. Chilled water temperature (22 °C), chilled water flow rate and ambient temperature are given as inputs to the ASHPs to meet the cooling load, with a chilled water supply temperature of 18 °C, which is a design parameter.

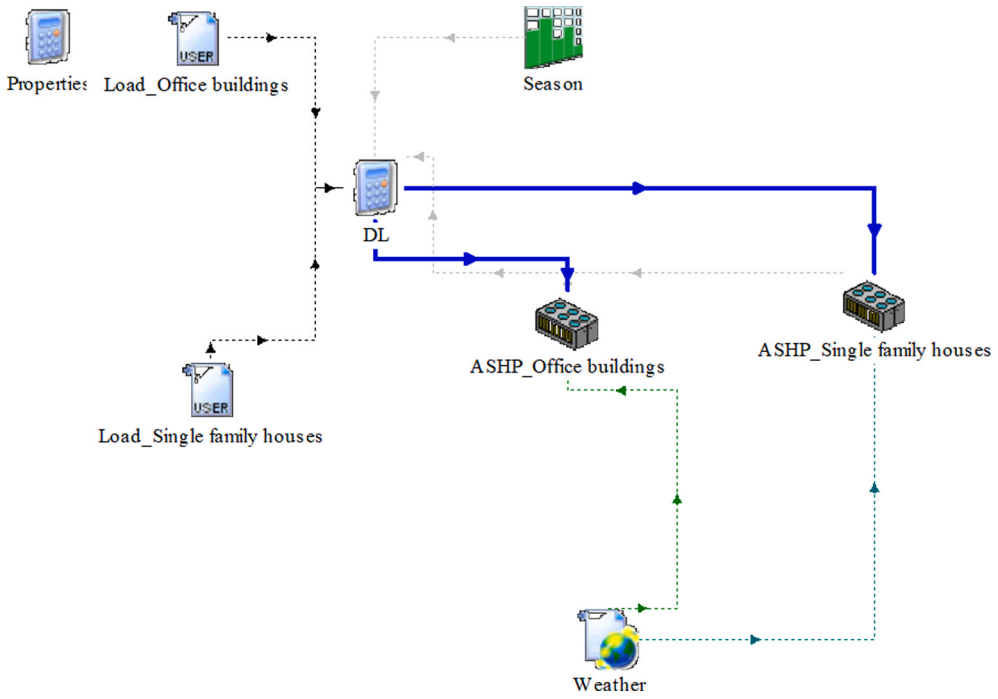


**Fig. B.6.1.** TRNSYS model of ASHPs.

## Appendix C. . MATLAB settings

See Table C.1.

**Table C.1**
NSGA II optimization settings [65].

| Parameter | Definition | Value |
|---|---|---|
| CrossoverFcn | The fraction of the population at the next generation, not including elite children, that the crossover function creates. | 0.8 |
| FunctionTolerance<br>MaxStallGenerations | The algorithm stops if the average relative change in the best fitness function value over MaxStallGenerations generations is less than or equal to FunctionTolerance. | 1e-4<br>100 |
| MaxGenerations | Maximum number of iterations before the algorithm halts. | 200 × number of variables |
| PopulationSize | Size of the population. | 50 |
| ParetoFraction | Sets the fraction of individuals to keep on the first Pareto front while the solver selects individuals from higher fronts | 0.35 |
| SelectionFcn | Function that selects parents of crossover and mutation children. | Selectiontournament[a] |

a) Tournament selection chooses each parent by choosing size players at random and then choosing the best individual out of that set to be a parent.

## References


[1] Ritchie H. Sector by sector: where do global greenhouse gas emissions come from?, https://ourworldindata.org/ghg-emissions-by-sector; 2021 [accessed 02 December 2021].
[2] European Commission. Energy performance of buildings directive, https://ec.europa.eu/energy/topics/energy-efficiency/energy-efficient-buildings/energy-performance-buildings-directive_en; 2021 [accessed on 02 December 2021].
[3] European Commission. Heating and Cooling, https://ec.europa.eu/energy/topics/energy-efficiency/heating-and-cooling_en; 2021 [accessed on 02 December 2021].
[4] Mutschler R, Rüdisüli M, Heer P, Eggimann S. Benchmarking cooling and heating energy demands considering climate change, population growth and cooling device uptake. Applied Energy. 2021;288:116636. . 10.1016/j.apenergy.2021.116636.
[5] Werner S. European space cooling demands. Energy. 2016;110:148–56. https://doi.org/10.1016/j.energy.2015.11.028.
[6] Eurostat. https://ec.europa.eu/eurostat; 2019 [accessed on 02 December 2021].
[7] UN. World urbanization prospects: The 2014 revision. United Nations Department of Economics and Social Affairs, Population Division: New York, NY, USA. 2015; 41.
[8] Rezaie B, Rosen MA. District heating and cooling: Review of technology and potential enhancements. Appl Energy 2012;93:2–10. https://doi.org/10.1016/j.apenergy.2011.04.020.
[9] Lund H, Werner S, Wiltshire R, Svendsen S, Thorsen JE, Hvelplund F, et al. 4th Generation District Heating (4GDH): Integrating smart thermal grids into future sustainable energy systems. Energy. 2014;68:1–11. https://doi.org/10.1016/j.energy.2014.02.089.
[10] Hemmatabady H, Formhals J, Welsch B, Schulte DO, Sass I. Optimized Layouts of Borehole Thermal Energy Storage Systems in 4th Generation Grids. Energies. 2020; 13:4405. 10.3390/en13174405.
[11] Connolly D, Lund H, Mathiesen BV, Werner S, Möller B, Persson U, et al. Heat Roadmap Europe: Combining district heating with heat savings to decarbonise the EU energy system. Energy policy. 2014;65:475–89. https://doi.org/10.1016/j.enpol.2013.10.035.
[12] Duffie JA, Beckman WA. Solar engineering of thermal processes. John Wiley & Sons 2013.
[13] Pinel P, Cruickshank CA, Beausoleil-Morrison I, Wills A. A review of available methods for seasonal storage of solar thermal energy in residential applications. Renew Sustain Energy Rev 2011;15(7):3341–59. https://doi.org/10.1016/j.rser.2011.04.013.
[14] Welsch B. Technical, Environmental and Economic Assessment of Medium Deep Borehole Thermal Energy Storage Systems. 2019.
[15] Dincer I, Rosen MA. Thermal energy storage systems and applications: John Wiley & Sons; 2021.
[16] Mangold D, Miedaner O, Tziggili EP, Schmidt T, Unterberger M, Zeh B. Technisch-wirtschaftliche Analyse und Weiterentwicklung der solaren Langzeit-Wärmespeicherung. Schlussbericht zum BMU-Forschungsvorhaben N. 2012; 329607.
[17] VDI. VDI 4640 Thermal Use of the Underground. VDI-Gessellschaft Energie und Umwelt (GEU), Berlin; 2019.
[18] Skarphagen H, Banks D, Frengstad BS, Gether H. Design Considerations for Borehole Thermal Energy Storage (BTES): A Review with Emphasis on Convective Heat Transfer. Geofluids 2019;2019:1–26. https://doi.org/10.1155/2019/4961781.
[19] Schulte DO, Rühaak W, Oladyshkin S, Welsch B, Sass I. Optimization of Medium-Deep Borehole Thermal Energy Storage Systems. Energy Technology. 2016;4(1): 104–13. https://doi.org/10.1002/ente.201500254.
[20] Reuss M. The use of borehole thermal energy storage (BTES) systems. Advances in thermal energy storage systems. Elsevier 2015:117–47.
[21] Geothermie A. Shallow Geothermal Systems-Recommendations on Design, Construction, Operation and Monitoring: Ernst et Sohn; 2016.
[22] Welsch B, Rühaak W, Schulte DO, Bär K, Sass I. Characteristics of medium deep borehole thermal energy storage. Int J Energy Res 2016;40(13):1855–68. https://doi.org/10.1002/er.3570.
[23] Formhals J, Hemmatabady H, Welsch B, Schulte DO, Sass I. A Modelica Toolbox for the Simulation of Borehole Thermal Energy Storage Systems. Energies. 2020;13: 2327. https://doi.org/10.3390/en13092327.
[24] Lanahan M, Tabares-Velasco PC. Seasonal thermal-energy storage: A critical review on BTES systems, modeling, and system design for higher system efficiency. Energies. 2017;10:743. https://doi.org/10.3390/en10060743.
[25] Rees S. Advances in ground-source heat pump systems. Woodhead Publishing 2016.
[26] Bauer D, Marx R, Nußbicker-Lux J, Ochs F, Heidemann W, Müller-Steinhagen H. German central solar heating plants with seasonal heat storage. Sol Energy 2010;84 (4):612–23. https://doi.org/10.1016/j.solener.2009.05.013.
[27] Bauer D, Drück H, Lang S, Marx R, Plaz T. Weiterentwicklung innovativer Technologien zur solaren Nahwärme und saisonale Wärmespeicherung. Forschungsbericht zum BMWi-Vorhaben A. 2016;325998.
[28] Welsch B, Göllner-Völker L, Schulte DO, Bär K, Sass I, Schebek L. Environmental and economic assessment of borehole thermal energy storage in district heating systems. Appl Energy 2018;216:73–90. https://doi.org/10.1016/j.apenergy.2018.02.011.
[29] Formhals J, Feike F, Hemmatabady H, Welsch B, Sass I. Strategies for a transition towards a solar district heating grid with integrated seasonal geothermal energy storage. Energy. 2021;228:120662. https://doi.org/10.1016/j.energy.2021.120662.
[30] Elhashmi R, Hallinan KP, Chiasson AD. Low-energy opportunity for multi-family residences: A review and simulation-based study of a solar borehole thermal energy storage system. Energy. 2020;204:117870. https://doi.org/10.1016/j.energy.2020.117870.
[31] Shah SK, Aye Lu, Rismanchi B. Multi-objective optimisation of a seasonal solar thermal energy storage system for space heating in cold climate. Appl Energy 2020; 268:115047. https://doi.org/10.1016/j.apenergy.2020.115047.
[32] Renaldi R, Friedrich D. Techno-economic analysis of a solar district heating system with seasonal thermal storage in the UK. Appl Energy 2019;236:388–400. https://doi.org/10.1016/j.apenergy.2018.11.030.
[33] Leidos Canada, https://www.dlsc.ca/reports/JUL2015/2012-2013%20Annual%20Report%20v07%20FINAL.pdf; 2014 [accessed on 02 December 2021].
[34] Klein S, Beckman W, Mitchell J, Duffie J, Duffie N, Freeman T, et al. TRNSYS 18 – A TRaNsient system simulation program, user manual. Solar Energy Laboratory Madison: University of Wisconsin-Madison. 2017.
[35] MATLAB. 9.2.0.556344 (R2017a). Natick, Massachusetts: The MathWorks Inc.; 2017.
[36] Razmi AR, Arabkoohsar A, Nami H. Thermoeconomic analysis and multi-objective optimization of a novel hybrid absorption/recompression refrigeration system. Energy. 2020;210:118559. https://doi.org/10.1016/j.energy.2020.118559.
[37] Mesquita L, McClenahan D, Thornton J, Carriere J, Wong B. Drake landing solar community: 10 years of operation. Proceedings of the ISES Conference Proceedings, Abu Dhabi; 02.11.2017; 2017.
[38] Sibbitt B, McClenahan D, Djebbar R, Thornton J, Wong B, Carriere J, et al. The performance of a high solar fraction seasonal storage district heating system–five years of operation. Energy Procedia 2012;30:856–65. https://doi.org/10.1016/j.egypro.2012.11.097.
[39] McDowell TP, Thornton JW. Simulation and model calibration of a large-scale solar seasonal storage system. Proceedings of SimBuild. 2008;3:174–81.
[40] Verstraete A. Étude d'une communauté solaire avec stockage thermique saisonnier par puits géothermiques. École Polytechnique de Montréal 2013.
[41] Government of Canada. Environment and natural resources, https://climate.weather.gc.ca/historical_data/search_historic_data_e.html; 2021 [accessed on 02 December 2021].
[42] Saloux E, Candanedo JA. Control-oriented model of a solar community with seasonal thermal energy storage: development, calibration and validation. J Build Perform Simul 2019;12(5):523–45. https://doi.org/10.1080/19401493.2018.1523950.
[43] Klein S, Beckman W, Mitchell J, Duffie J, Duffie N, Freeman T, et al. Trnsys 18—Volume 6 Multizone Building Modeling with Type 56 and Trnbuild. Solar Energy Laboratory, University of Wisconsin: Madison, WI, USA. 2017:199.
[44] Meteotest. Meteonorm: Irradiation data for every place on Earth, http://www.meteonorm.com/; 2020.
[45] DIN4108. Thermal protection and energy economy in buildings - Part 2: Minimum requirements to thermal insulation. Beuth, Berlin. 2013.
[46] VDI. VDI 4640 Thermal Use of the Underground. VDI-Gessellschaft Energie und Umwelt (GEU), Berlin; 2010.
[47] Nußbicker J, Mangold D, Heidemann W, Müller-Steinhagen H. Bau und Betrieb des Erdsonden-Wärmespeichers in Neckarsulm-Amorbach, 8. Geothermische Fachtagung & . 2004;5.
[48] Yang L, Entchev E, Rosato A, Sibilio S. Smart thermal grid with integration of distributed and centralized solar energy systems. Energy. 2017;122:471–81. https://doi.org/10.1016/j.energy.2017.01.114.
[49] Viessmann GmbH, https://www.viessmann.de/de/gewerbe/waermepumpe/grosswaermepumpen/vitocal-350-ht-pro.html; 2020 [accessed on 02.12.2021].
[50] Viessmann GmbH, http://www.energas.co.za/wp-content/uploads/2019/02/A12.-Heat-Pumps.pdf 2020 [accessed on 22.02.2021].
[51] Fritsche UR, Greß H-W. "Der nicht erneuerbare kumulierte Energieverbrauch und THG-Emissionen des deutschen Strommix im Jahr 2016 sowie Ausblicke auf 2020 bis 2050,". Internationales Institut für Nachhaltigkeitsanalysen und-strategien GmbH (IINAS), Darmstadt. 2018.
[52] IINAS. IINAS (2017): GEMIS - Globales Emissions-Modell Integrierter Systeme - model and database, version 4.95, in International Institute for Sustainability Analysis and Strategy, ed., Darmstadt. . 2017.
[53] Short W, Packey DJ, Holt T. A manual for the economic evaluation of energy efficiency and renewable energy technologies. Golden, CO (United States): National Renewable Energy Lab; 1995.
[54] Mauthner F, Herkel S. Technology and demonstrators-Technical Report Subtask C-Part C1: Classification and benchmarking of solar thermal systems in urban environments. Gleisdorf: IEA Solar Heating & Cooling Technology Collaboration Programme; 2016.
[55] Hellstrom G. Ground heat storage: Thermal analyses of duct storage systems. I. Theory, PhD thesis, Lund University. 1992.
[56] Bär K, Arndt D, Fritsche J-G, Götz AE, Kracht M, Hoppe A, et al. 3D-Modellierung der tiefengeothermischen Potenziale von Hessen-Eingangsdaten und Potenzialausweisung. Zeitschrift der Deutschen Gesellschaft für Geowissenschaften 2011;162(4):371–88.
[57] LIPP GmbH, https://www.lipp-system.de/tanks/thermal-storage-tanks; 2019 [accessed on 02 December 2021].
[58] Bauer D, Heidemann W, Müller-Steinhagen H. Der Erdsonden-Wärmespeicher in Crailsheim. Bad Staffelstein, Germany: Kloster Banz; 2007.
[59] Viessmann GmbH, https://www.viessmann.de/de/wohngebaeude/gasheizung/vitocrossal.html; 2020 [accessed on 02 December 2021].
[60] Gallagher K, Sambridge M. Genetic algorithms: a powerful tool for large-scale nonlinear optimization problems. Comput Geosci 1994;20(7-8):1229–36. https://doi.org/10.1016/0098-3004(94)90072-8.

[61] Kalogirou SA. Artificial neural networks in renewable energy systems applications: a review. Renew Sustain Energy Rev 2001;5(4):373–401. https://doi.org/10.1016/S1364-0321(01)00006-5.
[62] Jiang H, Xi Z, A. Rahman A, Zhang X. Prediction of output power with artificial neural network using extended datasets for Stirling engines. Appl Energy 2020; 271:115123. https://doi.org/10.1016/j.apenergy.2020.115123.
[63] Moré JJ. The Levenberg-Marquardt algorithm: implementation and theory. Numerical analysis: Springer; 1978. p. 105-16.
[64] Deb K, Pratap A, Agarwal S, Meyarivan T. A fast and elitist multiobjective genetic algorithm: NSGA-II. IEEE Trans Evol Comput 2002;6(2):182–97.
[65] The MathWorks Inc., https://www.mathworks.com/help/gads/gamultiobj.html; 2021 [accessed on 02 December 2021].
[66] KFW. Erneuerbare Energien – Premium, https://www.kfw.de/inlandsfoerderung/Unternehmen/Energie-Umwelt/Finanzierungsangebote/Erneuerbare-Energien-Premium-(271-281)/#; 2021 [accessed on 02 December 2021].
[67] Nuss P. Life Cycle Assessment Handbook: A Guide for Environmentally Sustainable Products; Curran, A.M., Ed.; John Wiley & Sons, Inc.: Hoboken, NJ, USA; Scrivener Publishing LLC: Salem, MA, USA. 2015.
[68] Greening B, Azapagic A. Domestic heat pumps: Life cycle environmental impacts and potential implications for the UK. Energy. 2012;39(1):205–17. https://doi.org/10.1016/j.energy.2012.01.028.
[69] Gebhardt M, Kohl H, Preisatlas ST. Ableitung von Kostenfunktionen für Komponenten der rationellen Energienutzung. Institut für Energie und Umwelttechnik eV (IUTA). Duisburg-Rheinhausen. 2002:1–356.
[70] Luo J, Rohn J, Bayer M, Priess A. Thermal performance and economic evaluation of double U-tube borehole heat exchanger with three different borehole diameters. Energy Build 2013;67:217–24. https://doi.org/10.1016/j.enbuild.2013.08.030.
[71] Croteau R, Gosselin L. Correlations for cost of ground-source heat pumps and for the effect of temperature on their performance. Int J Energy Res 2015;39(3):433–8.
[72] Lizana J, Ortiz C, Soltero VM, Chacartegui R. District heating systems based on low-carbon energy technologies in Mediterranean areas. Energy. 2017;120: 397–416. https://doi.org/10.1016/j.energy.2016.11.096.
[73] Statistisches Bundesamt. Preise–Daten zur Energiepreisentwicklung, https://www.destatis.de/DE/Themen/Wirtschaft/Preise/Publikationen/Energiepreise/energiepreisentwicklung-pdf-5619001.pdf?_blob=publicationFile; 2020 [accessed on 02 December 2021].
[74] Schlesinger M, Hofer P, Kemmler A, Kirchner A, Koziel S, Ley A, et al. Entwicklung der Energiemarkte-Energiereferenzprognose: Studie im Auftrag des Bundesministeriums für Wirtschaft und Technologie, https://www.bmwi.de/Redaktion/DE/Publikationen/Studien/entwicklung-der-energiemaerkte-energiereferenzprognose-endbericht.html; 2014 [accessed on 02 December 2021].